Properties and Potential Applications of Biomimetic and Bio-derived Nanofluidic Systems

A dissertation submitted to the
Indian Institute of Technology Guwahati as
partial fulfilment of the Degree of

DOCTOR of PHILOSOPHY

Submitted by

Tukhar Jyoti Konch

Roll No: 166122027

Department of Chemistry
Indian Institute of Technology Guwahati
Guwahati-781039 Assam, India
July 2021

Dedicated to My Family

INDIAN INSTITUTE OF TECHNOLOGY

GUWAHATI

Department of Chemistry

STATEMENT

I hereby declare that the matter embodied in this thesis entitled **"Properties and Potential Applications of Biomimetic and Bio-derived Nanofluidic Systems"** is the results of the investigations carried out by me at the Department of Chemistry, Indian Institute of Technology Guwahati, Assam, India under the guidance of Associate Professor, Dr. Kalyan Raidongia.

In keeping with the general practice in reporting scientific observations, due acknowledgement has been made whenever the work described is based on the findings of other investigators.

Tukhar Jyoti Konch

Date: July, 2021

IIT Guwahati

INDIAN INSTITUTE OF TECHNOLOGY

GUWAHATI

Department of Chemistry

CERTIFICATE

This is to certify that the matter embodied in this thesis entitled **"Properties and Potential Applications of Biomimetic and Bio-derived Nanofluidic Systems"** has been carried out by **Mr Tukhar Jyoti Konch** at the Department of Chemistry, Indian Institute of Technology Guwahati, Assam, India. It has not been submitted elsewhere for the award of any degree or diploma.

Date: July, 2021
IIT Guwahati

Dr. Kalyan Raidongia
(Thesis Supervisor)
Department of Chemistry
Indian Institute of Technology Guwahati
Guwahati-781039
Assam, India

PREFACE

The present thesis, entitled as "**Properties and Potential Applications of Biomimetic and Bio-derived Nanofluidic Systems**" is divided into two parts *viz* "Part A: Fabrications of bio-mimetic nanofluidic systems and their potential applications" and "Part B: Extraction of bio-derived nanochannels for nanofluidic study". The overall thesis consists of six chapters based on detailed investigation of various biomimetic and bio derived materials and their potential nanofluidic applications. Chapter 1 contains a general overview of biomimetic nanofluidic system, related electro-kinetic phenomena, their fabrication techniques and their various applications.

Chapter 2 elaborates the fabrication of nanofluidic membrane via intercalating humic acid moieties into the interlayer galleries of bare graphene oxide sheets. Crosslinking of humic acids in appropriate composition not only conferred mechanical strength but also enhanced chemical robustness of the membranes. The percolated network of molecularly sized channels of the humic acid intercalated graphene oxide membranes exhibits characteristic nanofluidic phenomena which is exploited to achieved time efficient molecular separation and harvest energy from salinity gradient.

In chapter 3, inherent anion selectivity of CoAl layered double hydroxide is exploited to achieved multidirectional applications. Unlike the conventional 2D materials, LDH possess permanent positive charge and LDH based nanofluidic conduits panoply remarkable anion conductivity in the surface charge governed region. The perm-selective nature of P-LDHM is also utilized to harvest electricity from salt concentration gradient via applying the principle of RED. Moreover, the p-LDHM based shows shape dependence ionic transport behaviour, while a rectangularly cut p-LDHM device shows linear *I-V* curve, the triangularly cut p-LDHM

shows non-linear *I-V* curves similar to a diode. The ionic current rectifying behaviour of triangular p-LDHM can also be utilized to achieve anion pumping under the presence of a fluctuating electrical potential with a mean value of zero.

Chapter 4, contain a general overview of bio-derived nanofluidic systems, their structural integrity and their potential applications in the field of nanofluidic study.

In chapter 5, we have demonstrated the utilization of biological nanochannels extracted from potato tuber for nanofluidic study. The biological nanochannels possess various elementary nanofibrils with permanent negative charges and this perm-selective property of bio-derived nanochannels can be utilized to harvest electricity aided by an enzymatic decomposition reaction. Moreover, the trans-membrane voltage generated as such can be utilized for label free electrical monitoring of enzymatic reaction.

In chapter 6, we have utilized another bio-derived material in the form of leaf vein network extracted from peepal tree via microbial delignification process. The naked leaf veins exhibit remarkable flux (evaporation rate 1.5 kg m^{-2} h^{-1}) of capillary evaporation under ambient condition (25 °C and 30 % RH), close to the photothermal material-based evaporators reported in the recent literature. Naked veins with remarkable evaporation efficiency are found to be suitable for applications like water desalination and streaming potential harvesting.

ACKNOWLEDGEMENTS

I would like to take the opportunity here to thank all the wonderful people who stood beside me throughout my doctoral journey. It would have been impossible to achieve my goals without all the helping hands.

Foremost, I wish to express my gratitude to my supervisor, Dr. Kalyan Raidongia, for giving me this opportunity to work under his supervision. I and my work have immensely benefited from his proficient guidance and mentorship, without his limitless efforts, expert guidance and valuable suggestions this thesis would not have been possible. He has been a continuous source of encouragement throughout my Ph.D. life and it is my good fortune to have him as my supervisor.

Besides my supervisor, my sincere gratitude goes out to my doctoral committee members: Prof. Biplab Mondal, Dr. Dipankar Srimani and Dr. Sunanda Chatterjee, for their insightful comments and encouragement throughout the evaluation process of my annual progress and synopsis seminars.

My sincere acknowledgement to Dr. Anki K. Reddy for extending his kind support to carry out molecular dynamics simulations and guiding us with the theoretical results.

I am thankful to the Indian Institute of Technology Guwahati for providing me the fellowship and to the Department of Chemistry and Central Instruments Facilities (CIF) for providing the research and instrumental facilities. I extend my sincere gratitude to the staff members of the chemistry office and student affairs. Thank you for providing all the assistance and reminders during five years of my PhD. Furthermore, I am thankful to all the FESEM, FETEM, RAMAN, AFM, and pXRD operators for their help. I would like to express honest appreciation to Mr.

Imdadul Islam and Mr Anirudha Gogoi for their kind assistance in teaching various scientific instrument.

My deepest gratitude to my past and present lab members Dr. Rajkumar Gogoi, Kundan Saha, Jumi Deka, Subhasmita Saikia, Arindom Bikash Neog, Trisha Dutta, Madhurjya Buraguhain, Priyamjeet Deka, Raktim Gogoi and Barsha Rani Bora for their kind and helping hands in every aspect during these five years. My heartiest appreciation to few of my project students Kushdeep, Akash and Kaushik for their helping hands in my research work.

I convey my special thanks to my teachers Dr. Raghav Parajuli, Dr. Biman Chandra Chetia, Dr. kusum Kumar Bania for their encouragement and motivation throughout my academic carrier.

I would like to thank my IITG colleagues Kangkan Talukdar, Bikash sharma, Monikha chetia, Adit Sah, Rabindranath Paul, Rahul Sharma, Rabu Changmai, Monoranjan Knower and other research scholars of the Department of Chemistry for their motivation and cooperation during my stay. Also, I am grateful to my friends Monti Gogoi, Gunjan Saikia, Bhargab Das, Uttam Pradhan, Rituparna Dutta, Dewan Sonowal, Monoranjan Gogoi and many more for their constant supports, encouragement and all the help they bestowed whenever required.

Finally, most importantly, my deep and honest gratefulness to my family for their constant and unparalleled love and support throughout my journey so far.

Synopsis report

Chapter 1: Introduction to biomimetic and bio-derived nanofluidic channels:

The branch of fluid dynamic that explore the flow of liquid in structure constrained to nano-meter size regime (1-100nm) is defined as nanofluidic. Fluidic transport in and around nanofluidic structures is dominated by interactions of otherwise weak effects such as the formation of electrical double layers (EDL), attractive or repulsive forces of charged species, and entropic barriers. Typically, transport of charged species through nanometer-sized channels are dominated by the overlapping electrical double layers. One of the major difficulties in designing nanofluidic devices is the inherent complexity. The overall transport characteristics are determined by the interplay of various nanoscale or even molecular level physical, geometric, and chemical factors. Biological ion channels, however, are known for their capability of elaborately manipulating these factors to regulate the transmembrane ionic flow, which plays a crucial role in a number of physiological processes. Mimicking the biological systems researchers has tried to demonstrate its artificial counterparts. In light of this feature, various ion-channel-mimetic smart 1D nanofluidic systems have been developed that can reproduce functions analogous to its parent biological systems. Although systematic research in single-pore devices makes the physical picture of this nanofluidic process much clear, it is still far from competent for practical applications. Toward practical applications, one major challenge is to extrapolate individual nanofluidic devices to macroscopic platform in a cost-efficient way. Interestingly solution to the above mentioned dilemma was also resolved from natural inspirations in the form of lamellar microstructure of nacre, in which soft materials (polysaccharides and proteins) are sandwiched between hard inorganic layers (aragonite platelets), forming an alternatively arranged layered structure. This novel method of material

designing and large-scale integration of individual artificial nanofluidic channels into a macroscopic platform give birth a new research filed known as the 2D nanofluidics. Via a simple vacuum filtration process, colloidal dispersions of individual 2D nanosheets can be reassembled into a densely stacked multi-layered structure. The interstitial space between opposite 2D nanosheets can be treated as lamellar channels for mass and charge transport.

With the rising global climate change and resource shortage, increased attention has been paid to design environmentally friendly materials. Bio-derived materials, being abundant, renewable and environmentally friendly are considered attractive alternatives that can potentially meet some of these challenges. Biopolymer nanofibrils are universal nano-building blocks in natural materials and there lies a significant possibility to extract this biomaterial to design and create new materials and nanostructures. Outstanding properties of biopolymer materials profit from their multiscale hierarchical structures. The common property of natural structural materials is the nanoscale interaction between polysaccharides and silk-like protein, where the structural proteins confer the mechanical properties, structure and function of biological systems. Nature creates sophisticated materials with such hierarchical structure with assembly of interconnected nanofibrils and elementary fibrils that make the percolated nanochannel networks. The abundant hydroxyl and carboxyl groups on the surface of these nanofibers and elementary fibrils provided the nanochannels permanent negative surface charges that can attract layers of counter ions adjacent to the fibres and ensure a surface charge-governed ion transport.

Chapter 2: Nanofluidic transport through humic acid modified graphene oxide nanochannels:

In this chapter we have exploited the chemical similarity of graphene oxide (GO) and humic acid to fine-tune the ionic and molecular transport properties of a lamellar GO membrane. Even

though layered material based lamellar membranes panoply excellent selectivity for ionic and molecular separation but they suffer from lower permeability issues. The sub-nanometer-size pores of lamellar membranes that facilitate unprecedented ionic/ molecular selectivity also impede molecular permeability. The natural choice to overcome the problem of low permeability is to increase the channels' heights by applying spacers between the sheets. However, application of incompatible inert spacers could sacrifice the selectivity and robustness of the pristine membranes. Here, we have explored the possibility of tuning the transport characteristics of GO membranes without sacrificing their lamellar structure or altering the channels' heights. Humic acid, a naturally occurring organic material, is applied here to tune the structure of GO nanochannels. With a structure chemically and physically similar to that of GO, humic acid causes an all-round improvement of the GO lamellar membrane. Humic acids, the mixtures of acidic organic polymers that are believed to be a product of the natural break-down process of plant- and animal based materials, were extracted and purified following the standard alkaline-acid treatment-based procedure. Introduction of humic acid (in 10, 15 and 20 wt. %) is found to improve the nanofluidic transport characteristics, such as ionic mobility, molecular selectivity, diffusivity and permeability, of the GO membrane. Remarkably, the membrane prepared with 15% humic acid displayed superior proton mobility (μ_H = 1.04 ×10^{-4} cm^2 V^{-1} s^{-1}), in-plane diffusivity (D = 4.8×10^{-6} cm^2 s^{-1}), and cross-plane permeability (P_L = 2.03×10^{-4} mm g cm^{-2} s^{-1} bar^{-1}) to the pure GO and other composite membranes. The favorable nanofluidic characteristics of the 15% membrane are attributed to the larger effective heights of the 2D nanochannels, derived from the onset point of the surface charge governed ionic conductivity of the membranes. The activation energy of proton transport (0.07 to 0.1 eV) confirmed the occurrence of a Grotthuss-like hopping mechanism in all the GO-HA membranes. Introduction of humic acid into two-dimensional GO channels also improved the solution stability and mechanical robustness of the pristine GO

membrane. The lamellar GO-HA membranes were also found to be suitable for energy harvesting applications such as direct methanol fuel cells and reverse electrodialysis.

Chapter 3: Uphill anion pumping through triangular nanofluidic device of reconstructed layered double hydroxide:

The synchronous growth in the research related to the novel 2D nanomaterials boosted diverse real time application related to two-dimensional nanofluidics. After the initial demonstration with graphene oxide, numerous other layered materials such as h-BN, clay minerals, Mxenes, carbon nitride were utilized to create nanofluidic devices with unique characteristics, mostly via reconstruction of their respective exfoliated layers. Remarkably, till date, most of these nanofluidic studies are limited to only cation-selective nanochannels. However, complimentary regulation of both the cation and anion is essential for futuristic applications such as osmotic power generation, seawater desalination, and regulated ionic/molecular transportations. Several indirect approaches, like modification of the reactive surface groups (-COOH or -OH) of the 2D sheets and intercalation of cationic polymers were adopted to imbue anion selectivity to the nanofluidic channels. The application of foreign materials/molecules not only involves tedious chemical processes but also disturb the well-defined 2D structure of the nanochannels. Along with decreasing nanofluidic confinements, it also exerts adverse effects on the mechanical, chemical, and thermal stability of the nanofluidic membranes. Therefore, direct utilization of positively charged 2D sheets for the fabrication of anion-selective nanofluidic nanochannels is the need of the hour. In the present work, we have utilized the inherent positive charges of the cationic Co-Al layered double hydroxide (CoAl LDH) to create anion-selective nanofluidic channels. The lamellar membrane of CoAl LDH was exploited for preparing a triangular ion-pump capable of transporting anions against the concentration gradient, as well as to fabricate salinity gradient-driven energy harvesting devices.

Nanofluidic membranes prepared by self-assembling exfoliated layers of CoAl LDH exhibit excellent anionic transport characteristics. At the surface-charge-governed regime, the positively charged CoAl LDH membrane (p-LDHM) showed a remarkable OH^- ion conductivity of ~ 2 mS cm^{-1}. The remarkable mobility of OH^- ions (4×10^{-4} cm^2 V^{-1} S^{-1}) in the atomically thin channel of p-LDHM is attributed to the tiny activation energy (0.09 eV) required for Grotthuss-like hopping of the ions between the positive charges of densely packed CoAl LDH layers. The lamellar p-LDHM was also found to be suitable for energy harvesting via salinity gradient, and power density up to 0.7 Wm^{-2} was achieved under a 1000-fold concentration gradient. The triangular p-LDHM displays a diode-like non-linear *I-V* curve, attributed to a combination of unipolar conductivity of counter-ions inside the 2D nanochannels and geometrical asymmetry. The triangular p-LDHM pumps anions against the concentration gradient (up to 1000 fold), under fluctuating external potentials of zero means.

Chapter 4: Disposable fluidic devices of bio-nanochannels for enzymatic monitoring and energy harvesting:

While artificial devices and machineries are providing countless conveniences to modern life, their disposals are creating major havoc in the environment. Therefore, in recent years, numerous research efforts are being dedicated to replace unsustainable materials and devices with environmentally benign alternatives of similar functionalities. For example, different kind of electronic devices such as solar cells, diagnostic tools, sensors, and artificial tissues, etc. have been developed based on sustainable materials obtained from the environment. Similarly, the outstanding new properties of liquids confined inside nanometer sized containers promise numerous technological breakthroughs in the areas of water treatment, energy harvesting, and molecular sieving. Studies on confined liquid also open up an avenue to understand the activity of biological nanochannels creating a platform to exploit them for various biomedical and chemical applications. However, in practice, the excellent properties of numerous biological

channels readily available to us have not been explored yet for the technological applications. Here, we have the possibilities of employing large number of bio-channels readily available in our surroundings for the technological advancements in multiple directions.

Solanum tuberosum or potato, taken here as a model system exhibits very interesting internal features in the micro and nanometer regime just like any other biological system. It also possesses a highly active fluidic network across the cell walls to facilitate communications and transport of materials between the plant cells. The nature of molecular/ ionic transport through the narrow (3-5 nm) channels of the cell walls are not free or bulk-like, and it is strongly influenced by the interactions with the non-diffusible anions of the cell wall, like the carboxyl groups of the galacturonic acids of pectin. These characteristics of the bio-nanochannel based nanofluidic devices give rise to various nanofluidic phenomena like surface-charged-governed ionic conductivity and development of the transmembrane potential. The cation-selective nature of the bio-channels was also exploited to harvest a continuous supply of power up to 74 mW m^{-2} for 3h from the enzymatic decomposition of urea. The transmembrane potential across the bio-channels was also explored for label-free electrical monitoring of the enzymatic reaction inside the biological medium. Electrical monitoring on the kinetics of urease at different reaction temperatures suggested that inside biological medium the reaction goes through a pathway of lower activation energy (31.1 kJ) than that in the bulk environment (34.1 kJ).

Chapter 5: Remarkable Rate of Water Evaporation through Naked Veins of Natural Tree-leaf:

In the last few decades, numerous unforeseen properties and phenomenon specific to systems confined in nanometer size regime have been uncovered, and many of them were also exploited for technological applications. One of the recently discovered astonishing nano phenomena are

the enormous rate of evaporation from capillary nanochannels. In this article, we have studied evaporation behaviour through the hierarchical structure of the vein network extracted from the fallen leaves and exploited the same for seawater desalinations. We observed that even in the absence of photoactive materials, the naked vein network exhibited an evaporation rate at par with the man-made systems with highly efficient photo-thermal materials. A remarkable kinetically controlled evaporation process powered by extended evaporation area, decreasing thermal resistance between the solid substrate and the liquid/vapour interface, and efficient exchange of heat and mass between water molecules confined inside porous biological channels and atmosphere is accounted for the remarkable performance of the leaf vein based natural evaporator. The network of hierarchical channels, precisely designed by nature for efficient transportation of liquids were extracted from matured and fallen leaf samples collected directly from nature. To begin with, the leaves of *Ficus religiosa* (Peepal tree) were soaked in tape water for around 25 days. During the prolonged soaking period, most of the soft cells of the leaf blade (cuticle, epidermis, the mesophyll) were digested by the microbes releasing a funky smell. Remarkably, the vein structure of leaf epipodium was not affected by the digestion process. The naked leaf veins exhibit remarkable flux (evaporation rate 1.5 kg m^{-2} h^{-1}) of capillary evaporation under ambient condition (25 °C and 30 % RH), close to the photothermal material-based evaporators reported in the recent literature. Even, inside a dark box, naked veins exhibit an evaporation rate up to 4.5 kg m^{-2} h^{-1} (at 30 % relative humidity (RH), and wind speed of 22 km h^{-1}). The evaporation rates can be further improved by tuning the environmental conditions like temperature, humidity, and wind speed. The mechanistic studies performed with variable atmospheric conditions (temperature, humidity, wind-speed) suggest the evaporation process through the naked veins to be a kinetic-limited process. Naked veins with remarkable evaporation efficiency are found to be suitable for applications like water desalination and streaming potential harvesting. Experiments with the naked veins also shows

that the biofluidic channels in leaf not only exhibit the characteristics of surface-charge-governed ionic transport but also support an exceptional water transport velocity of 1444 μm s^{-1}. Looking at the variety and abundance, the vein-based evaporator could provide an ideal platform for futuristic water treatment and energy harvesting devices.

Conclusion:

In conclusion, we have explored the properties of biomimetic and bio-derived nanochannels and of utilized the same to fabricate nanofluidic conduits for multiple application purposes, notably for manipulating molecular/ionic transportation, concentration gradient based energy harvesting, uphill ion pumping, level free monitoring of enzymatic reactions and water steam generation. Chapter-1 describes a general overview of biomimetic nanochannels with special emphasis on their structural integrity and peculiar electrokinetic properties. Chapter-2 demonstrates fabrication of mechanically robust composite membranes using graphene oxide and humic acids. Introduction of humic acid into two-dimensional GO channels was found crucial in improving the nanofluidic properties of the pristine GO membrane. The percolated network of ultra-thin nanochannel exhibiting fascinating transport properties could find applications in the areas of selective molecular/ionic transport, catalysis, energy harvesting and storage, methanol fuel cell and gas sensing. Chapter-3 demonstrated the direct utilization of positively charged 2D sheets (CoAl LDH) for the fabrication of anion-selective nanofluidic nanochannels. A biomimetic strategy was utilized to fabricate the anion selective lamellar membrane (p-LDHM). The lamellar membrane was exploited for preparing a triangular ion-pump capable of transporting anions against the concentration gradient, as well as to fabricate salinity gradient-driven energy harvesting devices. In chapter-4 we have we have demonstrated the utilization of bio derived disposable nanofluidic conduits extracted from potato tuber for nanofluidic study. The cation-selective nature of the bio-channels was also exploited to harvest

electrical energy from concentration driven process aided by an enzymatic decomposition reaction of urea. The transmembrane potential across the biochannels was also explored for label-free electrical monitoring of the enzymatic reaction inside the biological medium. In Chapter-5 we have demonstrated another bio-derived material in the form of precisely designed leaf network and exploited its technological applications. The naked leaf veins exhibit remarkable flux of capillary evaporation under ambient condition (25 °C and 30 % RH), close to the photothermal material-based evaporators reported in the recent literature. This feature makes our bio-derived evaporator a potential candidate to be utilized as low grade steam generator. Naked veins with remarkable evaporation efficiency are found to be suitable for applications like water desalination and streaming potential harvesting.

Table of contents

Part A: Fabrications of Bio-mimetic Nanofluidic Systems and their Potential Applications

Chapter 1

Introduction to Biomimetic Nanofluidic Channels

1.1: Introduction to nanofluidic phenomena

Water is one of the most precious molecules in nature and is vital for all known life forms. Most of the biological process involves water transportation through precisely designed micro/nano capillaries. Hence, it is crucial to explore the various properties of water under nanoscale confinement and exploit them to develop futuristic integrated engineering devices. This fluid dynamic branch that studies the flow of liquid in structures constrained to nano-meter size regime is defined as nanofluidic.[1] Unlike conventional bulk systems, nanofluidic transport is predominantly determined by the properties of the charges residing on the surface of channel wall, leading to diverse transportation phenomena. For instance, inside the charged nanochannels, the conductivity of ionic species is directed by the nature of the surface charge, mainly in the low electrolyte concentration regime and with adequately narrow nanochannels, the transporting species are sieved by either size exclusion principle or molecular recognition effects.[2-5]

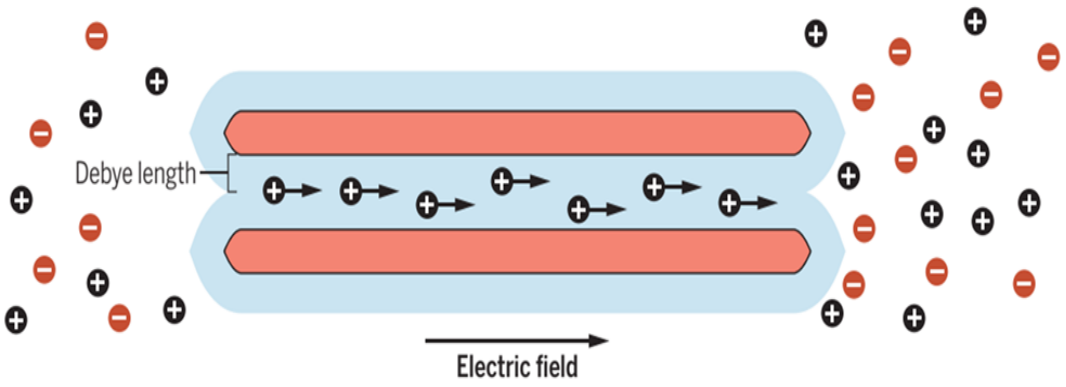

Fig. 1.1: Selective ion transport in nanochannel: Negatively charge nanochannel formed between two neighbouring sheets, where Debye layers overlap to create unipolar 2D ion channels with enhanced cationic conductivity. (Image copied from *Science*, 2016, **351**, 1395.)

The transportation of ions in nanofluidic channels is intensely influenced by forming an electric double layer (EDL) of ionic species at the nanochannels wall and electrolyte interface. The EDL can be defined by the Debye layer (λ) thickness and the difference in number densities of counter-ions and co-ions within the EDL regime.[6,7] The charge density gradient arising out of

perm-selectivity of the nanochannels ensures an utterly unique ion transport dynamic inside the nanochannels, which is significantly different from ionic transportation in the typical bulk electrolyte solution. Under such circumstances, the ionic conductance of the nanochannels becomes completely surface-charge-dominated and hence is feebly influenced by overall ion densities in the reservoir. So ionic conductance a few orders of magnitude higher than that of the bulk solution is observed inside the nanochannels, especially in lower electrolyte concentrations.[8-11] Following this peculiar conductivity pattern of nanochannels, tremendous attention has been paid to engineered nanofluidic channels' geometry and surface chemistry to manipulate the molecular/ionic transport behaviours. These studies provide a comprehensive understanding of the fundamental nanofluidic transport mechanisms and boost diverse applications in biomedical analysis, DNA sequencing, ultrafiltration and separation, seawater desalination, and nanofluidic energy conversion.[12-18]

1.2: Nature inspired strategy in nanofluidic study

The significant complexity in nanofluidic study lies in the device fabricating step.[19,20] The ionic/molecular transportation inside nanochannels entity is governed by synchronous interaction of numerous nano and molecular level geometric, chemical, and physical phenomena, which is very difficult to regulate in an artificially built unit. However, biological ion channels are known for their skill of intricately handling these elements to control diverse vital phenomena necessary for life. Mimicking these natural systems, researchers have tried to imbue unique functionalities to their artificial counterparts. In this context, various smart nanofluidic devices has been designed to replicate the gating, rectifying, and stimuli-responsive functions observed in biological systems.[21] Taking inspiration from several well-organized structure-function relationships in biological systems, modern innovative materials have been designed and applied accordingly in real-time intending to circumvent many of the previously

impossible challenges. For example, a negatively charged nanopore is required to mimic the cation-selective nature of the biological ion channels, which can be fabricated by drilling pores

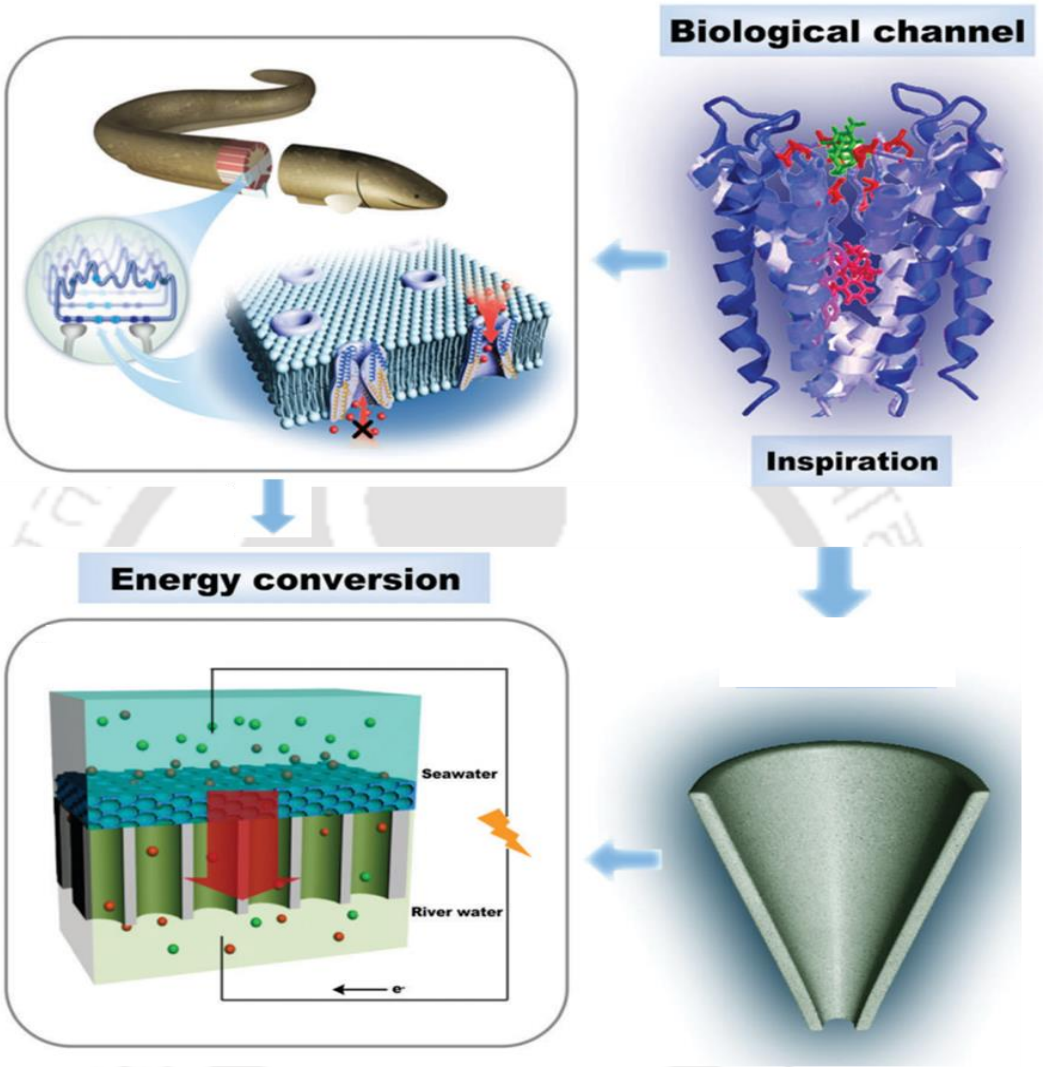

Fig. 1.2: Nature-inspired methodology of designing synthetic nanofluidic systems: Electric eel organ mimicking nanofluidic devices for osmotic energy conversion. To reproduce the bioelectric process, 1D solid-state conical nanopore is used. (Image copied from *Chem. Soc. Rev.*, 2018, **47**, 322.)

in polymeric thin films with a high energy focused ion beam.[22,23] Similarly, for mimicking the ion rectifying behaviour of bio channels, asymmetrically shaped nanopores are required, which can be fabricated from polymeric membranes via the track- etching method.[24-26] In early studies dealing with single nanopore-based devices, the foremost goal was to recognize the fundamental principles of nanofluidic transport. The extensive research on the fundamentals of nanofluidics in model single nanopore fabricated by semiconductor techniques such as

chemical etching and photolithography has enriched our knowledge of novel phenomena in nanofluidic such as high ionic conductivity, charge selectivity, and ion regulation. Even though systematic research in single-nanopore-based devices provided us with clear physical picture of these fundamental nanofluidic phenomena, it is still not adequate for real-time applications. The state-of-the-art model 1D nanofluidic structures are confined to only single-channel geometry, and their designing relies on highly sophisticated scientific tools and expensive material processing phases.

1.3: Self-assembly approach to fabricate bio-mimetic 2D nanofluidic systems

One major challenge faced by the researchers in this area is extrapolating the property and phenomena observed in the individual nanochannels into a macroscopic platform toward practical applications/demonstrations. Interestingly, this dilemma was also resolved by taking inspirations from natural systems, in the form of the lamellar microstructure of nacre, where soft materials (proteins and polysaccharides) were sandwiched between two hard inorganic layers (aragonite platelets) establishes a periodically stacked lamellar assembly.[27,28] This unique method of material designing and bulk scale integration of individual artificial nanofluidic channels into a macroscopic platform give birth new research field known as 2D nanofluidics. With the help of a simple vacuum-assisted filtration, colloidal dispersions of individual 2D nanoflakes can be reassembled into a multi-layered macroscopic dimension with numerous interstitial void spaces between two adjacent 2D nanoflakes for unprecedented transportation of charge and mass. More interestingly, before the self-assembly process, the individual nanosheets can be chemically modified in bulk solution, which offers a facile strategy to incorporate desired functional moieties into the 2D nanofluidic systems. This strategy provides very high efficacy compared to the infancy chemical modification method on 1D nanofluidic channels, which is highly diffusion-limited. The molecular transport through

the 2D layered membrane is confined in the inter-lamellar spaces, which can be accomplished either in the vertical (cross-plane) or in the horizontal direction (in-plane).[29]

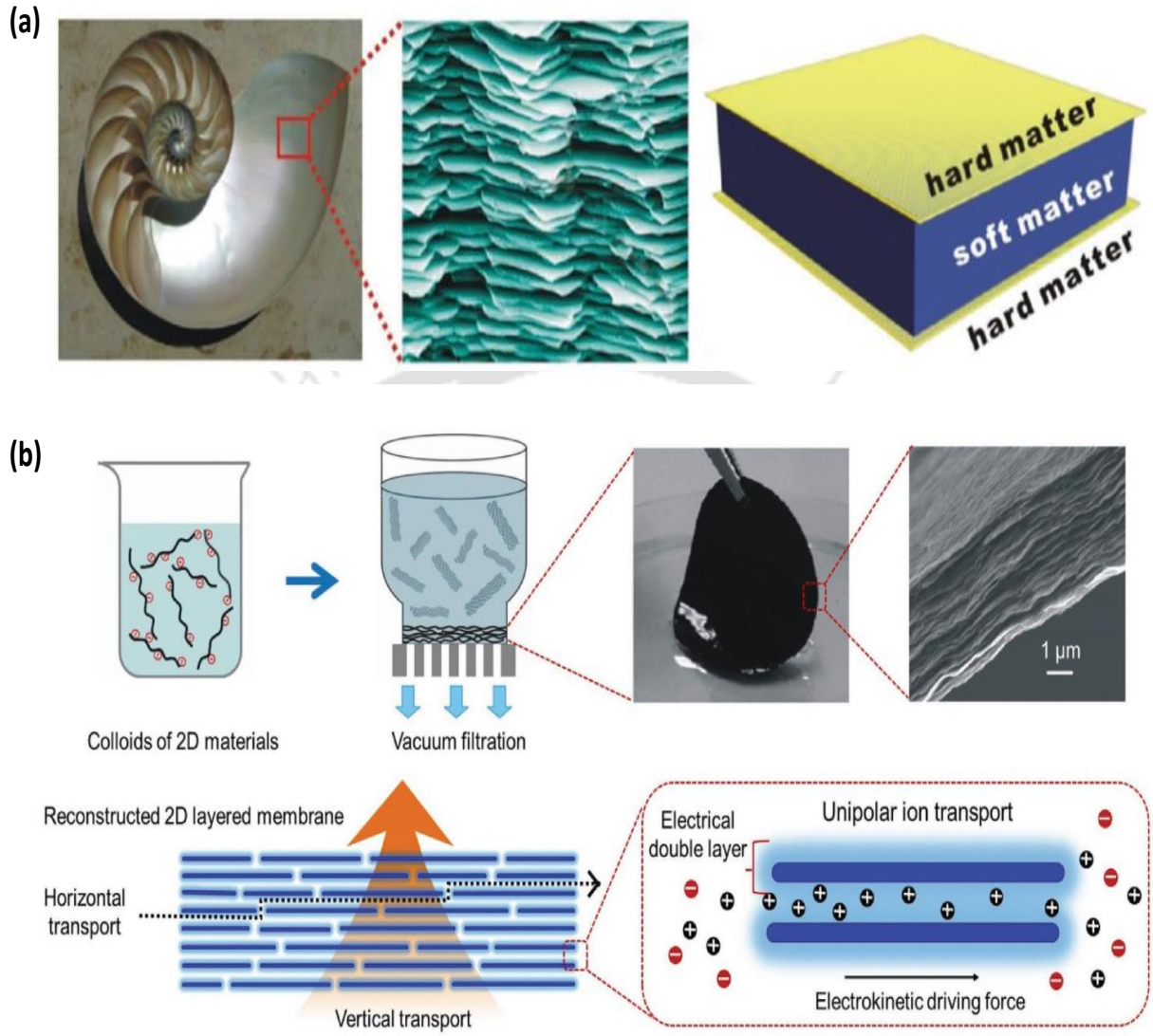

Fig. 1.3: Reconstruction of exfoliated colloids into a macroscopic 2D membrane inspired by the lamellar structure of nacre: (a) The lamellar microstructure of nacre. (b) Colloids of 2D materials can be self-assembled into a membrane structure following the microstructure of nacre. The percolated network between two individual sheets felicitated surface charge governed ion transport. (Image copied from *Chem. Soc. Rev*., 2017, **46**, 5400.)

Huang and his co-worker for the first time demonstrated that a 2D lamellar Graphene oxide membrane (GOM) is an ideal candidate for nanofluidic ion transport.[30] They showed surface-charge governed ionic transport through the self-assembled GOM in the horizontal (in plane) direction where the conductivity of different electrolyte at the low concentration regime was found be higher than that of the bulk electrolyte (shown in Fig.1.4).

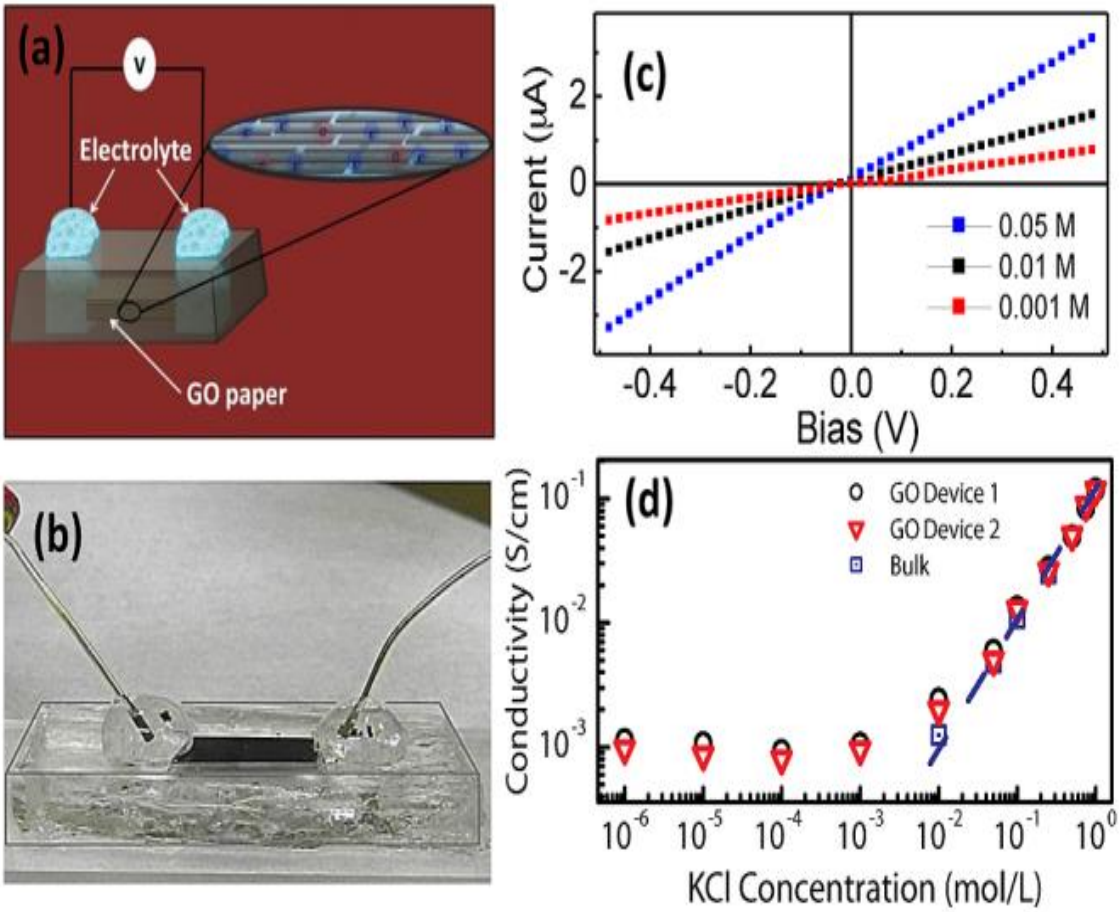

Fig. 1.4: In-plane water diffusion through lamellar GOM: (a) Schematic representation and (b) photo of the nanofluidic device of GO membrane. (c*) I-V* curves recorded through GOM at different KCl electrolyte concentrations and (d) ionic conductivity as a function of KCl electrolyte concentration measured through the nanofluidic channels of GO. (Image copied from *J. Am. Chem. Soc*., 2012, **134**, 16528.)

Geim and co-workers reported an ultra-thin GOM impermeable to all gases and liquids despite being only a few atoms thick, but showing super-permeability towards water and water vapour. [31]Water through the 2D nano-capillaries in GOM travels in the vertical direction (Shown in Fig.1.5). This vertical water transportation mode enables these 2D layered materials to be applied in membrane separation and filtration techniques. Inspired from the pioneering work of Huang *et al.* and Geim *et al.*, various 2D layered materials like hexagonal boron nitride (h-BN), clay minerals, transition metal dichalcogenide (TMDC), transition metal oxides (TMO), MXene, *etc.* has been demonstrated as building blocks to construct nanochannels.[32-34] Synthetic lamellar membranes made from 2D materials are attracting tremendous attention

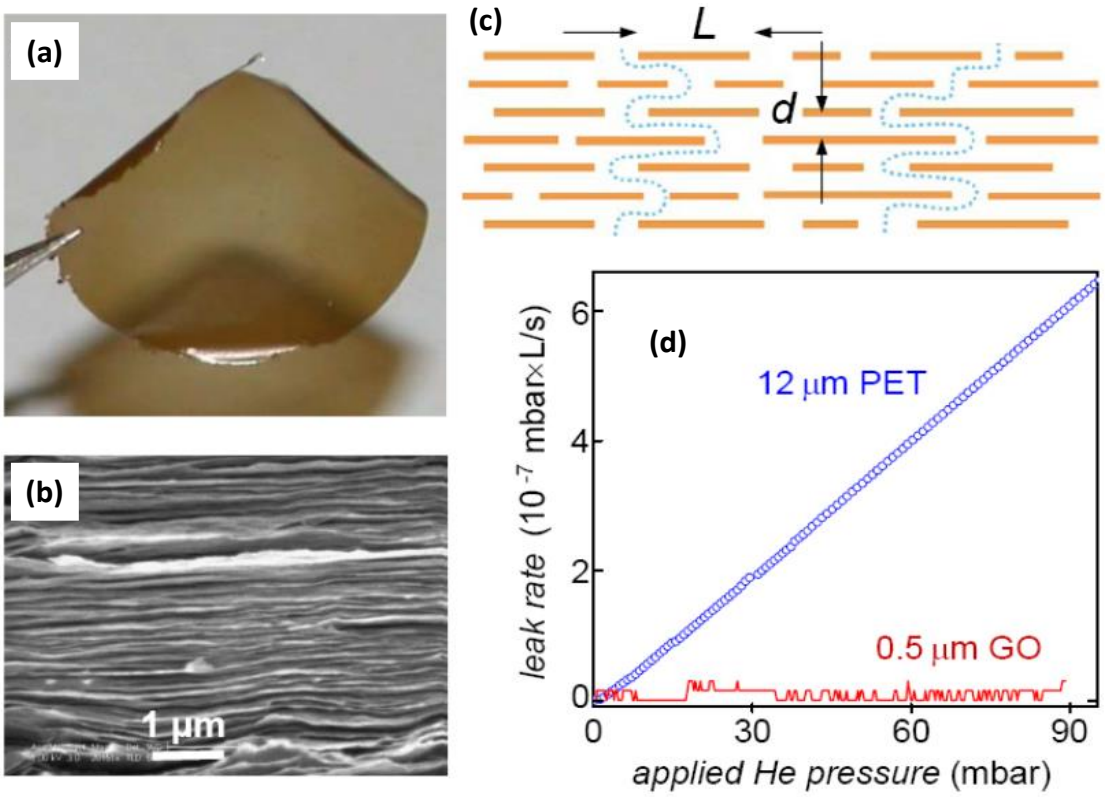

Fig. 1.5: Cross plane water diffusion through lamellar GOM: (a) Digital image of a GO membrane. (b) Cross-sectional FESEM image of a GO membrane showing the stacking of individual sheets in the reconstructed membrane. (c) Schematic illustration of the 2D capillaries in GO membrane showing the cross-plane water permeation through the defeats. (d) Helium permeation through GO membrane and a reference polyethylene terephthalate (PET) film. (Image copied from *Science*, 2012, **335**, 442.)

among researchers because of their exceptional properties. They can also be harnessed in a proficient way to mimic the vital activities of living organisms. Origin of inherent surface charge in the reconstructed 2D nanochannels favours guided ion transport similar to a biological charge selective membrane and opens up a new application window in hot areas such as osmotic energy conversion, biosensor, molecular separation and purification, etc.[35-37]

1.4: Application of biomimetic 2D nanofluidic channels

1.4.1: Waste water treatment and molecular separation

Mining freshwater from wastewater is a global requisite, and providing access to fresh water is an intimidating challenge because of the ever-rising population, unfurled droughts, and

thriving demands. The upsurging discrepancies compelled us to contemplate innovative technologies that can afford a clean water supply in a more energy proficient and environmentally benign way. Nature-inspired technology is abundant in our society, and exploring biological machinery's functions is our prime focus for continuing sustainable development. One representative class of these biological machinery is those of the proteins belonging to the Aquaporins (AQPs) family. AQPs are small, hydrophobic, intrinsic membrane

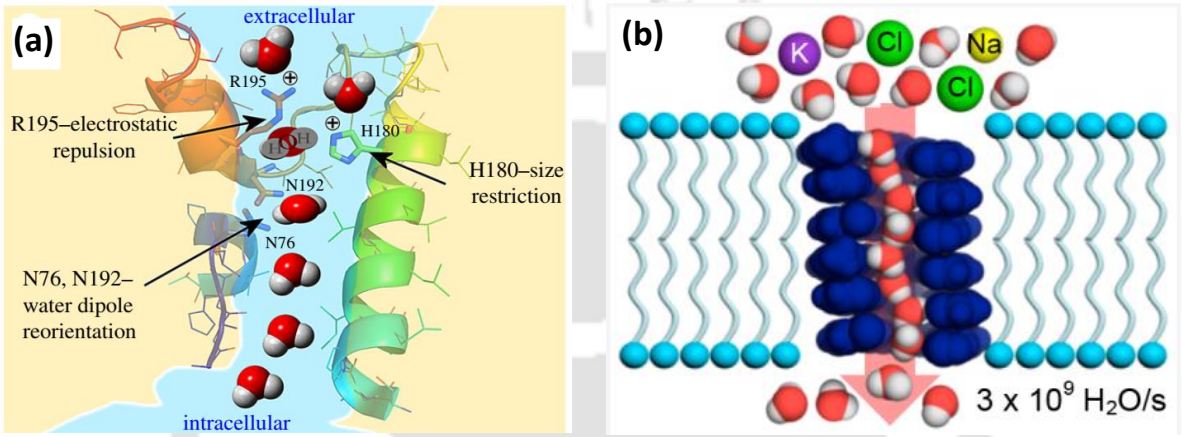

Fig. 1.6: Functional schematic view AQP1: (a) Structure of AQP1 where the presence of a specific functional group enables various charged-based separation of unwanted species. (b) Schematic presentation of aquaporin showing the ultimate water to solute rejection with unprecedented water permeation rate. (Image copied from (a) *Interface Focus*, 2018, **8**, 20170066. (b) *J. Am. Chem. Soc*. 2020, **142**, 10050.)

based proteins that facilitate water transportation across membrane barriers at an unprecedented rate while maintaining an ultimate selectivity of water-to-ion.[38] AQPs are self-assembly of multiple protein subunits within trans- membrane domains with an hourglass pore profile with a narrow constriction of ~3 A˚ in diameter. The ultimate water to ion selectivity of AQPs can be attributed to (Ar/R) selectivity filter residing at the narrowest region of the pore. The hydrophobicity of the aromatic phenylalanine group forced the water molecule to re-orient for rapid translocation via weakening the water-water H-bonding. Meanwhile, the positively charged arginine group rejects co-ionic species via electrostatic repulsions. Additionally, molecules possessing size larger than the Ar/R constriction sites are rejected via size sieving and desolvation effects.[39-41]

Following these unique features of AQPs, it has been utilized as a functional element in membranes modules for waste treatment purposes. Notwithstanding, issues regarding their low stability and difficult processability have encouraged researchers to develop their function mimicking artificial counterparts, termed artificial water channels (AWCs).[42,43] These channels provide several advantages over biological media, mainly when the fabrication of scalable membranes for applications is considered. For this purpose, carbon nanostructures are usually used to design nanofluidic devices with sub-nanometer hydrophobic pores for rapid translocation of confined water molecules. Noy *et al.* studied the permeability and selectivity of subnanometric CNTs porins inserted into lipid membranes.[44] Osmotically driven transport

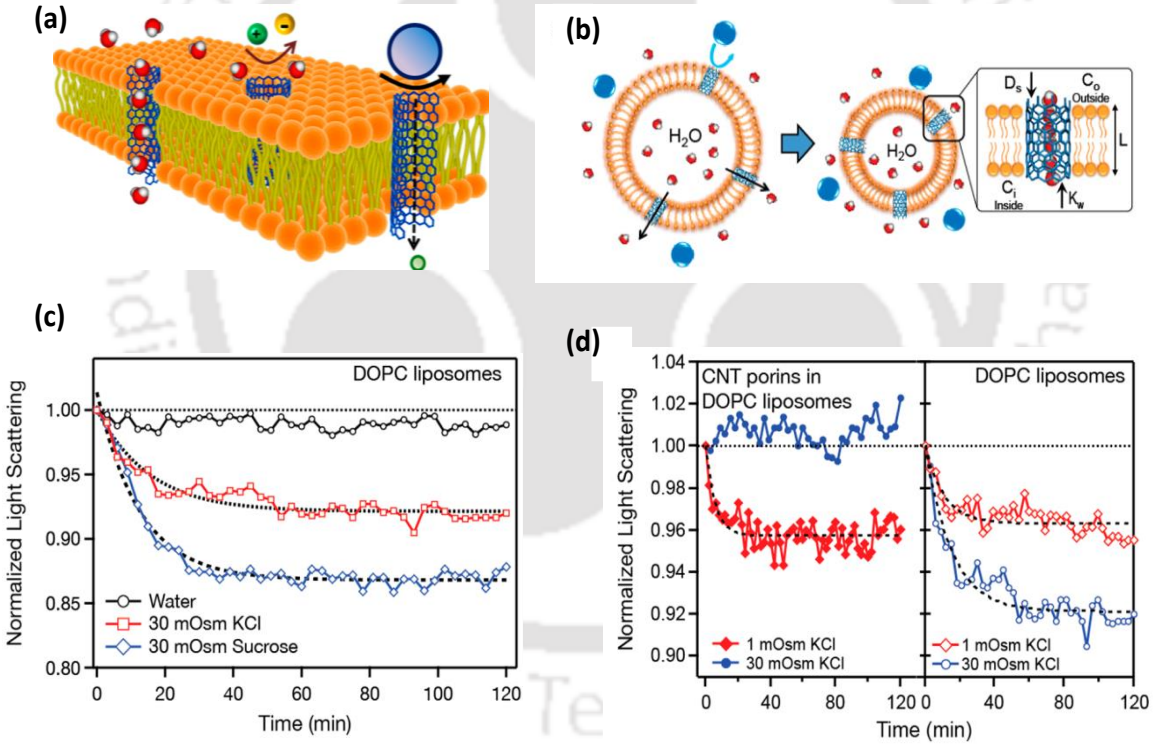

Fig. 1.7: CNT porins inserted into lipid membranes: (a) Schematic of a 3D model showing the CNT porin inserted into a lipid membrane. (b) A schematic diagram describing the conformational changes in the vesicle size under osmotic stress. The osmotic pressure difference across the lipid bilayer drive water towards outside direction and accordingly the vesicle lumen shrink in dimension. (c) Control experiments showing the size change of pure 1,2-dioleoyl-sn-glycerol-3-phosphocholine (DOPC) vesicles after exposure to sucrose, water, and KCl solutions. (d) Comparison of the vesicle conformational changes on exposure to different concentrations of KCl. The Left and right graphs correspond to kinetics obtained for the DOPC vesicles with and without CNT porins, respectively. (Image copied from *Nano Lett.* 2014, **14**, 7051.)

experiments show that ion transport rates through CNT porins are strongly influenced by the ionic strength and the hydration radii of the cationic species. When the diameter of the CNT tubes approaches 0.8 nm, it shows ultimate solute rejection while maintaining a high water permeation rate that exceeds the value of biological AQP. The rapid translocation of water can be ascribed to a single-file chain type diffusion of organized water bodies, where ion exclusion can be attributed to a Donnan type rejection mechanism. Despite the remarkable performance of CNT porins, there are still some issues such as low poly-dispersity of open CNTs, low rejection in high electrolyte concentration, the difficulty of proper alignment in the membrane matrix, and additional bulk scaling for affordable applications.

Recently, self-assembled membranes, prepared from reconstructing their corresponding exfoliated dispersions, are becoming promising candidates for controlling ionic/molecular transportation under sub-nanometre confinement. The ultrathin nanosheets of these materials on reassembling produced lamellar membrane with an ordered layer-like structure. The percolated network between the neighbouring nanosheets can serve as fast and selective channels for permeants to pass through. This facile fabrication method creates percolated channels with relatively uniform size and smaller size distribution that promises better and more predictable membrane selective performance. The properties of the individual nanosheets can also be tuned before self-assembly modification, allowing the flexible control of permeant passage to meet various selectivity requirements.

In the past decade, the discovery of graphene has enthused the synthesis of other 2D materials (2DMs), including graphene oxide (GO), layered clay minerals, layered hexagonal boron nitride (h-BN), layered double hydroxide (LDH), transition-metal dichalcogenides (TMDCs), MXenes (2D transition-metal carbide or nitrides), 2D metal-organic framework (MOF). Under these advantages, lamellar membranes have been constructed out of these 2D materials and

employed as selective ion recovery and removal units, water treatment, energy conversion, and storage devices. Behind the versatile applications of a 2D lamellar membrane in the water purification process, a fundamental question arises: why is fast water translocation achieved while maintaining a reasonable water selectivity to solute rejection. Let's consider graphene oxide membrane (GOM) as a model membrane system. The lamellar arrays of individual flakes in reconstructed GOM create numerous nano-channels that enable only the permeation of water while preventing undesired solutes according to the size exclusion principle (shown in Fig1.8).

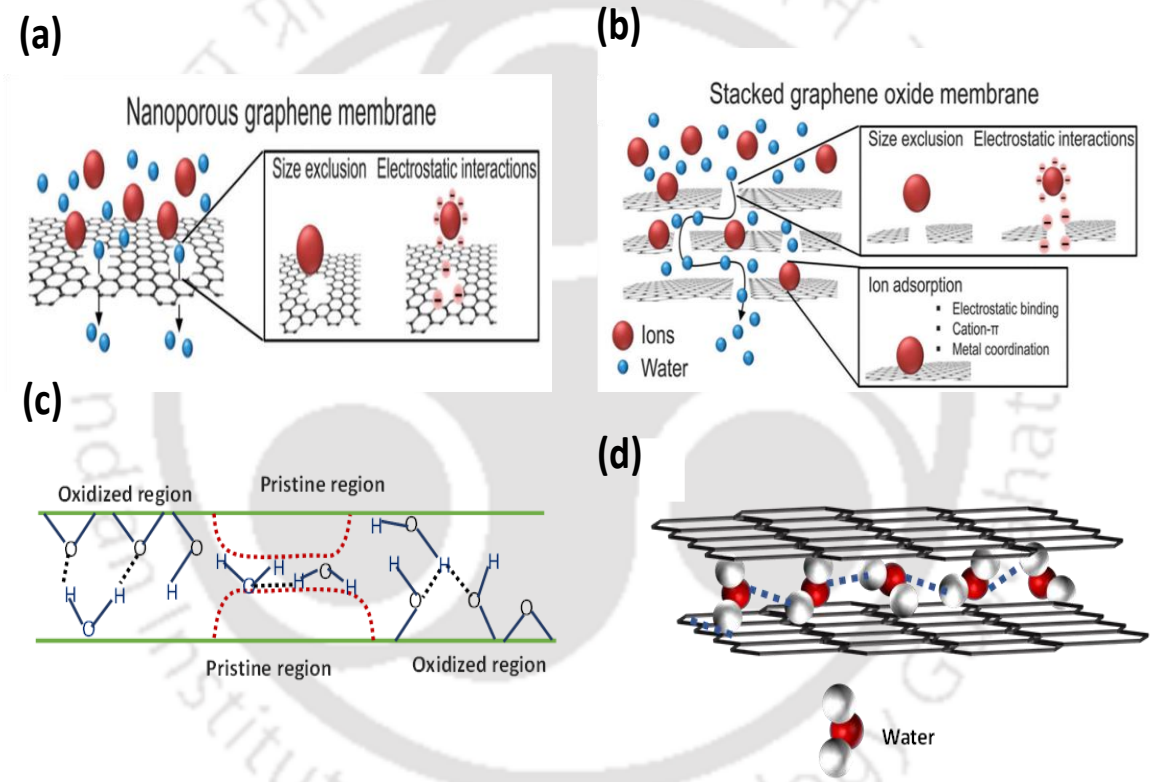

Fig. 1.8: Sieving mechanism of GOM: (a) Solute rejection in GO is achieved by size exclusion or charge-based interactions between charged species and the functional groups present in the pores. (b) In GOM, water is transported through the interlayer galleries between the sheets, the wrinkles and holes present within the GO nanosheets. (c) The pristine region allows smooth water transport, but the oxidized region perturbed the fluidity of water by invoking an H-bonding interaction. This interaction results in between the intercalated water molecules and the oxygen-containing moieties present in the channel walls. (d) Frictionless permeation of single-file chain of water molecules combined with H-bonding through hydrophobic (pristine) regions of GO nano-channels. (Image Image copied from (a-b) *J. Phys. Chem. Lett.* 2015, **6**, 2806. (c-d) *Nature*, **2015,** *519*, 443.)

In addition to that, the presence of oxygenated functionalities on the GO nanosheets, such as

hydroxyl, epoxy, and carboxyl groups, enables various covalent and non-covalent functionalization and thus executes related charge-based interactions with water pollutants. [45,46] The reason for appreciable water permeation through the GO nano capillaries is the presence of pristine regions (hydrophobic areas) where water diffusion follows a single-file diffusion type mechanism. The water molecules enter into the GO nano-channels through the defects or holes, where a capillary-like pressure created by the pristine graphene layers allows fast translocation of the entered water molecules. Meanwhile, the hydrogen bonding interactions between water molecules and the oxidized regions act as the driving force to pump more water molecules into the nano-channels.[47]

Gao *et al.* designed and fabricated ultrathin graphene membranes (uGNMs) with 2D nanochannels for organic and ionic solute rejection.[48] The uGNMs were prepared by filtering

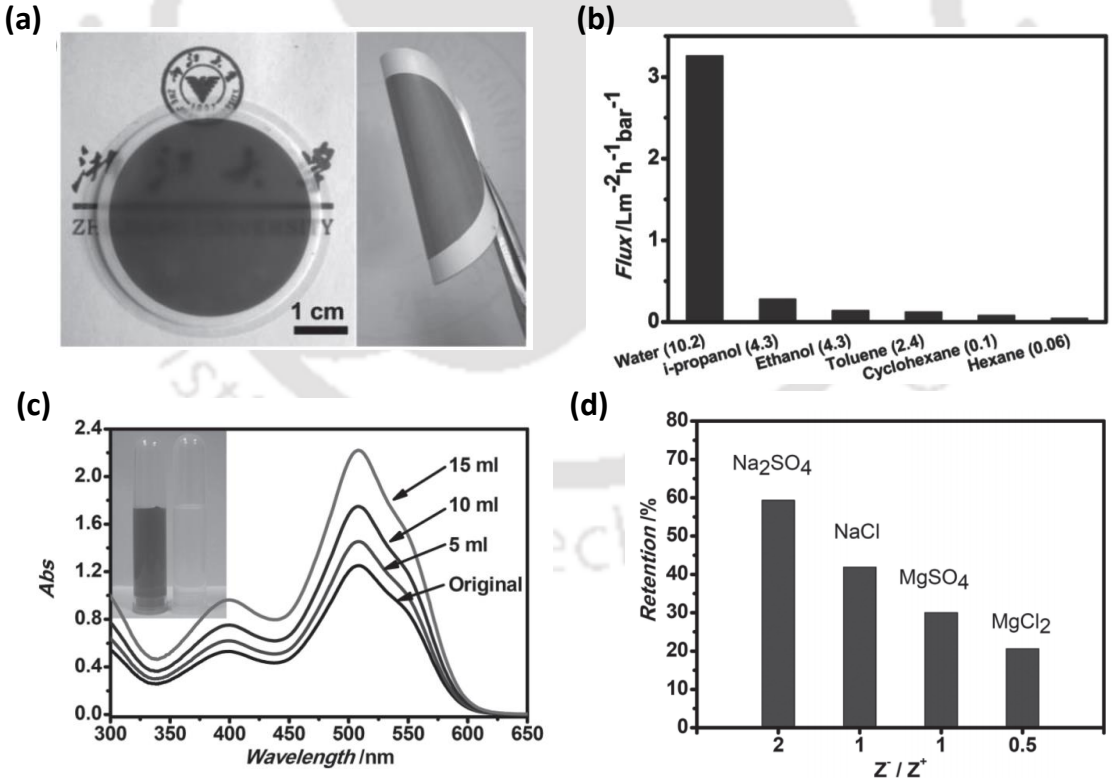

Fig. 1.9: GOM for nanofiltration: (a) Digital image of an uGNM membrane (b) Flux of various solvents when passed through uGNM under a pressure of 5 bar. (c) UV-vis spectra showing the enhancement of DR 81 concentration in the retentate side when the permeation volume was 5, 10, and 15 mL. (d) Retention of different salt solutions (0.02 M) showing as function of ion valencey. (Image copied from *Adv. Funct. Mater.* 2013, **23,** 3693.)

dilute base-refluxing reduced GO (b-rGO) dispersion on PVDF micro-filter and utilized as nanofiltration membrane (NFM) for water purification. The resulting uGNMs showed excellent retention efficiency for organic dyes and salts, accompanied by a pure water flux of 21.8 L m^{-2} h^{-1} bar^{-1}.

Nair *et al.* investigate water permeation through micro-meter-thick GO laminates both with theoretical and experimental observation.[49] The GOM is vacuum-tight in the dry state, but upon immersing in water, the percolated nano capillaries get activated and start functioning as molecular sieves. In the activated state, it can block all solutes exceeding hydrated radii 4.5 Å

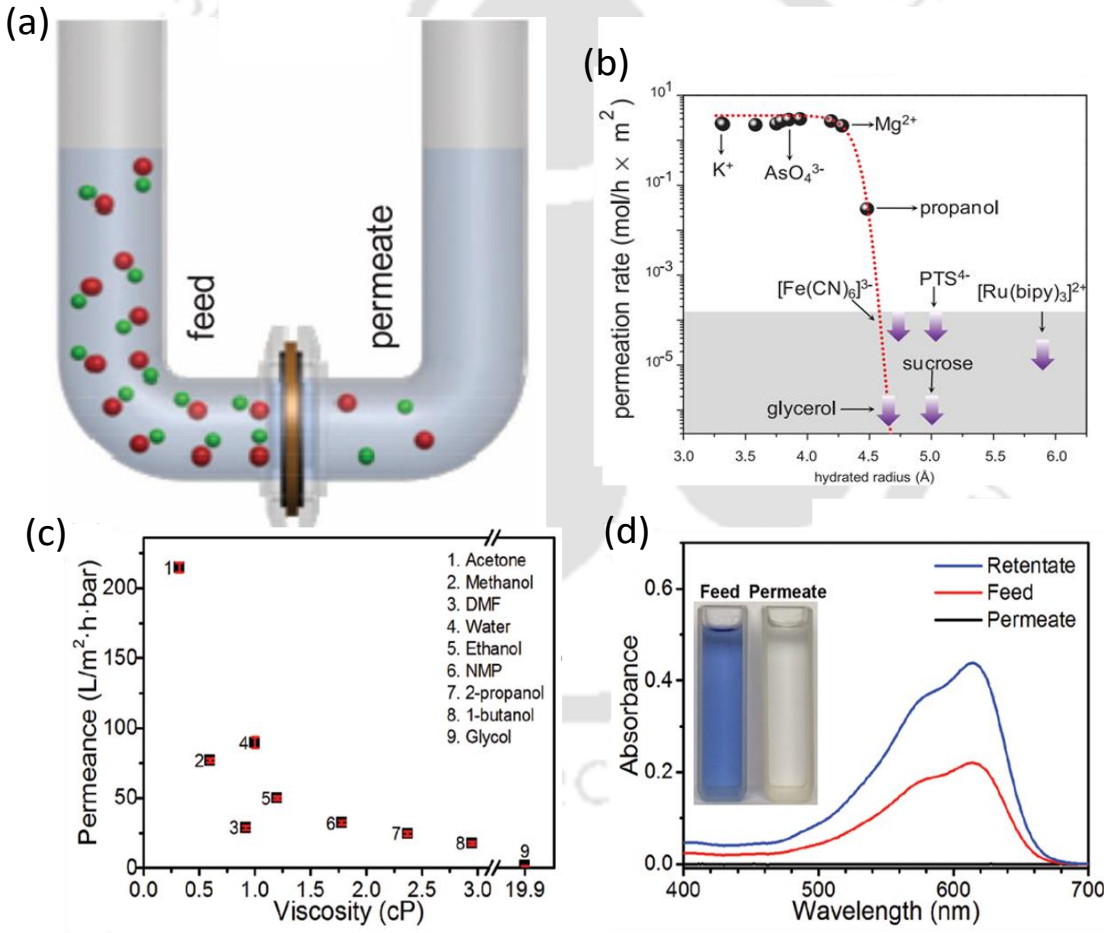

Fig. 1.10: Ionic and molecular selectivity of GOM: (a) experimental setup used to study solvent permeation through GOM. (b) Size-selective permeation of ions and molecules through lamellar GOM. (c) The permittivity of various solvents through the S-rGO membrane shows a function of solvent viscosity. (d) UV-vis spectra of a methanolic EB solution before and after filtrating through an S-rGO membrane; inset shows the photo of the feed and permeates solution. (Image copied from (b-c) *Science*, 2014, **343**, 752. (c-d) *Adv. Mater.* 2016, **28,** 8669.)

while maintaining an exceptional water permeation rate of 10 L m^{-2} h^{-1}. The network of nano capillaries activating in the hydrated state accept only species that fit in, and species exceeding this limit are sieved out. The fast water permeation is a consequence of capillary-like high pressure acting inside graphene capillaries. GOM can also be used for the separation of organic solvent. Shi *et al.* reported an organic solvation nano-filtration (OSN) membrane fabricated from ultrathin layers of solvent solvated reduced graphene oxide (S-rGO).[50] The S-rGO based OSN membrane showed viscosity dominant solvent permeation and high permeance rate as high as 215 L m^{-2} h^{-1} bar^{-1} is achieved for acetone. Because of residual carboxyl groups, S-rGO possesses a negative surface charge and exhibits excellent rejection to small molecules with negative charges. Neutral solutes having hydration radii larger than their channel height (about 3.4 nm) are also rejected based on the size exclusion principle. By functionalizing with hyperbranched poly (ethylene imine) (HPEI), the surface charge of the S- rGO membrane can also be altered to sieved small solute molecules bearing positive charges.

Reconstructed lamellar GOM shows excellent rejection efficiency towards hydrated ionic species and dye molecules, but it is associated with a lower water permeability issue. The percolated thin nano-capillaries provide a hindrance to water flow in the in-plane direction (horizontal flow). To enhance the horizontal mass flow, Gao *et al.* fabricated a hybrid membrane (G-CNTm) via synergistic intercalation of multiwall carbon nanotubes (MWNTs) into the inter-laminar galleries of graphene sheets.[60] In the hybrid membrane matrix, graphene acts as molecular sieving units, and MWNTs played the role of spacer via expanding the interlayer space between neighboured graphene sheets. With the hybrid membrane matrix, water flux up to 11.3 L m^{-2} h^{-1} bar^{-1} was achieved, which was found to be twofold higher than that of that pristine graphene nanofiltration membrane (GNm). Moreover, good rejection yield both for organic dye (>99% for Direct Yellow and >96% Methyl Orange) and ionic salt (i.e.,

83.5% for Na_2SO_4, 51.4% for NaCl) was achieved with their hybrid membrane system.

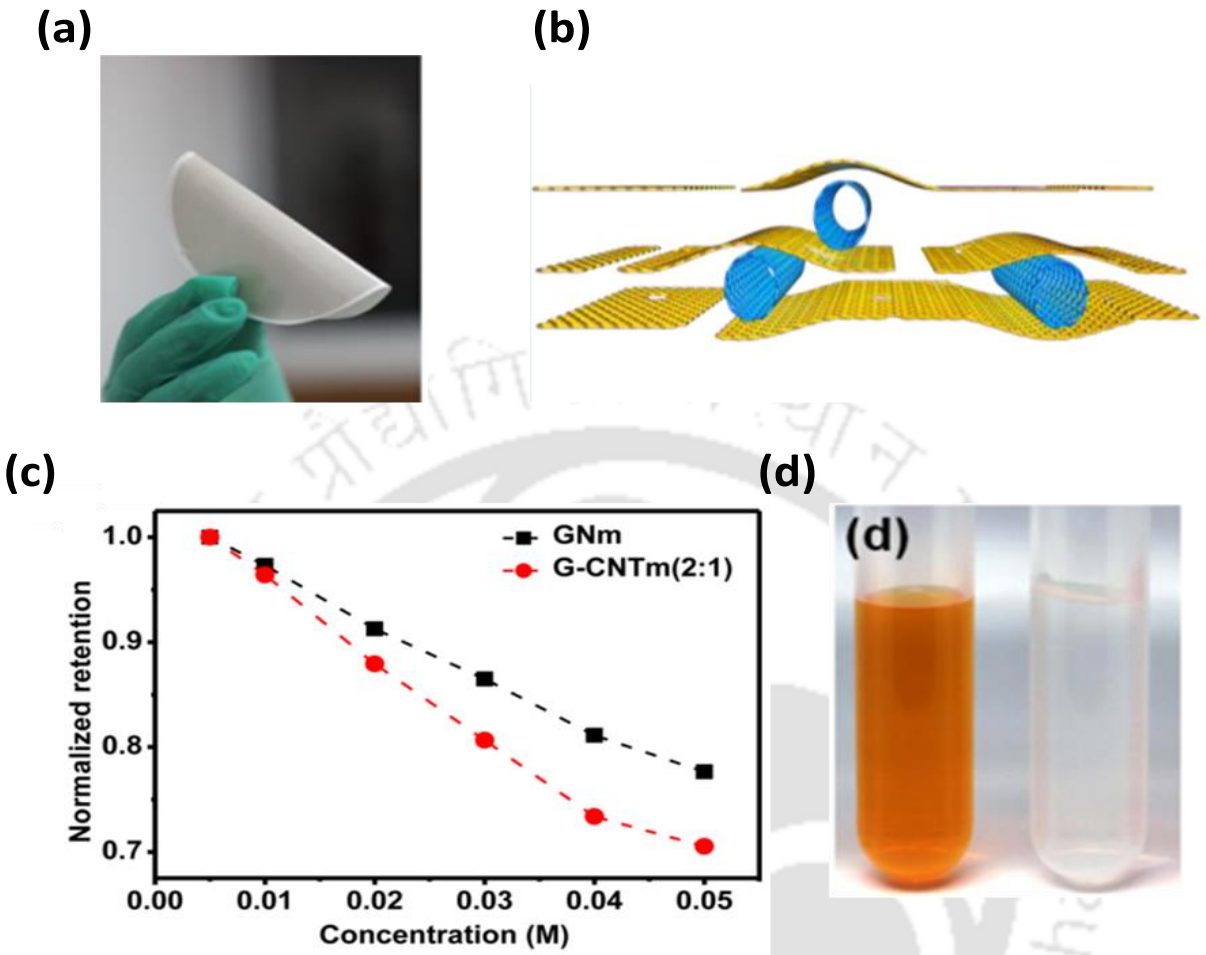

Fig. 1.11: CNT as spacer in GOM: (a) Digital image of G-CNTm. (b) Schematic representation of the structure in G-CNTm. (c) Rejection performance of bare graphene membrane (GNm) and hybrid membrane (G-CNTm) as a function of feed electrolyte (Na_2SO_4) concentration. (d) Image showing the colour change of methyl orange (0.05 g L^{-1}) dye before (left) and after (right) filtering through the G-CNTm. (Image copied from *ACS Appl. Mater. Interfaces* 2015, **7**, 8147.)

Yu *et al.* reported a bio-mimicking water purification membrane inspired by the frog's skins water collecting mechanism from the humid environment.[52] The bioinspired strategy involved synergistic intercalation of lignin moieties into the reduced graphene oxide (rGO) layers and observed high water flux which is demanded for efficient waste water purification. The water molecules travel at a high rate of 11820 L m^{-2} h^{-1} bar^{-1} through the nanocomposite membranes, which is 300 times higher than conventional GO membranes. Moreover, nearly 100% rejection was achieved for organic dye molecules with their hybrid membrane system. In the hybrid

biomimetic membrane system, the lignin moieties enlarged the water passage channels via cross-linking with GO layers, leading to an enhancement in the water driving force. The cross-linking of lignin moieties within the GO nanochannel laminates restricts the movement of nanosheets, thereby providing good solvent stability to the membrane system. In addition to GO laminates, lignin can also serve as a molecular sieve that explains the hybrid membrane's superior selectivity for the organic dye molecules.

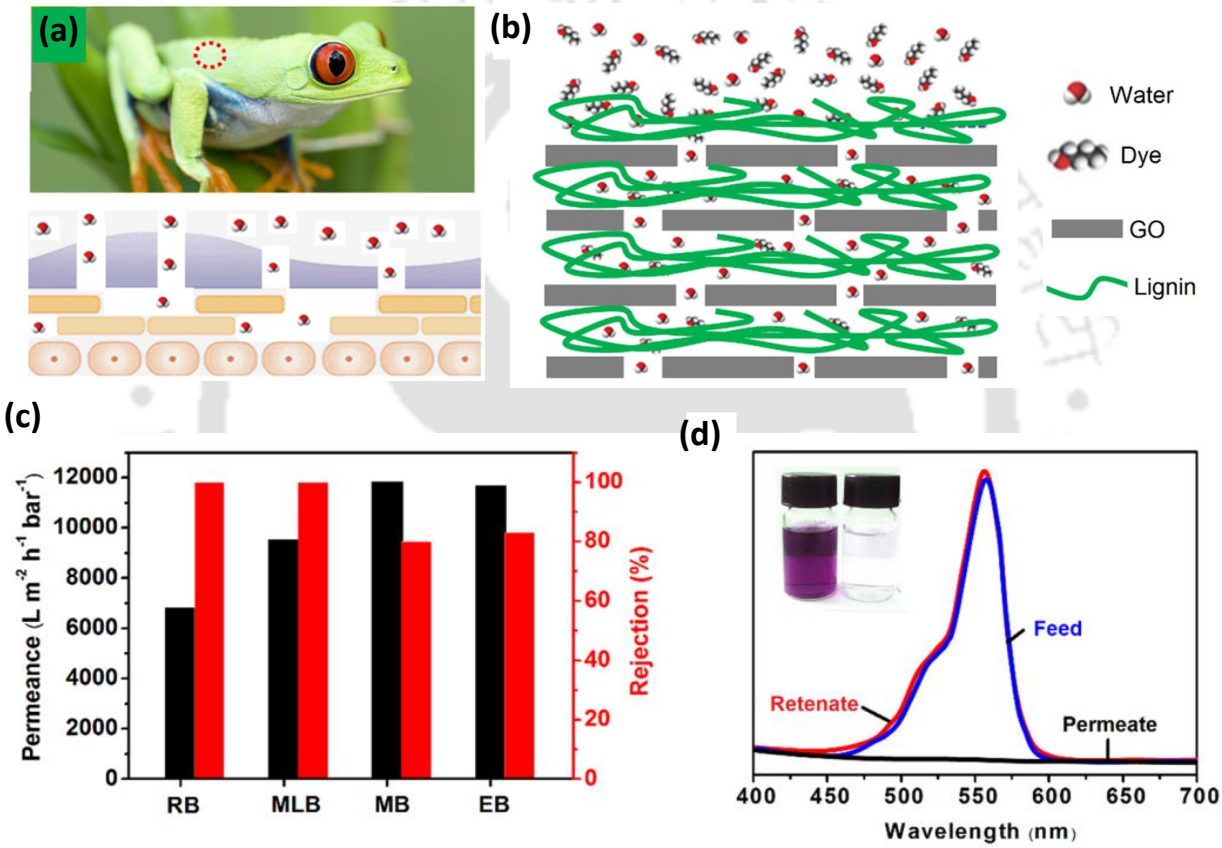

Fig. 1.12: Lignin as a spacer in GOM, an inspiration from frog skin: (a) Water permeation mechanism of frog skin where it can collect water from humid environment. (a) Schematic diagram showing the probable structure and ion sieving mechanism in the rGO-lignin biomimetic membrane. (c) Water permeance and (d) separation performance of the rGO-Lignin hybrid membranes. (Image copied from *ACS Sustainable Chem. Eng*. 2020, **8**, 8986.)

The emergence of GOM as an excellent tool in water purification and molecular separation process offered other 2D materials a new zeal, and different 2D materials beyond graphene have been successfully demonstrated. To enhance the water permeability through the 2D nanochannel network of the lamellar membrane, Ma *et al.* utilize a two-dimensional (2D)

cationic Covalent organic framework (COF), EB-COF: Br, which entirely possess vertical nanochannel across the cross-plane direction.[53] Vertically aligned nanochannels in the COF framework mitigate the permeability issue related to in-plane diffusion, and higher solvent permeability than graphene-oxide membranes and commercial nano-filtration membranes can be achieved. Moreover, the positive surface charges present in the EB-COF: Br framework endows the system with a high magnitude of charge-induced selectivity. Hence, the membrane demonstrates an excellent sieving performance for dye molecules/ ions with different sizes and charges. With these superiorities, the EB-COF: Br membrane can reject (>98%) anionic dye molecules/ions while maintaining a high solvent permeability.

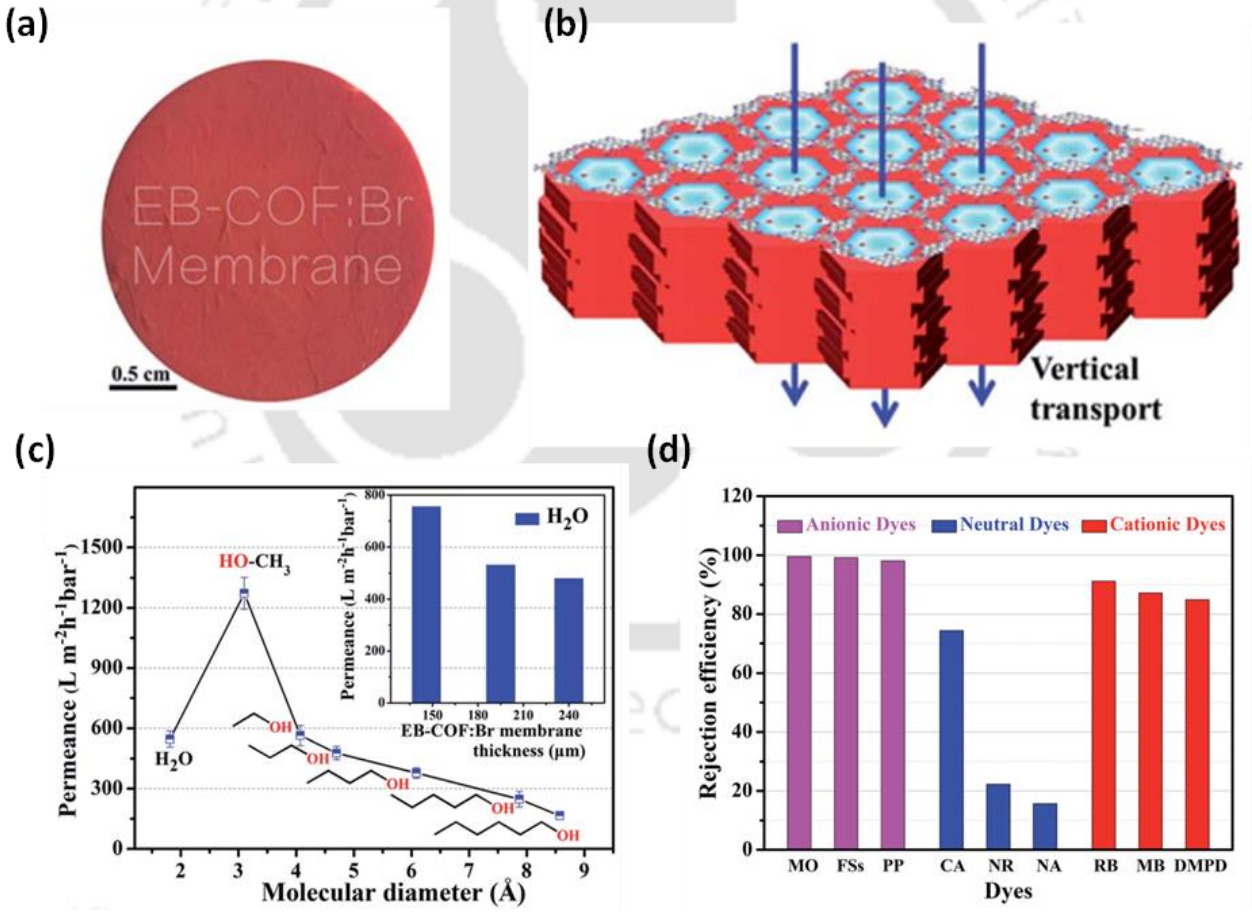

Fig 1.13: Vertically aligned COF nanochannels for molecular separation: (a) Digital image of an EB-COF: Br membrane. (b) Schematic showing the vertical transportation of mass in COFs framework along the 1D nanochannels in the cross-plane direction. (c) Solvent permeance showing as a function of the molecular diameter of the corresponding solvents. (d) Dye rejection efficiency of the EB-COF: Br membrane. (Image copied from *J. Mater. Chem. A*, 2018, **6**, 13331.)

Kim *et al.* reported a 2D lamellar hexagonal boron nitride nanoflakes (h-BNF) membrane for high-efficiency ionic separation.[54] The h-BNF membranes show outstanding rejection efficiency for small-sized ions and as well as for anionic dyes (>97%), with a concomitant water permeability of ≈ 10^{-3} L m m^{-2} h^{-1} bar^{-1}. Experiments with h-BNF show that the rejection efficiency can be fine-tuned on exposure to a pH gradient, confirming the presence of Donnan type exclusion between fixed negative charges on the BN surface and the mobile ions. Wang *et al.* demonstrated a 2d lamellar MXene membrane supported on anodic aluminum oxide (AAO) substrate for wastewater treatment.[55] The MXene membrane shows an unprecedented water permeance rate of 1000 $Lm^{-2}h^{-1}bar^{-1}$ and appreciable rejection efficiency (90%) for molecules bearing sizes larger than 2.5 nm.

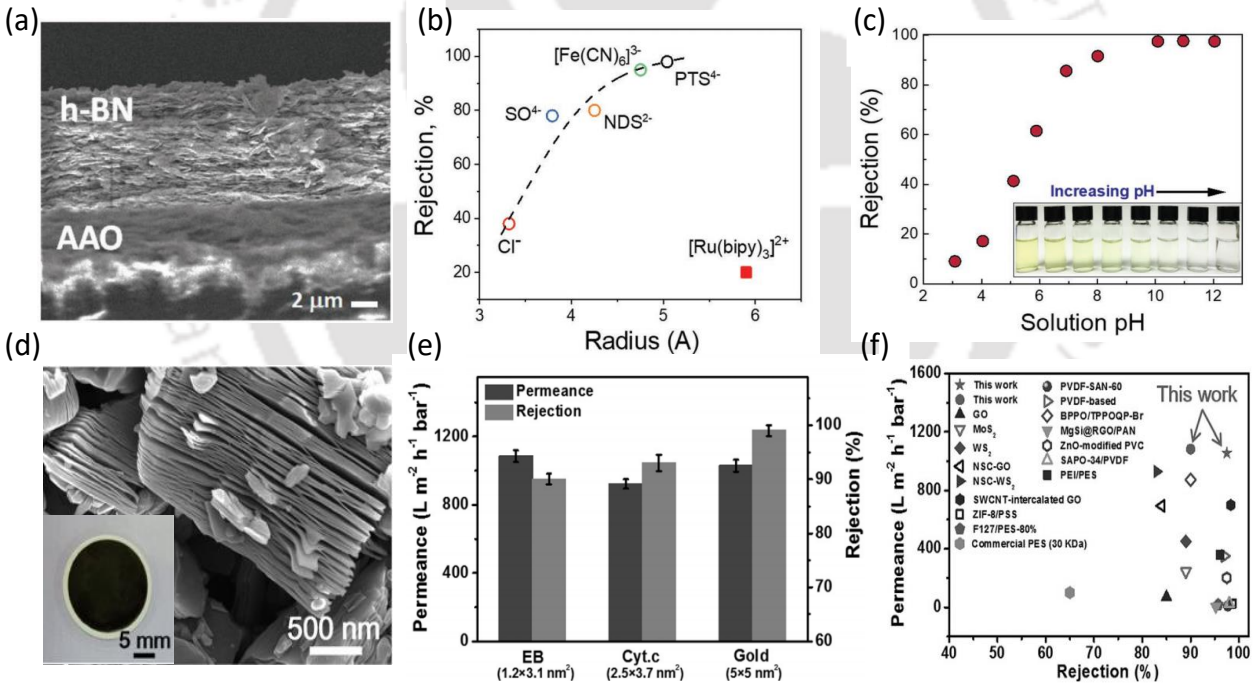

Fig. 1.14: Promising 2D materials employed in molecular separation: (a) cross-section FESEM images of an h-BNF membrane fabricated over AAO support showing the presence of lamellar stacking. (b) Rejection efficiency of h-BNF membrane showing as a function hydration radius of the corresponding salts. (c) Rejection efficiency of h-BNF membrane for potassium ferricyanide showing as a function of solution pH. (d) SEM image of $Ti_3C_2T_X$ powder, inset shows an MXene membrane prepared from its corresponding colloidal dispersion. (e) Water permanence and Separation performance of the MXene membranes for molecules with different sizes. (f) Comparison of the separation performance of the MXene membrane and various previously reported membranes. (Image copied from (a-c) *Small*, 2019, **15**, 1904590. (d-e) *Angew. Chem. Int. Ed.* 2017, **56**, 1825.)

Naturally, available clay minerals can also be demonstrated as a 2D platform for preparing high-performance selective membrane modules. Sun *et al.* prepared free-standing 2D montmorillonite (MMT) based membranes by restacking modified individual MMT nanosheets.[56] The membrane showed water permeance of 429 L m^{-2} h^{-1} atm^{-1}, accompanied by a high separation efficiency for both cationic and anionic dye molecules. The membrane was also utilized for salinity gradient energy conversion, and under a 1000-fold salt concentration gradient, an output power density of 0.18 W m^{-2} was achieved.

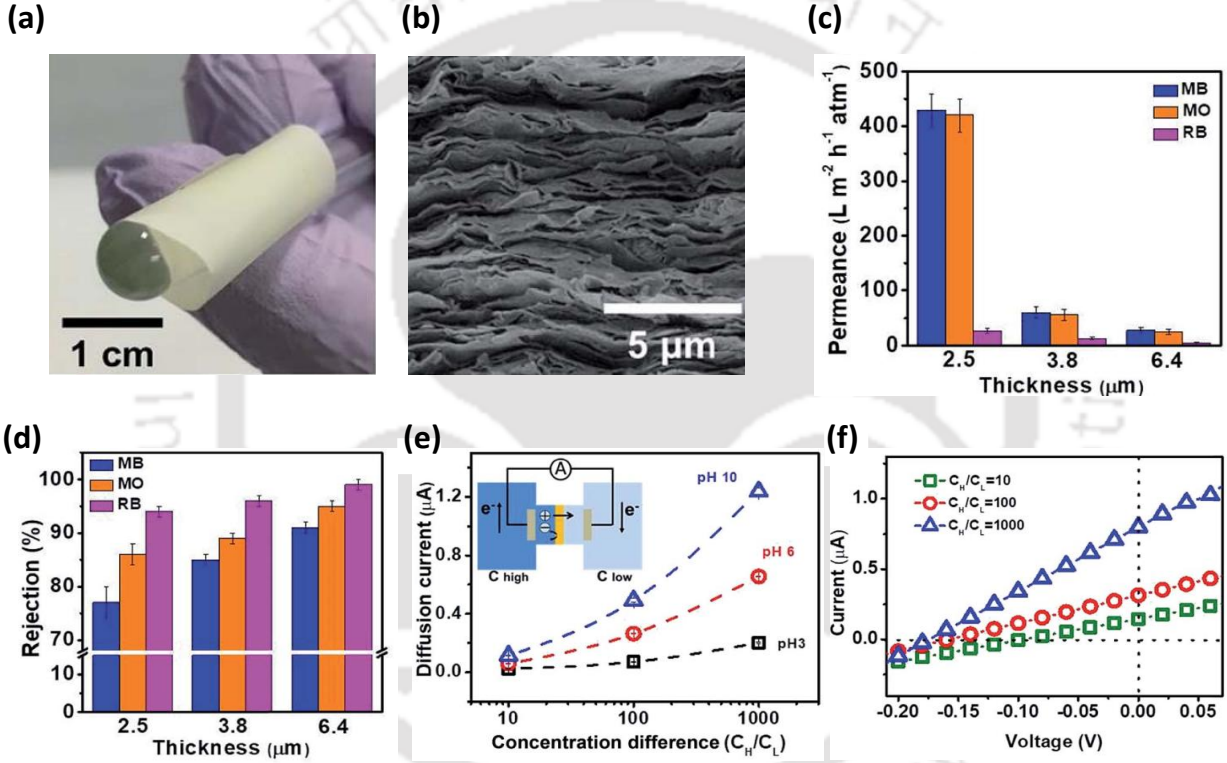

Fig. 1.15: Clay-based membrane for molecular separation: (a) Digital picture of a free-standing MMT membrane. (b) Cross-sectional FESEM image of an MMT membrane showing its lamellar structure. (c) The permeance of different organic dyes solutions (5 mM) through the MMT membrane with thicknesses of 2.5, 3.8, and 6.4 mm. (d) Rejection of MB, MO, and RB through the MMT membrane with thicknesses of 2.5, 3.8, and 6.4 mm. (e) Diffusion current generated under different salt concentration gradient at pH values of 3.0, 6.0 and 10.0. Inset shows the schematic of the experimental setup. (d) *I-V* Curves were recorded through the MMT membrane at different salt concentration gradients. (Image copied from *J. Mater. Chem. A*, 2019, **7**, 14089.)

1.4.2: Osmotic energy harvesting

Since the 1950s, people have recognized that it is possible to extract electricity as a completely

new renewable energy source from the free energy stored in salinity gradient by interposing a suitable device injunction between seawater and river water. Notwithstanding, extraction of salinity gradient as a valuable form of energy remains a challenge to date. With the advent of membrane science and technology, membrane-based techniques for blue energy harvesting have become a promising candidate, and mainly two such techniques *viz* pressure-retarded osmosis (PRO) and reverse electrodialysis (RED) had been widely explored to fulfill this energy requirement.[57] Among them, RED is a more promising approach for upscaling the osmotic energy harvesting process, and tremendous efforts have been carried out to understand the science behind it and develop technologies. The concept of RED is complementary to the operation of electrodialysis. In electrodialysis (ED), external electrical energy is consumed to bring about changes in the ionic composition. On the contrary, in RED, electrical power is generated with a chemical potential gradient resulting from a reversible mixing of two kinds of water-bearing different ionic concentrations.

The reverse Electrodialysis (RED) principle is based on the fact that ionic compounds when disintegrating in an aqueous environment, produce hydrated cation and anions. The solution as a whole remains neutral. Now a RED device breaks this electro neutrality by separating the so formed cations, and anions with the help of two distinguish membrane systems known as the cation exchange membrane (CEM) and anion exchange membrane (AEM).[58-60] Suppose we placed salt water and fresh water across these ion-exchange membranes, then ion will migrate from the highly concentrated saltwater chamber to the low concentrated freshwater chamber. Still, ions will have to migrate only through a preferential pathway due to the restrictions imposed by the ion exchange membranes. Typically, cations will migrate through the CEM and anion through the AEM. As a consequence, the overall transport of cations and anions will be in the opposite direction. This opposing migration of cationic and anionic species will

ultimately create oppositely charged dipole analogous to a battery, and hence RED device can be redefined as an electrochemical cell.[61] The extent of free energy extraction via the RED system is dependent on the concentration gradient between the two solutions placed across the membrane, the nature of the electrolytes, and the temperature of the water used in the RED cell.[62-64]

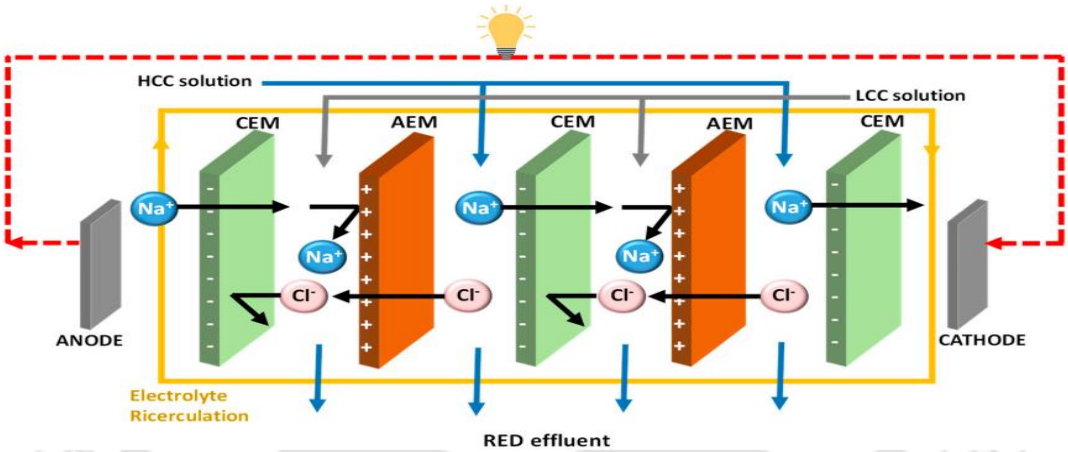

Fig. 1.16: Illustration of RED setup: Schematic representation of a reverse electro-dialysis (RED) setup employed for salinity gradient power generation. (Image copied from *Membranes* 2020, **10,** 7.)

The generated electricity in RED is dependent on a greater extent to the properties of the membrane. Issues such as membrane selectivity, durability, and fouling resistance are considered to develop a new membrane structure based on advanced materials, including ceramic, polymers, metal-organic framework (MOF), hybrid microporous materials, etc.[65-68] The most substantial growth in enhancing power generation via RED is achieved when 2D materials were introduced in this field. Inspired by the bioelectricity production mechanism of electric eel (*Electrophorus electricus*), whose electric organ comprises of parallel and series circuits of hierarchically assembled nanofluidic conduits, various biological ion-channel-mimetic artificial nanofluidic conduits have been developed from reconstructed 2D nanomaterials for energy conversion.[69,70] The mechanism of the RED with nanofluidic devices is shown in Fig 1.17. Assuming the nanochannels walls to be negatively charged, a cluster of positively charged counter-ions will be accumulating in the vicinity of the charge channel, and

the so-called electrical double layer (EDL) will be formed. When the height of the channels wall is comparable to the Debye length, the EDLs on both sides of the channels will overlap. A counter ion selective ion transportation will occur by rejecting the co-ionic species via electrostatic interaction. Under such circumstances, if we connect the high and low concentration chamber through nanofluidic channel, only the counter ionic species will migrate

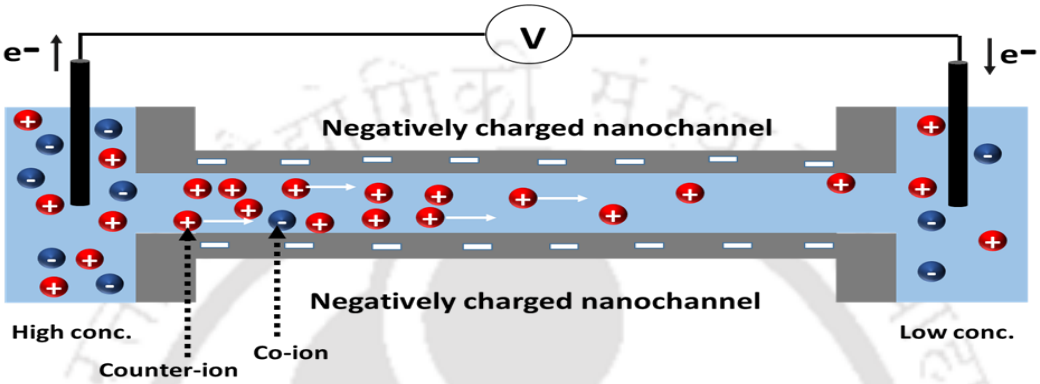

Fig. 1.17: Mechanism of RED with nanofluidic device: Counter ion selectivity in the nanopore device creates charge imbalance that causes electrochemical redox reactions allowing the electrons to flow in the external circuit. (Image copied from *J. Mech. Sci. Technol.*, 2011, **25**, 5.)

from the high to the low concentration chamber to equilibrate the chemical potential. This type of asymmetric ion transportation will create a charge imbalance across the membrane phase. To maintain charge neutrality, electrochemical redox reactions will take place on electrode surfaces. If connected to an external circuit, the so formed elections can be transferred to produce electric energy at an electric load.[71-73] These nanofluidic reverse electro-dialysis systems (NREDS) provide a higher ionic flux and a lower fluidic resistance compared to the conventional membrane-based reverse electro-dialysis systems. Hence, they considerably enhanced the performance of the osmotic energy harvesting process. Moreover, modifying the parent nanofluidic channels or nanopore to accommodate high ion/charge selectivity is possible. Hence, these functional nanofluidic channels or nanopores are the suitable solution to reduce the overall high expenditure associated with conventional RED operational setup.[74]

Ji *et al.* have utilized a cascading pair of oppositely charged graphene oxide nanochannels for

fabricating a 2D nanofluidic reverse electrodialysis system.[75] Via preassembly modification, the surface charge of inherent GO was altered from negative to positive. Both the GOM pairs were demonstrated as RED units to achieve high-performance osmotic energy conversion. The complementary ionic diffusion in the tandem alternating GOM pairs produces appreciable charge separation, resulting in high trans-membrane potential difference and diffusion flux. The output power density achievable from this GOM pair approaches as high as 0.77 Wm^{-2}, which is about 54% higher than commercial ion-exchange membranes.

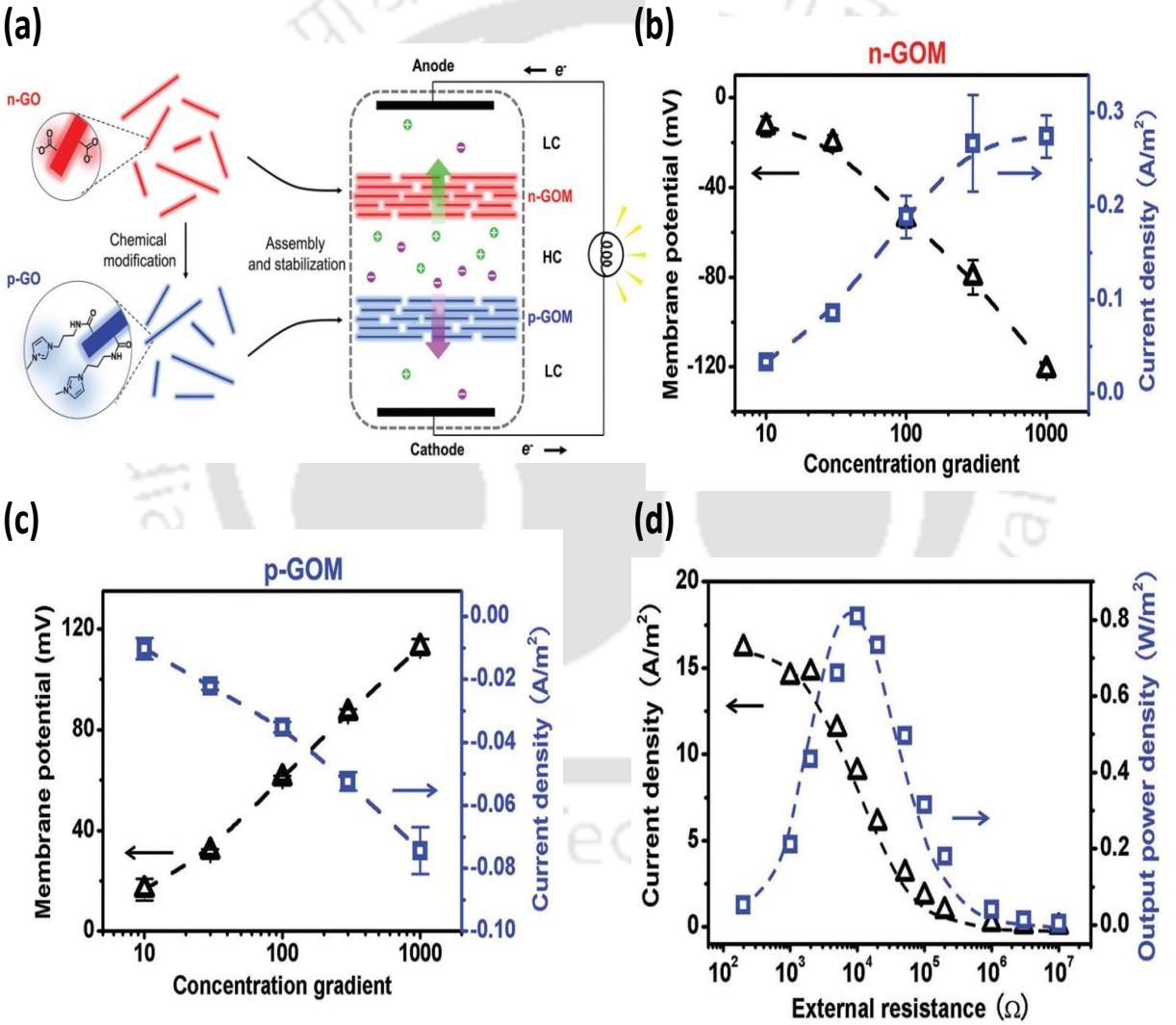

Fig. 1.18: Osmotic energy harvesting using oppositely charged GO nanoflakes: (a) Schematic illustration of the experimental set-up and the corresponding ion transport mechanism. Transmembrane potential and observed current density generated via selective diffusion of counter ionic species (b) for negatively charged GOM and (c) for positively charged GOM. (d) Obtained power density by combining a pair of a complementary charge selective GOM. (Image copied from *Adv. Funct. Mater.*, 2017, **27**, 1603623.)

Lin *et al.* have reported a graphene-based energy harvesting device that is powered by an enzymatic bio-waste reaction.[76] The 2D nanofluidic membrane was fabricated by functionalizing polyacrylic acid (PAA) with graphene. The incorporation of PAA introduced negative surface charges on graphene and endowed the membrane with cation-selectivity. The experimental setup consists of two chambers, as shown in Fig.1.19b. With the help of Enzyme-aided catalysis, urea was decomposed in the reaction chamber producing OH^-, and HCO_3^- anions and NH_4^+ cation. Because of the inherent cation selectivity of the hybrid membrane, only the NH_4^+ ion produced in the reaction chamber will migrate across the membrane to the receiving chamber following the principle of chemical equilibration, resulting in transmembrane voltage and a net ionic current.

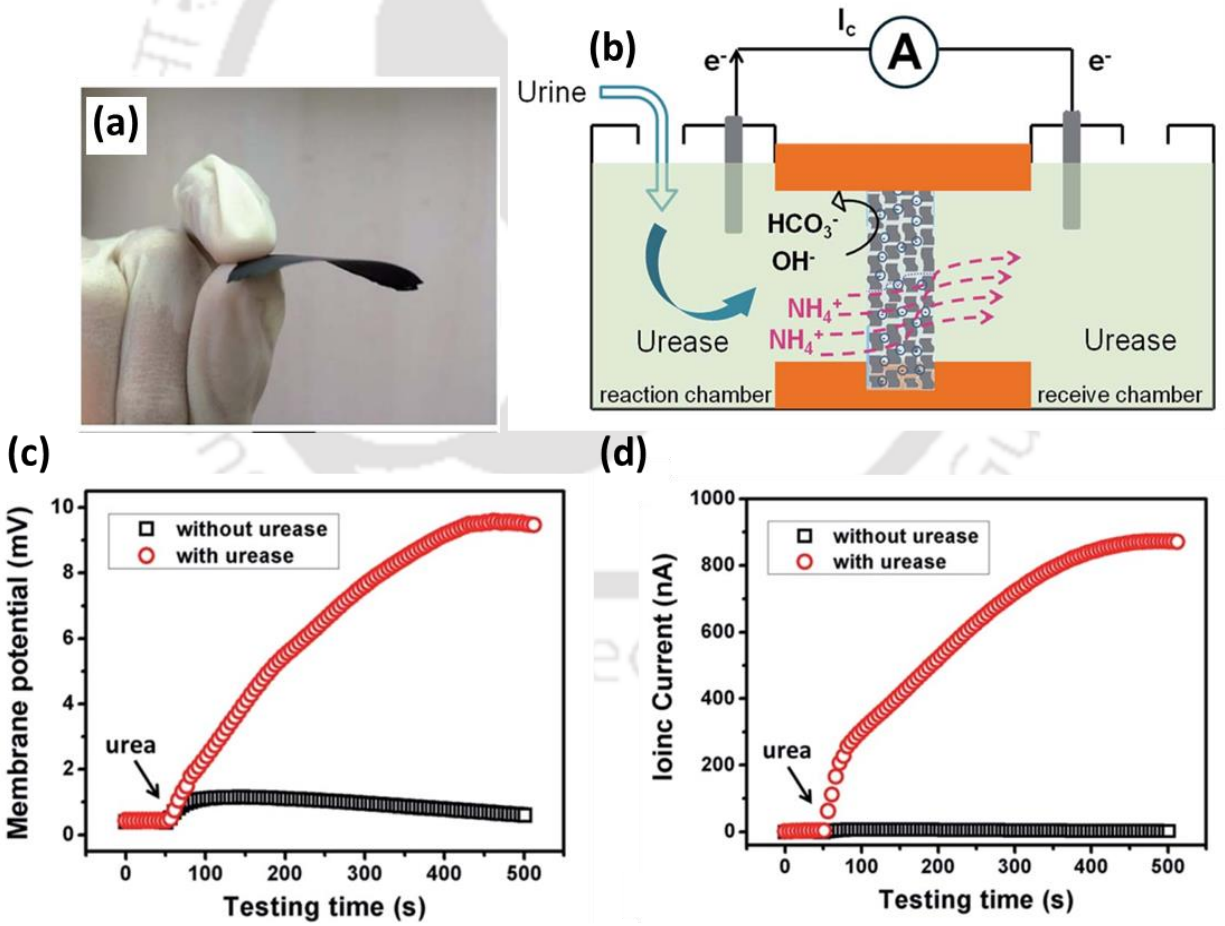

Fig. 1.19: Energy from enzymatic reaction: (a) Digital image of the GO-PAA membrane. (b) Schematic diagram of the experimental setup. (c) Trans membrane voltage and (d) diffusion current harvested from enzymatic decomposition reaction of urea through the GO-PAA membrane. (Image copied from *Chem. Sci.*, 2016, **7**, 3645.)

Antonietti *et al.* demonstrated a 2D ultrathin free-standing polymeric carbon nitride membrane (UFSCNM) fabricated from melamine through chemical vapour deposition polymerization.[77] The 2D membrane exhibits excellent nanofluidic ion-transport phenomena. Under its perm selective nature, the UFSCNMs membrane can effectively convert salinity gradients into electric energy with a high output power density of 0.21 Wm^{-2} under a 1000-fold salt concentration gradient. Jiang *et al.* demonstrated the construction of 2D nanofluidic channels with kaolinite-based Janus nano-building block for osmic and electrokinetic energy conversion.[78] Pristine kaolinite sheets were negatively charged, converted into positive charge via covalent modification with Si-69 moieties. The newly incorporated Si-69 molecules are exclusively attached to the Al-OH groups on an aluminium octahedral sheet (AOS), resulting in a Janus-like structure on its opposing surfaces. The reconstructed kaolinite membranes (RKM) show surface charge governed ionic transport phenomena with nearly perfect cation-selectivity, and hence they exhibit excellent performance in osmotic energy conversion. The resulting output power density from the RKM approaches 0.18 Wm^{-2} under a 100-fold salt concentration gradient which is very close to graphene-oxide membranes (GOM). Lei *et al.* engineered a hybrid membrane consisting of aramid nanofibers and boron nitride nanosheets (ABN) with high mechanical and chemical rigidity for blue energy conversion.[79] The hybrid membrane can produce high power density up to 0.6 Wm^{-2} which was stable for 200 h covering 20 consecutive operational cycles. Moreover, the membrane was also found to be operative efficiently in harsh experimental conditions such as wide ranges of temperature and pH variations, demonstrating its economic viability as an excellent osmotic energy generator. Wang *et al*. showed that the lamellar MXene membrane is also suitable for harvesting osmotic power as a renewable energy source.[80] The 2D nanofluidic channels of MXene membranes exhibit prominent surface-charge-governed ionic transport characteristics and as well as high cation selectivity. When employed, the MXene membranes can deliver a power density up to

21 Wm^{-2}, concomitants with an energy conversion efficiency of 40.6% under a 1000-fold salt concentration gradient. Moreover, the achievable power density through the MXene membranes can be scaled up to 54 Wm^{-2} by employing a thermal treatment.

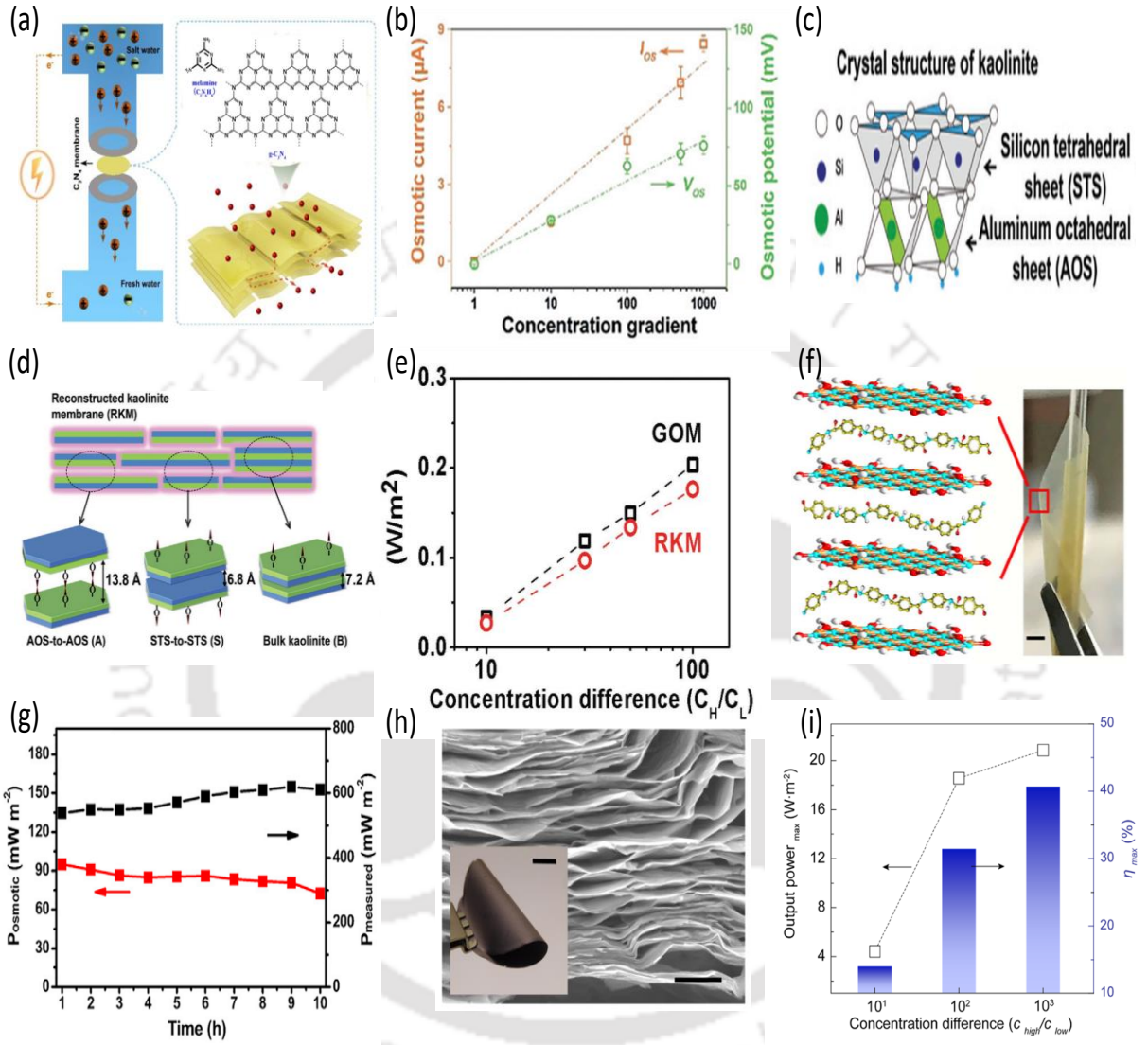

Fig. 1.20: 2D material beyond graphene employed for osmotic energy harvesting: (a) Ion transport across the UFSCNMs. (b) The transmembrane potential and osmotic current recorded through a UFSCNM. (c) Crystal structure of kaolinite showing its tetrahedral silicon sheet (STS) and an aluminium octahedral sheet (AOS). (d) Reconstruction of the 2D Janus clay nanosheets. (e) Osmotic power generation with GOM and RKM. (f) Schematic showing the lamellar structure of ABN membranes. (g) The measured power density and osmotic power density recorded through ABN membranes showing as a function of time. (h) Cross-sectional SEM image of $Ti_3C_2T_x$ membrane. (i) Output power density and its corresponding energy conversion efficiency recorded through a $Ti_3C_2T_x$ membrane showing as a function of the salt concentration gradient. (Image copied from (a-b) *Angew. Chem. Int. Ed.* 2018, **57,** 10123. (c-e) *Adv. Mater.* 2017, **29**, 1700177. (f-g) *Joule*, 2020**, 4**, 247. (h-i) *ACS Nano* 2019, **13**, 8917.)

Feng *et al*. demonstrated lamellar black phosphorus (BP) membrane fabricated via self-assembly method in salinity gradient conversion.[81] They explored the impact of the oxidation process on BP in energy generation performance. It was observed that, controllable oxidation of BP in water greatly enhanced the magnitude of output power generation via the formation of a high valence phosphorus species. Controlling the concentration of dissolved oxygen, the valency of the BP can be accurately controlled. Moreover, the perm-selectivity of the BP membrane can be enhanced by ~80% via constructing an ordered hetero assembly of GO and BP, and the resulting high charge separation in the hetero-assembly contributes to the further upscaling of the output power density up to ~4.7 Wm^{-2}.

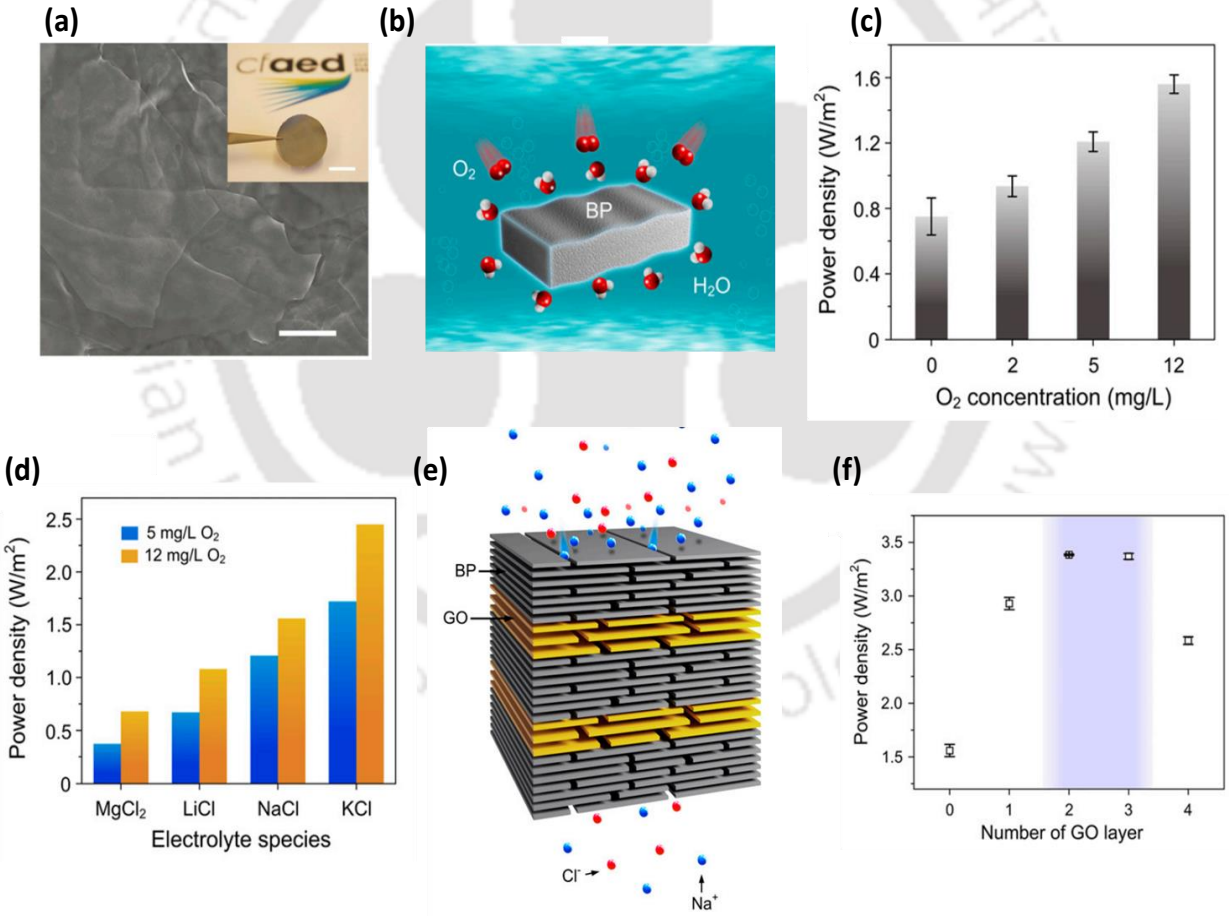

Fig.1.21: Black phosphorus membranes for osmotic energy conversion: (a) Surface SEM image of the BP membrane, inset: free-standing membrane. (b) Schematic of the treatment of BP membrane: immersed in O_2-containing water. (c) Output power density as a function of O_2 concentration. (d) Output power density as a function of electrolyte species. (e) Schematic of the ion transportation in a GO-BP hetero-assembly. (f) overall power density. (Image copied from *Proc. Natl. Acad. Sci. U. S. A.* 2020, **117,** 13959.)

1.4.3: Ionic transport regulation

The controlled transport of ionic/molecular species through synthetic micro/nanoporous medium is becoming a prime interest in the fields of interdisciplinary science and technologies because of its tremendous potential in areas like, exquisite chemical separation, energy harvesting, and biomedical applications.[82-87] In nature, there exist such ion-specific cell membranes that regulate numerous physiological phenomena. Biological ion channels and ion pumps are examples of such carriers that control the distribution of countless ionic/molecular species in all living bodies. Notable examples of such specific ion transporter systems are the proton pump in cytochrome c oxidase, sodium-potassium exchange pump in the cell membrane, and Ca^{2+} pumps in the plasma membrane.[88-90] The outstanding structure-function characteristics of the biological ion channels and pumps have been a source of inspiration in designing their artificial counterparts due to their fundamental importance and real-time applications. The main features of a natural ion pump are the inherent asymmetries present in their physical structures and asymmetry in the distribution of chemical composition over the entire system. Due to such asymmetries, they possess three basic elemental features: ionic selectivity, ionic gating, and ionic rectification. Typically, ion selectivity refers to the capability of the ion channel to recognize specific ions/molecules based on the specific binding interaction with its molecular recognition sites distributed along the channel walls. Ionic gating generally refers to the ability of the ion channel to respond via opening or closing its transport route upon exposure to external stimuli. Ionic rectification is the capability of the ion channel to act as an ionic diode and realize unidirectional ionic transport, analogous to that of the electronic p-n junction.[91,92]

In the last decade, proficiency of the bio-ion channels in accomplishing these peculiar ionic transportation features has inspired scientists to mimic these properties using synthetic

bioinspired intelligent asymmetric nanochannel membrane (BSANM) systems.[93] The generic design strategy of BSANM involves a principle factor; either we have to impart asymmetry into the artificial membrane system (built-in factors) or to the membrane environment (external factors). The built-in factors refer to the introduction of asymmetry in the nanochannel geometrical structures or their surface properties such as charge distribution, wettability, and chemical composition. In contrast, external factors refer to the exposure of external stimuli such as the pH change, electrolyte concentration gradient, light illumination, pressure drop, and voltage change.[94,95] The initial studies dealing with conical nanopores have demonstrated that these devices are ideal candidates to mimic the biological ion regulation activities. The fundamental feature of conical pores is that the ion transporting nanopores are asymmetric in structure and possess surface charges, which enables them to rectify the *I-V* characteristics of the channel along with prominent perm-selectivity. Fulinski *et al.* investigated ionic transport characteristics of asymmetric single conical nanopores fabricated in polyethylene terephthalate (PET) membrane.[96] The conical nanopores were created via the track etching method with the irradiation of heavy ions on the PET foils followed by subsequent chemical etching. Conductivity experiments show that the PET nanopores are cation-selective and rectify the ionic current in the preferential direction via controlling the flow of counter ionic (cation) species from the narrow entrance (tip side) to the larger opening (base side) of the pore. Moreover, the conical nanopores can act as an ion pump if stimulated by external field fluctuations and transports potassium ions against the concentration gradient. Li *et al.* demonstrated the use of a single glass conical nanopore channel decorated with homopolymer poly [2-(dimethylamino) ethyl methacrylate] (PDMAEMA) and observed both pH and temperature-responsive ion-transport properties.[98] PDMAEMA exhibits both temperature and pH-responsive properties. Hence, the nanopore device can be reversibly switched between the high conducting “on” state and the low conducting “off” state with a high gating efficiency by

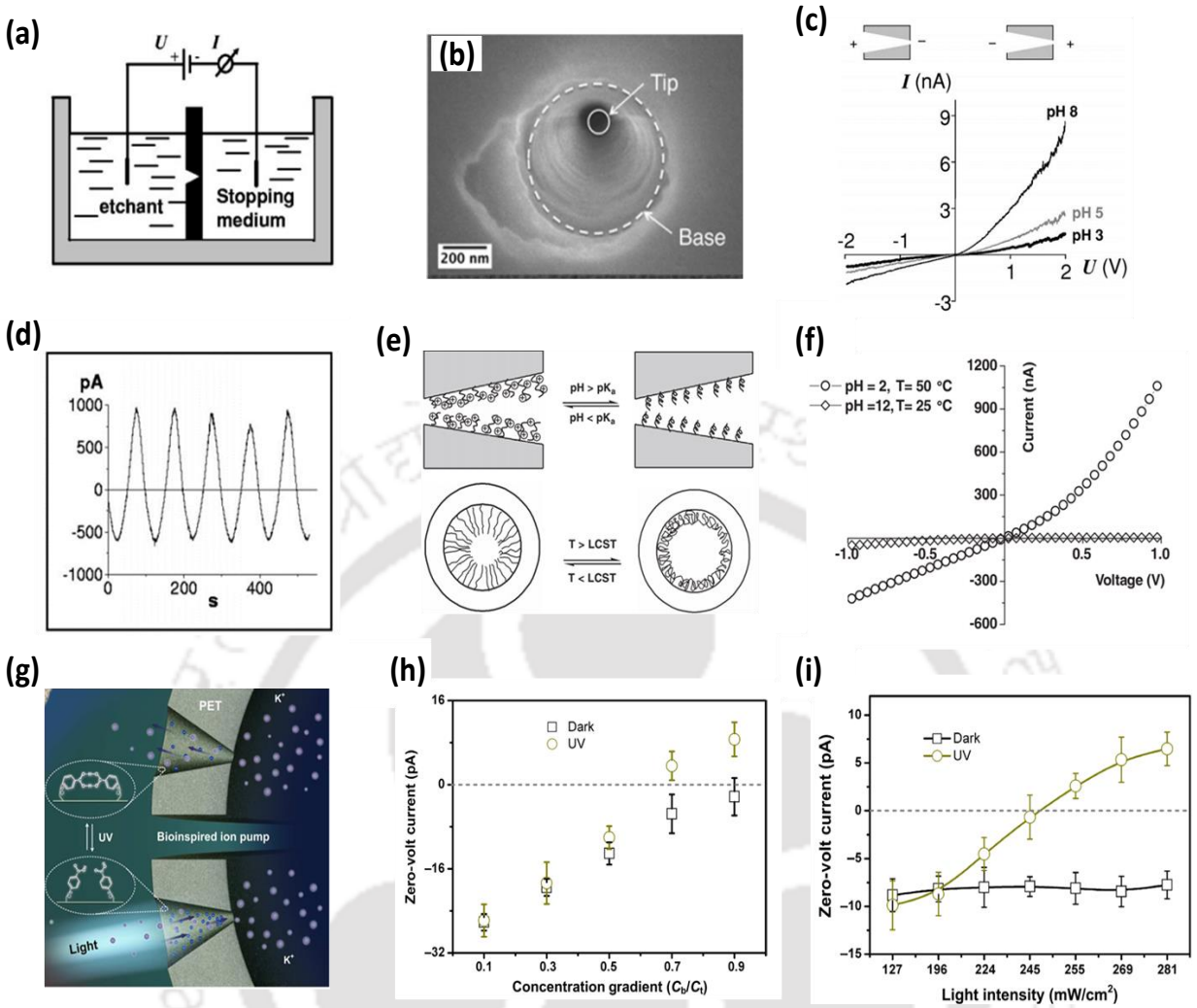

Fig 1.22: Ion pump fabricated from charged conical nanopore: (a) Schematic of the experimental set up utilized for preparing single conical pores. (b) FESEM image of a PET membrane showing the single conical nanopore. (c) *I*-*V* curve recorded through a single conical PET pore on exposure to symmetric electrolyte conditions across the membrane. (d) Net ionic current generation through a conical nanopore when the applied field was fluctuated maintaining a mean value of zero. (e) PDMAEMA-modified nanopore exhibiting pH responsive functional moieties and temperature-responsive swollen state. (e) *I*-*V* curves of "on" state (pH 2, T = 50 °C) and "off" state (pH 12, T = 25 °C) of PDMAEMA-modified conical nanopore. (g) Schematic illustration of the light-responsive ion pump based on PET conical nanopore. (h) Inversion of zero-volt current in the presence of light indicates the uphill transportation of ions. (i) UV light of appropriate intensity can reverse cation flow inside the nanochannels and enhance the pumping process. (Image copied from (a, c & d) *Am. J. Phys.*, 2004, **72**, 567. (b) *ACS Nano* 2016, **10**, 4637. (e-f) *Adv. Funct. Mater.*, 2011, **21,** 2103. (g-i) *Sci. Adv.*, 2016, **2**, e1600689.)

simply varying the surrounding media's temperature and pH. Jiang *et al*. establish a bioinspired nanoscale photo-driven cation pump based on a single PET conical nanochannel.[99] When UV

radiation was showered on the base side of the cone by placing a high concentration solution in its vicinity, a cation pumping phenomenon was observed. The ion pumping phenomena can be identified by monitoring the inversion of zero-volt current. Under UV irradiation, enhanced dissociation of the benzoic acid derivative dimers existing on the inner walls of the PET cone will create more mobile carboxyl groups. The observed cation pumping phenomenon on exposure to UV light can be attributed to the enhanced electrostatic interaction between the counter-ions entering the nanochannel and the charged groups (-COO) residing in the channel.

It has been demonstrated that to fabricate artificial ion pumps or ion channels; an energy conversion stimuli-responsive centre needs to be incorporated with the operating asymmetric nanopores. So it is necessary to realize an extremely robust and precise ion transport system with a sub-nanometre narrow capillary to be impactful in broad applications. While addressing any of these problems is straightforward, managing them in a single material is quite challenging. Recently, a range of novel 2D nanomaterials has been introduced to fulfil these requirements, and 2D layered materials provided a new zeal to accomplish these goals. Compared to conventional 1D nanofluidic devices, the 2D ion-pump displays several benefits like facile fabrication and scalability. Many 2D materials and their facile functionalization offer several ways to fine-tune the desired parameters like ionic selectivity, ionic flux, and pumping efficiency. The facile functionalization of the nanosheets before self-assembling also makes it possible to incorporate stimuli-responsive moieties that could create new properties such as photo-switchable, temperature-switchable, and pH-switchable smart ion-pumps. Moreover, the macroscopic dimensions of the 2D nanochannel assemblies mitigate the requirement of sophisticated instrumentation and expensive material processing steps, thereby providing exciting opportunities to study the fascinating ion transport characteristics of biological systems in an artificially made unit.

For the first time, yeo *et al.* demonstrated that symmetric GOM exhibit peculiar ionic current rectification behaviour, significantly below a specific electrolyte concentration when EDL starts overlapping to provide a counter ion-selective nature.[100] The observed uncommon rectification behaviour can be explained by the occurrence of Fore-aft asymmetry in the symmetric GOM, especially at the diffusion boundary layers of the entrance and exit ends of the membrane. This asymmetry arises because of the reversal between the low conducting

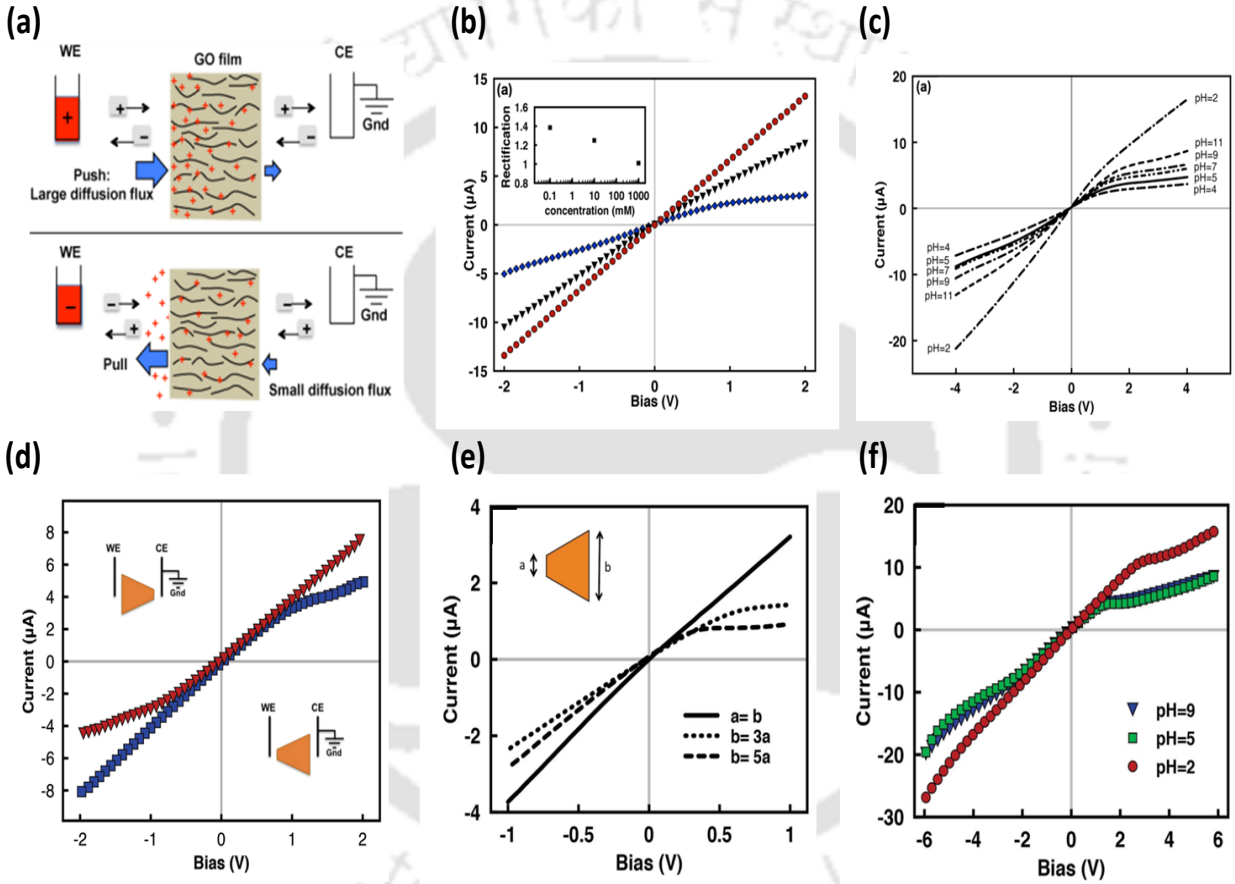

Fig.1.23: Ionic current rectification (ICR) with GOM: (a) ICR mechanism through symmetric GOM. (b) Representative *I-V* curves recorded through symmetric GOM at different KCl concentrations. Diamonds represent 0.1 mM, inverted triangles for 10 mM, and circles for 1000 mM KCl. The inset shows the corresponding ion current rectification ratios. (c) *I-V* characteristics recorded through the symmetric GOM showing as a function pH values at a 0.1 mM KCl electrolyte solution. (d) ICR recorded through an asymmetric GOM, the effect of reversing the working and counter electrodes with respect to the geometrically asymmetric film on its *I-V* characteristics is demonstrated here. (e) Representative *I-V* curves for GO films with different cross-sectional areas at the entrance and exit ends. (f) *I-V* characteristics of the geometrically asymmetric GO film (b/a = 3) showing as a function pH of the electrolyte solution. (Image copied from (a-c) *J. Phys. Chem. C*, 2014, **118**, 21856. (d-e) *Adv. Sci.* 2015, **2**, 1500062.)

positive bias state and the high conducting negative bias state of GO film, fuelled by the effects of trapping or releasing of counter ionic species and non-uniformity of the electric field in the tortuous nanochannels. The solution pH has also imparted strong influence on the surface charging of the GO channel walls, and hence the rectification behaviour of the GO film can be fine-tuned by adjusting the solution pH.

The same group later demonstrated that ionic current rectification through 2D GOM could be enhanced simply by enhancing the perm-selectivity by breaking the symmetry of the surface charge distribution across the film.[101] In the geometrically asymmetric GOM, it was observed that with increasing asymmetry of the cross-sectional areas between the two extreme ends of the film, typically known as the tip and base side, the rectification ratio increases. The observation can be explained to the reduction of the limiting current due to the increased perms-selectivity when more asymmetry was imposed on the GOM system. The rectification ratio can be enhanced further by decreasing the medium's acidity, leading to more dissociation of the carboxylic group residing on the channel wall and imparting more perm-selectivity to the membrane system.

To introduce photo responsive ionic rectification in 2D nanofluidic systems, Jiang *et al.* incorporated photo-sensitive spiropyran (SP) molecules into the lamellar GO nanochannels.[102] The GOM-based 2D nanofluidic diodes can be switched reversibly between high-and-low rectifying states simply by controlling the light illumination process. Upon exposure to UV irradiation (wavelength of 365 nm), photoisomerization of the neutral SP molecules occurs. It subsequently gets converted into a cationic merocyanine (MCH^+) state by opening its pyran bond in an acidic medium. Meanwhile, on exposure to visible light (wavelength of 520 nm), the cationic MCH^+ species reversibly converted back into its neutral SP isomer, yielding a fully photo-switchable ionic diode. The formation of light-induced cationic MCH^+ reduces the

overall negative charge density on the GO nanochannels walls via charge neutralization, which accounts for the enhanced rectification performance of the device on exposure to UV radiations. This GO-SP-based charged hetero-assembly collaboratively results in a prominently enhanced ionic rectification, and a high ICR ratio of 48 is achieved with the 2D nanofluidic system.

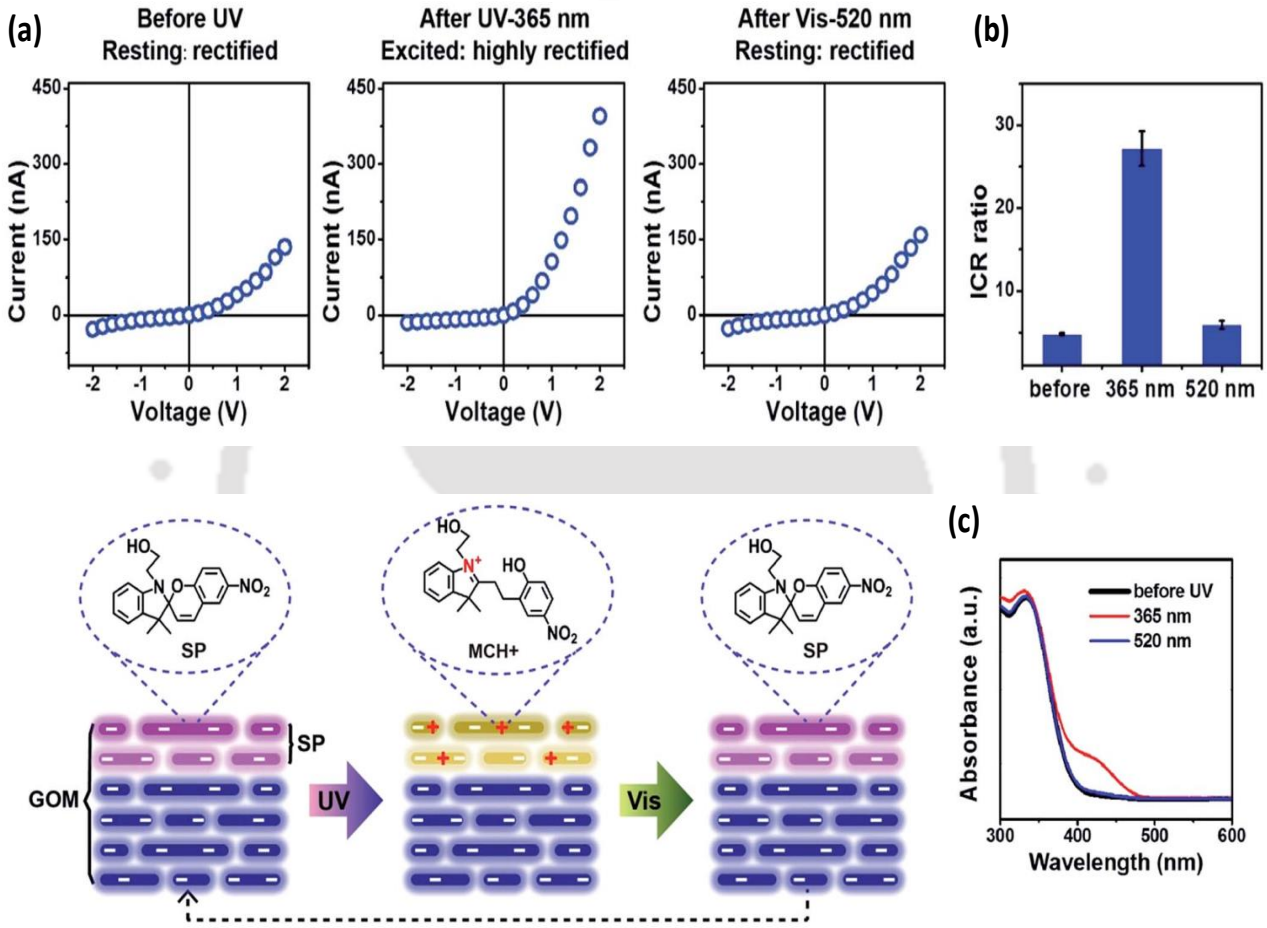

Fig. 1.24: Photo-induced ICR in GOM: (a) *I-V* responses of spiropyran-GO membranes on exposure to different light intensities (UV-light, 365 nm and visible light, 520 nm) and the corresponding mechanism of the changes in the molecular and charge state in the membrane system. (b) ICR ratio in presence and absence of different light intensity. (c) UV-vis spectra of SP in solution phase. An absorption peak at 420 nm is observed (red), confirming the photo-isomerization process in SP. This transformation can be fully retrieved under the irradiation of visible light (blue). (Image copied from *Chem. Sci*., 2017, **8,** 4381.)

2D ionic current rectifier other than GO has also been reported in the literature. Shao *et al.* designed a nanofluidic conduit fabricated from naturally available Montmorillonite clay minerals and demonstrated ionic current rectification by adopting a trapezoid geometric shape

MMT membrane.[103] The 2D nanochannel arrays of MMT are reconstructed via self-assembling their corresponding colloidal dispersions, and the as-constructed MMT laminates display excellent counter ion selectivity. The clay-based ionic diode is thermally stable up to 400° C and shows ionic current rectification with a rectification ratio of ~2.6 and ~3.5 with KCl and HCl electrolytes solution.

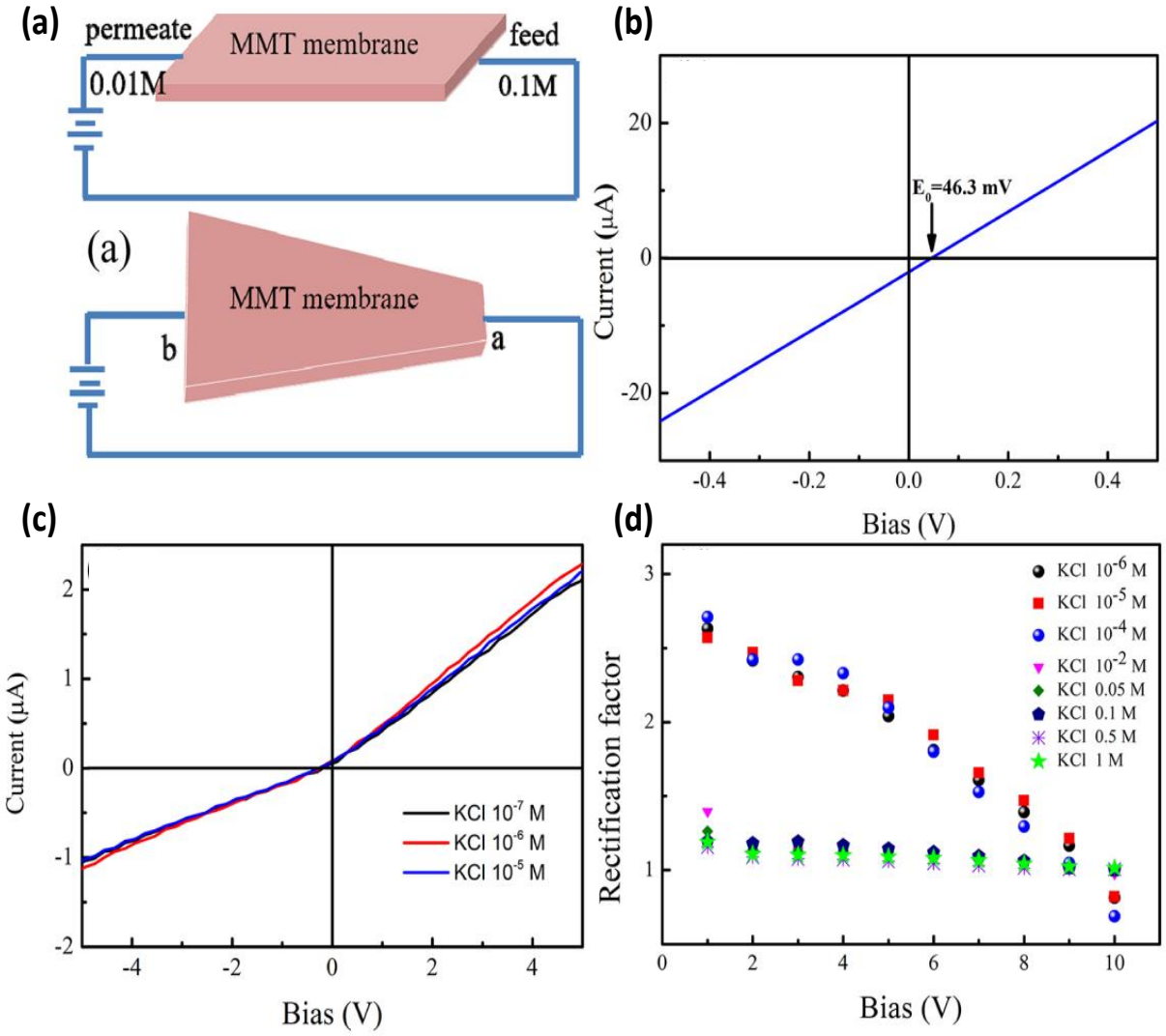

Fig.1.25: ICR in clay-based conduit: (a) Schematic illustration of a rectangular (up) and triangular (down) MMT based nanofluidic conduit (b, c) their corresponding *I-V* curves. (d) Rectification factor as a function of applied bias at KCl electrolyte of various concentrations. (Image copied from *ACS Appl. Mater. Interfaces*. 2018, **10**, 44915.)

Raidongia *et al*. demonstrated a flexible and freestanding membrane of vanadium pentoxide (V_2O_5), which exhibits membrane shape-dependent ionic transport characteristics.[104] While the rectangularly cut V_2O_5 membranes show linear *I-V* curves, the triangular shape of the V_2O_5

membranes displays nonlinear diode-like *I-V* curves in the surface-charge-governed regime. The rectification ratio through the 2D asymmetric V_2O_5 membrane is easily controlled by adjusting the base to tip the balance of the triangle. Moreover, the triangular ion rectifier of the V_2O_5 membrane can also be utilized as an ion pump to promote uphill transportation of ionic species against the concentration gradient under the influence of a fluctuating external potential with a mean value of zero.

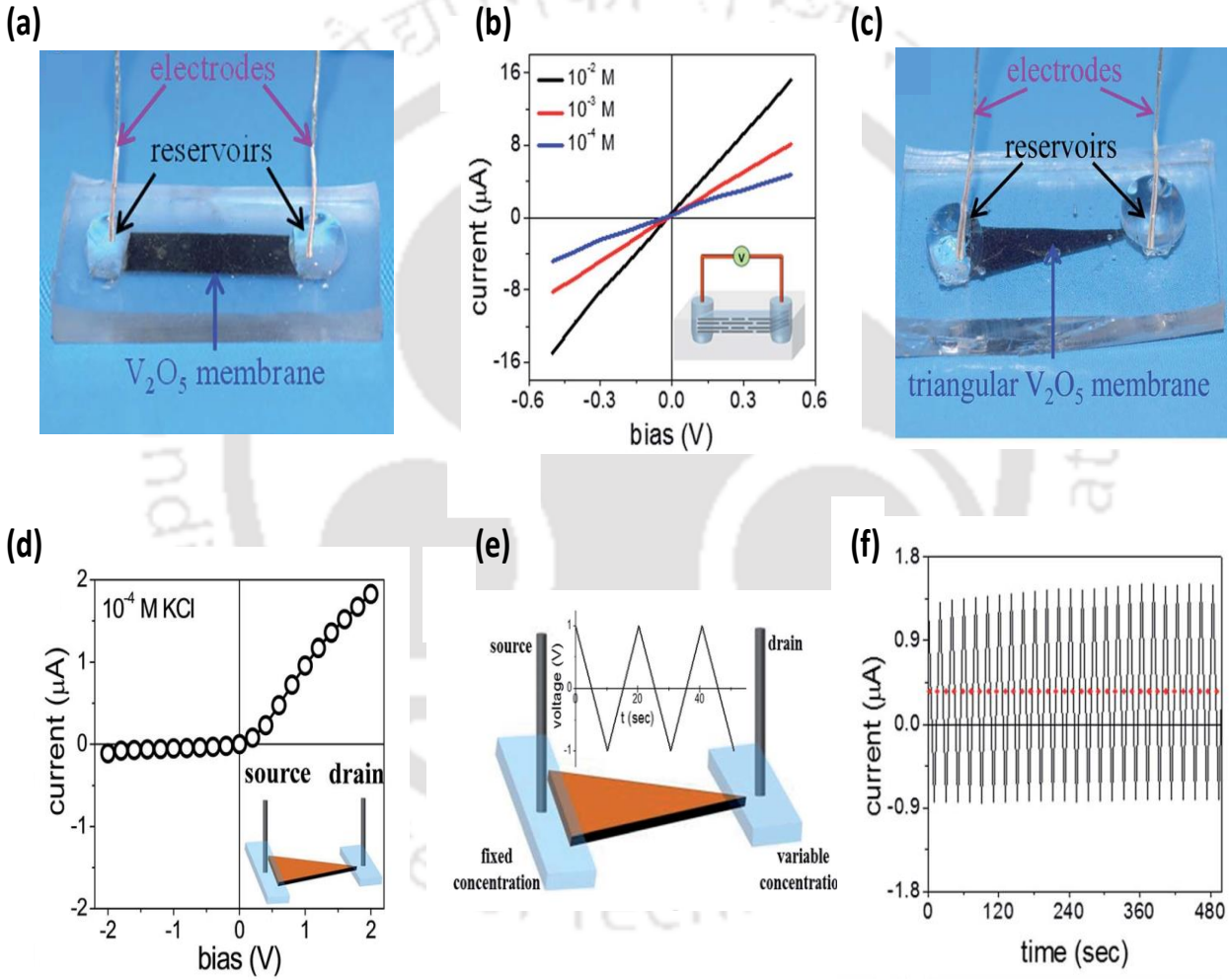

Fig.1.26: Reconstructed V_2O_5 ionic conduits as 2D cation pump: (a) Digital photo of a rectangular V_2O_5 based nanofluidic conduit. (b) *I-V* curves recorded through rectangular V_2O_5 membrane. (c) Digital photo of triangular V_2O_5 membrane-based nanofluidic conduit. (d) *I-V* curves recorded through the triangular V_2O_5 conduit at 10^{-4} M KCl electrolyte concentration. (e) Schematic representation of the triangular nanofluidic ion pump operates under a fluctuating electric field with a mean value of zero. (f) The plot of current recorded through a V_2O_5 triangular strip shows as a function of time under a fluctuating electric field with a mean value of zero (between +1 V and 1 V). (Image copied from *J. Mater. Chem. A*, 2019, **7**, 10552.)

Inspired by the transpiration mechanism of plants, Luo *et al.* demonstrated an artificial ion pump based on the 2D MXene ($Ti_3C_2T_x$) membrane.[105] The Mxene membrane has a high near-infrared wave absorption capacity for excellent light-to-heat conversion, which accelerates macroscale water evaporation and pumping ions against a 200-fold concentration gradient upon asymmetric infrared light irradiation. The uphill ion transportation can be realized by monitoring the zero-volt current, which shows sign reversal upon light irradiation. Moreover,

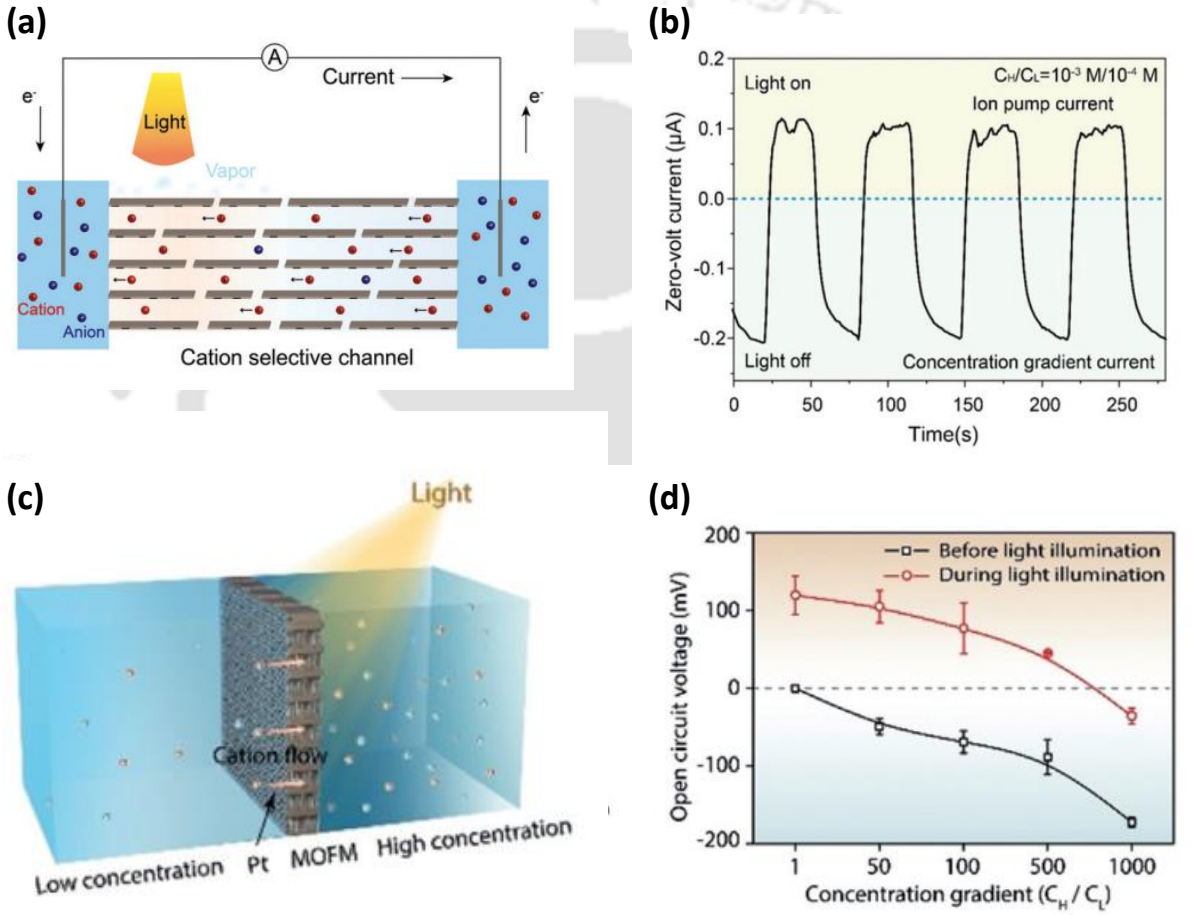

Fig. 1.27: 2D ion pump: (a) Schematic illustration of the generation of net ionic flow through the MXene membrane upon asymmetric light illumination. Upon IR light illumination, the diffusion of cations occurs from the un-irradiated area to the irradiated area, and the ionic current flows from the un-irradiated area to the irradiated area. (b) Zero-volt current curves with alternating light illumination at 10-fold (C_H = 10^{-3} M; C_L = 10^{-4} M) KCl concentration. (c) Schematic illustration of photo-driven uphill ion transport through MOF membrane. (d) Open-circuit voltage as a function of concentration gradient before (black) and during (red) illumination. Positive voltage represents cations being transported uphill from the C_L side to the C_H side. (Image copied from (a-b) *Mater. Chem. Front.*, 2020, **4**, 3361. (c-d) *Angew. Chem.* 2020, **132,** 12895.)

the MXene membrane devices can harvest electricity from salinity gradient due to their excellent perm-selectivity. It generates a stable current and voltage of about 7.3 mA and 13.6 mV, respectively, on exposure to infrared light. Mao *et al*. demonstrated a biomimetic photo-responsive ion channel and photo-driven ion pump using a porphyrin-based metal-organic framework membrane.[106] The molecular-size pores in the MOF membrane enable precise and robust optoelectronic ion transport modulation in a broad range of concentrations. Introduction of platinum nanoparticles into the MOF framework realized a Schottky barrier photodiode, where photo-voltage is generated across the membrane via uphill transportation of ions from a region of low concentration to a region of high concentration, i.e., against the concentration gradient. The light irradiation generates an additional surface charge on the dielectric surface. The induced surface charge attracts additional counter-ions, providing an extra driving force for cation transport in an alternate pathway of lower activation energy.

1.5: Conclusion:

Mighty nature always motivates us with new life lessons, and learning from nature is an everlasting subject in human survival and sustainable development. Inspired by this astonishing biological machineries' structural integrity and functioning, tremendous research efforts have been put forward to mimic these bio-functioning properties in different artificial nanofluidic devices. But regulating the mysterious biochemical and biophysical phenomena in an artificial unit is quite challenging. However, the advent of nanoscience and nanotechnology made it possible to handle these constraints and provided an avenue to create novel integrated nanofluidic devices. Recently lamellar membranes reconstructed from 2D nanosheets have been invoked in the field of nanofluidic, where they display features like surface-charged governed ionic transport, size-selective ionic transportation, ionic current rectifications, and environment responsiveness analogous to biological types of machinery and hence provided a

macroscopic platform to study the vital activities proficiently. Even though numerous efforts are devoted to developing and understanding these membranes, an exhaustive investigation from researchers across the disciplines is required to achieve their true potential in practical applications.

1.6: References:

1. H. Daiguji, *Chem. Soc. Rev*., 2010, **39**, 901.
2. J. C. T. Eijkel and A. van den Berg, *Microfluid. Nanofluid*., 2005, **1**, 249.
3. R. B. Schoch, J. Han and P. Renaud, *Rev. Mod. Phys*., 2008, **80**, 839.
4. P. Abgrall and N. T. Nguyen, *Anal. Chem*., 2008, **80**, 2326.
5. W. Sparreboom, A. van den Berg and J. C. Eijkel, *Nat.Nanotechnol*., 2009, **4**, 713.
6. A. van den Berg, H. Craighead and P. Yang, *Chem. Soc. Rev*., 2010, **9**, 889.
7. W. Sparreboom, A. van den Berg and J. C. T. Eijkel, *New J. Phys*., 2010, **12**, 015004.
8. L. Bocquet and E. Charlaix, *Chem. Soc. Rev*., 2010, **39**, 1073.
9. J. Lee, T. Laoui and R. Karnik, *Nat. Nanotechnol*., 2014, **9**, 317.
10. K. Zhou, J. M. Perry and S. C. Jacobson, *Annu. Rev. Anal. Chem*., 2011, **4,** 321.
11. A. R. Koltonow and J. Huang, *Science*, 2016, **351**, 13950.
12. S. L. Levy and H. G. Craighead, *Chem. Soc. Rev*., 2010 ,**39**, 1133.
13. . M. Napoli, J. C. T. Eijkel and S. Pennathur, *Lab Chip*, 2010, **10**, 957.
14. A. Piruska, M. Gong, J. V. Sweedler and P. W. Bohn, *Chem. Soc. Rev*., 2010, **39**, 1060.
15. H. C. Chang, G. Yossifon and E. A. Demekhin, *Annu. Rev. Fluid Mech*., **2012**, 44, 40.
16. L. Zhang and X. D. Chen, *Angew. Chem., Int. Ed*., 2013, **52**, 7640.
17. W. Han and X. Chen, *J. Chem. Technol. Biotechnol*., 2020, **95**, 1622.
18. G. Liu, T. Chen, J. Xu and K. Wang, *J. Mater. Chem. A*, 2018, **6**, 18357.
19. D. Mijatovic, J. C. T. Eijkel and A. van den Berg, *Lab Chip*, 2005, **5**, 492.
20. S. M. Stavis, E. A. Strychalski and M. Gaitan, *Nanotechnology*, 2009, **20**, 165302.
21. Z. Zhang, L. Wen and L. Jiang, *Chem. Soc. Rev*., 2018, **47**, 322.
22. S. Arscott and D. Troadec, *Nanotechnology*, 2005, **16**, 2295.
23. Y. Xu and N. Matsumoto, *RSC Adv*., 2015, **5**, 50638.

24. L. T. Sexton, L. P. Horne and C. R. Martin, *Mol. BioSyst*., 2007, **3**, 667.

25. J. Kudr, S. Skalickova, L. Nejdl, A. Moulick, B. RuttkayNedecky, V. Adam and R. Kizek, *Electrophoresis*, 2015, **36**, 2367.

26. X. Hou, W. Guo and L. Jiang, *Chem. Soc. Rev*., 2011, **40**, 2385.

27. M. Kong, M. Li, R. Shang, J. Wu, P. Yan, D. Xu and C. Li, *ACS Appl. Mater. Interfaces*, 2018, **10**, 2850.

28. H. Zhao, Z. Yang and L. Guo, *NPG Asia Mater*., 2018, **10**, 1.

29. X. Feng, X. Ding and D. Jiang, *Chem. Soc. Rev*., 2012, **41**, 6010.

30. K. Raidongia and J. X. Huang, *J. Am. Chem. Soc*., 2012, **134,** 16528.

31. R. R. Nair, H. A. Wu, P. N. Jayaram, I. V. Grigorieva and A. K. Geim, *Science*, 2012, **335**, 442.

32. Y. Xu, *Adv. Mater*., 2018, **30**, 1702419.

33. L. Bocquet, *Nat. Mater*., 2020, **19**, 254.

34. M. Macha, S. Marion, V. V. R. Nandigana and A. Radenovic, *Nat. Rev. Mater*., 2019, **4**, 588.

35. S. Dervin, D. D. Dionysiou and S. C. Pillai, *Nanoscale*, 2016, **8**, 15115.

36. S. Prakash, M. Pinti and B. Bhusha, *Philos. Trans. R. Soc. London, Ser. A*, 2012, **370**, 2269.

37. D. Gillespie, *Nano Lett*., 2012, **12**, 1410.

38. J. Jakowiecki, A. Sztyler, S. Filipek, P. Li, K. Raman, N. Barathiraja, S. Ramakrishna, R. Eswara Jairam, A. Altaee, O. Sharif Adel, M. Ajayan Pulickel and V. Renugopalakrishnan, *Interface Focus*, 2018, **8**, 20170066.

39. A. S. Verkman and A. K. Mitra, *Am. J. Physiol. Renal Physiol*., 2000, **278**, F13–F28.

40. W. Song, C. Lang, Y.-X. Shen and M. Kumar, *Annu. Rev. Mater. Res.*, 2018, **48**, 57.

41. J. Shen, R. Ye, A. Romanies, A. Roy, F. Chen, C. Ren, Z. Liu and H. Zeng, *J. Am. Chem. Soc*., 2020, **142**, 10050.

42. I. Kocsis, Z. Sun, Y. M. Legrand and M. Barboiu, *npj Clean Water*, 2018, **1**, 13.

43. M. Barboiu and A. Gilles, *Acc. Chem. Res*., 2013, **46**, 2814.

44. K. Kim, J. Geng, R. Tunuguntla, L. R. Comolli, C. P. Grigoropoulos, C. M. Franklin and A. Noy, *Nano Lett*., 2014, **14**, 7051.

45. L. Huang, M. Zhang, C. Li and G. Shi, *J. Phys. Chem. Lett*., 2015, **6**, 2806.

46. F. Perreault, A. Fonseca de Faria and M. Elimelech, *Chem. Soc. Rev*., 2015, **44**, 5861.

47. G. Algara-Siller, O. Lehtinen, F. Wang, R. Nair, U. Kaiser, H. Wu, A. Geim and I. Grigorieva, *Nature*, 2015, **519**, 443.

48. Y. Han, Z. Xu and C. Gao, *Adv. Funct. Mater*., 2013, **23**, 3693.

49. R. K. Joshi, P. Carbone, F. C. Wang, V. G. Kravets, Y. Su, I. V. Grigorieva, H. A. Wu, A. K. Geim and R. R. Nair, *Science*, 2014, **343**, 752.

50. L. Huang, J. Chen, T. Gao, M. Zhang, Y. Li, L. Dai, L. Qu and G. Shi, *Adv. Mater*., 2016, **28**, 8669.

51. Y. Han, Y. Jiang and C. Gao, *ACS Appl. Mater. Interfaces*, 2015, **7**, 8147.

52. J. Ding, H. Zhao, B. Xu, and H. Yu, *ACS Sustainable Chem. Eng.* 2020, 8, **24**, 8986.

53. W. Zhang, L. Zhang, H. Zhao, B. Li and H. Ma, J. *Mater. Chem. A*, 2018, **6**, 13331.

54. A. Pendse, S. Cetindag, M. H. Lin, A. Rackovic, R. Debbarma, S. Almassi, B. P. Chaplin, V. Berry, J. W. Shan and S. Kim, *Small*, 2019, **15**, 1904590.

55. L. Ding, Y. Wei, Y. Wang, H. Chen, J. Caro and H. Wang, *Angew. Chem., Int. Ed*., 2017, **56**, 1825.

56. Y. Zhou, H. Ding, A. T. Smith, X. Jia, S. Chen, L. Liu, S. E. Chavez, Z. Hou, J. Liu, H. Cheng, Q. Liu and L. Sun, *J. Mater. Chem. A*, 2019, **7**, 14089.

57. 2 J. W. Post, J. Veerman, H. V. M. Hamelers, G. J. W. Euverink, S. J. Metz, K. Nijmeijer and C. J. N. Buisman, *J. Membr. Sci*., 2007, **288**, 218.

58. A. T. Besha, M. T. Tsehaye, D. Aili, W. Zhang and R. A. Tufa, *Membranes* 2020, **10**, 7.

59. J. G. Hong, B. Zhang, S. Glabman, N. Uzal, X. Dou, H. Zhang, X. Wei and Y. Chen, *J. Membr. Sci*., 2015, **486**, 71.

60. 0 J. W. Post, H. V. M. Hamelers and C. J. N. Buisman, *Environ. Sci. Technol.*, 2008, **42**, 5785.

61. R. S. Kingsbury, K. Chu and O. Coronell, *J. Membr. Sci*., 2015, **495**, 502.

62. D. A. Vermaas, E. Guler, M. Saakes and K. Nijmeijer, *Energy Procedia*, 2012, **20**, 170.

63. S. Lin, A. P. Straub and M. Elimelech, *Energy Environ. Sci*., 2014, **7**, 2706.

64. A. M. Benneker, T. Rijnaarts, R. G. Lammertink and J. A. Wood, *J. Membr. Sci*., 2018, **548**, 421.

65. V. MLinkov, V. NBelyakov, *Sep. Pur. Technol*., 2001, **25**, 57.

66. X. Tong, B. Zhang and Y. Chen, *J. Membr. Sci*., 2016, **516**, 162.

67. Y.-C. Liu, L.-H. Yeh, M.-J. Zheng and K. C.-W Wu. *Sci. Adv*., 2021, **7**, eabe9924.

68. R. Li, J. Jiang, Q. Liu, Z. Xie and J. Zhai, *Nano Energy*, 2018, **53**, 643.

69. C. Wang, E. Choi and J. Park, *Nano Energy*, 2018, **43**, 291.

70. T. B. Schroeder, A. Guha, A. Lamoureux, G. VanRenterghem, D. Sept, M. Shtein, J. Yang and M. Mayer, *Nature*, 2017, **552**, 214.

71. D. K. Kim, *J. Mech. Sci. Technol*, 2011, **25**, 5.

72. D. K. Kim, C. Duan, Y. F. Chen and A. Majumdar, *Microfluid. Nanofluidics*, 2010, **9**, 1215.

73. W. Guo, L. Cao, J. Xia, F. Q. Nie, W. Ma, J. Xue, Y. Song, D. Zhu, Y. Wang and L. Jiang, *Adv. Funct. Mater*., 2010, **20**, 1339.

74. W. Guo, L. Cao, J. Xia, F. Q. Nie, W. Ma, J. Xue, Y. Song, D. Zhu, Y. Wang and L. Jiang, *Adv. Funct. Mater*., 2010, **20**, 1339.

75. J. Ji, Q. Kang, Y. Zhou, Y. Feng, X. Chen, J. Yuan, W. Guo, Y. Wei and L. Jiang, *Adv. Funct. Mater*., 2017, **27**, 1603623.

76. 3 L. Lin, L. Zhang, L. Wang and J. Li, *Chem. Sci*., 2016, **7**, 3645.

77. K. Xiao, B. Tu, L. Chen, T. Heil, L. Wen, L. Jiang and M. Antonietti, *Angew. Chem., Int. Ed.*, 2019, **58**, 12574.

78. Y. Zhou, W. Guo, J. Cheng, Y. Liu, J. Li and L. Jiang, *Adv. Mater*., 2012, **24**, 962.

79. C. Chen, D. Liu, L. He, S. Qin, J. Wang, J. M. Razal, N. A. Kotov and W. Lei, *Joule*, 2020, **4**, 247.

80. S. Hong, F. Ming, Y. Shi, R. Li, I. S. Kim, C. Y. Tang, H. N. Alshareef and P. Wang, *ACS Nano*, 2019, **13**, 8917.

81. Z. Zhang, P. Zhang, S. Yang, T. Zhang, M. Loffler, H. Shi, M. R. Lohe and X. Feng, *Proc. Natl. Acad. Sci. U. S. A*., 2020, **117**, 13959.

82. 3 A. S. Prabhu, T. Z. N. Jubery, K. J. Freedman, R. Mulero, P. Dutta and M. J. Kim, *J. Phys.: Condens. Matter*, 2010, **22**, 454107.

83. L. Lin, J. Yan and J. H. Li, *Anal. Chem*., 2014, **86**, 10546.

84. V. Gomez, P. Ramirez, J. Cervera, S. Nasir, M. Ali, W. Ensinger and S. Mafe, *Appl. Phys. Lett.*, 2015, **106**, 073701.

85. J. Gao, W. Guo, D. Feng, H. Wang, D. Zhao and L. Jiang, *J. Am. Chem. Soc*., 2014, **136**, 12265.

86. R. Wei, V. Gatterdam, R. Wieneke, R. Tampe ´ and U. Rant, *Nat. Nanotechnol*., 2012, **7**, 257.

87. W. Guo and Y. Tian, *Acc. Chem. Res*., 2013, **46**, 2834.

88. I. Belevich, M. I. Verkhovsky and M. Wikstro¨m, *Nature*, 2006, **440**, 829.

89. J. C. Skou, *Angew. Chem., Int. Ed*., 1998, **37**, 2320.

90. B. P. Pedersen, M. J. Buch-Pedersen, J. P. Morth, M. G. Palmgren and P. Nissen, *Nature*, 2007, **450**, 1111.

91. M. Tagliazucchi and I. Szleifer, *Mater. Today*, 2015, **18**, 131.

92. I. Vlassiouk, S. Smirnov and Z. Siwy, *ACS Nano*, 2008, **2**, 1589.

93. Z. Zhang, L. Wen and L. Jiang, *Chem. Soc. Rev*., 2018, **47**, 322.

94. T. Plett, W. Shi, Y. Zeng, W. Mann, I. Vlassiouk, L. A. Baker and Z. S. Siwy, *Nanoscale*, 2015, **7**, 19080.

95. X. Hou, W. Guo and L. Jiang, *Chem. Soc. Rev*., 2011, **40**, 2385.

96. Z. Siwy and A. Fulinski, *Am. J. Phys*., 2004, **72**, 567.

97. X. Wu, P. Ramiah Rajasekaran and C. R. Martin, *ACS Nano*, 2016, **10**, 4637.

98. L. Zhang, S. Cai, Y. Zheng, X. Cao and Y. Li, *Adv. Funct. Mater*., 2011, **21**, 2103.

99. Z. Zhang, X. Y. Kong, G. Xie, P. Li, K. Xiao, L. P. Wen and L. Jiang, *Sci. Adv*., 2016, **2**, e1600689.

100. M. Miansari, J. Friend, P. Banerjee, M. Majumder and L. Yeo, *J. Phys. Chem. C*, 2014, **118**, 21856.

101. M. Miansari, J. R. Friend and L. Y. Yeo, *Adv. Sci*., 2015, **2**, 1500062.

102.L. Wang, Y. Feng, Y. Zhou, M. Jia, G. Wang, W. Guo and L. Jiang, *Chem. Sci*., 2017, **8**, 4381.

103. M.-L. Liu, M. Huang, L.-Y. Tian, L.-H. Zhao, B. Ding, D.-B. Kong, Q.-H. Yang and J.-J. Shao, *ACS Appl. Mater. Interfaces*, 2018, **10**, 44915.

104. R. K. Gogoi, A. B. Neog, T. J. Konch, N. Sarmah and K. Raidongia, *J. Mater. Chem. A*, 2019, **7**, 10552.

105. X. Li, J. Lao, G. Li, J. Song and J. Luo, *Mater. Chem. Front*., 2020, **4**, 3361.

106. Y. Jiang, W. Ma, Y. Qiao, Y. Xue, J. Lu, J. Gao, N. Liu, F. Wu, P. Yu, L. Jiang and L. Mao, *Angew. Chem., Int. Ed*., 2020, **59**, 12795.

Chapter 2

Nanofluidic Transport through Humic acid modified Graphene Oxide Nanochannels

Summary*

In this chapter, the chemical similarity of graphene oxide (GO) and humic acid has been exploited to fine-tune ionic and molecular transport properties of lamellar GO membrane. The introduction of humic acid (HA) (in 10, 15, and 20 weight %) improves nanofluidic transport characteristics, such as ionic mobility, molecular selectivity, diffusivity, and permeability of the GO membrane. Crosslinking of GO layers with purified humic acids conferred mechanical strength and enhanced the membranes' chemical robustness. Remarkably, membranes prepared with 15 % HA displayed superior proton mobility, in-plane diffusivity, and cross-plane permeability than that of pure GO and other composite membranes. The favourable nanofluidic characteristics of the 15 % membrane are attributed to the larger effective heights of the 2D nanochannels, derived from the onset point of surface charge governed ionic conductivity of the membranes. The lamellar GO-HA membranes were also suitable for energy harvesting applications such as the direct methanol fuel cell and reverse electrodialysis.

---

* Paper based on these studies has appeared in *Mater. Chem. Front*., 2018, **2**, 1647.|

2.1: Introduction

Graphene oxide (GO) or graphitic acid is a two-dimensional layered material decorated with sp^2 and sp^3 hybridized carbon atoms extended into a honeycomb lattice of adjacent carbon hexagon. Various oxygen functionalities, *viz.*, epoxy, alcohol, carbonyls, and carboxylic group, prevailed in GO, render it a high magnitude of hydrophilicity, but on the contrary, interrupted its subtle ring aromaticity.[1-3] So unlike pristine graphene, GO is an insulator of electricity. Due to the existence of oxygen groups, GO becomes hydrophilic, which could cause GO fakes to form homogenous dispersions with pure water and other polar organic solvents. Meanwhile, the non-oxidized regions of GO fakes are hydrophobic as pristine graphene, which could explain that GO is an amphiphilic material. As a result, GO nanosheets perform similar to the surfactants rendering GO to stay at the interface of two phases for reducing the free energy.[4,5] The discovery of GO has celebrated a centennial, and thanks to its unique characteristics, despite being a classical material, GO still offers its hotspots for unveiling new exciting insights. The accessibility of various types of reactive oxygen-containing functional moieties allows GO to fuse with a wide range of organic and inorganic materials *via* covalent, non-covalent, and ionic manner, which is the intentional strategy to synthesized functional hybrids and composites with unusual properties.[6-9]

Humic acid, a decomposed product of organic biomass, is ubiquitous in a natural environment. They are amorphous long-chain organic polymers with a wide range of molecular weights. The elementary structure comprises aromatic rings of the di- or trihydroxy-phenol type bridged facilitated by -O-, -NH-, -N=, -S-, and other groups that contain both free OH groups and double bond linkage of quinones.[10,11] The outstanding chemical functionalities of humic acid is known for more than 150 years. Still, it has not been applied much in advanced technologies due to the uncertainties in the chemical structure. The recent studies demonstrated that the

morphology and composition of humic acid are very similar to that of GO.[12] Moreover, like GO, it produces conductive 2D sheets upon reduction.[13,14] The structural and chemical similarities show that humic acid molecules are intercalated into the graphene oxide membrane's interlayer galleries to improve the bare graphene oxide ionic/molecular transportation characteristics.

2.2: SCOPE OF THE PRESENT INVESTIGATION

The major bottleneck in the study of sub-nanometer-size fluids is the limitation in device fabrication techniques. The traditional methods employed for this purpose are either low throughput or require highly expensive and sophisticated instrumentations.[15-17] To overcome these shortcomings, molecularly thin nanochannels were prepared by self-assembling exfoliated layers of two-dimensional (2D) materials.[18-24] The space between the layers of reconstructed-layered materials forms a percolated network of two-dimensional nanochannels, providing a new platform for studying ionic/molecular transport under sub-nanometer confinement. Thanks to the abundance of layered materials, and ease of preparation and scalability, the reconstructed lamellar membranes also promise practical applications in the areas like water desalination, molecular sieving, energy storage, and harvesting.[25,26]

Even though layered materials-based lamellar membranes have several advantages over polymer and inorganic membranes, they are not free from drawbacks. The sub-nanometer-size pores of lamellar membranes that facilitate unprecedented ion/molecular selectivity also impede molecular permeability. The natural choice to overcome low permeability is to increase the height of the channel by applying spacers between the sheets.[27-29] However, the application of foreign spacers sacrifices both selectivity and robustness of the pristine membranes. Here, we have explored the possibility of tuning the transport characteristics of GO membranes without sacrificing their lamellar structure or altering the channel's heights. Humic acid, a

naturally occurring organic material, is applied here to tune the network of GO nanochannels. With a structure chemically and physically similar to that of GO, humic acid caused an all-around improvement of the GO lamellar membrane.

2.3: Experimental section

Extraction of Humic acid:

Humic acid was extracted following the standard conjugative alkaline-acid treatment method. In typical experiments, 100 g of soil sample was mixed with 300 ml of 0.1 M NaOH solution and stirred for 2 hours at room temperature. The brown-coloured supernatant obtained after allowing the reaction mixture to stand overnight was collected by centrifugation. The pH of the brownish dispersion was adjusted to 1 to precipitate out the acid-insoluble humic acid. As precipitated, humic acid was thoroughly washed with deionized (DI) water and oven-dried at 60 ºC.

Preparation of GO membrane:

GO was synthesized following the modified Hummers method. Typically, 6 g of $KMnO_4$ was gradually added to ice-cold sulphuric acid (17 M, 50 ml) mixed with 1 g of graphite powder under constant stirring. The mixture was then stirred at 35 ºC for two hours, followed by slow addition of 100 ml of DI water. The reaction was terminated by adding 8 ml of H_2O_2 (30 %) solution. The as-obtained yellow suspension was subjected to two-step washing with HCl (1 M) and acetone. Freestanding membranes were prepared by vacuum filtering the aqueous dispersions of GO through polytetrafluoroethylene (PTFE) membrane.

Fabrication of composite membrane:

Aqueous dispersions of GO and humic acid (1 mg/ml each) were mixed in appropriate amounts

(10, 15, and 20 % humic acid by weight) and sonicated for 15 minutes. The hybrid dispersions were then passed through a cellulose nitrate membrane to prepare GO-HA composite membranes.

Surface charge governed ionic transport:

Measurement of ionic conductivity was done with Ag/AgCl electrodes dipping into both the exposed ends filled with electrolytes, and a source meter (Keithley 2450 model) was used as the electronic load.

Measurements of bending stiffness:

Bending stiffness of the composite membranes were calculated employing Lorentzen & Wetre 2-point method. A known load was placed to one end of the strip, by keeping the other end fixed to a glass slide. The following equation was used to calculate the bending stiffness values (S_b).

$$S_b = \frac{60 \times F \times l^2}{\pi \times \theta \times b}$$

Where, F is defined as bending force (F= weight × gravitational constant), l is the distance between the clamp and the load, θ is the angle of deflection under the influence of load, b is the width of the strip.

Simulation Methodology:

The equilibrium MD simulation was carried by Dr Abhijit Gogoi and Prof. K. Anki Reddy using NAMD 2.11 with optimized potentials for liquid simulations-all atom (OPLS-AA) force field. TIP3P water model was used for the water molecules. The bond length of the water molecules is held constant using SETTLE algorithm. The van der Waals interaction through Lennard-Jones potential was computed with a cut off distance of r_c = 12 Å. Particle

mesh Ewald method (PME) is used for the long range electrostatic interactions. The equation of motions is integrated through velocity Verlet integration method with a time step of 1 *fs*. The simulation system is then energy minimized and equilibrated for 1 *ns* at a constant pressure of 1 *atm* and temperature of 300 *K*. After equilibration the production run is carried out for each of the system for 8 *ns*. During the simulation the pressure was kept constant with modified Nosé-Hoover method where the barostat oscillation time and damping factors both were set to 0.3 *ps*. Similarly, temperature was kept constant using Langevin dynamics with a damping factor of 5 ps^{-1}. In most of the existing literature in membrane simulation. membrane is constraint during the simulations. However, in the present work no constraint was applied in the membrane to have a better resemblance with the experiment.

Characterisation:

The functional groups present in humic acid were characterized by Fourier transform infrared (FTIR) spectroscopy. The morphology of humic acid and graphene oxide was examined by atomic force microscopy (AFM) (Agilent, Model 5500 series), field emission scanning electron microscopy (FESEM) (Zeiss, Model: Gemini) and field emission transmission electron microscope (FETEM) (JEOL, Model: 2100F). X-ray diffraction was studied using Bruker D-205505 Cu-kα radiation (λ=1.5406 Å). Dye separation experiments were analysed using UV-Vis Spectrophotometer (Systronics, Model: 117).

2.4: Results and discussion

Humic acid extracted from native soils following standard procedures [30,31] were characterized with TEM analysis and various spectroscopic techniques such as IR, UV-Vis, and fluorescence spectroscopy (Fig. 2.1). The purified humic acid samples displayed Infra-Red (IR), UV-Vis and fluorescence spectra similar to those reported in the contemporary literature.[32-34] Peaks

around 3440 cm^{-1} and 1657 cm^{-1} in FTIR corresponds to O-H vibrational and aromatic C=C stretching band, respectively. The small shoulder peaks around 2850 cm^{-1} and 1731 cm^{-1} can

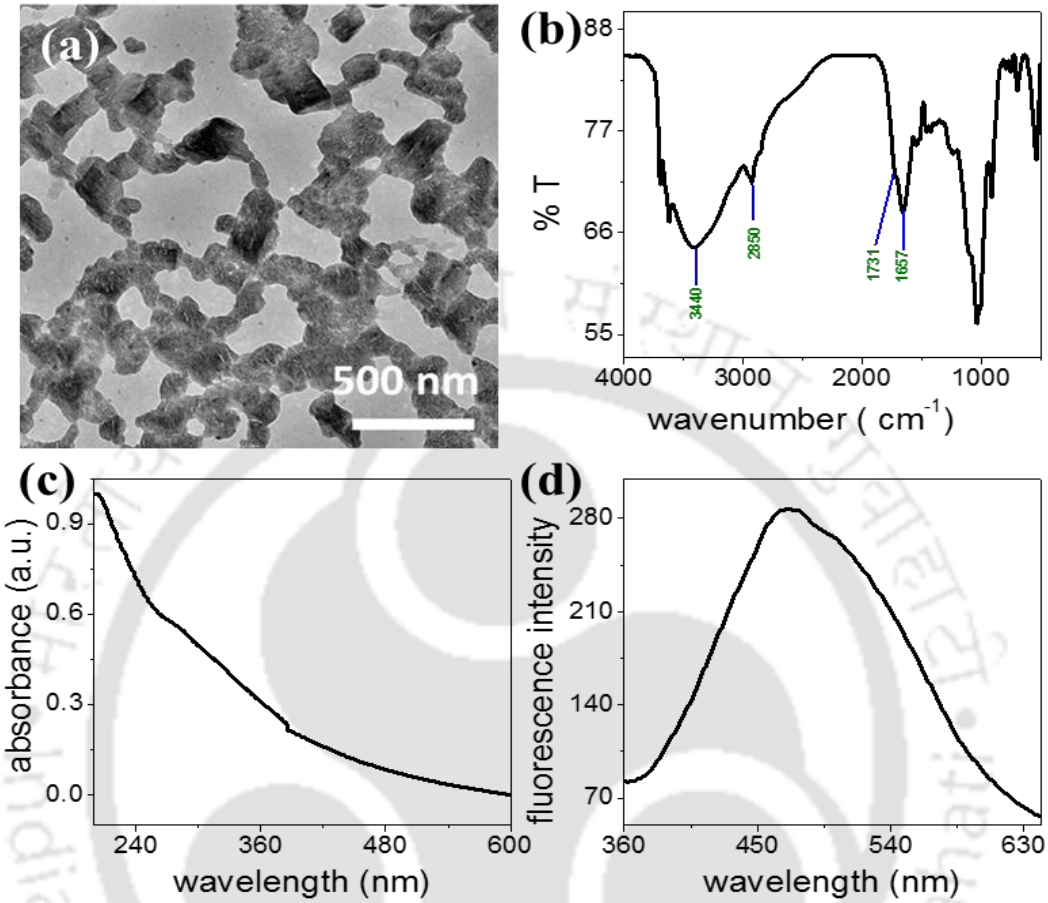

Fig. 2.1: Characterization of humic acids: (a) FE-TEM image. (b) FTIR-spectrum. (c) UV-Vis spectrum and (d) Fluorescene spectrum of humic acid, extracted following standard alkaline-acid treatment method.

be assigned to stretching of aliphatic C-H and C=O of COOH groups. The UV-vis spectrum of humic acid is broad and monotonously decreases with increasing wavelength with a minor shoulder at around 265 nm. Humic acid exhibits emission bands around 470 nm due to aromatic fluorophores with electron-donating functional groups. Fulvic acid shows a stronger emission band at 360 nm; the absence of the same reveals successful extraction of humic acid from the soil. The X-ray photoelectron spectroscopy-based analysis reveals the O/C ratio of the purified humic acid samples to be 0.3 (Fig. 2.2), which was also supported by the EDX elemental quantification carried out under an electron microscope as shown in Fig. 2.2 (O/C was found to be in between 0.25 to 0.3).

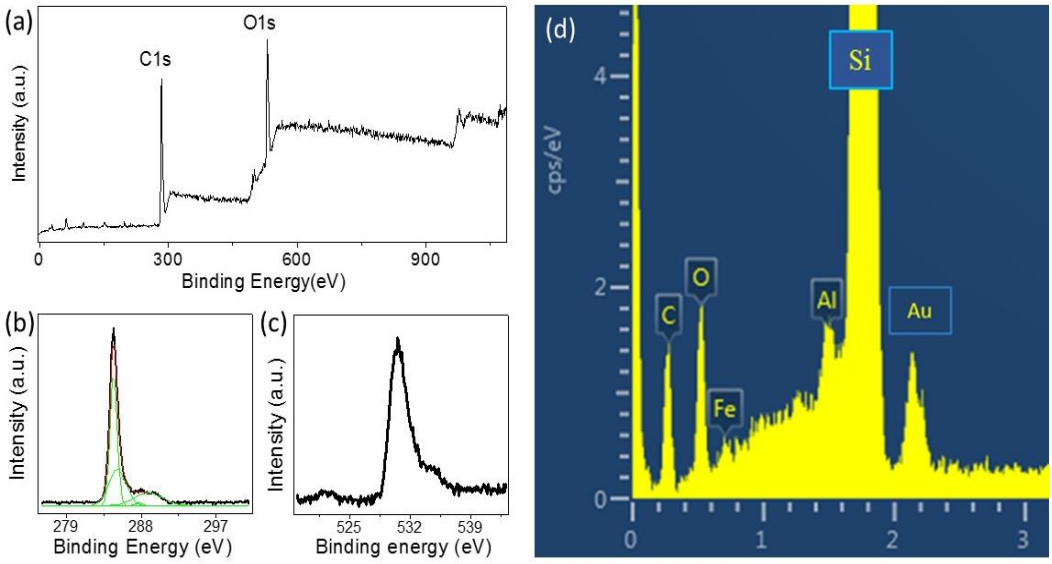

Fig.2.2: Composition analysis of humic acid: (a), (b) and (c) XPS analysis of humic acid sample which shows that the approximate O/C ratio ~ 0.3. (d) EDX elemental quantification of humic acid sample carried out under an electron microscope.

The GO sample used here was synthesized following modified Hummers method and characterized with electron and atomic force microscopy as shown in Fig. 2.3.

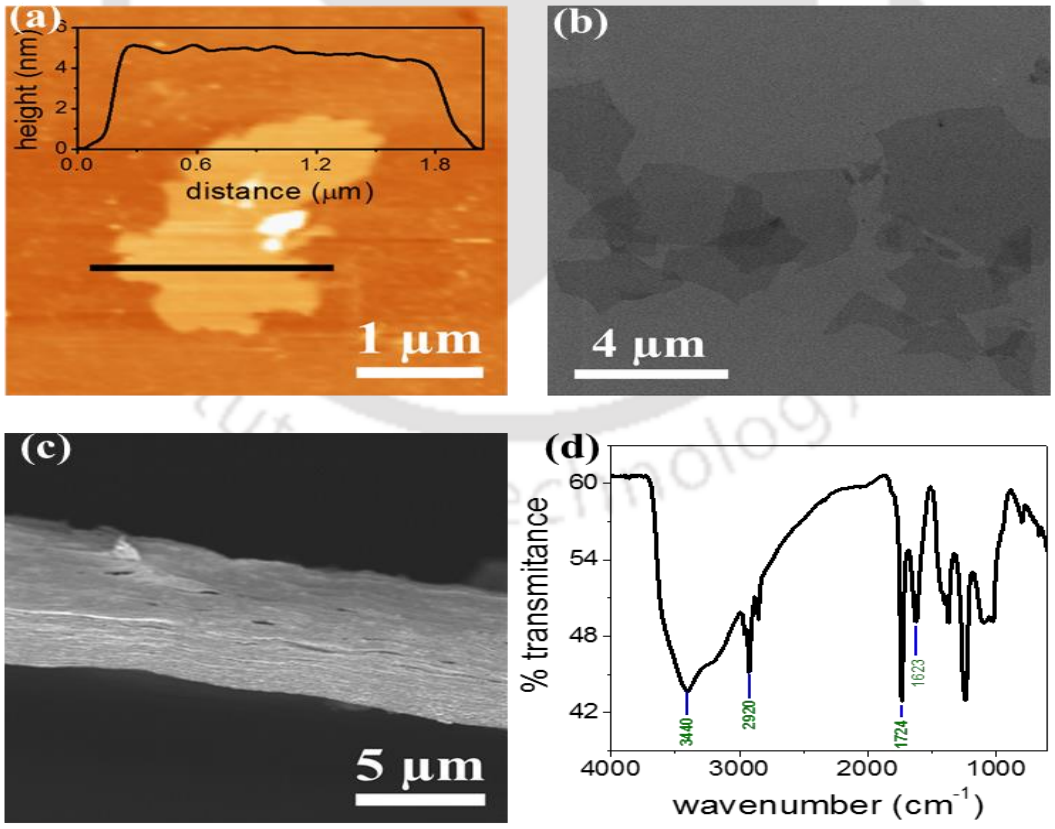

Fig. 2.3: Characterization of GO: (a) AFM image with corresponding height profile and (b) FESEM images of GO sheets prepared by following modified Hummers method. (c) Cross-sectional FESEM image and (d) IR-spectrum of GO membrane.

The interactions between GO and humic acid can be visualized by studying colloidal stability of the mixtures. In Fig. 2.4a, aqueous dispersions of GO and humic acid are compared with that of the mixtures (10, 15, or 20 % humic acid with GO). While dispersions of humic acid started settling down after around 72 undisturbed hours, the mixtures remained unaltered for 60 days (Fig. 2.4b), suggesting the existence of favourable interactions between these two negatively charged nanomaterials. Comprised of synergistic blends of aromatic and oxygenated carbon atoms, both humic acid and GO sheets are amphiphilic. Both these materials' surfactant-like properties have been exploited to disperse hydrophobic nanomaterials like carbon nanotubes through π-π stacking.[35,36]

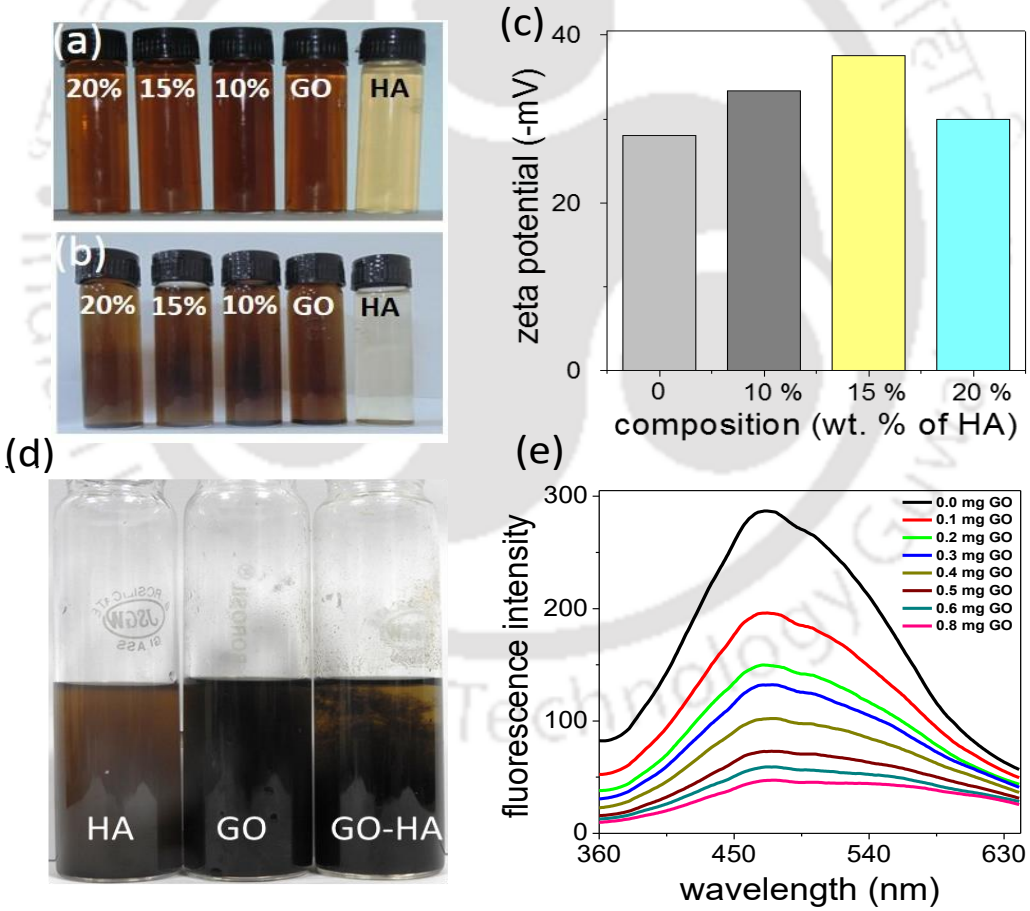

Fig. 2.4: Colloidal stability of GO-HA dispersion: Aqueous dispersions of GO, humic acid and their mixtures (10, 15 and 20 % humic acids in GO) after (a) 5 minutes and (b) 60 days of preparation. (c) Zeta potential of GO-HA composite systems are compared with that of neat GO. (d) Agglomeration behaviour of HA, GO and composite (15% GO-HA) dispersion upon decreasing polarity of the medium. (e) Quenching of fluorescence intensity of humic acid dispersion upon addition of GO.

In the HA-GO dispersion, the aromatic segments of humic acid molecules are expected to interact with hydrophobic regions of the GO surface through π-π stacking, projecting away from the oxygen-containing hydrophilic areas. As a result, the negative zeta potential of humic acid and GO dispersions increases upon mixing (Fig. 2.4c), attributed to the superior dispersibility of the mixtures in polar solvents like water. As the polarity of the medium was decreased by adding ethyl acetate and isopropanol, the HA-GO mixture agglomerated before pure GO and humic acid dispersions, as can be seen from Fig. 2.4d. The existence of π-π stacking between hydrophobic regimes of humic acid and GO sheets was also verified through the fluorescence quenching experiment shown in Fig. 2.4e. The purified humic acid samples display a characteristic emission spectrum ($\lambda_{excitation}$ =320 nm and $\lambda_{emission}$ =470 nm) originated from the conjugated carbon atoms (both aromatic and non-aromatic) bonded various chromophores.[37,38] The addition of GO quenched the fluorescence of humic acid dispersion, but the extent of quenching was directly proportional to the amount of GO added. It supports the existence of definite interactions between the two materials, as GO is known to quench fluorophores through excited-state energy transfers via π-π stacking.[39-41]

Similarly, upon vacuum filtration except for pure humic acid, all other dispersions yielded freestanding membranes. Inset of Fig. 2.5a shows a digital photo of a composite membrane (GO-HA) obtained from 15 % humic acid dispersion. The cross-sectional field emission electron microscopy (FESEM) examinations on the broken edges of GO-HA membranes revealed the formation of densely packed lamellar structures. Under the electron microscopy examinations, no large pores or agglomerated chunks of humic acid were observed. A characteristic cross-sectional FESEM image of 15 % GO-HA membrane is presented in Fig. 2.5a. The lamellar structures of GO-HA membranes were also confirmed by characteristic (002) reflections in the XRD patterns (Fig. 2.5b). The addition of humic acid marginally increased the interlayer spacing, from 8.2 Å of GO to 8.8 Å in 20 % GO-HA membranes.

Moreover, small pieces of membranes (15 mm × 7 mm) were soaked in water for a prolonged time to test the solution's stability. As shown in Fig. 2.5c, the GO membrane started disintegrating within 3 days of soaking, but GO-HA membranes remained unaltered for more than 60 days.

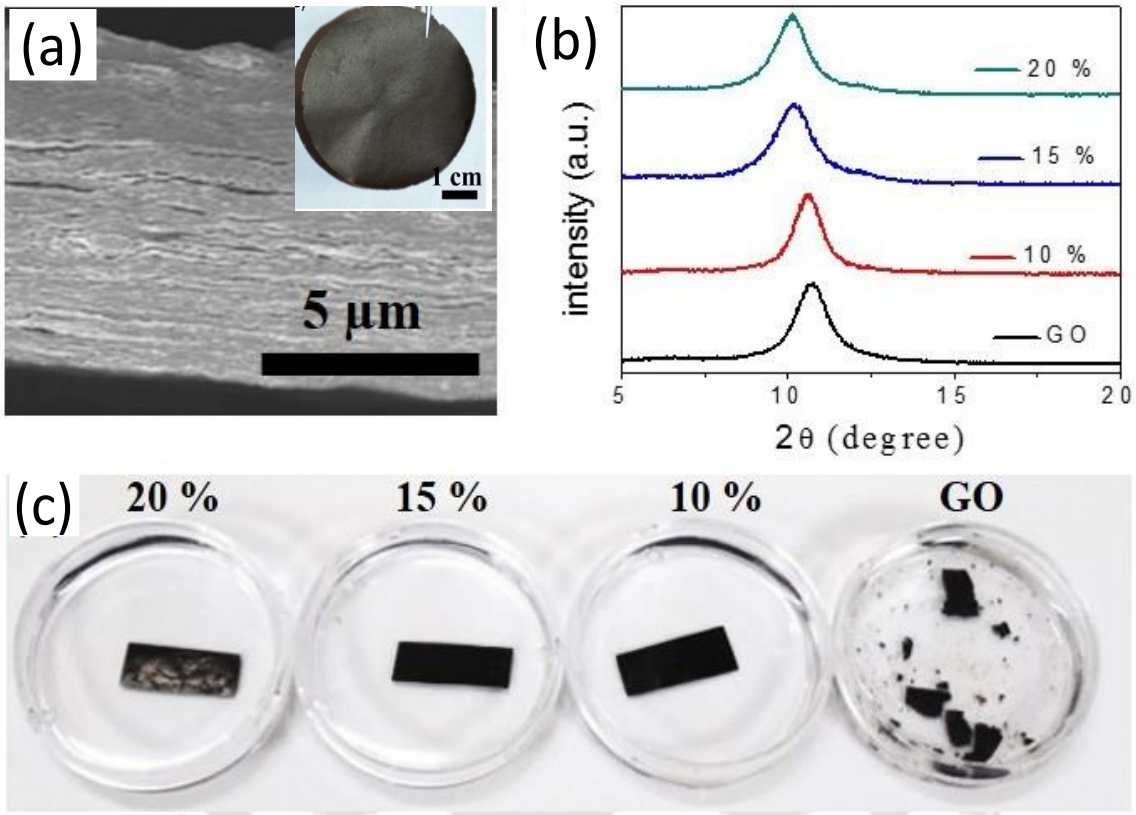

Fig. 2.5: GO-HA free-standing membrane: (a) Cross-sectional FESEM images of 15 % GO-HA membrane. Insets shows a free-standing GO-HA membrane. (b) XRD patterns of air-dried membranes. (c) Photos of GO and GO-HA membranes soaked in water for 60 days.

The enhanced stability of GO-HA membranes is attributed to crosslinking of lamellar GO sheets by the humic acid molecules. During the vacuum filtration, humic acid-modified GO sheets are forced into a tightly packed lamellar structure, providing a geometrically favourable situation for the crosslinking interactions such as π-π stacking, H-bonding, and CH-π stacking. These interactions in the composite membrane are evident from the Fourier Transform Infrared (FTIR) spectra shown in Fig. 2.6. The π-π interaction weakens the aromatic rings' double bond character, causing a red-shift of the C=C stretching vibration band of humic acid from 1657 cm^{-1} to 1620 cm^{-1}. Similar π-π interaction is also seen in the pure GO membranes. The

weakening of the stretching vibrations of the C-H bond (2920-2850 cm^{-1}) in the hybrid system compared to that of humic acid and GO can be attributed to the CH-π interaction between the sheets.[42] Likewise, in the O-H stretching regime, decrease in peak intensity, broadening, and shifting of peak position (from 3440 cm^{-1} to 3340 cm^{-1}) indicate the occurrence of intermolecular H-bonding between the hydrophilic functionalities of the two materials.[43]

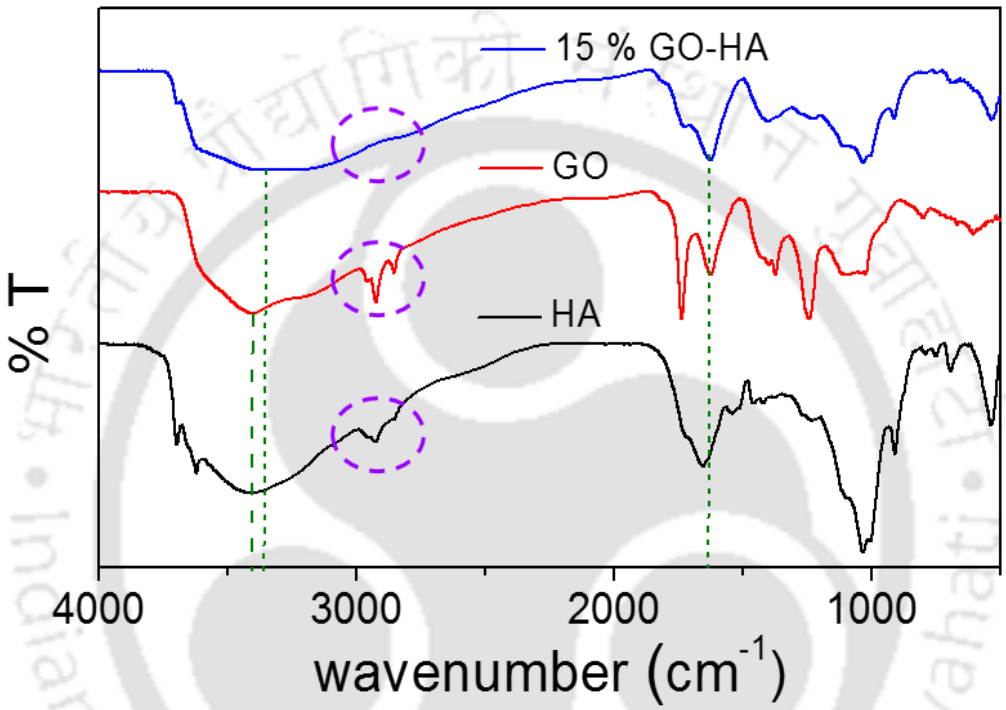

Functional group	GO (cm^{-1})	HA (cm^{-1})	15 % GO-HA (cm^{-1})
C=C	1623	1657	1620
C-H	2920	2850	--
OH	3440	3440	3340

Fig. 2.6: Non-covalent interaction in GO-HA composite: FTIR spectra for HA, GO and 15 % GO-HA composite membrane and comparison of stretching frequencies of different functional groups.

The crosslinking effect of humic acid was further confirmed by studying mechanical properties of the membranes. Fig. 2.7a and 2.7b show that the tensile strength values of the membranes, determined from maximum loads lifted by a rectangular strip (dimensions of 20 mm × 3 mm × 0.027 mm) before failure, improves with increasing humic acid contents on it. The same trend is also followed by the bending stiffness values of the membranes, discussed in the Fig. 2.7c and 2.7d.

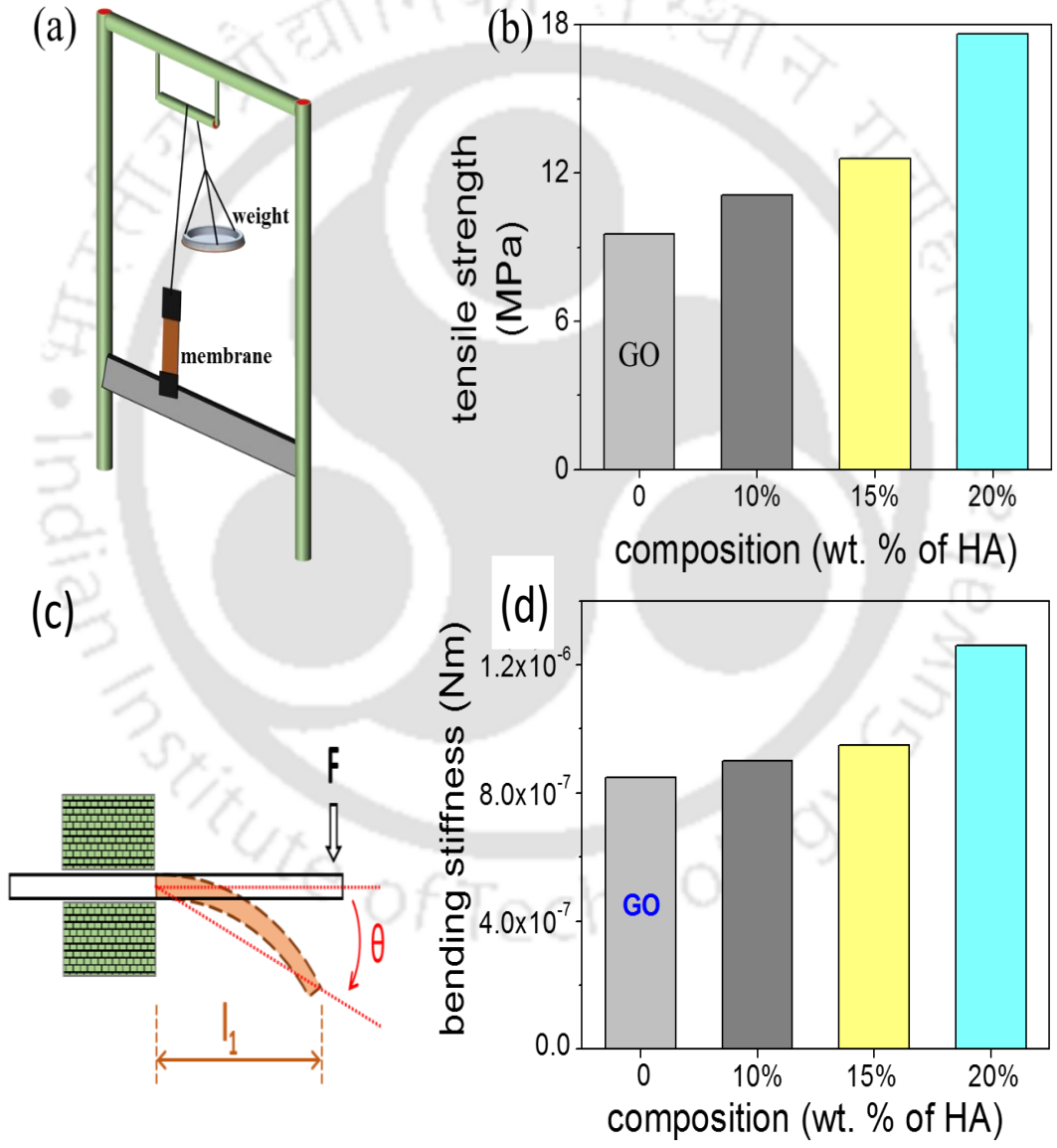

Fig. 2.7: Mechanical strength of the membranes: (a) Schematic illustration of the set-up used for measuring tensile strength of the membranes. (b) Bar diagram representation of tensile strength of different GO-HA composite membranes. (c) Schematic representation of bending stiffness measurement. (d) Bar diagram comparing of tensile strength of different membranes with thickness (20 µm).

One of the most widely anticipated applications of reconstructed layered materials is in the water treatment processes. The requirements of ideal water purification membranes include, chemical/mechanical robustness, high permeability and great selectivity. The solution stability and mechanical robustness of GO-HA membranes are already described in Fig. 2.5c and Fig. 2.7, respectively. The next key is to improve permeability and selectivity, concurrently. With the intention to test permeability and selectivity, fixed volumes (3 ml) of aqueous dye solutions (200 ppm) were vacuum filtered through the composite membranes. From the "time" required to complete the filtration process, permeability of the membranes was calculated by employing equation (*1*).

$$Permeability = \frac{(membrane\ thickness)\times(amount\ of\ permeate)}{(membrane\ surface\ area)\times(time)\times(differential\ pressure\ )} \quad -- \quad (1)$$

The bar diagrams of Fig. 2.8c show liquid permeability of the membranes of different compositions. Surprisingly, 15 % GO-HA membrane shows higher permeability than that of 10 %, 20 % and pure GO membranes. The selectivity of the membranes was studied by measuring the concentration of the methylene blue (MB) dye in the solution before and after filtration by recording its UV-Vis spectra. The weight of the dye molecules separated from their aqueous dispersions during the filtration process is shown as bar diagrams in Fig. 2.8a. Interestingly, pure GO and membranes with 15 % humic acids removed slightly more dye molecules than 10 % and 20 % GO-HA membranes. But the dye removal efficiencies ($F_{(aff)}$) of the membrane with 15 % humic acid was calculated to be far better than that of pure GO and other composite membranes, bar diagram in Fig. 2.8d. $F_{(aff)}$ of the membranes was calculated by dividing weight (w) of the dye molecules removed from the solution with time (t) required for the filtration and weight (m_w) of the membranes ($F_{(aff)} = w/(t\times m_w)$). It demonstrates the possibility of enhancing both permeability and selectivity of lamellar membrane just by tuning the compositions of the correct spacer.

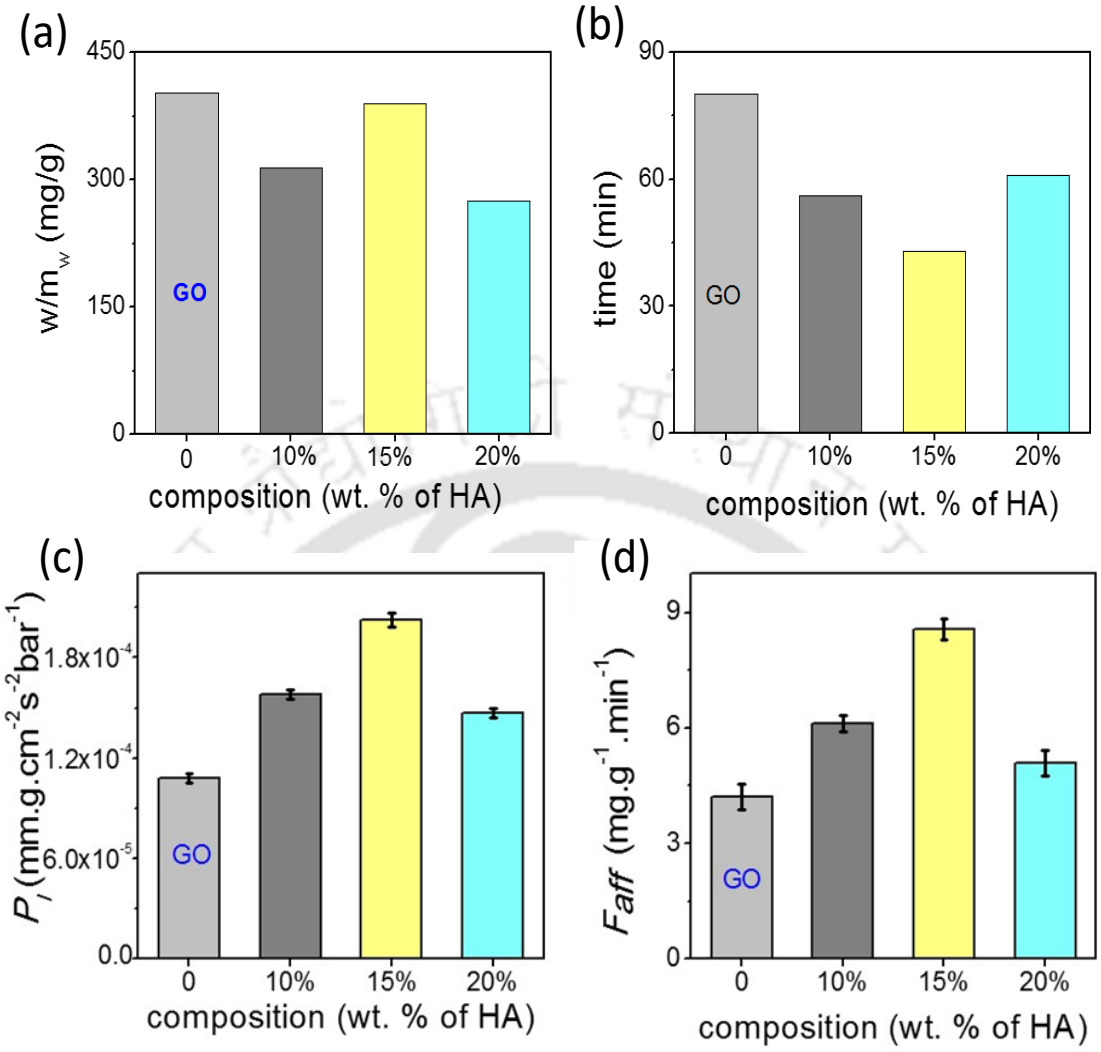

Fig. 2.8: Molecular selectivity and permeability: (a) Weight of the dye molecules separated, and (b) time consumed by different membranes to complete the filtration process. (c) Liquid (water) permeability (P_l) and (b) dye removal efficiencies (F_{aff}) of different GO-HA membranes are compared with that of GO.

To further confirm the prospect of creating favourable channel structures for molecular diffusion, the permeability of water vapours through the membranes was studied gravimetrically. Fig. 2.9 shows the evaporation rate of water from a glass vial covered by different membranes with a thickness of ~ 20 microns. Here again, GO-HA membranes allowed permeation of water vapour at a much higher rate than GO membranes. Membrane with 15% humic acids displayed permeation value (1.02×10^{-6} mm g cm^{-2} s^{-1} bar^{-1}), almost equal to the one with no barrier on it (1.3×10^{-6} mm g cm^{-2} s^{-1} bar^{-1}).

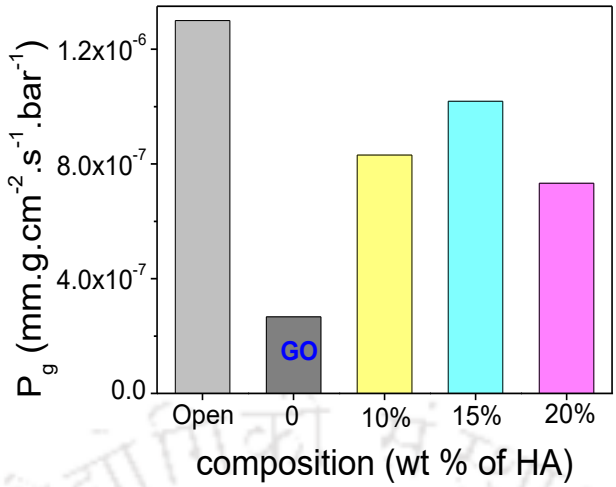

Fig. 2.9: Water vapour permeation: Evaporation rate of water from a glass vial covered by different membranes with thickness of ~ 20 microns.

Data shown in Fig. 2.8 and 2.9 show permeability of water molecules across the membrane in the vertical direction, where water molecules travel through long zig-zag channels. In lamellar membranes, the preferred movement of the molecules should be in the horizontal order, *i.e.*, in the plane of the sheets. To get insights into the in-plane molecular diffusivity, rectangular strips of membranes were encapsulated into freshly prepared polydimethylsiloxane (PDMS) elastomer. As shown in the schematic of Fig. 2.10a, liquid water was introduced to the channels through the holes cut out at both ends of the strip. The diffusion process was monitored by measuring response current across the membranes after applying a voltage (0.5 volts) for 50 ms through the Ag/AgCl electrodes at regular intervals of 30 minutes. In the beginning, no

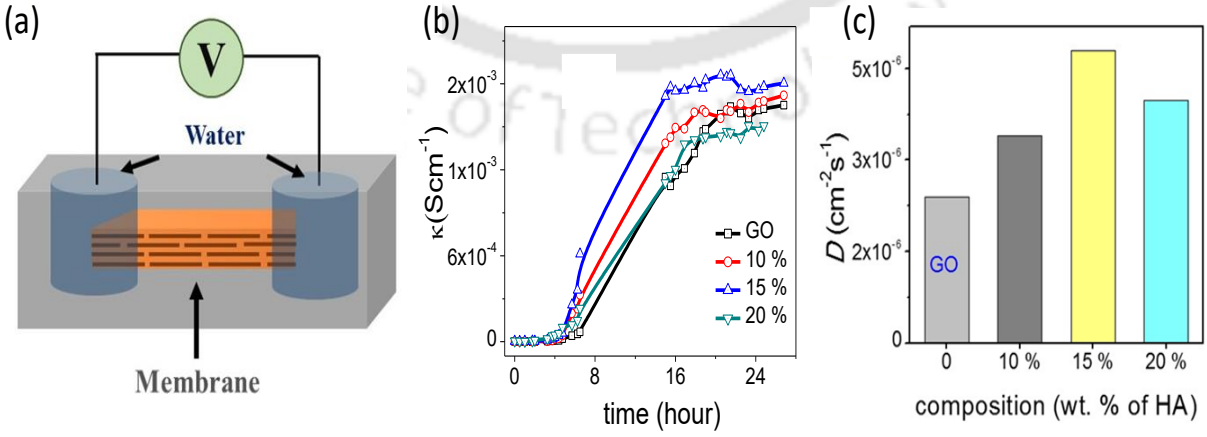

Fig.2.10: In-plane diffusion: (a) Schematic diagram of the device employed for determining in-plane water diffusivity (b) Current response plot of in-plane water diffusivity measurement. (c) In-plane water diffusivities of the different GO-HA membranes.

current was observed; the measurable ionic current was seen only when water molecules diffusing from both ends of the membranes met each other to complete the circuit. As the water molecules diffused to other regions of the membranes, current values started increasing with time and reached saturation when all the channels became completely hydrated (Fig. 2.10b). The time (*t*) taken by the water molecules to diffuse into channels of entire membrane reflect the characteristics of channels in the respective membranes. Fig. 2.10c shows diffusivity values (*D)* of the membranes calculated using Einstein's approximation for two dimensional diffusions, equation (*2*).

$$x^2 = 4.D.t \qquad \text{---------- (2)}$$

Where, the diffusion distance (*x*) is taken as half of the membranes length.

Another essential characteristic of reconstructed lamellar membranes is their high nanofluidic ionic conductivity. Ionic currents through 2D channels of different GO-HA membranes were measured after exposing water-soaked devices with aqueous KCl solutions of different concentrations. The slopes of the *I-V* curves (shown in Fig. 2.11a) measured after 7 hours of KCl soaking were normalized with membranes dimensions to determine conductivity. The conductivity-concentration plot of Fig. 2.11b and Fig 2.11c revealed that each membrane exhibit two distinct regimes of conductivity. At the high concentrations, the conductivity of the devices varies linearly with a concentration similar to that of bulk solutions. Still, for the concentrations below 10^{-2} M, conductivity did not vary even for four orders of magnitude change in the concentration. This typical characteristic of nanofluidic channels, known as the surface-charge-governed ionic conductivity, originates from the overlapping Debye layers of the channel walls under nanofluidic confinement. It confirms the formation of a percolated nanofluidic network and indicates an absence of large macrospores.

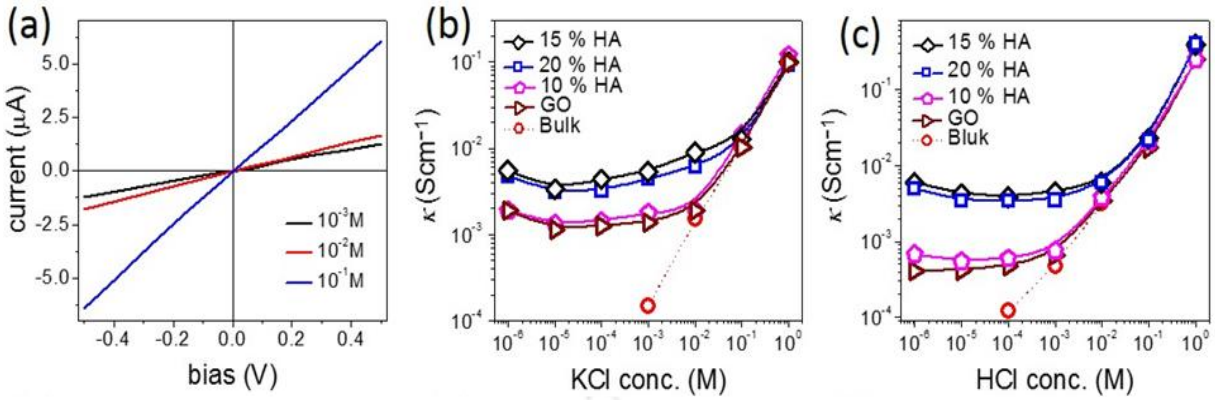

Fig. 2.11: Surface charge governed ionic conductivity: (a) Representative *I-V* curves recorded with a nanofluidic device made from 15 % GO-HA membrane after soaking the same with aqueous KCl solutions of different concentrations. Ionic conductivity (κ) of different nanofluidic devices as a function of (b) KCl, and (c) HCl concentration.

Moreover, the transition point (C_t), defined as the concentration at which the characteristics of ionic conductivity change from bulk-like to surface-charge-governed, throws light on the effective dimensions of the nanochannel.[44] From the conductivity versus concentration plots of Fig. 2.11b, C_t of different membranes was determined from the intersection of the lines laid over two distinct conductivity regimes as shown in Fig. 2.12.

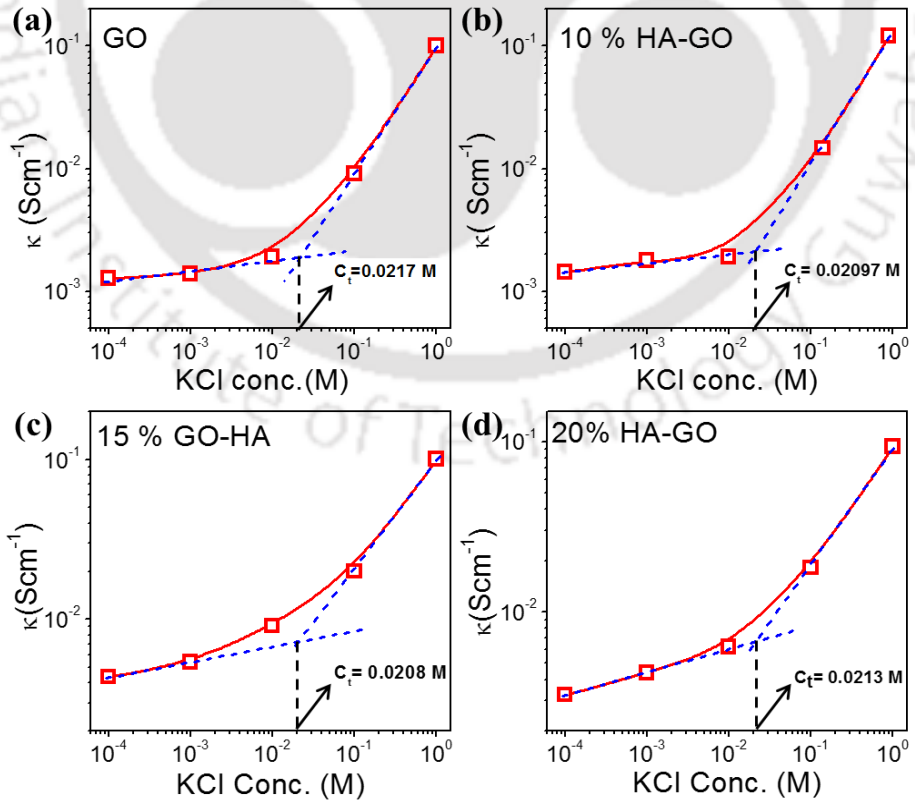

Fig. 2.12: Transition concentration point: Ionic conductivity of different nanofluidic devices as function of electrolyte concentration showing the point of transition concentration.

The effective channel heights (h) and C_t is connected through equation (*3*).[44]

$$h = 10^{-3}\frac{\sigma_s}{eN_AC_t} \quad ------ \quad (3)$$

Where, σ_s, N_A, and e stands for surface charge density, Avogadro's constant, and elementary charge, respectively. The effective channel height obtained as such for different HA-GO membranes are shown in Table 1.

Fig. 2.11b also reveals that, at the surface-charge-governed regime membrane with 15 % and 20 % humic acid contents shown ~ 4 times higher ionic conductivity than that of GO and 10 % GO-HA membranes. In order to verify this unusual trend, conductivity of the membranes was also measured with HCl solutions of similar concentrations. Here again, at the low concentration regime 15 % and 20 % GO-HA membrane shown one order of magnitude higher ionic conductivity than other membranes, see Fig. 2.11c. The measured ionic conductivity of the channels is a product of surface charge density (equivalent to ionic concentration) and ionic mobility. To understand the unusual enhancement in the surface-charged-governed ionic conductivity of 15 % and 20 % GO-HA membranes it is important to determine one of these parameters, independently. The surface charge density of the channel walls was determined by employing an ion-exchange based method.[13] In the first step, all the movable ions of the membranes were exchanged with Li^+ by stirring a piece of membrane (11 mm × 7 mm × 0.013 mm and 0.8 mg) with 10 ml of 2 M LiCl solution, for 24 hours. The excess Li^+ ions were then removed by washing with excess water. The movable, Li^+ were then re-exchanged with H^+, by stirring the membranes with 1 mM HCl solution for 20 hours. The total number of proton exchanged (N_p) with Li^+ ions were determined from the decrease in the conductivity value of the supernatant liquid, by considering limiting conductance of HCl and LiCl as 425 Ω^{-1} and 115 Ω^{-1}, respectively. Surface charge density (σ_s) of different membranes were determined from N_p by following equation (*4*).

$$\sigma_s = \frac{N_p \times q}{N_n \times l \times w} \quad ----(4)$$

Where, N_n is number of nanochannels obtained by dividing membrane thickness with height of one channel (d spacing of (002) plan), q is elementary charge, l and w represents length and width of the membranes.

Surface-charge-density determined as such for different GO-HA membranes are shown in Fig. 2.13a. Walls of the channels with 15 % GO-HA exhibits slightly higher surface-charge-density than that of other membranes, but not enough to explain one order of magnitude increase in the ionic conductivity. The σ_s values obtained as such were used to determine proton mobility (μ) through the channels, by employing its relationship with surface-charge-governed conductivity (G) (*5*).[45]

$$G = 2\mu\sigma_s \frac{w}{l} \quad --------- (5)$$

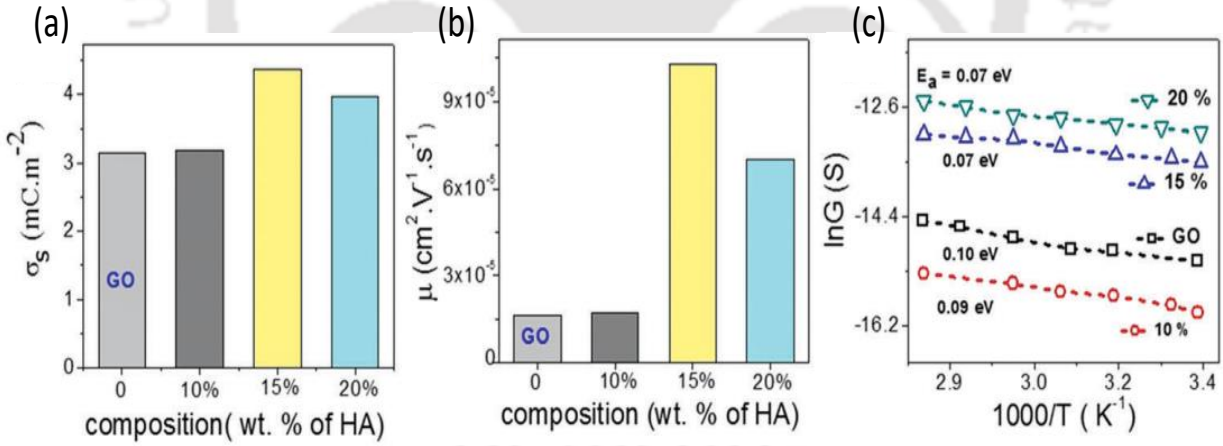

Fig. 2.13: Nanofluidic parameter: (a) Surface charge density (σ_s), (b) proton mobility (μ), and (c) Arrhenius plot of proton conductance of different GO-HA membranes are compared with that of GO.

As shown in Fig. 2.13b, membranes with 15 % humic acid contents exhibit much higher proton mobility than GO and 10 % GO-HA membranes. It is remarkable to observe that the structure of nanofluidic channels of reconstructed lamellar membranes can be finely tuned to support higher molecular diffusivity and higher ionic mobility. To understand the mechanism of proton

transport, the conductance of 10^{-4} M HCl through composite membranes was studied as a function of temperature. The conductance of GO and GO-HA membranes follows an Arrhenius-like behaviour. From the Arrhenius plot, shown in Fig. 2.13c, the activation energy for proton transport through all the membranes was found to be in the range of 0.07 to 0.1 eV. The activation energy values suggest a Grotthuss-like hopping, where charge is transported the through coordinated hopping of protons between water molecules and surface OH^- groups of nanochannels.[46]

Table 1. Various nanofluidic parameters for GO and GO-HA membranes are compared with their corresponding effective channel heights.

Membranes	Effective channel height (nm)	Liquid permeability ($mm.g.cm^{-1}s^{-1}bar^{-1}$)	Gas permeability ($mm.g.cm^{-1}s^{-1}bar^{-1}$)	In-plane diffusivity (cm^2s^{-1})	Proton mobility ($cm^2V^{-1}s^{-1}$)	Activation energy (eV)
GO	1.54	1.0×10^{-4}	2.6×10^{-7}	2.4×10^{-6}	1.6×10^{-5}	0.10
10 %	1.60	1.5×10^{-4}	8.3×10^{-7}	3.4×10^{-6}	1.7×10^{-5}	0.09
15 %	2.19	2.0×10^{-4}	1.0×10^{-6}	4.8×10^{-6}	1.0×10^{-4}	0.07
20 %	1.99	1.4×10^{-4}	7.3×10^{-7}	3.9×10^{-6}	7.0×10^{-5}	0.07

To understand the unusual behaviour of the 15 % HA-GO membrane, the effective channel heights of the membranes are compared with their ionic mobility, molecular diffusivity, and permeability values. The data listed in Table 1 connect the superior mobility and diffusivity of 15% GO-HA membrane to the larger effective channel height of the 2D nanochannels. To understand the origin of a larger effective channel height of 15 % membrane, HA-GO dispersions were investigated under a transmission electron microscope, revealing that the

surface of GO sheets with 15 % humic acid is more rough and uneven than that of other compositions (Fig. 2.14). The exact reason for the same is not known yet. This inhomogeneous coating would create channels with non-uniform heights, having localized regions of slightly larger channels. These localized regions of larger channels would provide additional space or pathways for ion/molecular transportation and reduce the viscosity of permeates in those regimes.[47] However, it's worth mentioning that as long as the overlapping of Debye lengths occurs in the different regimes of the nanofluidic network, the selectivity of the membrane would not be compromised.

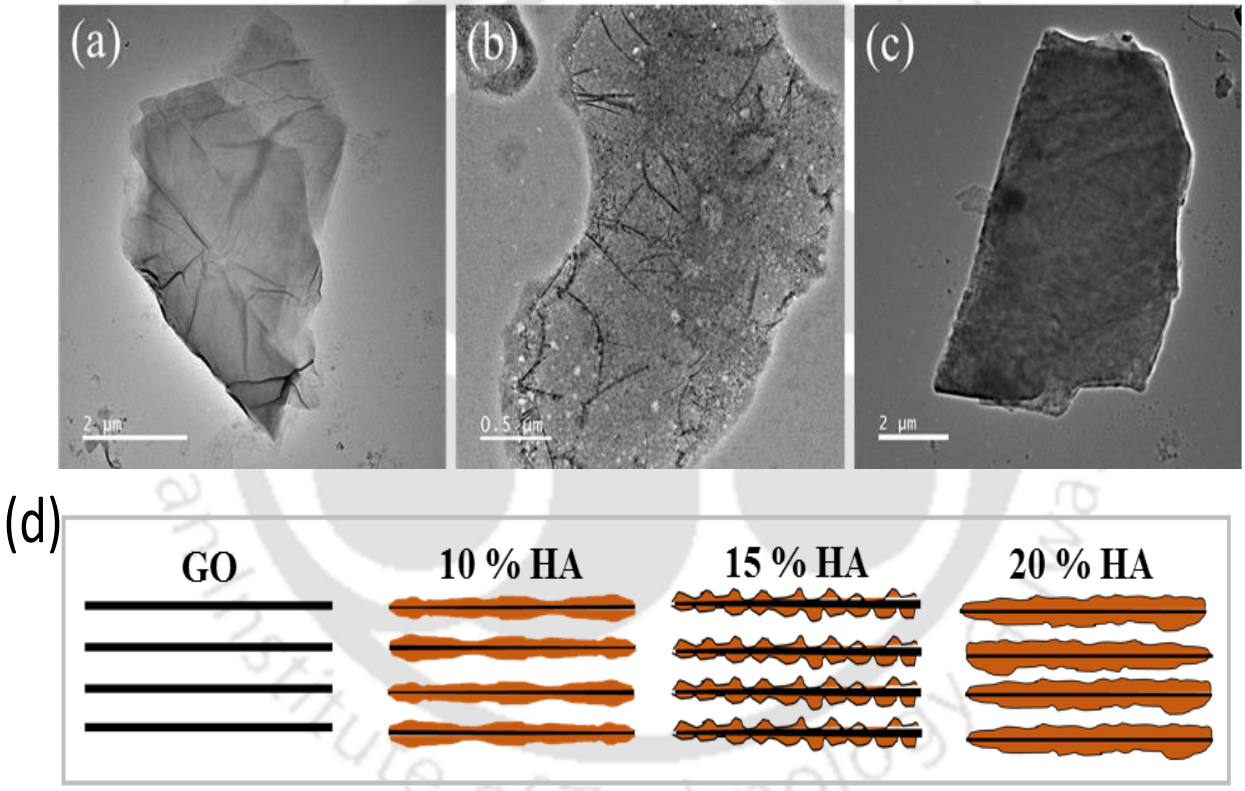

Fig. 2.14: Nanochannel morphology in GO-HA membranes: TEM examinations of the dispersions of (a) 10 %, (b) 15 % and (c) 20 % GO-HA mixtures. (d) Schematic diagrams depicting probable channel structures of lamellar membranes with varying contents of humic acids.

To get further insights into the nanofluidic transport of humic acid-modified GO nanochannels, permeation of water molecules in different compositions' HA-GO membranes was investigated by Dr Abhijit Gogoi and Prof. K. Anki Reddy through equilibrium molecular dynamics (MD) simulation. As both GO, and humic acid possess similar chemical structures, representative

structures of both these nanoflakes were constructed by locating hydroxyl and epoxy functional groups on the basal planes of aromatic carbon atoms, the carboxylic functional groups were placed at the edges of the aromatic networks by fixing the elemental compositions at $C_{10}O_1(OH)_1(COOH)_{0.5}$.[48-50] The nanoflakes of GO and humic acids are arranged in space to get the GO-Humic acid composite membrane of desired proportion (0, 10, 15 and 20 % humic acids with GO) as shown in the Fig. 2.16a, 2.16b, 2.16c, and 2.16d

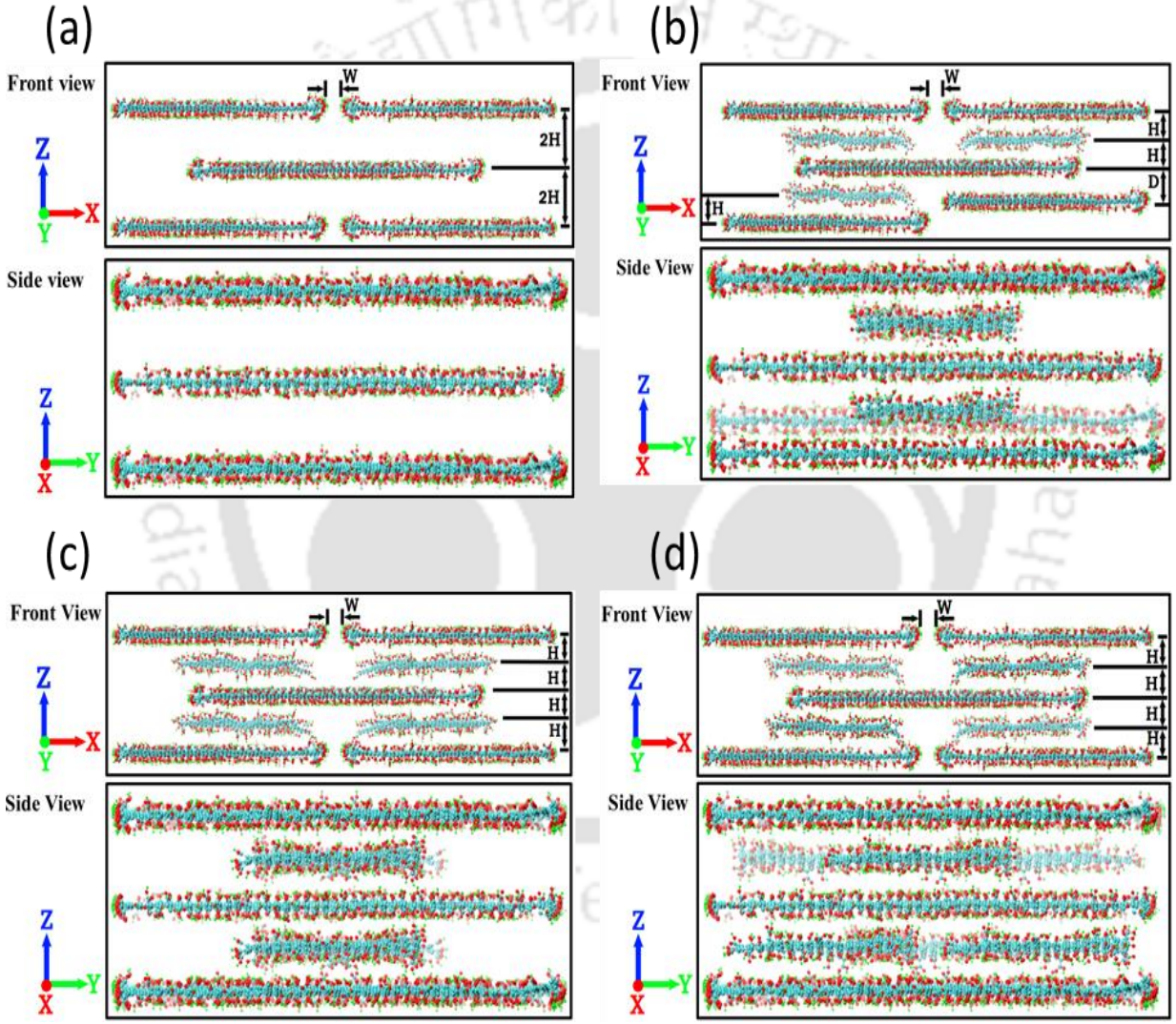

Fig. 2.16: MD simulation: MD simulated structure of (a) Pure GO membrane (b) 10 % GO-HA membrane (c) 15 % GO-HA membrane and (d) 20 % GO-HA membrane. Red color is for oxygen atoms, green color is for carbon atoms and cyan color is for hydrogen atoms.

The geometric parameters of the membrane are kept as, **H** = 8 Å, **W** = 5 Å and **D** = 10 Å. After the construction of the layered GO membrane each of the membrane is hydrated with a water

box of size 147 × 102 × 64 $Å^3$ containing 19894 number of water molecules, the water molecules within 2 Å of the GO nanosheets are removed. Methylene blue (MB) solution box (4 MB molecules and 7745 water molecules in box of size 147 × 102 × 32 $Å^3$) is placed above and below the hydrated membrane. Equilibrium molecular dynamics (MD) simulations are performed to investigate the permeation of water molecules. The simulation setup is shown in the Fig. 2.17.

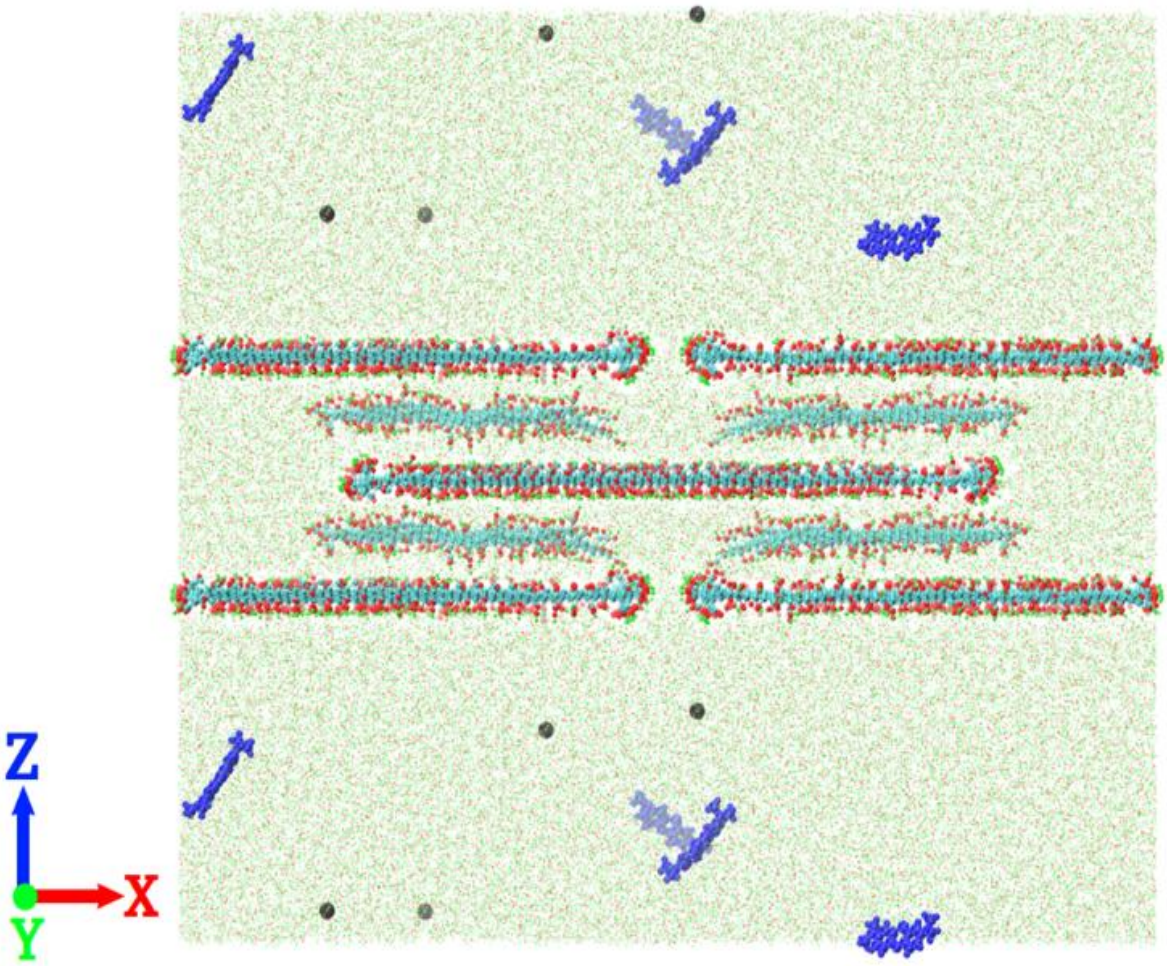

Figure 2.17: Simulation system with 15% GO-HA membrane: In the GO-HA membrane red color is for oxygen atoms, green color is for hydrogen atoms, cyan color is for carbon atoms. Water molecules are shown with red and green dots with red color for oxygen atoms and green color for hydrogen atoms. The MB^+ ions are shown with blue color and Cl^- ions are shown with black color.

During the simulation, no MB molecules were permeated through any of the membranes. Typically, when a water molecule travels from one end of the membrane to the other end, a

water permeation event is counted. During the simulation, 15 % GO-HA membrane showed better permeability with 571 water molecules permeated. For comparison, pure GO and membrane with 10 and 20 % humic acid displayed permeation of 416, 480, and 512 number water molecules, respectively. The permeability of water (*Nw*) through different HA-GO membranes obtained as such is shown in Fig. 2.18a.

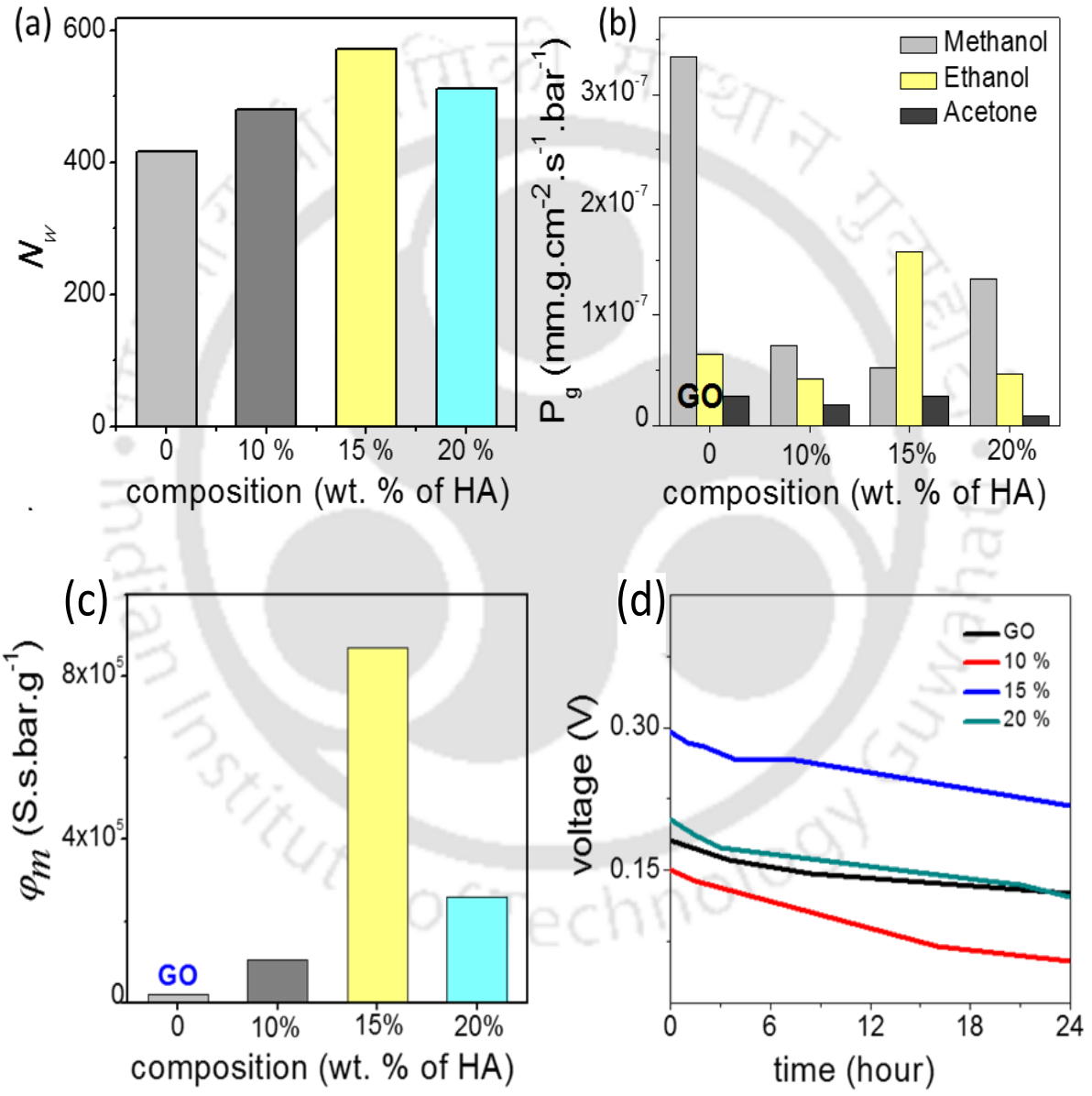

Fig. 2.18. Applications of GO-HA membrane system: (a) Water molecules permeated through different membranes under equilibrium MD simulation. (b) Experimental permeability (P_g) of solvent vapours through different membranes. (c) Membrane selectivity (φ_m) and (d) open circuit voltage harvested from concentration gradient across the different GO-HA membranes. The data shows voltages obtained on 3rd consecutive cycle, where each cycle was run for 24 hours.

The work here demonstrated that the interlayer space of GO membranes can be modified with humic acid to further improve its ionic conductivity, solution stability and mechanical robustness. Such improved membranes should be ideal for energy harvesting applications such the direct methanol fuel cell (DMFC) and reverse electrodialysis (RED). A major problem faced by the traditional proton exchanged membranes like nafion in DMFC applications, is the high methanol permeability, which leads to a crossover effect.[51,52] In order to verify the prospects GO-HA membranes in DMFC application, permeability of different solvent vapours through the membranes were studied by the gravimetric method. The rate of solvent evaporation from glass vials covered with membranes of 20 μm thick are shown in Fig. 2.18b. Interestingly, all the GO-HA membranes blocked methanol vapours much more effectively than that of pure GO membrane. Typically, the membrane performance for DMFC is evaluated by the selectivity value defined as the ratio of proton conductivity to methanol permeability.[51.52] The bar diagrams shown in Fig. 2.18c clearly show that GO-HA membranes will be more preferred over GO membranes for DMFC applications. Similarly, applicability of GO-HA membranes for RED were tested by measuring open circuit voltages obtained from concentration differences of the electrolytes across the membranes.[53] Devices comprising two compartments separated by GO-HA membrane were fabricated by using freshly prepared PDMS elastomer. Compartments were filled with KCl solutions of different concentrations, 10^{-3} M in low (C_L) and 1 M in the high (C_H) concentration chamber. The transmembrane potentials and diffusion currents were measured by inserting Ag/AgCl electrodes into the solutions. In Fig. 2.18d, transmembrane potentials recorded as a function of time are shown for different membranes, after 72 hours of experiment. Remarkably, even after 3rd consecutive cycle (each cycle 24 hours long) the open circuit potential due to concentration gradient driven transport of cations across the membranes were calculated to be 0.125 V, 0.05 V, 0.21V and 0.12 V, for GO, 10 %, 15 % and 20 % membranes respectively

2.5: CONCLUSION

In summary, we have demonstrated that the ionic and molecular transport properties of reconstructed lamellar membranes can be finely tuned by applying appropriate spacers in right composition. Application of humic acid not only improved nanofluidic transport of GO membrane but also enhanced its solution stability and mechanical robustness. Among different compositions of GO-HA, 15 % membrane shown remarkable enhancement in ionic mobility and molecular permeability and selectivity. The data presented in this manuscript indicate that slight variations in the channels dimensions within the Debye-length-overlapping-regime does not deteriorate its selectivity, but significantly enhance permeability and mobility by providing additional pathways for ion/molecular transportation and reducing viscosity of the permeates. With such improvement reconstructed lamellar membranes should be ideal for applications like water desalination and energy harvesting from the direct methanol fuel cell and reverse electrodialysis.

2.6: References:

1. H.-P. Cong, J.-F. Chen and S.-H. Yu, *Chem. Soc. Rev*., 2014, **43**, 7295.
2. F. Kim, L. J. Cote and J. X. Huang, *Adv. Mater*., 2010, **22**, 1954.
3. S. Saxena, T. A. Tyson, S. Shukla, E. Negusse, H. Chen and H. Bai, *Appl. Phys. Lett*., 2011, **99**, 013104.
4. D. Chen, H. Feng and J. Li, *Chem. Rev*., 2012, **112**, 6027.
5. J. Kim, L. J. Cote, F. Kim, W. Yuan, K. R. Shull and J. X. Huang, *J. Am. Chem. Soc*., 2010, **132**, 8180.
6. Y. Wang, S. S. Li and H. Y. Yang, *RSC Adv*., 2020, **10**, 15328.
7. D. R. Dreyer, A. D. Todd and C. W. Bielawski, *Chem. Soc. Rev*., 2014, **43**, 5288.
8. V. Georgakilas, J. N. Tiwari, K. C. Kemp, J. A. Perman, A. B. Bourlinos, K. S. Kim and R. Zboril, *Chem. Rev*., 2016, **116**, 5464.
9. C. Cheng, S. Li, A. Thomas, N. A. Kotov and R. Haag, *Chem. Rev*., 2017, **117**, 1826.
10. Evangelou, V. P. Environmental Soil and Water Chemistry: Principles and Applications; John Wiley & Sons: New York, 1998; pp 476-49
11. C. A. Coles and Yong, R. N. *Eng. Geol*. 2006, **85**, 26.
12. X. Y. Zhou, B. Wang, T. Lan, H. Q. Chen, H. L. Wang, Y. Tao, Z. H. Li, K. Ibrahim, D. Q. Wang and W. Y. Feng, *J. Phys. Chem. C*, 2016, **120**, 25789
13. E. S. M. Duraia and G. W. Beall, *Sens. Actuator B-Chem*., 2015, **220**, 22.
14. B. L. Xing, R. F. Yuan, C. X. Zhang, G. X. Huang, H. Guo, Z. F. Chen, L. J. Chen, G. Y. Yi, Y. D. Zhang and J. L. Yu, *Fuel Process. Technol*., 2017, **165**, 112.
15. P. Mao and J. Y. Han, *Lab Chip*, 2005, **5**, 837.
16. H. Cao, Z. N. Yu, J. Wang, J. O. Tegenfeldt, R. H. Austin, E. Chen, W. Wu and S. Y. Chou, *Appl. Phys. Lett*., 2002, **81**, 174.

17. H. T. Liu, J. He, J. Y. Tang, H. Liu, P. Pang, D. Cao, P. Krstic, S. Joseph, S. Lindsay and C. Nuckolls, *Science*, 2010, **327**, 64.

18. J. Z. Ji, Q. Kang, Y. Zhou, Y. P. Feng, X. Chen, J. Y. Yuan, W. Guo, Y. Wei and L. Jiang, *Adv. Funct. Mater*., 2017, **27**, 1603623.

19. L. Lin, L. Zhang, L. D. Wang and J. H. Li, *Chem. Sci*., 2016, **7**, 3645.

20. R. K. Joshi, P. Carbone, F. C. Wang, V. G. Kravets, Y. Su, I. V. Grigorieva, H. A. Wu, A. K. Geim and R. R. Nair, *Science*, 2014, **343**, 752.

21. R. R. Nair, H. A. Wu, P. N. Jayaram, I. V. Grigorieva and A. K. Geim, *Science*, 2012, **335**, 442.

22. K. Raidongia and J. Huang, *J. Am. Chem. Soc*., 2012, **134**, 16528.

23. J. J. Shao, K. Raidongia, A. R. Koltonow and J. Huang, *Nat. Commun*., 2015, **6**, 7602.

24. J. Gao, Y. P. Feng, W. Guo and L. Jiang, *Chem. Soc. Rev*., 2017, **46**, 5400.

25. J. Gao, Y. P. Feng, W. Guo and L. Jiang, *Chem. Soc. Rev*., 2017, **46**, 5400.

26. H. Li, Z. N. Song, X. J. Zhang, Y. Huang, S. G. Li, Y. T. Mao, H. J. Ploehn, Y. Bao and M. Yu, *Science*, 2013, **342**, 95.

27. M. Hu and B. X. Mi, Environ. *Sci. Technol*., 2013, **47**, 3715.

28. Y. Han, Y. Q. Jiang and C. Gao, *ACS Appl. Mater. Interfaces*, 2015, **7**, 8147.

29. J. W. Burress, S. Gadipelli, J. Ford, J. M. Simmons, W. Zhou and T. Yildirim, *Angew. Chem. Int. Edit*., 2010, **49**, 8902.

30. S. S. Shenvi, A. M. Isloor, A. F. Ismail, S. J. Shilton and A. Al Ahmed, *Ind. Eng. Chem. Res.* 2015, **54**, 4965.

31. M. O. Deserra and Schnitze, M. *Can. J. Soil Sci.* 1972, **52**, 365.

32. I. A. Schepetkin, A. I. Khlebnikov, S. Y. Ah, S. B. Woo, C. S. Jeong, O. N. Klubachuk and B. S. Kwon, *J. Agric. Food Chem.* 2003, **51**, 5245.

33. A. Rodrigues, A. Brito, P. Janknecht, M. F. Proenca and R. Nogueira, *J. Environ. Monitor*., 2009, **11**, 377.

34. C. Bayer, L. Martin-Neto, J. Mielniczuk, S. D. Saab, D. M. P. Milori and V.S. Bagnato, *Geoderma*, 2002, **105**, 81.

35. D. W. Lee, T. Kim and M.Lee, *Chem. Commun*., 2011, **47**, 8259.

36. Q. Yang, X. Pan, F. Huang and K. Li, *J. Phys. Chem. C*, 2010, **114**, 3811.

37. I. A. Schepetkin, A. I. Khlebnikov, S. Y. Ah, S. B. Woo, C. S. Jeong, O. N. Klubachuk and B. S. Kwon, *J. Agric. Food Chem*., 2003, **51**, 5245.

38. K. Ghosh and M. Schnitzer, *Can. J. Soil Sci.*, 1980, **60**, 373.

39. V. Georgakilas, J. N. Tiwari, K. C. Kemp, J. A. Perman, A. B. Bourlinos, K. S. Kim and Radek Zboril, *Chem. Rev*., 2016, **116**, 5464.

40. S. Li, A. N. Aphale, I. G. Macwan, P. K. Patra, W. G. Gonzalez, J. Miksovska and R. M. Leblanc, *ACS Appl. Mater. Interfaces*, 2012, **4**, 7069.

41. B. Wang, X. Zhou, D. Wang, J. J. Yin, H. Chen, X. Gao, J. Zhang, K. Ibrahim, Z. Chai, W. Feng and Y. Zhao, *Nanoscale*, 2015, **7**, 2651.

42. K. L. Vincent Joseph, J. Lim, A. Anthonysamy, H. Kim, W. Choib and J. K. Kim, *J. Mater. Chem. A*, 2015, **3**, 232.

43. M. Gorman, *J. Chem. Educ*., 1957, **34**, 304.

44. R. B. Schoch and P. Renaud, *Appl. Phys. Lett*., 2005, **86**, 253111.

45. R. Fan, S. Huh, R. Yan, J. Arnold and P. D. Yang, *Nat. Mater*., 2008, **7**, 303.

46. D. D. Ordinario, L. Phan, W. G. Walkup, J. M. Jocson, E. Karshalev, N. Husken and A. A. Gorodetsky, *Nat. Chem*., 2014, **6**, 597.

47. H. Huang, Z. Song, N. Wei, L. Shi, Y. Mao, Y. Ying, L. Sun. Xu and X. Peng, *Nat. Commun*., 2013, **4**, 2979.

48. A. Lerf, H. He, M. Forster and J. Klinowski, *J. Phys. Chem. B*, 1998, **102**, 4477.

49. H. Tang, D. Liu, Y. Zhao, X. Yang, J. Lu and F. Cui, *J. Phys. Chem. C*, 2015, **119**, 26712.

50. C. J. Shih, S. Lin, R. Sharma, M. S. Strano and D. Blankschtein, *Langmuir*, 2012, **28**, 235.

51. I. Nicotera, C. Simari, L. Coppola, P. Zygouri, D. Gournis, S. Brutti, F. D. Minuto, A. S. Arico, D. Sebastian and V. Baglio, *J. Phys. Chem. C*, 2014, **118**, 24357.

52. P. Bunlengsuwan, N. Paradee and A. Sirivat, *Polym. Plast. Technol. Eng*., 2017, **56**, 1695.

53. S. W. Lee, H. J. Kim and D. K. Kim, *Energies*, 2016, **9**, 49.

Chapter 3

Uphill Anion-Pumping through Triangular Nanofluidic Device of Reconstructed Layered Double Hydroxide

Summary*

In this Chapter, we have exploited the inherent anion selectivity of layered double hydroxide (LDH) materials for achieving uphill pumping of anionic species. Unlike the conventional 2D materials, LDH possesses positive surface charges, and the percolated nanochannels fabricating via self-assembling the exfoliated dispersion of CoAl layered double hydroxide (CoAl LDH) exhibit excellent anionic transport characteristics. The excellent anion selectivity of CoAl LDH can also be utilized for converting salinity gradient into electrical energy, where selective diffusion of anionic species under a 1000-fold salt concentration gradient can produce power density up to 0.70 Wm^{-2}. The positively charged CoAl LDH membrane (p-LDHM) also displayed a shape-dependent ionic transport characteristic. While the rectangular pieces of membranes exhibit linear *I-V* curves, the triangularly cut p-LDHM displays a diode-like ionic current rectification behaviour in the surface-charged-governed regime. The ICR behaviour of triangular p-LDHM can also be exploited to pump anions against the concentration gradient under a fluctuating external potential with a mean value of zero.

---

* An article based on these studies has been just accepted for publication in *J. Phys. Chem. C.*

3.1: Introduction

Ion pumps with intricate transport properties play critically essential roles in various physiological functions of living organisms. For example, the specific internal composition of the biological ion channels is regulated by the Na^+/K^+ ion pump, which is essential for maintaining the cells' osmotic equilibrium and membrane potential.[1,2] Similarly, PMCA (plasma membrane Ca^{2+} ATPase) is vital for regulating Ca^{2+} ion concentration within eukaryotic cells.[3,4] The energy needed to control different ion pumps is supplied through sources like light, redox chemicals, and ATP.[5,6] Inspired by the exceptional properties of the biological ion pumps, several efforts have been devoted to fabricating their artificial counterparts.[7-10] Bio-inspired synthetic pumps capable of transporting ions/molecules in the uphill direction in a highly selective manner have great relevance to futuristic applications in areas like bio-sensing, environmental studies, and energy harvesting.[11-13] Most of the 2D materials possess negative surface charges that imbue them with cation selectivity. Hence, most nanofluidic studies related to biomimetic ion pumps are limited to only cation-pumping phenomena.

Here, we report the fabrication of an ion pump based on anion-selective p-LDHM that can push anions from a region of low concentration to a region of high concentration with the help of a fluctuating electric field with a mean value of zero. Moreover, the excellent anion selectivity of p-LDHM also paved the way for harvesting electricity from concentration gradient with the help of a reverse electrodialysis (RED) like process. Layered double hydroxides (LDHs) represent a class of lamellar compounds with a general formula of $[M^{2+}_{1-x}M^{3+}_{x}(OH)_2]^{x+}\cdot[A_{n-x/n}].mH_2O$, where M represents metal cations, and A represents anions.[14] Typically, LDHs are consist of alternatively staked positively charged brucite-like host layers and charge balancing hydrated exchangeable anions located in the interlayer gallery. In the brucite host layers, the

hydroxide ions that connect to form infinite 2D sheets. The charges of the brucite-like layers arise from the isomorphous substitution of divalent metal ions with trivalent ones.[15] The positive charges on the host layers attract the water molecules and provide an extensive hydrogen-bonding network along the 2D surface. The hydrogen-bonding network facilitates swift conduction of OH^- ions through the rapid cleavage-reconstruction process of hydrogen bonds.[16,17] In clear contrast to typical layered materials, LDHs like CoAl LDH are comprised of positively charged host layers with interlayer spaces occupied by charge balancing anions. The lamellar crystallites of LDH can be exfoliated into atomically thin 2D sheets with a high density of positive charges.

3.2: Scope of the present investigation

The demonstration of the feasibility of creating an unprecedentedly massive array of nanofluidic channels by restacking exfoliated sheets of layered material provided a macroscopic platform to study nano-scales phenomena occurring at the liquid state.[18] By its unique advantages such as cost-effectiveness and scalability, ease of modifications, and high-flux, reconstructed layered materials initiated a new era of nanofluidic studies. It also creates novel avenues to exploit nanofluidic phenomena for various practical applications like harvesting electrokinetic energy, ultrafiltration, biomedical analysis, seawater desalination, and DNA sequencing.[19-24] The synchronous growth in the research related to the novel 2D nanomaterials further boosted the research in two-dimensional nanofluidics. After the initial demonstration with graphene oxide, numerous other layered materials such as h-BN, clay minerals, transition metal dichalcogenide, Mxenes, carbon nitride were utilized to create nanofluidic devices with unique characteristics, primarily via reconstruction of their respective exfoliated layers.[25-29] Remarkably, to date, most of these nanofluidic studies are limited to only cation-selective nanochannels. However, utilization of both the cation and anion-selective membrane is desired to enhance the operational performance of several futuristic applications

such as osmotic power generation, seawater desalination, and regulated ionic/molecular transportations. Several indirect approaches, like reactive surface groups (COOH or OH) modification of the parent cation-selective 2D sheets and intercalation of cationic polymers, were adopted to imbue anion selectivity to the nanofluidic channels. Subsequently, both the parent and modified nanofluidic channels were utilized with synchronization to achieve better performance in osmotic energy harvesting and seawater desalination. [30-32] The application of foreign materials/molecules involves additional chemical processes and disturbs the well-defined 2D structure of the nanochannels. Along with decreasing nanofluidic confinements, it also exerts adverse effects on the nanofluidic membranes' mechanical, chemical, and thermal stability. Therefore, efforts have been devoted to prepare anion-conductive materials by using layered double hydroxide based materials.[16,17]

In the present work, we have utilized the inherent positive charges of the cationic Co-Al layered double hydroxide (CoAl LDH) to fabricate anion-selective nanofluidic devices. The lamellar membrane of CoAl LDH was exploited for preparing a triangular ion pump capable of transporting anions against the concentration gradient and as well as for fabricating salinity gradient-driven energy harvesting devices. The ease of fabricating the bio-inspired 2D anion pump compared to its 1D conical analog would help researchers fabricate devices for futuristic applications in areas like bio-sensing, environmental studies, and energy harvesting. Moreover, systematic investigation of the ion transport characteristic through the interlayer spacing of LDH could help in understanding the functioning of the biological systems and improve the performance of devices in diverse areas like water purification and anion sensing, osmotic energy harvesting, and catalysis.

3.3: Experimental section

Synthesis of CoAl LDH:

The hexagonal CoAl LDH-Co_3^{2-} platelets were synthesized following a previously developed soft chemical procedure from a mixed solution of $CoCl_2 \cdot 6H_2O$ and $AlCl_3 \cdot 6H_2O$, using urea [$CO(NH_2)_2$] as a hydrolysis agent. Typically, $CoCl_2 \cdot 6H_2O$, $AlCl_3 \cdot 6H_2O$, and urea were dissolved in a 1L round bottom flask where the final concentration of the reactants is maintained as 10, 5, and 35 mM, respectively. Then, the final mixture was refluxed for 48 hours in the presence of a nitrogen atmosphere under constant stirring. The resulting pink solid mass was filtered, washed with deionized water and ethanol, and air-dried at room temperature. Decarbonization and anion exchange into Cl^- forms (CoAl LDH-Cl^-) was mediated by a salt-acid treatment of 1g of LDH with a 1L mixed solution of 1M NaCl and 3.3 mM HCl under mechanical stirring for 12 hours.

Exfoliation of CoAl LDH:

Delamination/exfoliation of CoAl LDH-Cl^- platelets into 2D sheets are done in a 1:1 mixture of formamide and N, N-dimethyl formamide (DMF) under mechanical shaking for a duration of 48 hours. Exfoliation of LDH into few layers of 2D Sheets is unlikely to achieve in aqueous environment as the interlayer water molecules forms dense hydrogen bonding network to the hydroxyl groups of the LDH host and as well as with the coordinated interlayer anionic guests. So an equimolar mixture of formamide and DMF is used as the dispersing medium and as well as the exfoliating agent. Owing to its highly polar nature, formamide molecules enters into the interlayer galleries of LDH lamellae replacing the interlayer water molecules, where its carbonyl group would have strong interaction to the LDH host. Simultaneously the NH_2 moieties of the formamide molecules having lesser extent of hydrogen bonding as compared

to that of hydroxide group, may not be able to build a strong interaction with the interlayer guest anions. Accordingly, once the replacement of water molecules for formamide takes place, it weakens the interlayer force of attraction disrupting the strong hydrogen-bonding network, thereby inducing delamination. The role of using DMF as an additional exfoliating agent is to impede the strong hydrogen bonding network in between the interlayers of the LDH framework, thereupon inducing better delamination.

Surface Charge Governed Ionic Transport:

Nanofluidics devices of positively charged CoAl LDH membrane (p-LDHM) were fabricated by encapsulating rectangular strips of known dimensions into the freshly prepared PDMS elastomer. To expose the nanochannel networks to different electrolyte solutions, two holes (~0.4 mL) were cut open through the fully cured PDMS stub at either end of rectangular strips. Ag/AgCl electrodes connected to the terminals of a Keithley source meter (model 2450) were immersed in the reservoirs filled with electrolytes at both ends of the strip to measure the ionic current. Representative *I-V* curves for the LDH strips were recorded at different electrolyte concentrations ranging from 10^{-6} M to 1 M by sweeping voltage from -1 V to +1 across each strip. Conductivity calculations were done using the following equation: C= G × cell constant, where C is the conductivity, and G is the conductance.

Characterization:

CoAl LDH Nanosheets were characterized by Field Emission Transmission Electron Microscope (FETEM) (JEOL, Model: 2100F), Field Emission Scanning Electron Microscope (Make: Zeiss, Model: Sigma) and Atomic Force Microscope (AFM) (Make: Oxford; Model: Cypher). The membranes cross-sections were examined by the Field Emission Scanning Electron Microscope (Make: Zeiss, Model: Sigma). Ion intercalation and exfoliation of LDH platelets were investigated with the help of Fourier transform infrared (FTIR) spectrometer

(maker: Perkin Elmer; model: Spectrum two) and X-ray diffraction studies (Rigaku, Model: Micromax-007HF instrument). Zeta potential were measured with zeta potential analyser (Malvern Zetasizer Nano ZS90). Energy dispersive X-ray analysis were performed with Field Emission Scanning Electron Microscope (FESEM) (Zeiss, Model: - Sigma).

3.4: Results and discussion

The hexagonal CoAl LDH-CO_3^{2-} platelets were synthesized from a mixed solution of $CoCl_2 \cdot 6H_2O$ and $AlCl_3 \cdot 6H_2O$ by using urea [$CO(NH_2)_2$] as a hydrolysis agent, adopting a method reported earlier.[33] Formation of LDH material in CO_3^{2-} form was confirmed by recording powder XRD pattern (Fig. 3.1c) of the material. The XRD reflections were matched with rhombohedral structure of LDH, and the interlayer spacing was calculated as 0.72 nm (003).[34,35] The as synthetized CoAl LDH-CO_3^{2-} platelets were transformed into CoAl LDH- Cl^- through an anion exchange process performed with an aqueous solution of HCl and NaCl under vigorous mechanical stirring.[17] Successful decarbonation process was confirmed by the absence of strong bands at 1360 cm^{-1} and 795 cm^{-1} corresponding to the ν_3 vibration and bending modes of CO_3^{2-} in FT-IR spectra (Fig. 3.1b).[33] Moreover, in the chloride exchanged form, the interlayer spacing of LDH was found to be 0.74 nm, slightly higher than that of carbonate form. The decarbonated CoAl LDH-Cl^- platelets was further exfoliated into 2D sheets by stirring the sample in a 1:1 mixture of formamide and N, N-dimethyl formamide (DMF) for 48 hours. The formamide treatment transformed the colour of as-prepared CoAl LDH-Cl^- platelets into a pink dispersion (1mg/ml) (Fig. 3.1d), indicating occurrence of the delamination process. The successful delamination process of the platelets was confirmed by the absence of the sharp basal reflections of the parent CoAl LDH-Cl^- in the powder XRD pattern.[35] Transmission electron microscopic (TEM) and field emission scanning electron microscopy (FESEM) investigation on the drop casted aqueous dispersion of exfoliated LDH sample displayed presence of hexagonal 2D sheets with lateral dimensions in the range of 1 to

1.5 µm. Representative images are shown in Fig. 3.1e and Fig. 3.1f, respectively. In the Atomic Force Microscopic (AFM) examination, the thicknesses of the exfoliated sheets were found to be in the range of 2 to 4 nm. A typical AFM image along with the corresponding height profile of an exfoliated CoAl LDH-Cl^- sheet is shown in Fig. 3.1g. The lamellar restacking of the exfoliated 2D sheets in the p-LDHM is also revealed by the cross-sectional FESEM image shown in Fig.3.1h.

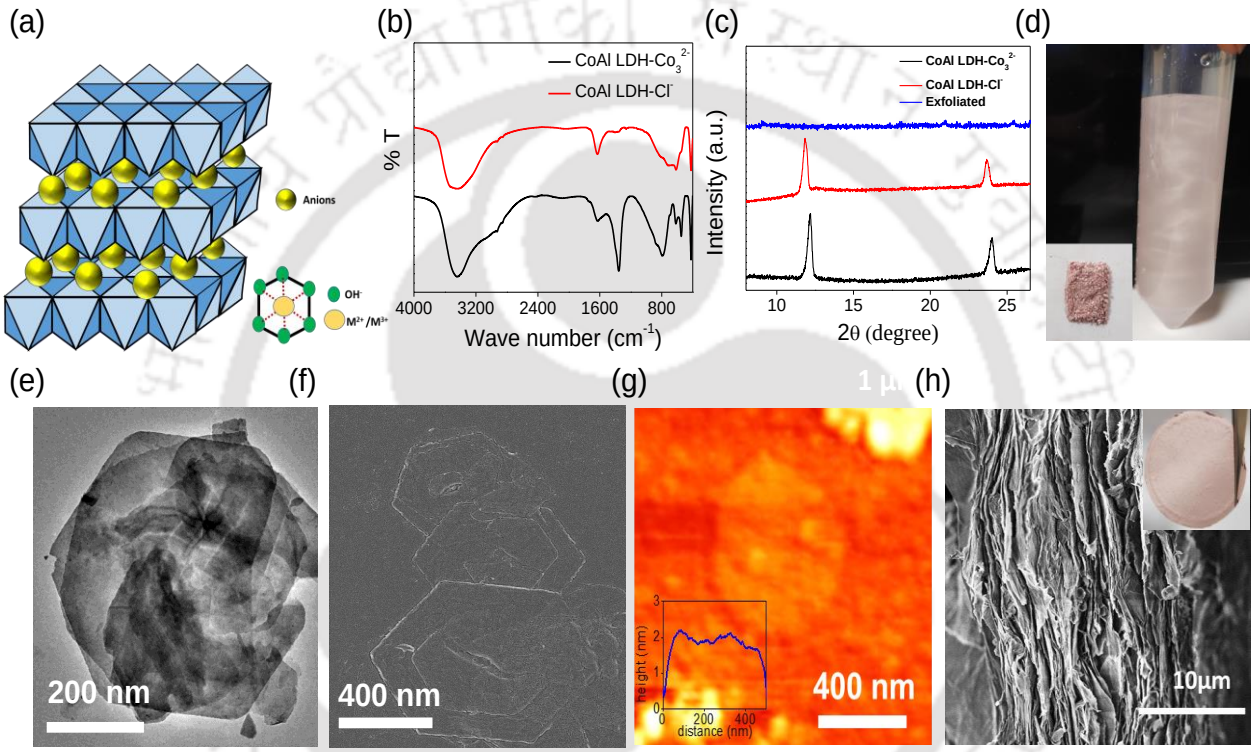

Fig. 3.1: Characterization of CoAl LDH: (a) Schematic representation of the lamellar structure of layered double hydroxide (LDH) (b) Comparison of FT-IR spectra of CoAl LDH-Co_3^{2-} and CoAl LDH-Cl^-, disappearance of the peaks at 1360 cm^{-1} and 795 cm^{-1} signifies the removal of intercalated carbonate ions in the chloride exchanged product. (c) PXRD pattern of powdered CoAl LDH-CO_3^{2-}, CoAl LDH-Cl^- and exfoliated flakes of CoAl LDH-Cl^- in formamide. (d) Digital photo of the colloidal dispersion of CoAl LDH-Cl^- in formamide (inset shows a photo of CoAl LDH-Cl^- powder). (e) FETEM (f) FESEM and (g) AFM images of exfoliated CoAl-LDH flake. (h) Cross-sectional FESEM images of the reconstructed LDH membrane. Inset shows the digital image of a freestanding LDH membrane.

The zeta potential measurements of the aqueous dispersion revealed the surface of the nanosheets is composed of +29 mV charges. The positive charges in CoAl LDH-Cl^- sheets are attributed to the isomorphous substitution of a part of the divalent metal-ions with trivalent ones, details are discussed in Fig. 3.2.

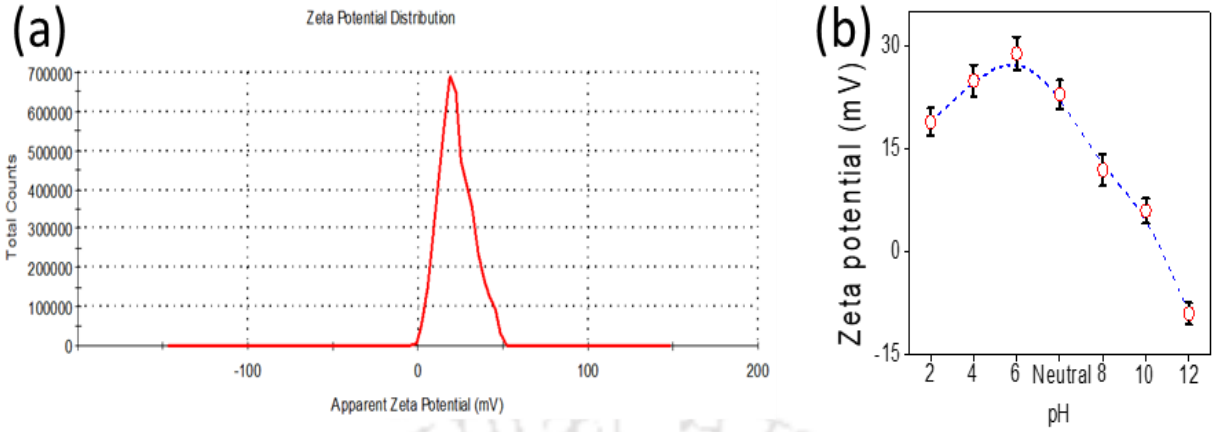

Fig. 3.2: zeta potential of LDH: (a) Zeta potential distribution of LDH dispersion. (b) Zeta potential of LDH dispersion as a function of p^H of the dispersion medium.

In order to create ultra-confined spaces for nanofluidic transportation of anions, a dispersion (1mg/ml) of exfoliated CoAl LDH-Cl^- in formamide was vacuum filtered through a PTFE filtration membrane. Due to its large aspect-ratio, during the vacuum assisted filtration process, nanosheets of CoAl LDH-Cl^- were self-assembled in a lamellar fashion creating a positively charged LDH membrane (p-LDHM). Upon air-drying for 24 hours, under ambient conditions, the p-LDHM got detached by itself from the PTFE membrane. The pXRD pattern in Fig. 3.3, suggest that periodic stacking of CoAl LDH-Cl^- platelets were regained in their reconstructed membrane. Upon soaking in water for 2 hours, the interlayer spacing of LDH membrane was

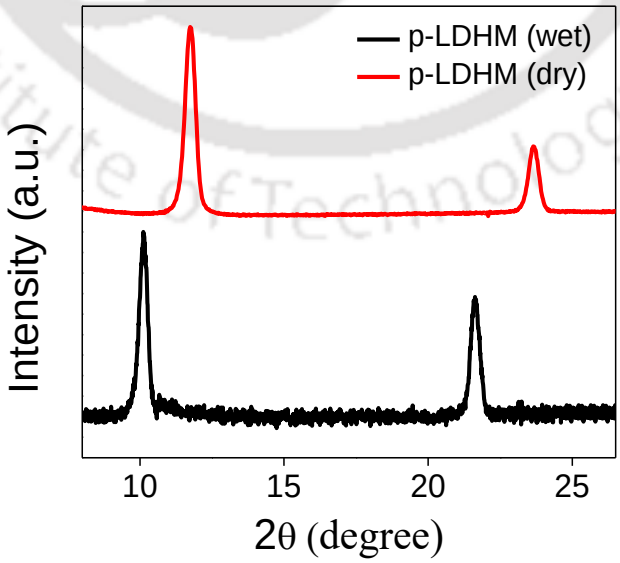

Fig. 3.3: PXRD of LDH: PXRD pattern comparison of the reconstructed LDH membrane in dry state and wet state.

found to be increased from 0.74 to 0.86 nm, confirmed by the in-situ XRD experiment, (Fig. 3.3). As the thickness of an individual CoAl LDH-Cl^- layer is reported to be 0.46 nm, the space available for the nanofluidic transport can be estimated to be around 0.40 nm.

The ionic transportation characteristics of p-LDHM nanochannels were investigated by fabricating nano-fluidic devices out of reconstructed LDH membrane. In brief, freestanding p-LDHM (thickness 40 μm) was cut into rectangular strips of dimensions of 20 mm × 5 mm and immersed into freshly prepared polydimethylsiloxane (PDMS) elastomer solution before curing the same at 60 °C. In order to expose the p-LDHM strip to desired electrolyte solutions, two reservoirs of about 0.4 ml in volume were carved out at both ends of the PDMS stub (Fig. 3.4a). After hydrating nanofluidic channels with DI water for 24 hours both the reservoirs were filled with electrolyte solutions of known concentration. The ionic current through the p-LDHM nanofluidic device was measured via Ag/AgCl electrodes inserted into the electrolyte solutions placed in the reservoirs. The linearity of the *I-V* curve measured with aqueous KCl solutions of different concentrations (Fig. 3.4b) confirmed the formation of an interconnected network of the nanochannels. The ionic conductivity values at different electrolyte concentrations were calculated by normalizing the slope of the *I-V* curves with the overall dimensions (length (l), width (w), and thickness (t) of the rectangular pieces used for the device fabrication). In Fig. 3.4c, Fig. 3.4d, and Fig. 3.4e, conductivity values calculated through p-LDHM with aqueous solutions of KCl, KOH and NaOH are plotted as a function of salt concentration. The freestanding p-LDHM shown the characteristics of surface-charge governed ionic conductivity, wherein the high concentration regime (0.1 to 1 M), similar to that of the bulk solution, the conductivity of the LDH nanochannels varied linearly with salt concentration. But in the low concentration regime (10^{-2} to 10^{-6} M), conductivity values did not change for four orders of magnitude change in the electrolyte concentrations, which is in clear contrast to the bulk solution. This peculiar conductivity pattern in the low concentration

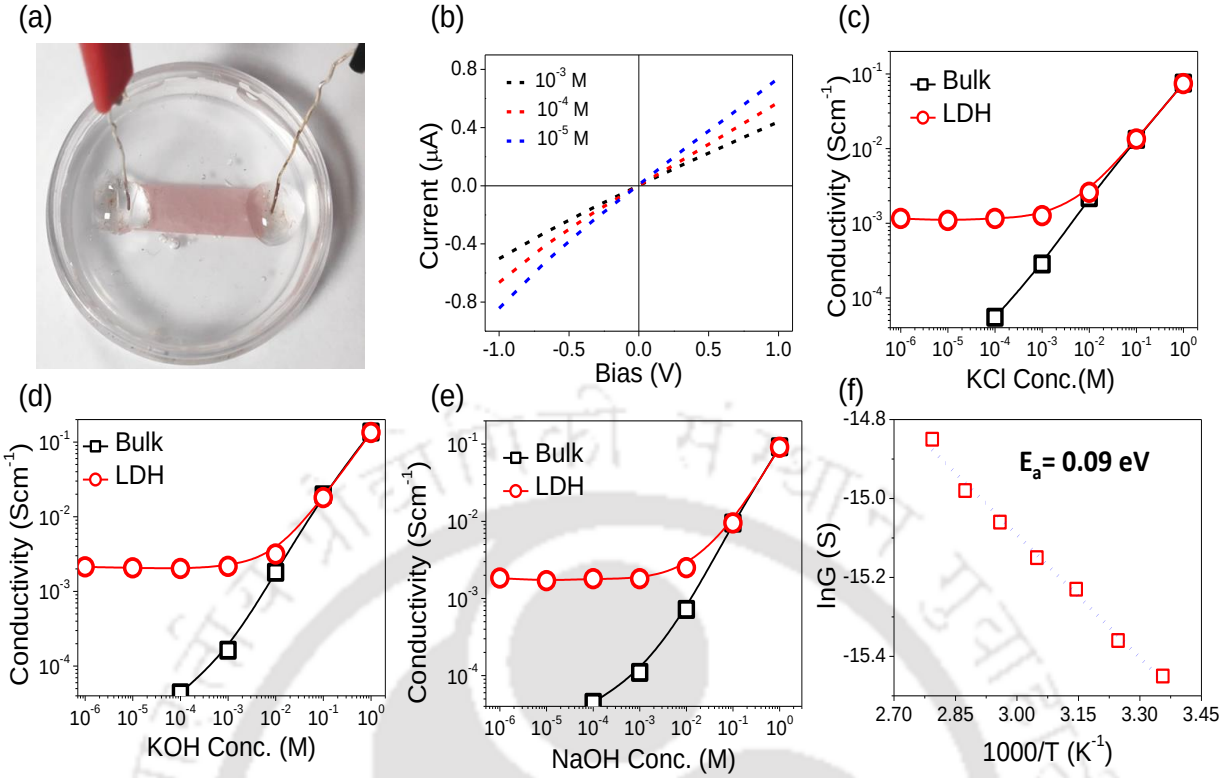

Fig. 3.4: Nanofluidic study through p-LDHM: (a) Digital image of a p-LDHM based nanofluidic device. (b) *I-V* curves recorded with a nanofluidic device made from rectangular strip of p-LDHM after soaking the same in aqueous KCl solutions of different concentrations. Ionic conductivities as a function of concentration for aqueous solutions of (c) KCl (d) KOH and (e) NaOH. (f) Arrhenius plot of hydroxyl ion conductivity.

regime is attributed to the overlapping of Debye lengths of the channel surfaces. Under such circumstances, the intrinsic surface charge density of the walls of the channels preferentially draw the counter ions, and the concentration of the counter ions inside the nanochannels is governed by the density of the surface charge, not by the concentration of the electrolytes present in the reservoirs.[18,26] The occurrence of surface-charge-governed ionic conductivity also indicates the absence of large macroscopic voids in the lamellar membrane.

The dominance of the anions in the nanofluidic conductivity of the p-LDHM-based devices was verified by replacing the electrolyte KCl with KOH. Substitution of Cl^- with OH^-, keeping cationic counterpart (K^+) unaltered, enhanced conductivity values in the surface-charge-governed regime by a factor of 8 (Fig. 3.4c and Fig. 3.4d). A similar replacement of cations from K^+ to Na^+ by keeping the anionic part constant (OH^-) did not alter the conductivity values

(Fig. 3.4d and Fig. 3.4e). As can be seen from Fig. 3.4, conductivity values at the surface-charge-governed regime was found to be proportional to hydration radius/bulk mobility of the anions. Nanofluidic membrane with remarkable OH^- ion conductivity could find large number of applications in areas like energy harvesting, charge transportation, and molecular sensing. In order to gain further insights into the mechanism of rapid OH^- transportation though the nanochannels of p-LDHM, hydroxide conductivity was measured as a function of temperature. The conductivity value (G) obtained by using aqueous NaOH (10^{-4} M) solution as the electrolyte is plotted in the Arrhenius-form (lnG vs. 1/T). From the Arrhenius-plot, the activation energy for the OH^- conduction was calculated to be of 0.09 eV (Fig. 3.4f). The tiny value of activation energy indicates a Grotthuss-like hopping of OH^- ions inside the LDH nanochannels.[36] In Grotthuss-like hopping process charge is transported through synchronised hopping of ions (OH^-) between the well-organized chains of water molecules in strict two-dimension. The counter ion selectivity of p-LDHM was also verified by analysing the samples under Energy dispersive x-ray spectroscopy (EDX). In brief, a strip of p-LDHM was soaked in1 mM NaCl solution for 30 minutes, which was followed by drying in air for 6 hours. The salt soaked p-LDHM strip was mapped for different elements with EDX and shown in Fig. 3.5. The EDX map revealed the overwhelming presence of Cl^- as compared to that of the Na^+.

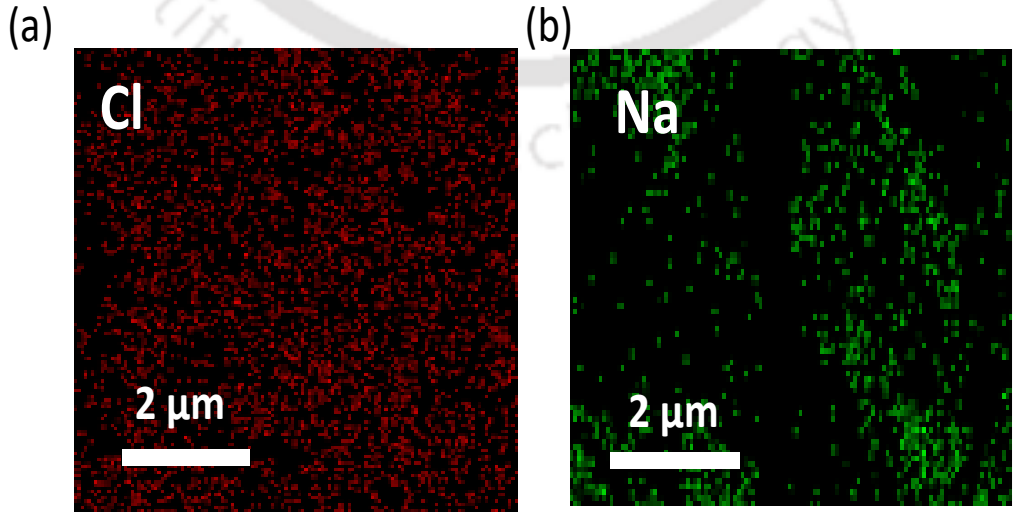

Fig. 3.5: Ion Selectivity of LDH: EDX elemental mapping of the (a) chlorine and (b) sodium atoms in the cross-section of p-LDHM after soaking in 1mM NaCl solution.

In nanofluidic systems, the nature and concentration of ions present inside the channels is dictated by the polarity and density of charges on the channel walls. Therefore, it is important to determine the surface charge density (σ_s) of the p-LDHM channels. The σ_s value calculated by using Grahame equation [37] (Eqn 1) was found to be ~ 2 mCm^{-2}.

$$\sigma_s = \frac{\varepsilon\varepsilon_o\zeta}{\lambda_d} - - - -(1)$$

In Grahame equation, ε is the dielectric constant, ε_o is the permittivity of vaccum and λ_d is the Debye length calculated as $\frac{0.304}{\sqrt{I\,(M)}}\,nm$, where I (M) is the ionic strength in molarity and **ζ** is the zeta potential. The σ_s value obtained as such were used to determine mobility (μ) of different anionic species in the p-LDHM channels using Eqn 2, which correlates ionic mobility and surface charge densities to surface charged governed conductivity (G_s).[38]

$$G_s = 2\mu_{-}\sigma_s\frac{w}{l} - - - - - (2)$$

Where, w (.040mm) and l (20 mm) corresponds to the width and length of the membrane respectively. Remarkably, in the surface charge governed region, mobility values of all the anionic species μ were calculated to be close to that of the bulk water, shown in the Fig. 3.6.

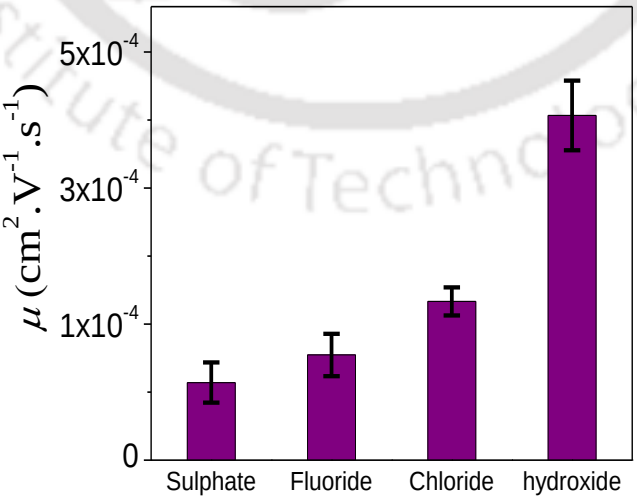

Fig. 3.6 Ionic mobility: Mobility of different anions through the interlayer galleries of p-LDHM.

In order to verify these experimental findings, the calculated σ_s value was used to determine the effective height (h_{eff}) of the p-LDHM nanochannels in aqueous environment. The h_{eff} of the LDH nanochannels determined from the transition point concentration (C_t) of conductivity vs concentration plot was found to be 0.38 nm, which is very close to the one calculated from the powder XRD pattern (002 plan) of the hydrated p-LDHM. For this calculation, C_t was obtained from the regime where the transport characteristics varied from surface charge-governed regime to bulk-like behaviour, details are shown in Fig. 3.7. σ_s is connected to C_t by Eqn 3.[39]

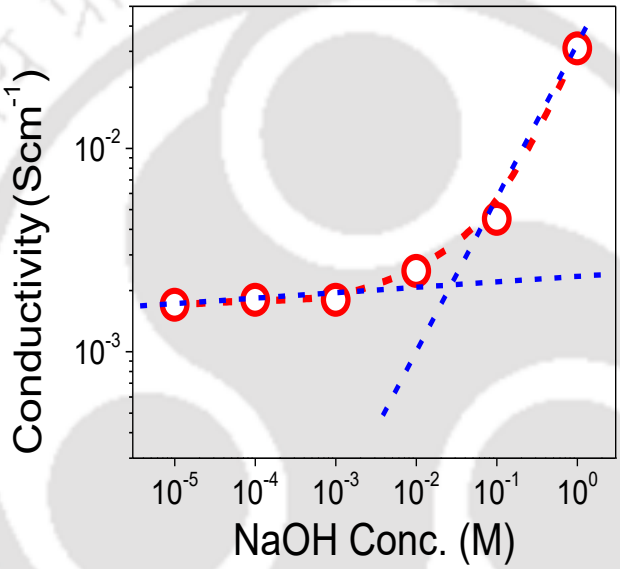

Fig. 3.7: Transition concentration point determination: Plot of ionic conductivity *vs* NaOH concentration used for the determination of transition point concentration (C_t).

$$h_{eff} = 10^{-3}\frac{\sigma_s}{eN_A C_t} - - - -(3)$$

Where N_A corresponds to Avogadro number and e for elementary charge

Further insights on the ion selectivity behaviour of the p-LDHM was obtained by measuring trans-membrane-potential and trans-membrane-current under pre-defined concentration gradient. As shown in Fig 3.8a, the experimental set-up employed for this measurement is comprised of two compartments separated by a p-LDHM. The electrolyte concentration at one side of the membrane was fixed at 10 µM, while the concentration at the other side was

increased from 100 µM to 10 mM. Two Ag/AgCl electrodes were inserted into the electrolyte solutions to measure the open-circuit voltage (V_{OC}) and short-circuit current (I_{SC}) across the p-LDHM. The V_{OC} measured as such consists of two parts, trans-membrane or simply membrane potential (V_m) and redox potential (V_{redox}). The membrane potential (V_m) has three contributions: The Donnan potentials at each edge of the nanopore and the diffusion potential attributes to the trans-membrane salinity gradient and greater mobility of cations over anions, while the redox potential (V_{redox}) is originated from the unequal potential drop at the electrode-solution interface.[40-43] The employment of Ag/AgCl electrodes with saturated KCl bridges offset the electrode potential, so V_{redox} can be ignored and hence the measured V_{OC} is attributed to the membrane potential (V_m) originating from the migration of counter-ions through the p-LDHM nanochannels along with the contribution of Donnan potentials at each edges of electrolyte/nanpore interface.[30] Fig. 3.8b and Fig. 3.8c compare the V_m and osmotic current (I_{OS}) of p-LDHM with that of negatively charged graphene oxide membrane (GO) under a1000-fold concentration gradient. Under the identical experimental condition, the V_m and I_{OS} of the p-LDHM (-144mV) was measured to be of opposite to that of the anionic GO membrane (+155 mV). The observed values of V_m is higher than its theoretically predicated limit of 120 mv in1000-fold concentration gradient, which is attributed to the combined effect of Donnan and diffusion potential. The V_m of the LDH membrane was also measured with different electrolyte solutions (NaCl, NaF, Na_2SO_4 same cation but different anions) under 1000-fold transmembrane concentration gradient. As can be seen from Fig. 3.8d, the V_m values decreases with the increasing hydration radii of the anionic species, confirming that the selective diffusion of anionic counter-ions through the p-LDHM has a significant contribution to the observed potential difference. With the increasing hydration radii, the anionic species will face more hindrance in diffusing through the nanofluidic channels, and this slow cross over of

anionic species will in turn reduce the output values of V_m.[44] The V_m values originating in p-LDHM membrane is also used for the calculation of counter-ion transference number (t_-) by

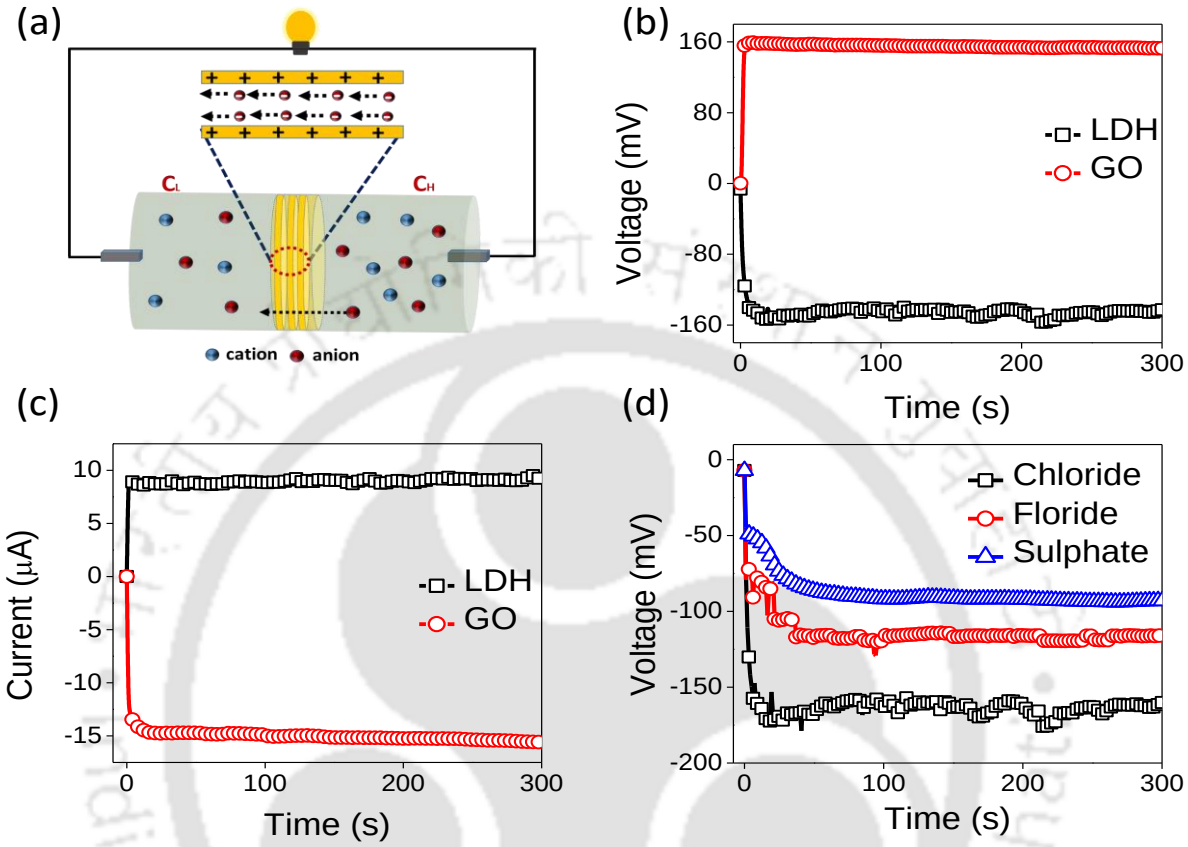

Fig. 3.8: Charge selectivity of p-LDHM: (a) Schematic diagram of the device utilized for concentration gradient based energy harvesting process. (b) Trans-membrane potential and (c) osmotic current generated with p-LDHM as a function of time. (d) Trans-membrane potential generated with p-LDHM as a function of time with increasing hydration radii of the anionic species, the corresponding hydration radii of chloride, fluoride and sulphate are 0.33 nm, 0.35 nm and 0.38 nm respectively. A thousand-fold concentration gradient was maintained by placing 10 mM KCl in the high concentrated chamber and 10 μM KCl in the low concentrated chamber respectively throughout all the experiment.

employing Eqn 4, assuming that the membrane transference numbers are constant throughout the membrane phase. The Eqn 4 for membrane potential (V_m) can be derived from the Donnan potentials and diffusion potential which is summarized by Geise *et al.*[41]

$$V_m = (t_+ - t_-)\frac{RT}{F} ln \frac{C_{High}}{C_{Low}} - - - (4)$$

The p-LDHM displayed a remarkable preference for the chloride anions with transference number (t_-) approaching 0.95 under 1000-fold concentration difference. The high transport number and excellent nanofluidic transport of the pLDHM paved the way for harvesting electrical energy from salinity gradient. As shown in Fig. 3.9a and Fig. 3.9b, both V_m and I_{OS} values of the p-LDHM devices were found to be increasing with the increase in the concentration gradient. The osmotic power density for different concentration gradient was calculated according to the Eqn 5 [30,45], and a remarkable 0.7 Wm^{-2} power density was achieved under a 1000-fold concentration gradient of KCl electrolyte, as shown in Fig. 3.9c.

$$P_{OS} = \frac{I_{OS} \times V_{OS}}{Area} - - - - - (5)$$

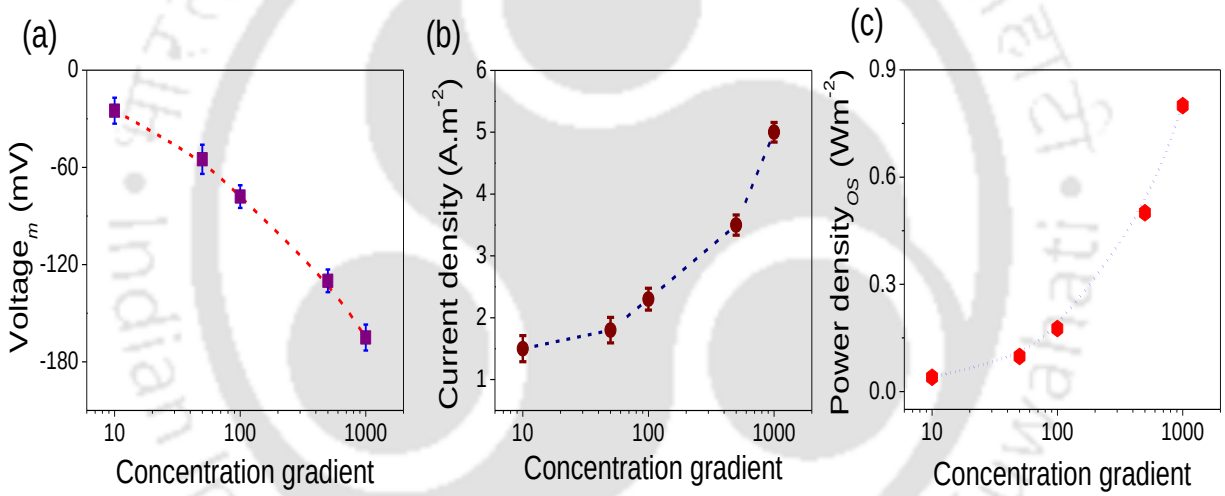

Fig. 3.9: Osmotic energy conversion: (a) Trans-membrane potential, (b) Current density defined as the total osmotic current divided by the area of the membrane in contact with the electrolyte (area of ionic interface ~ 2.5 mm^2) and (c) power density obtained with p-LDHM as a function of concentration gradient.

The energy conversion efficiency is defined as the ratio of the total/integrated electric power produced over time to the total Gibbs free energy supplied. Energy conversion efficiency indicates the percentage of the chemical energy consumed within the RED stack which is converted into electrical power. It is expressed as shown in Eqn 6[40]

$$\eta = \frac{\Delta E_m \, Q_t}{\Delta E_{ideal} Q_{t.ideal}} - - - (6)$$

Where ΔE_{ideal} is the ideal equilibrium voltage, ΔE_m is the measured voltage , Q_t the actual transferred charge and $Q_{t,ideal}$ the ideal transferred charge.

In nanofluidic energy conversion device, power is harvested from the selective transport of either cations or anions and hence for the condition of maximum power generation, ΔE_m is further reduced from ΔE_{ideal} by a factor of 2. Now expressing the transferred charge in terms of anion transferred number and applying the condition of maximum power generation the energy conversion efficiency can be expressed as in shown in Eqn (7) [46] and η_{max} was calculated to be ~ 44 % for 1000-fold concentration difference of KCl electrolyte with our p-LDHM device.

$$n_{max} = \frac{1}{2}(2t_- - 1)^2 - - - -(7)$$

It is clear from Eqn7 that even with a perfect perm selective membrane, the maximum energy efficiency of a nanofluidic osmotic energy generator is limited to only 50%. Therefore, fabrication of anion-selective nanofluidic membrane is of utmost interest where we can utilize both the complementary charge selective membrane in synchronization for achieving better performance in osmotic energy conversion.

Nanofluidic devices of p-LDHM demonstrated an interesting shape-dependent ionic transport behaviour. As shown in Fig. 3.4b, nanofluidic devices of rectangular p-LDHM strips (symmetric) exhibit linear *I-V* curves. On a clear contrast, nanofluidic devices fabricated with triangular (asymmetric) p-LDHM strips displayed non-linear *I-V* curves, where the current values in forward bias were found to be significantly higher than in the reversed bias (shown in Fig. 3.10b). This phenomenon of exhibiting diode-like behaviour in asymmetric nanopore is known as the ionic current rectification (ICR). The origin of ICR in the asymmetric nanofluidic channel is attributed to preferential migration of ionic species in one direction and restricting

the same in the opposite direction. Under such conditions, the ionic current recorded at forward-bias (+V) is found to be higher than the one recorded at an equal voltage of reverse-bias (-V). Such ion-selective behaviour is common in biological ion pumps, and they play vital

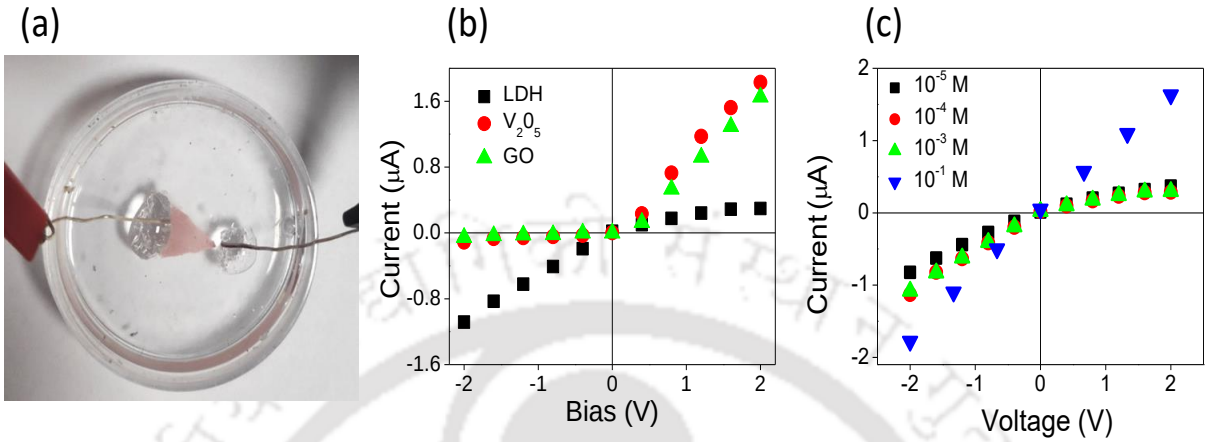

Fig. 3.10: Ionic current rectification (ICR) via triangular p-LDHM device: (a) Digital image of the triangular nanofluidic device of p-LDHM. (b) *I-V* curves recorded with triangular p-LDHM device is compared with that of GO and V_2O_5 devices. (c) ICR as a function of KCl concentrations.

roles in maintaining ionic concentration gradient across the cellular membrane. Inspired by the biological systems, ICR behaviour was repeated in several artificial systems, like the conical nanopores, [47] longitudinal hetero-structured nanotubes, [48] homogeneous nanochannels with asymmetric bath concentrations,[49] and triangular membranes of reconstructed graphene oxide [50] and vanadium pentoxide.[10] The *I-V* curve shown in Fig. 3.10b (black line) was recorded through an isosceles triangle cut from p-LDHM (15mm (altitude) × 5 mm (base) × 0.030 mm (thickness)), aqueous solution of KCl (10^{-4} M) was placed on both the reservoirs. The non-linearity of the *I-V* curve clearly reveals that the current values at positive bias are significantly lower than that of the negative bias of similar magnitude. The *I-V* curve of the triangular p-LDHM strip is also compared with that of GO and V_2O_5 strips. In all these devices, bias was applied at the base side of the triangle. Remarkably, the direction of ICR in p-LDHM was found to be opposite to that of GO and V_2O_5 triangle, due to the opposite polarity of charges in the channel walls. The ICR ratio (ratio of the magnitude of the current recorded at +1 and -1 V) for triangular p-LDHM with 10^{-4} M KCl was found to be 3 (Fig. 3.10c). In the surface charge

governed regime (10^{-5} to 10^{-3} M), the ICR ratio was found to be independent of salt concentration. However, in the high concentration regime (10^{-2} to 1 M), the ICR value decreases with the increasing salt concentrations. This observation indicates the origin of ICR to be the unipolar conductivity of p-LDHM in the surface-charge-governed region. In addition to surface-charge-governed conductivity, another requisite parameter for achieving ICR is the geometrical asymmetry. ICR was not observed in rectangular devices even in the surface-charge-governed region.

The probable mechanism of ICR in triangular p-LDHM is illustrated in the schematic of Fig. 3.11. In the surface-charge-governed regime (10^{-2} to 10^{-6} M), the overlapping EDL rejects the co-ions and builds up an elevated concentration of counter ions (Cl^- ions), which is significantly higher than that of the reservoirs. Due to the geometrical constraints, the total current flowing through the p-LDHM triangle in any direction is determined by the number of ions flowing through the tip of the triangle. On forward bias, Cl^- ions residing inside the nanochannel flows from the p-LDHM triangle to the bulk reservoir through the tip side. In this bias, ions flow from a region of higher ionic concentration to a reservoir of lower concentration, and hence produced higher ionic flux (Fig. 3.11, "forward bias"). Similarly, at the reverse bias, ions flow

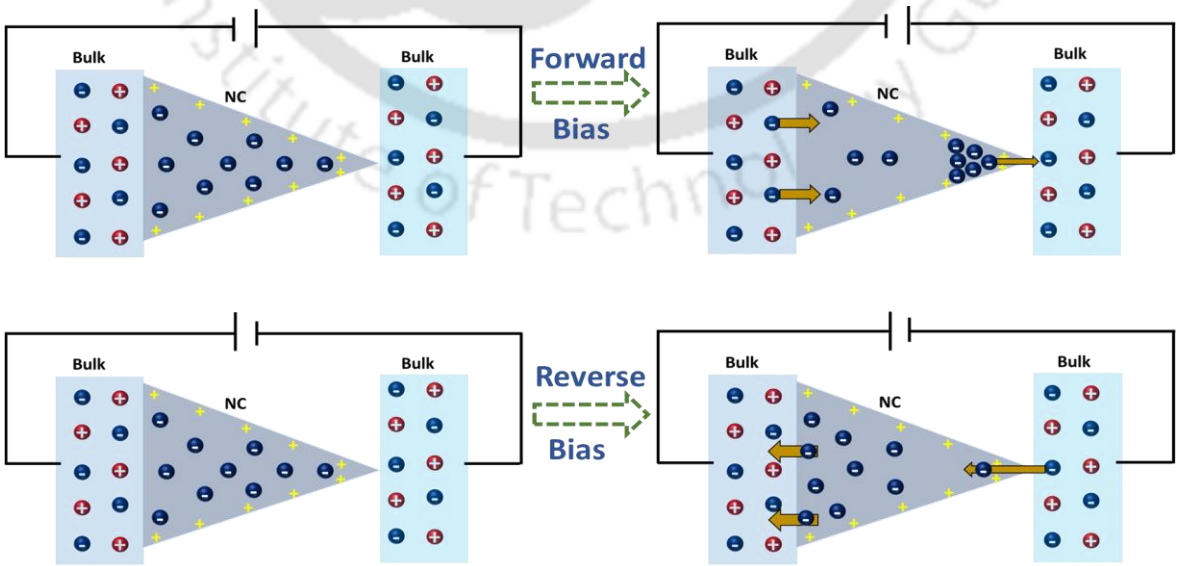

Fig. 3.11: Mechanism of ICR: Schematic illustration of ICR with 2D triangular devices of p-LDHM.

from a region of lower ionic concentration (from the reservoir) to a region of higher ionic concentration (at the p-LDHM triangle), which leads to lower ionic flux. Moreover, the higher ionic current in the forward bias is supported by a larger entrance (base)/exit (tip) ratio. In contrast, in the reverse bias, anions experience a much lower entrance (base)/exit (tip) ratio. The ion rectifying nature of the triangular p-LDHM can also be exploited as an ion-pump to push anions against the concentration gradient under a fluctuating external potential with a mean value of zero, where the applied potential was varied between +1V and -1V maintaining a mean voltage value of zero and the corresponding current response was plotted as a function of time. A schematic of the triangular device fabricated for attaining the active anion pumping effect is shown in the schematic of Fig. 3.12a.

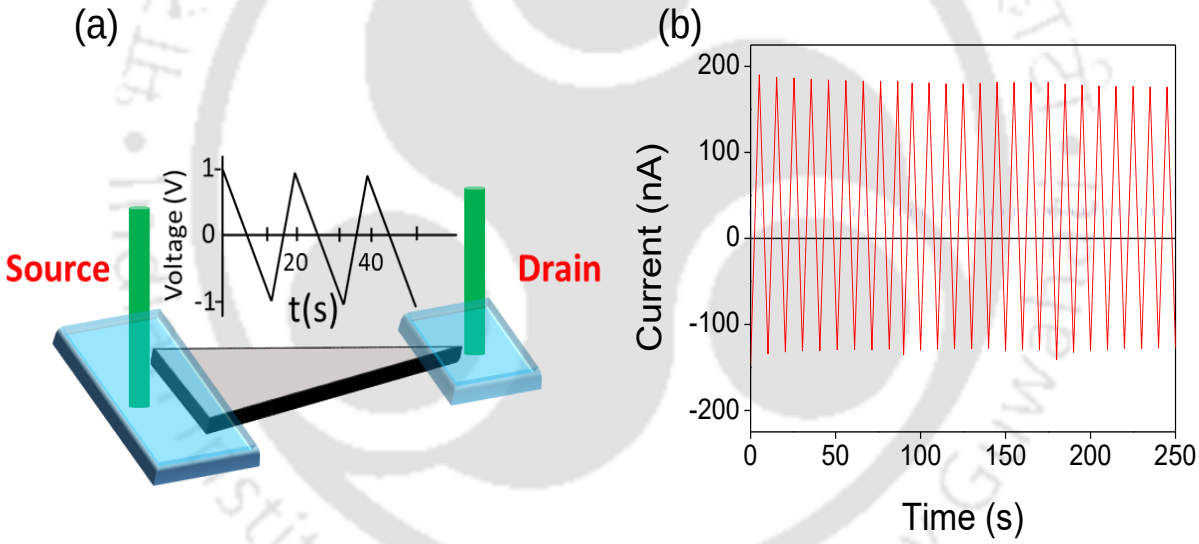

Fig. 3.12: Ion-pumping by triangular p-LDHM nanofluidic device: (a) Schematic representation of the experimental set-up utilized for ion pumping under fluctuating electric field with a mean value of zero. (b) Plot of current as a function of time recorded under a fluctuating electric field of zero means (between +1V and -1V) against a 1000-fold concentration gradient.

In order to verify the anion pumping behaviour, both the reservoirs were filled with aqueous KCl solution of different concentrations, the concentrations of the base and tip reservoirs of a triangular p-LDHM device were fixed at 10^{-5} M and 10^{-3} M, respectively. The electric field between the reservoirs was periodically varied between +1 and -1 V through Ag/AgCl electrodes placed at the reservoirs. The current response of the triangular device under the

influence of fluctuating electric field was recorded as a function of time. As shown in Fig. 3.12b, for a 1000-fold concentration difference **(**10^{-2} to 10^{-5} M**),** a positive average current of 2.5×10^{-8} A (dotted blue line) was observed. It indicates a net flow of the Cl^- ions in the uphill direction (against the concentration gradient), under the fluctuating electric field. The uphill migration of ions was also confirmed by measuring the initial and final concentrations of the electrolytes in the source reservoir. The magnitude of ion pumping was further enhanced by fabricating a device with six triangular membranes (Fig. 3.13a), where all the drain and source reservoirs are interconnected. After applying a fluctuating electric field (between +1 V and -1V) with zero mean, for 3 minutes, the initial and final conductivity of the electrolytes in the

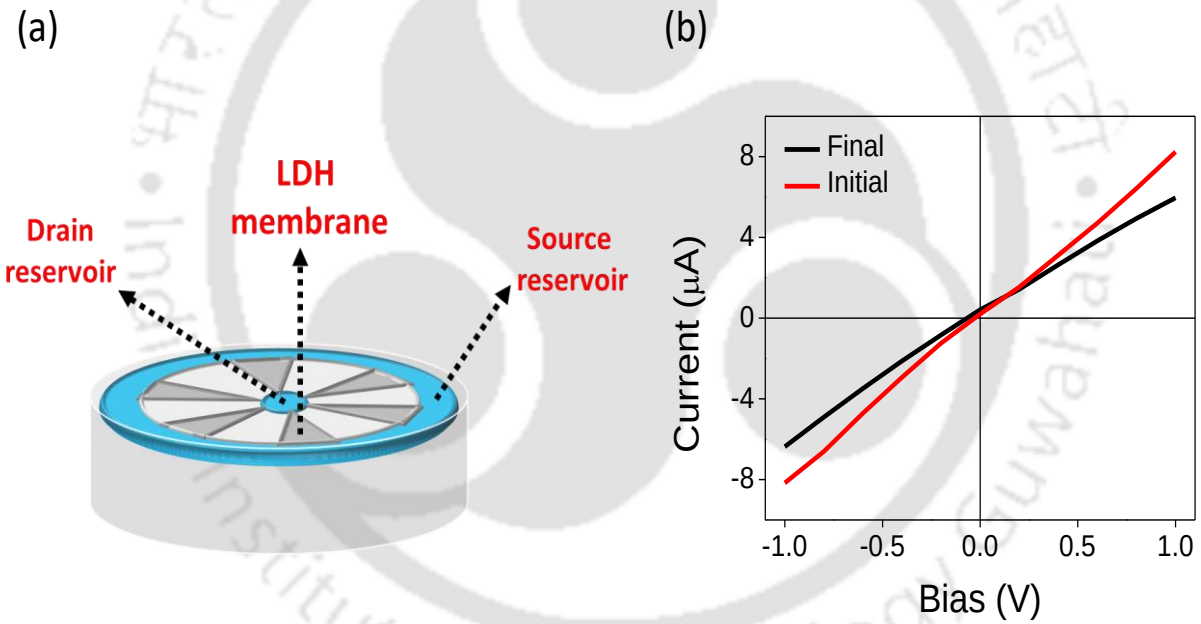

Fig. 3.13: Verification of Ion pumping process through triangular p-LDHM: (a) Schematic representation of anion-pump consisting of six triangular strip of p-LDHM. (All the tips of the triangular p-LDHM are connected to same source reservoir, and all the bases are connected to the same drain reservoir). (b) Comparison of the *I-V* curves of the KCl electrolytes in the source (low starting concentration) reservoirs before and after ion pumping for 3 minutes.

source reservoirs were measured from the slopes of the *I-V* curves (Fig. 3.13b). From the difference in the conductivity values, concentrations difference of the ions in the source reservoir before and after ion pumping (for 3 minutes) was found to be 2.23×10^{-6} M, details of the calculation are presented in Table 1. The decreasing concentration of the ions in the low

concentration reservoir, after applying fluctuating electric field confirms the ion pumping effect of triangular p-LDHM against the concentration gradient.

Table 1 Calculation of concentrations difference of the ions in the source reservoir before and after ion pumping (for 3 minutes).

Reservoir	Initial concentration (M)	Initial Conductance (S)	Final Conductance (S)	Final concentration (M)	Concentration difference (M)	Average Concentration difference (M)
Source	10^{-5}	8.05×10^{-6}	6.25×10^{-6}	7.7×10^{-6}	2.4×10^{-6}	$2.23 \times 10^{-6} \pm 2.13 \times 10^{-7}$
	10^{-5}	8.05×10^{-6}	6.13×10^{-6}	7.6×10^{-6}	2.3×10^{-6}	
	10^{-5}	8.05×10^{-6}	6.45×10^{-6}	8.01×10^{-6}	1.99×10^{-6}	

3.5: Conclusions

Inherent positive surface charge of CoAl LDH is exploited here to fabricate nanofluidic device with excellent anion selective characteristics. The p-LDHM based nanofluidic conduits panoply remarkable anion conductivity in the surface charge governed region. The perm-selective nature of p-LDHM is also utilized to harvest electricity from salt concentration gradient via applying the principle of RED. Moreover, the p-LDHM based shows shape dependence ionic transport behaviour, while a rectangularly cut p-LDHM device shows linear *I-V* curve, the triangularly cut p-LDHM shows non-linear *I-V* curves similar to a diode. The ionic current rectifying behaviour of triangular p-LDHM can also be utilized to achieve anion pumping under the presence of a fluctuating electrical potential with a mean value of zero. Looking at the ease fabrication of 2D anion pump along with its tremendous potential in areas like biomedical analysis, anion sensing, osmotic energy harvesting, and catalysis, the p-LDHM 2D anion conductor may provide enthusing opportunities for preparing next generation smart nanofluidic devices.

3.6: References:

1. K. Decker, M. Page and A. Aksimentiev, *J. Phys. Chem. B*, 2017, **121**, 7899.
2. N. Reyes and D. C. Gadsby, *Nature*, 2006, **443**, 470.
3. J.P. Morth, B.P. Pedersen, M.J Buch-Pedersen, J.P. Andersen, B. Vilsen, M.G. Palmgren and P. Nissen, *Nat. Rev. Mol. Cell Biol*., 2011, **12**, 60.
4. B. P. Pedersen, M. J. Buch-Pedersen, J. P. Morth, M. G. Palmgren and P. Nissen, *Nature*, 2007, **450**, 1111.
5. C. L. Slayman, W. S. Long and C. Y. H. Lu, *J. Membr. Biol*., 1973, **14**, 305.
6. A. K. Verma, A. G. Filoteo, D. R. Stanford, E. D. Wieben, and J. T. Penniston, *J. Biol. Chem*., 1988, **263**, 14152.
7. Z. Zhang, X. Y. Kong, G. Xie, P. Li, K. Xiao, L. Wen and L. Jiang, *Science*, 2016, **2**, 1600689.
8. K. Xiao, L. Chen, R. Chen, T. Heil, S. D. C. Lemus, F. Fan, L. Wen, L. Jiang and M. Antonietti, *Nat, Commun*., 2019, **10**, 1.
9. J. Yang, P. Liu, X. He, J. Hou, Y. Feng, Z. Huang, L. Yu, L. Li, and Z. Tang, *Angew. Chem. Int. Ed*., 2020, **59**, 6244.
10. R. K. Gogoi, A. B. Neog, T. Konch, N. Sarmah, and K. Raidongia, *J. Mater. Chem. A*, 2019, **7**, 10552.
11. J. Rabinowitz, C. Cohen and K. L. Shepard, *Nano Lett*., 2019, **20**, 1148.
12. C. Wu, T. Xiao, J. Tang, Q. Zhang, Z. Liu, J. Liu and H. Wang, *Nano Energy*, 2020, **76,** 105113.
13. Z. Zhang, X. Y. Kong, K. Xiao, Q. Liu, G. Xie, P. Li, J. Ma, Y. Tian, L. Wen, and L. Jiang, *J. Am. Chem. Soc*., 2015, **137**, 14765.
14. P. Sun, R. Ma, X. Bai, K. Wang, H. Zhu and T. Sasaki, *Sci. Adv*., 2017, **3**, 1602629.

15. J. Sun, P. Lia, J. Qu, X. Lu, Y. Xie, F. Gao, Y. Li, M. Gang, Q. Feng, H. Liang, X. Xia, C. Li, S. Xu and J. Bian, *Nano Energy*, 2019, **57**, 269.
16. X. He, L. Cao, G. He, A. Zhao, X. Mao, T. Huang, Y. Li, H. Wu, J. Sun and Z. Jiang, *J. Mater. Chem. A*, 2018, **6**, 10277.
17. P. Sun, R. Ma, W. Ma, J. Wu, K. Wang, T. Sasaki and H. Zhu, *NPG Asia Mater.*, 2008, **8**, 259.
18. K. Raidongia and J. Huang, *J. Am. Chem. Soc*., 2012, **134**, 16528.
19. T. Mouterde, A. Keerthi, A. Poggioli, S. Dar, A. Siria, A. Geim, L. Bocquet and B. Radha, *Nature*, 2019, **567**, 87.
20. K. Saha, J. Deka and K. Raidongia, *ACS Appl. Nano Mater*., 2019, **2**, 5850.
21. H. Huang, Y. Ying and X. Peng, *J. Mater. Chem. A*, 2014, **2**, 13772.
22. D. Chimene, D. L. Alge and A. K. Gaharwar, *Adv. Mater*., 2015, **27**, 7261.
23. S. Homaeigohar and M. Elbahri, *NPG Asia Mater*., 2017, **9**, 427.
24. S. K. Min, W. Y. Kim, Y. Cho and K. S. Kim, *Nat. Nanotechnol*., 2011, **6**, 162.
25. S. Qin, D. Liu, G. Wang, D. Portehault, C. J. Garvey, Y. Gogotsi, W. Lei and Y. Chen, *J. Am. Chem. Soc*., 2017, **139**, 6314.
26. J. J Shao, K. Raidongia, A. R. Koltonow and J. Huang, *Nat. Commun*., 2015, **6**, 1.
27. M. Deng, K. Kwac, M. Li, Y. Jung and H. G. Park, *Nano Lett*., 2017, **17**, 2342.
28. Z. Zhang, S. Yang, P. Zhang, J. Zhang, G. Chen and X. Feng, *Nat. Commun*., 2019, **2**, 1.
29. K. Xiao, P. Giusto, L. Wen, L. Jiang and M. Antonietti, *Angew. Chem. Int. Ed*., 2018, **57**, 10123.
30. J. Ji, Q. Kang, Y. Zhou, Y. Feng, X. Chen, J. Yuan, W. Guo, Y. Wei, and L. Jiang, *Adv. Funct. Mater.*, 2017, **27**, 1603623.

31. Q. Y. Wu, C. Wang, R. Wang, C. Chen, J. Gao, J. Dai, D. Liu, Z. Lin, and L. Hu, *Adv. Energy Mater.* 2019, **10**, 1902590.

32. L. Ding, D. Xiao, Z. Lu, J. Deng, Y. Wei, J. Caro, and H. Wang, *Angew. Chem. Int. Ed.* 2020, **59**, 8720.

33. Z. Liu, R. Ma, M. Osada, N. Iyi, Y. Ebina, K. Takada and T. Sasaki, *J. Am. Chem. Soc.*, 2006, **128**, 4872.

34. J. Liang, R. Ma, N. Iyi, Y. Ebina, K. Takada and T. Sasaki, *Chem. Mater*., 2010, **22**, 371.

35. F. Song and X. Hu, *Nat. Commun*., 2014, **5**, 1.

36. D. D. Ordinario, L. Phan, W. G. Walkup, J. M. Jocson, E. Karshalev, N. Hösken and A. A. Gorodetsky, *Nat. Chem*., 2014, **6**, 596.

37. H. J. Butt, K. Graf and M. Kappl, Physics and Chemistry of Interfaces, Wiely-VCH, Weinheim, Germany, 3rd Edition, 2006.

38. C. Duan and A. Majumdar, *Nat. Nanotechnol*., 2010, **5**, 848.

39. R. B. Schoch and P. Renaud, *Appl. Phys. Lett*., 2005, **86**, 253111.

40. W. Li, Z. Wang, S. K. Patel, S. Lin and M. Elimelech, *ACS Nano*, 2021, **15**, 4093.

41. G. M. Geise, H. J. Cassady, D. R. Paul, B. E. Logan and M. A. Hickner, *Phys. Chem. Chem. Phys.*, 2014, **16**, 21673.

42. R. B. Schoch, J. Han and P. Renaud, *Rev. Mod. Phys*., 2008, **80**, 839.

43. D.K. Kim, C. Duan, Y.F. Chen and A. Majumdar, *Microfluid. Nanofluid*., 2010, **9**, 1215.

44. Y. Wang, H. Zhang, Y. Kang, Y. Zhu, G. P. Simon and H. Wang, *ACS Nano*, 2019, **13**, 11793.

45. S. Hong, F. Ming, Y. Shi, R. Li, I. S. Kim, C. Y. Tang, H. N. Alshareef, and P. Wang, *ACS Nano*, 2019, **13**, 8917.

46. W. Xin, Z. Zhang, X. Huang, Y. Hu, T. Zhou, C. Zhu, X.-Y. Kong, L. Jiang and L. Wen, *Nat. Commun*., 2019, **10**, 3876.

47. J.J. Kasianowicz, E. Brandin, D. Branton and D.W. Deamer, *Proc. Natl. Acad. Sci*., 1996, **93**, 13770.

48. R. Yan, W. Liang, R. Fan and P. Yang, *Nano Lett*., 2009, **9**, 3820.

49. L. J. Cheng and L. J. Guo, *Nano Lett*., 2007, **7**, 3165.

50. J. Gao, A. R. Koltonow, K. Raidongia, B. Beckerman, N. Boon, E. Luijten, M. Olvera de la Cruz and J. Huang, *Mater. Chem. Front*., 2018, **2**, 475.

Part B: Extraction of Bio-derived Nanochannels for Nanofluidic Study

Chapter 4

Introduction to Bio-derived Nanofluidic Channels

4.1: Structural integrity of bio-materials

Amidst the rising concerns over climate change and energy scarcity, tremendous research efforts have been devoted towards the designing and development of technologically important functional materials in an environmentally friendly and sustainable manner. This era of technological development is dominated by the materials possessing advance properties and unique characteristics, and preparation of such materials are typically very energy intensive and detrimental to the environment. In contrast, bio-derived materials are renewable, abundant, and eco-friendly, and can be considered as attractive alternatives that can potentially meet some of these burning global challenges. Biopolymer nanofibrils are universal building blocks in naturally occurring materials, and there lies a significant possibility to extract this biomaterial to design and create new innovative materials and nanostructures.

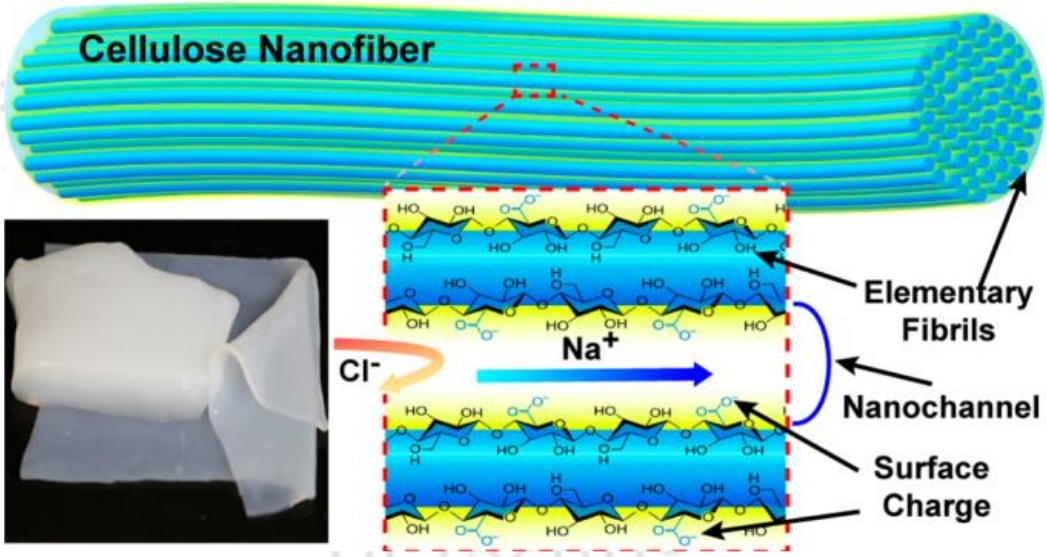

Fig. 4.1: Nanofluidic in bio-derived materials: Schematic diagram of a naturally biosynthesized bacterial cellulose showing the different nanofibrils. The nanofibrils possess permanent negative surface charges that endows them with perm-selective properties. (Image copied from *Chem. Mater.* 2018, **30,** 7707.)

Outstanding properties of natural bio-polymers profit from their hierarchically assembled multiscale organizations. The universal property of naturally available building blocks is the diverse micro and nanoscale interaction between the existing polysaccharides and fibres protein units. The organized protein subunits confer mechanical rigidity, structure, and functional

properties to the biological systems.[1-3] Nature creates a plethora of bio-materials with well-organized hierarchical structure, such as wood and silk. In particular, wood cellulose exhibits a hierarchical 3-dimensional (3D) assembly of nanofibrils (diameter ~10nm) with orderly running of several elementary fibrils (3-5 nm) in between them that make the percolated nanochannel networks necessary for nanofluidic transportation.[4-6] The fibers of silkworm silk (e.g., Bombyx mori) have a hierarchical fibrous organization (~30 nm in diameter) of β-pleated-sheet-based crystals within the amorphous matrix of silk fibroin (SF) and sericin that are packed densely to provide molecular chains facilitates.[7,8] The abundant carboxyl and hydroxyl groups on the surface of these nanofibers and elementary fibrils provided the nanochannels with permanent negative surface charges that can attract a cluster of counter ionic species into its vicinity and thereby ensured a surface charge-governed counter-ion selective transport property.[9,10] The geometry and the surface charge property of these bio-derived nanochannels can also be easily fine-tuned to accommodate desired ion selectivity. Moreover, the desired nanofibrils can also be extracted from the macro fibrils portion via mechanical, chemical, and enzymatic methods.[11-14] These features enable bio-derived materials to be used as an alternative to artificial nanochannels in diverse practical applications.

4.2: Application of bio-derived nanofluidic channels

4.2.1: Ion conductor

Bio-derived nanochannels with precisely designed hierarchical micro and nanofibrils provide an exciting platform to study ionic transport phenomena under extreme state confinement. Wang *et al.* reported a mechanically rigid, flexible, and bio-compitable scalable bacterial cellulose (BC) membrane as an ion conductor unit.[6] The BC film contains numerous negatively charged nanochannels (1-2 nm) units with a zeta potential -13 mV that can be further upscaled to -45mV by a facile TEMPO (2,2,6,6-tetramethylpiperidine-1-oxyl radical) oxidation process.

The surface oxidation of the nanochannels leads to an increase in the ionic conductivity by a factor of over 40 times. Based on the TEMPO-treated BC film, a wearable, flexible, ultrasensitive humidity sensor was designed which respond to in vitro changes in moisture during inhalation and exhalation.

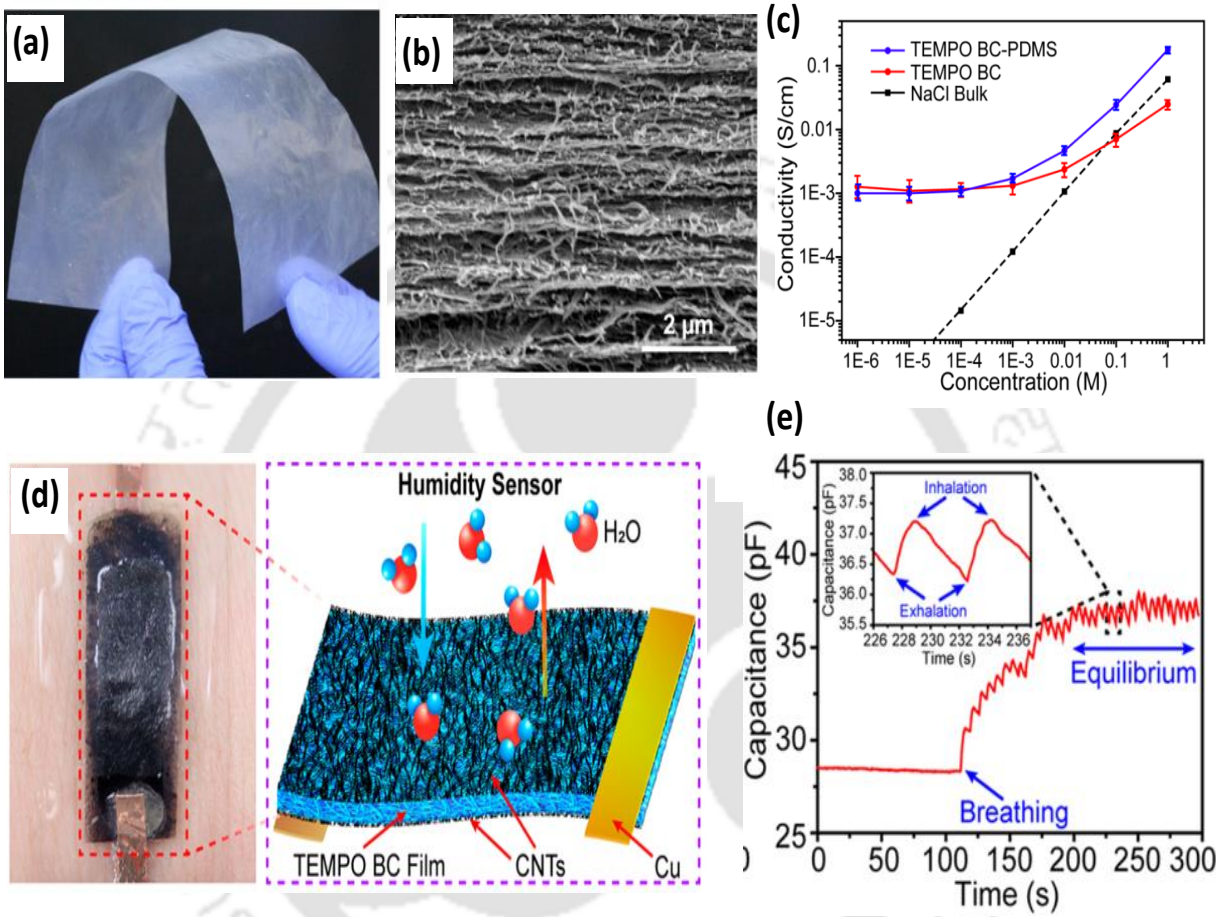

Fig.4.2: Bio-Compatible nanofluidic ion conductor based on BC: (a) Flexible transparent TEMPO-oxidized BC membrane. (b) SEM images showing the Cross-section of a TEMPO-treated BC. (c) Ionic conductivity recorded through the BC nanofluidic device showing as a function of NaCl concentrations. (d) Digital image of the flexible humidity sensor coated with carbon nanotubes electrodes on both sides and the corresponding humidity sensing mechanism. (e) Ionic resistances at different relative humidities during adsorption and desorption processes. (Image copied from *Chem. Mater.* 2018, **30,** 7707.)

Inspired by the design of muscle tissues, Kong *et al.* fabricated a biocompatible, anisotropic, and ionically conductive polyacrylamide (PAM) cross-linked natural wood hydrogel membrane.[15] Due to the cross-linking effect of PAM, the aligned cellulose nanofibers (CNFs) in wood exhibit excellent mechanical properties, and high-tensile strength up to 36 MPa is

achieved along the longitudinal direction. Moreover, the negatively charged aligned CNF in the wood hydrogel act as an excellent nanofluidic conduit, and high ionic conductivity of 5 × 10^{-4} Scm^{-1} was achieved, particularly at low electrolyte concentration where the system becomes perfectly perm-selective.

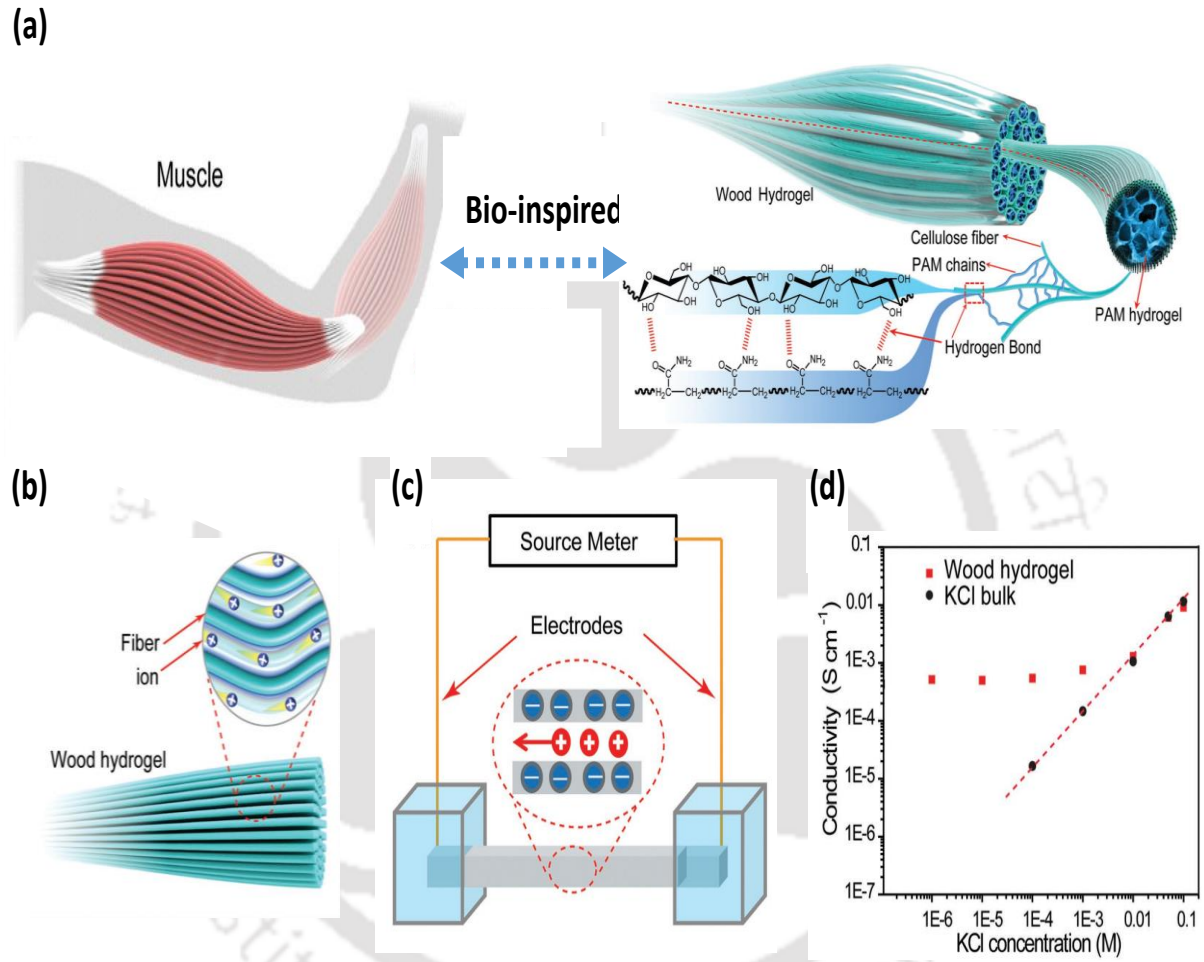

Fig. 4.3: Muscle-inspired ion-conductive wood hydrogels: (a) Schematic diagram of a skeletal muscle tissue (left) and its mimicking wood hydrogel system (right) showing the cross-linking interaction between PAM chains and wood CNF. (b) Schematic representing the plausible ion transport mechanisms in the wood hydrogel. (c) Depiction of the nanofluidic conduits (d) Ionic conductivity recorded through the wood hydrogel showing as a function of the KCl concentration. (Image copied from *Adv. Mater.*, 2018, **30**, 1801934.)

Li *et al.* reported a perm-selective de-lignified wood-based nanofluidic conduit derived from natural balsa wood featuring aligned cellulose nanofibers.[16] The de-lignification process introduces numerous open nanochannels within the wood cellulose matrix, which dimensions can be adjusted to 2 to 20 nm in diameter to promote desired size selectivity. Moreover, with

facile chemical modification, the surface charge density of the nanochannels wall can also be enhanced up to -5.7 m Cm^{-2} to achieved highly efficient ion transportation. In addition, the bio-derived ionic conductor can act as a transistor. Ionic rectification was observed under different gating potentials from -2 to 2 V. The cellulose membrane can preferentially accumulate positive counter ion under V_g = -2 V. The corresponding ionic conductivity was higher by one order of magnitude when we compared the same under V_g = 2 V.

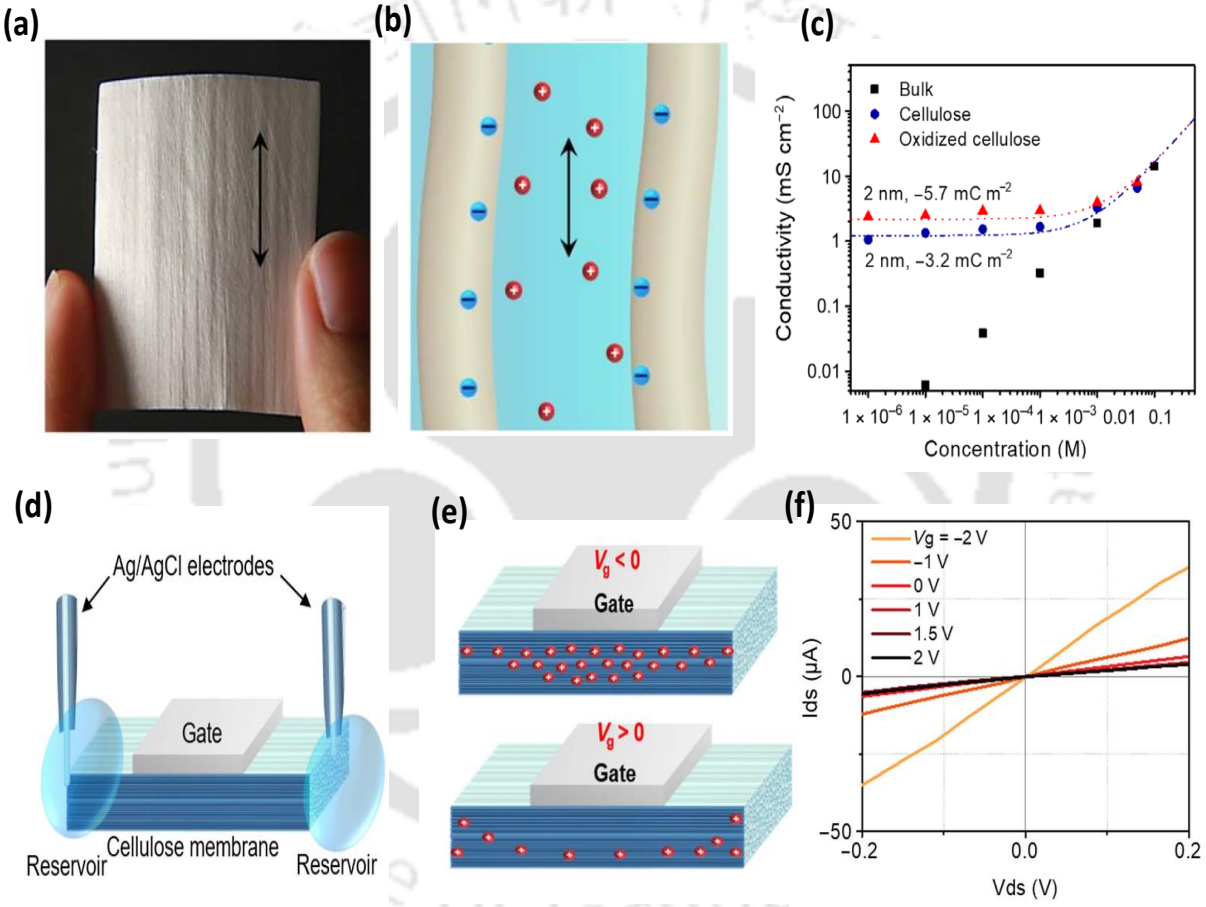

Fig. 4.4: Nanofluidic ion conductor based on aligned cellulose nanofibers: (a) Digital image of a wood-based nanofluidic membrane. (b) Schematic showing the ion transport mechanism in wood based nanofluidic membrane. (c) Comparison of ionic conductivity for different wood-based systems showing as a function of KCl electrolyte concentration. The presence of additional surface charge in the oxidized wood interprets its high ionic conductivity value. (d) Schematic of a wood-based nanofluidic transistor with a painted metal contact for gating. (e) Schematic showing the ion distribution within the cellulose membrane and its corresponding gating mechanism. (f) *I-V* characteristics of the cellulose nanofiber membrane with different gating voltages from -2 to 2 V. (Image copied from *Sci. Adv.* 2019, **5**, eaau4238.)

Again the same group of scientists demonstrates a TEMPO-oxidized cellulosic membrane possessing sub-nanometer aligned molecular chains to enhance selective diffusion under a thermal gradient.[17] When infiltrated with electrolyte (polyethylene oxide and sodium hydroxide), the TEMPO-oxidized cellulosic membrane exhibits a thermal gradient ratio of 24 mVK^{-1} on exposure to an axial temperature gradient. The enhanced heat to electricity conversion in the polymer-filled cellulose membrane (Na-cellulose complex) can be attributed to the negatively charged and well-aligned nanochannels that show enhanced counter ionic selectivity in the charged molecular chains in conjunction with synergistic Soret effect on exposure to a temperature gradient.

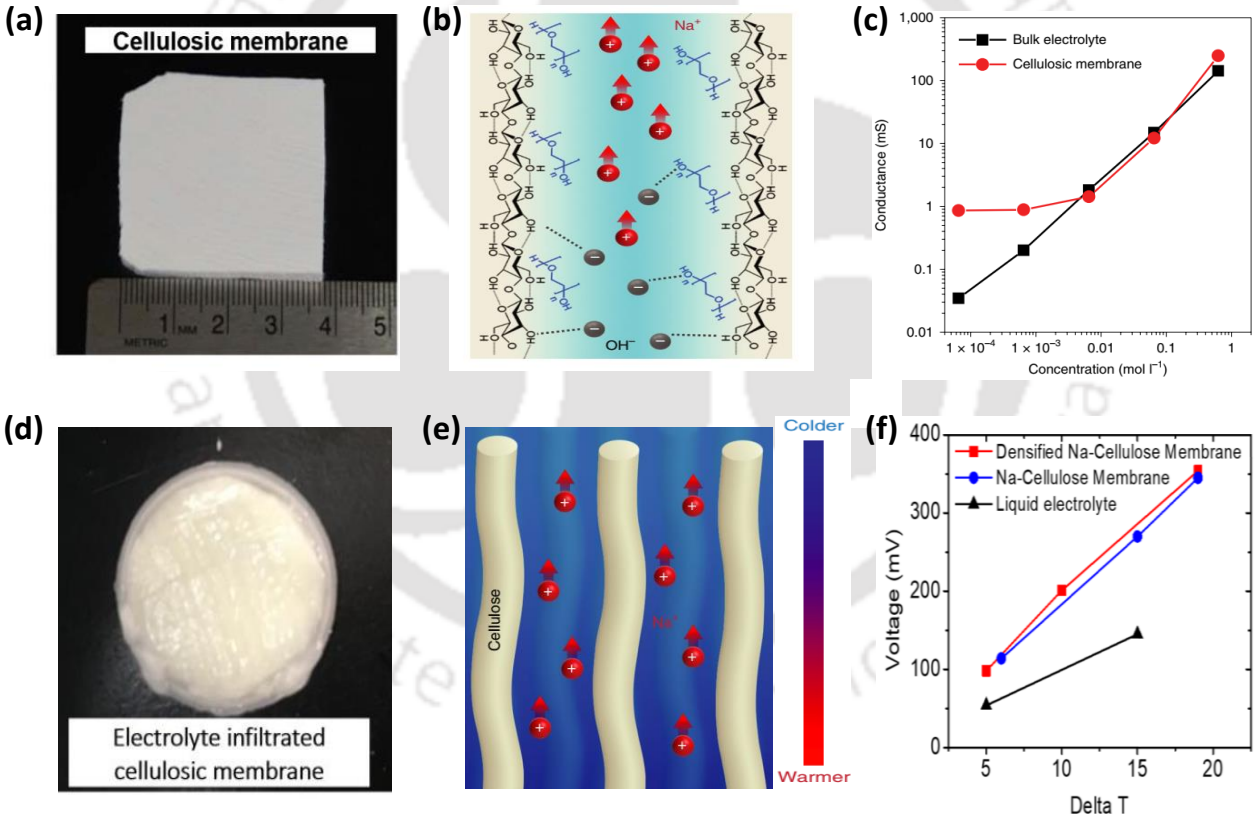

Fig. 4.5: Cellulose ionic conductors operating under the influence of differential thermal gradient: (a) Digital images of the cellulosic membrane. (b) Schematic showing the ionic mobility and selectivity of the cellulosic membrane. (c) Ionic conductance of the cellulosic membrane measured at different NaOH concentrations. (d) Digital image of an electrolyte infiltrated cellulosic membrane. (e) Schematic of the enhanced ion mobility and selectivity under the influence of a thermal gradient. (f) Measured thermally-generated open-circuit voltage. (Image copied from *Nat. Mater.*, 2019, **18**, 608.)

Kong *et al.* reported a mechanically rigid and ion conductive jellyfish hydrogel cable derived from natural jellyfish organs via a facile two-step synthesizing process of wet-drawing followed by wet-twisting.[18] Due to its highly dense and hierarchically aligned structure, the jellyfish ionic cable exhibit excellent tensile strength up to 149 MPa in the dry state. Moreover, the hierarchically aligned system possesses numerous nanochannels with positive surface charge, demonstrating a surface-charge-governed ion transport property. In addition, the outstanding structural integrity of the jellyfish cable ensures excellent water stability, and the ionic conduit remains fully functional under a water environment for about 20 days.

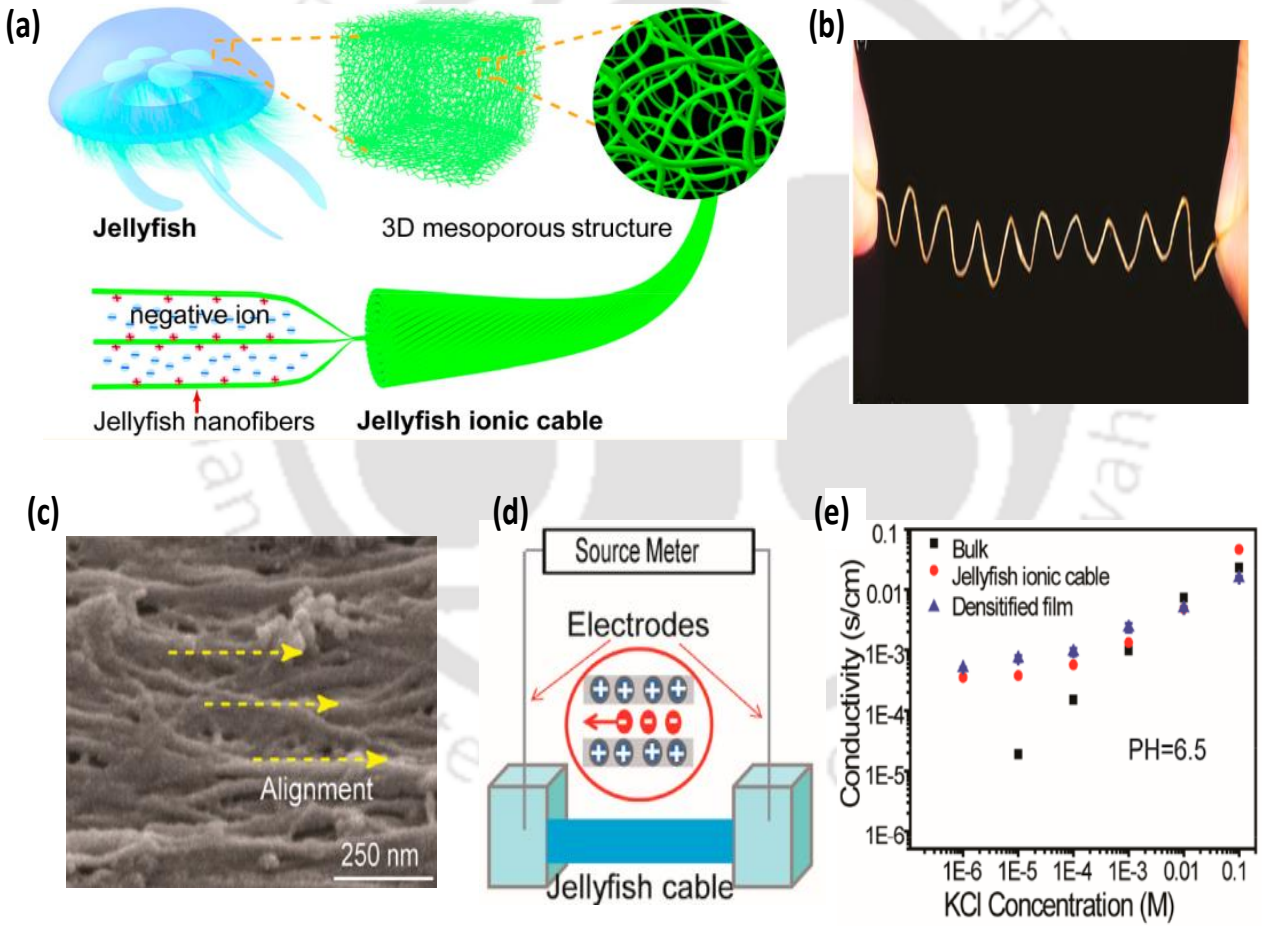

Fig. 4.6: Ionic conduit prepared from jellyfish cable: (a) Schematic demonstrating the working principle of the jellyfish cable. (b) Digital image of a dry jellyfish cable demonstrating its excellent flexibility. (c) SEM image showing the nanostructure assembly in the jellyfish cable. (d) Schematic of the jellyfish based nanofluidic conduit and its corresponding ion selective mechanism. (e) Ionic conductivity recorded through different types of jellyfish conduits showing as a function of KCl electrolyte concentration. (Image copied from *Chem. Mater.* 2019, **31**, 9288.)

Yang *et al.* reported bio-derived asymmetric ionic aerogels fabricated via the directional-freeze casting of carboxylated (TEMPO-CNFs) and quaternized cellulosic nanofibrils.[19] These asymmetric NFs couple capture moisture and create an ion-conducting hydrated nanochannel network on exposing to a humid environment. Ion dissociation and perm-selective ionic diffusion within the complementary charged NFs block lead to preferential movement of ionic species, thereby produces a potential gradient across the membrane matrix. On connecting to an external load, the asymmetric ionic aerogel could induce an open circuit potential (*V*oc) of ~115 mV with a maximum short circuit current (*I*sc) of 45 nA in a humid environment.

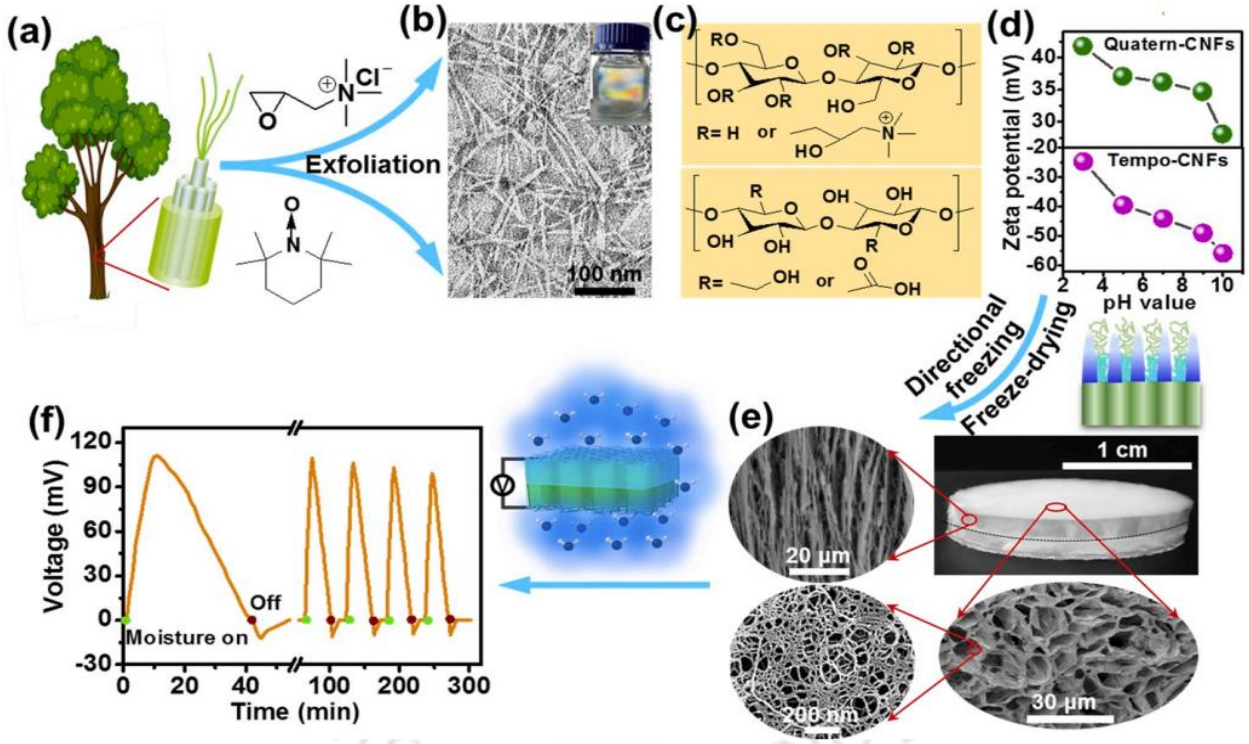

Fig. 4.7: Asymmetric ionic aerogel of biological nanofibrils: (a) Schematic illustration of synthesizing oppositely charged CNFs from wood via mechanical exfoliation. (b) Typical TEM image of negatively charged TEMPO-CNFs. (c) Chemical structures and (d) Zeta potentials of Quatern-CNFs (top) and TEMPO-CNFs (bottom). (e) Optical and SEM images of asymmetric ionic aerogel fabricated by directional freezing and freeze-drying. (f) V_{oc} generated with asymmetric ionic generator under periodic moist stimuli. RH = 99%. (Image copied from *Nano Energy*, 2020, **71**, 104610.)

4.2.2: Osmotic energy conversion

Osmotic energy conversion is a proficient way of harvesting renewable energy stored in the salinity gradient between sea and water river water. The reliability and applicability of the

process depend on the fabrication of ion exchange membranes which should be of low cost, highly abundant, sustainable, and easy to scale up. Interestingly bio-derived perspective membrane fulfils the requirements and hence is an ideal candidate of choice. For the first time, Wu *et al*. demonstrated an ionized wood membrane with aligned nanochannels of the cellulose nanofibers for this application.[20] The natural wood nanochannels can be chemically modified to accommodate positive (p-Wood) or negative (n-Wood) surface charges. These complementary charge selective nanochannels, upon synchronous alignment, serve as a perm-selective ion channel to produce trans-membrane potential and net ionic current. Using a tandem stack of 100 such opposite polarity wood membrane pairs, an output voltage as high as 9.8 V can be achieved with a salinity gradient of synthetic river water and seawater.

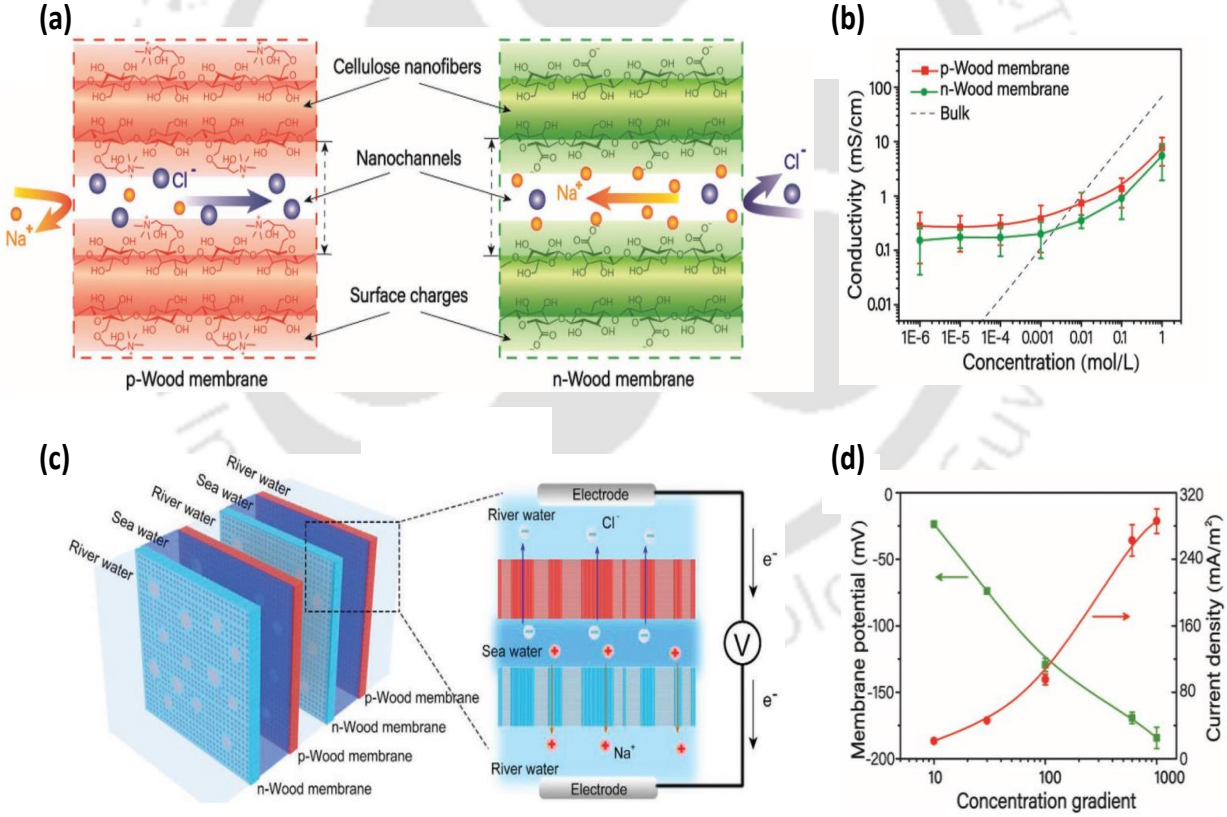

Fig.4.8: Salinity-Gradient harvesting with Wood Membranes: (a) Schematic representation showing the different functional groups and ion selectivity of the p-wood and n-Wood membranes, respectively. (b) Ionic conductivity of the p-wood and n-Wood membranes showing as a function of the NaCl concentration. (c) Schematic showing the working principle of the stacked ionized wood nano-generator. (d) The overall membrane potential and current density recorded through the wood nano-generator showing as a function of the concentration gradient. (Image copied from *Adv. Energy Mater.*, 2019, **10**, 1902590.)

Xin *et al.* engineered an osmotic energy conversion device from colloidal dispersion of silk nanofibrils (SNF) coated over anodic aluminium oxide (AAO) support.[21] The silk nanofibril possesses a condensed negative surface charge with precisely aligned nanochannels and dominates the ion transport. On the other hand, the AAO support offers tunable channels with amphoteric groups, and hence in the resulting hybrid membrane, an asymmetric geometry and charge polarity is established. When employed to a salinity gradient, the silk-based membrane delivers a maximum power density of 2.86 Wm^{-2} which can be further fine-tuned by changing the pH of the medium.

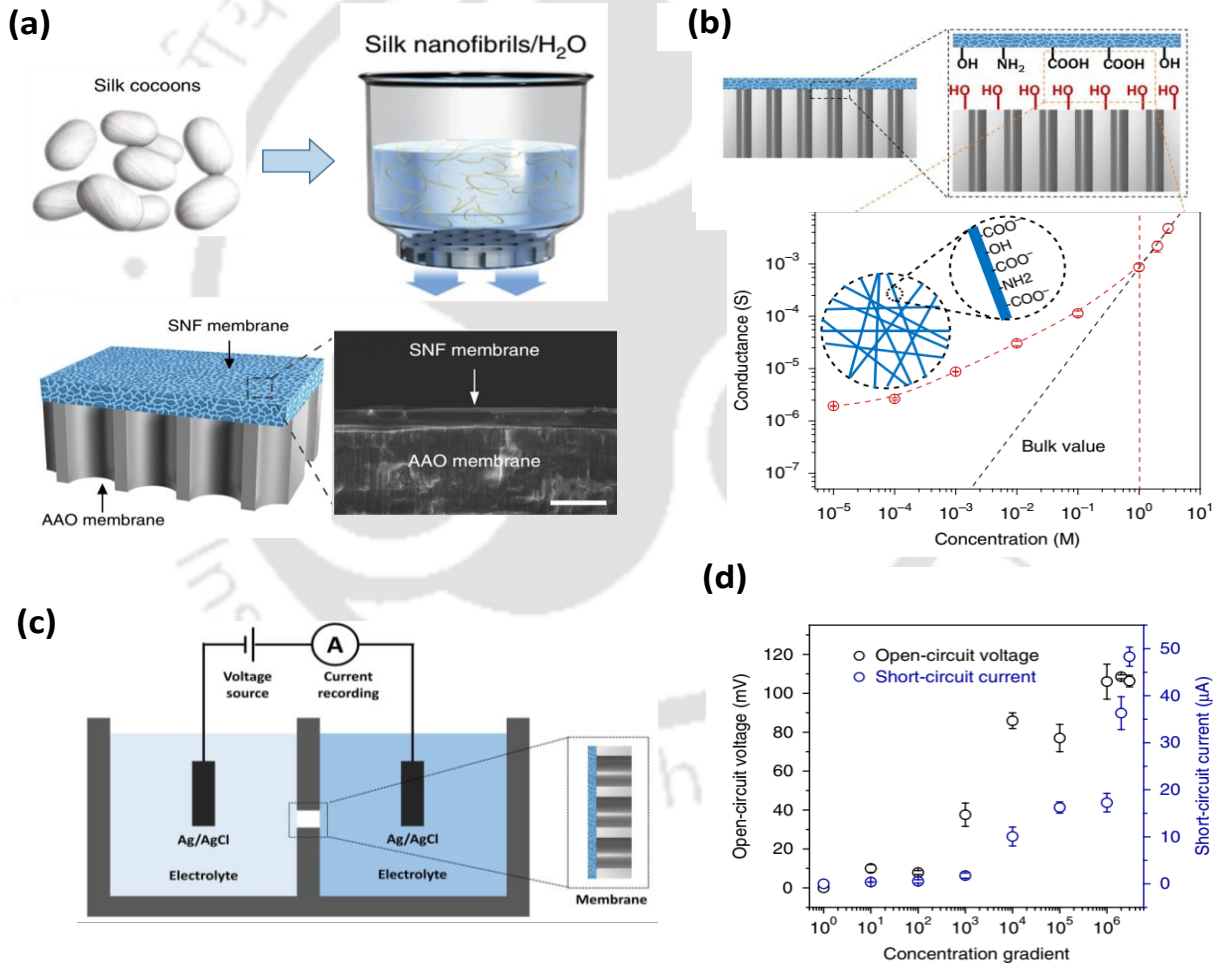

Fig. 4.9: silk-based hybrid membrane for osmotic energy conversion: (a) Schematic showing the fabricating process of silk nanofibril (SNF)/anodic aluminium oxide (AAO) membranes. (b) Ionic conductance of the hybrid membrane showing as a function of the electrolyte concentration and the corresponding perm-selective mechanism. (c) Schematic of the energy harvesting device. (d) Measured V_{OC} and I_{SC} of the hybrid membrane under a different concentration gradient. (Image copied from *Nat. Commun.*, 2019, **10**, 3876.)

Wu *et al.* reported an osmotic energy harvesting device based on negatively and positively charged aligned bacterial cellulose (N-ABC and P-ABC) membranes.[22] The pure bacterial cellulose (BC) was converted into negatively and positively charged membranes via a facile TEMPO mediated oxidation and quaternization process. The high surface charge density and narrow nanochannels realize a high ion selectivity and fast ion transmissibility in the ABC membrane system. When coupled in series connection, these complementary charge selective ABC membrane pairs can effectively promote the energy density up to 0.23 Wm^{-2} on exposure to a salinity gradient (C_H is 0.5 M and C_L is 0.01 M). In addition, by connecting 18 units of such ABC membrane pairs, the output voltage can be improved to 2.34 V, which is sufficient to power small electronic devices such as a calculator.

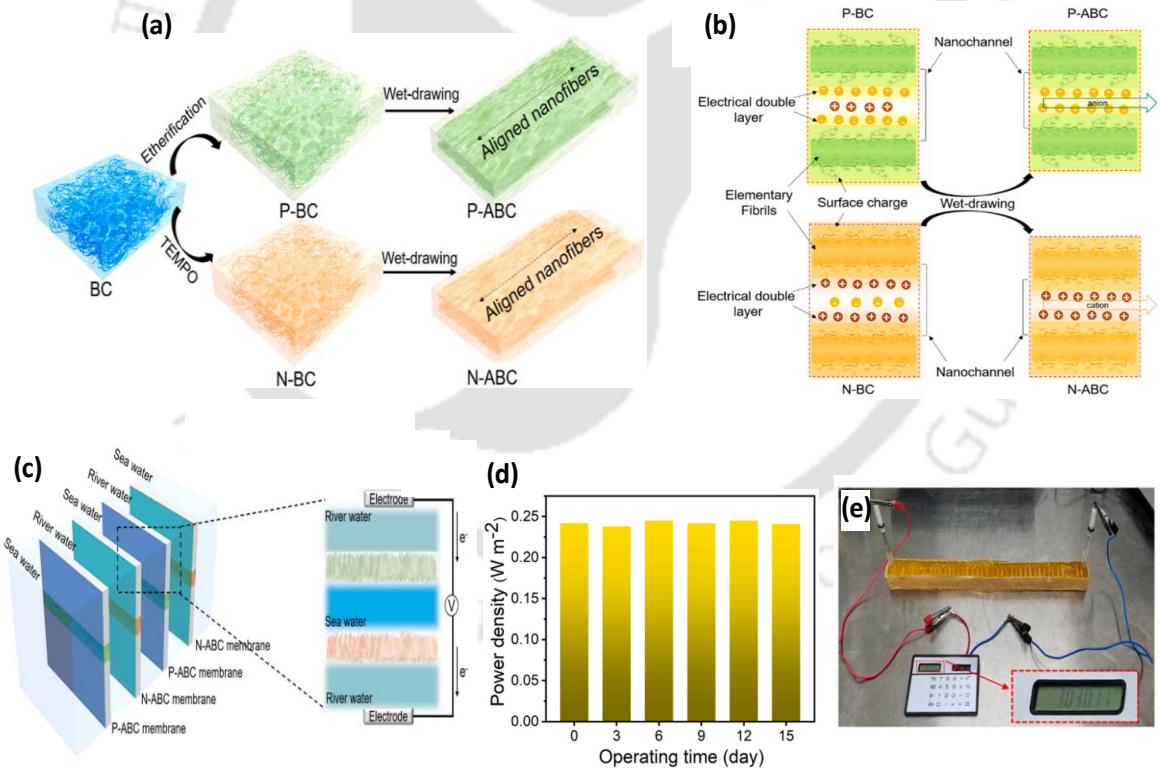

Fig.4.10: Oppositely charged aligned bacterial cellulose (ABC) biofilm for osmotic energy harvesting: (a) Schematic showing the fabrication of the ionized ABC membranes. (b) Schematic of the ion transport mechanism in P-ABC (above) and N-ABC (below) membrane, respectively. (c) Schematic of the ABC-based nanofluidic energy harvesting device. (d) The stability of ABC based RED device under the concentration gradient of 50 folds. (e) Image showing the 18 stacks of ABC utilized in empowering a calculator (Image copied from *Nano Energy*, 2021, **80** 105554.)

4.2.3: Waste water treatment

Due to their low-cost abundance and environmentally friendly nature, bio-derived materials have found tremendous attention in the field of wastewater treatment in recent days. The unique hierarchically porous, charged multi-channelled structure of bio-derive materials offers both size and charge-based sieving and facilitates the separation of molecules, ions, and various contaminants from wastewater. Among the affordable water treatment techniques like reverse osmosis, membrane filtration, sedimentation, distillation and solar steam generation,[23-27] membrane filtration, and solar steam generation show some advantageous features such as simple devices fabrication, low energy consumption, and large scale integration and hence both the techniques mentioned above have been frequently employed in the wastewater treatment process.

4.2.3.1: Filtration membrane based on bio-derived materials:

Membrane-based technology is a promising way to harvest clean water from wastewater. Being simple in operational techniques, convenient in terms of cost-effectiveness, and having high separation performance provided a viable platform to achieve bulk scale purification of sewage. Buehler *et al.* demonstrated bio-derived multi-layered nano-porous membranes fabricated from silk nanofibril (SNF) and hydroxyapatite (HAP) for wastewater treatment.[28] The SNF/HAP membrane can be obtained from simple vacuum-assisted filtration from their corresponding hybrid colloidal dispersion. The so-formed membrane possesses highly ordered multilayer structures, where HAP and SNF layers are oriented alternately. The hybrid membrane shows ultrafast water penetration and exhibits high-efficiency removal and even reuse of a broad range of water contaminants, such as organic dyes, toxic heavy metal ions, proteins, and other nanoparticles.

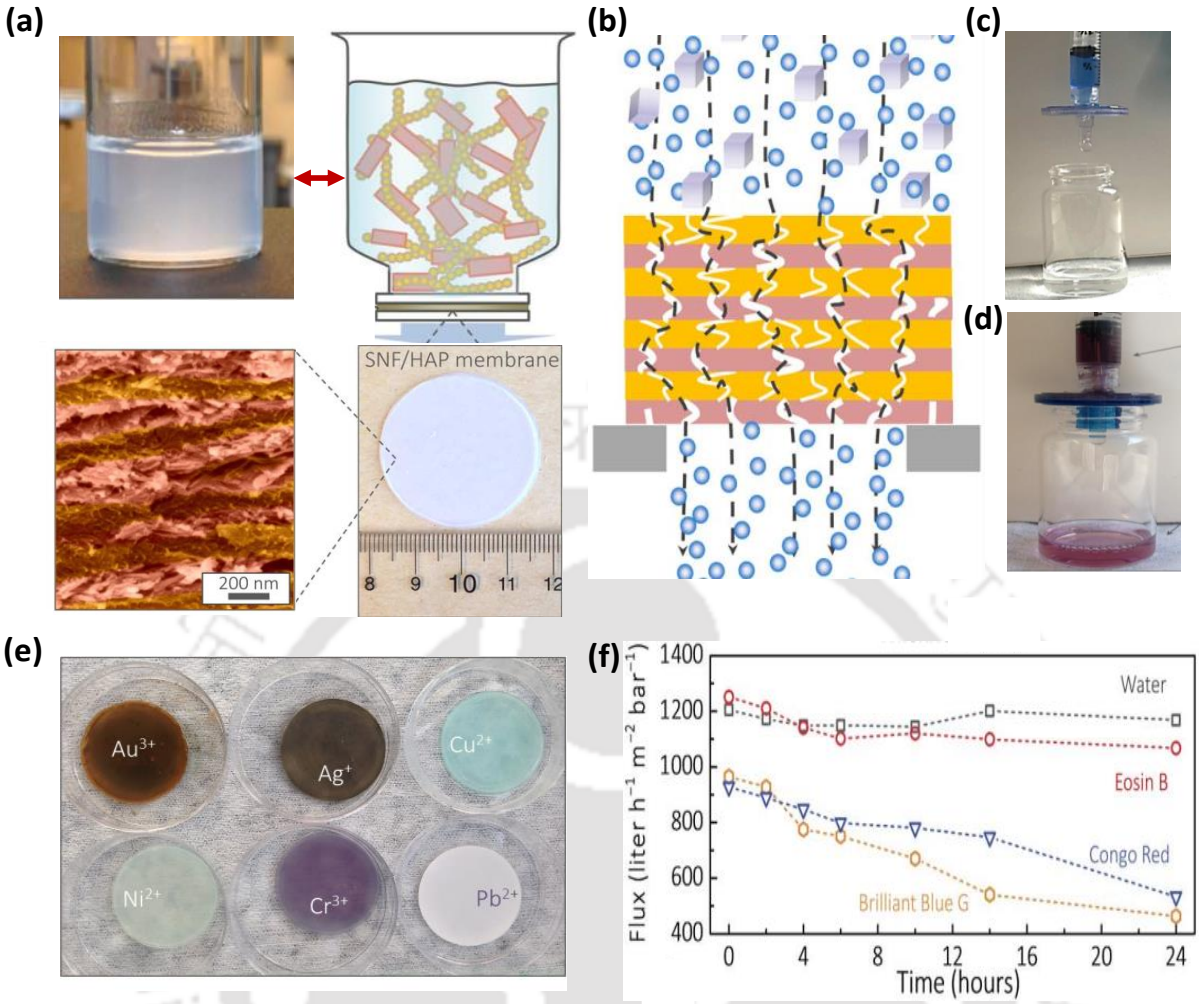

Fig. 4.11: Biomimetic multilayer water purification membranes of silk nanofiber: (a) A fabrication process of SNF/HAP membranes and visualization of the multilayer structures via SEM imaging. (b) Schematic representation of the multilayer SNF/HAP membrane and its corresponding filtration mechanism. (c-d) Image of the SNF/HAP-based syringe nanofiller employed for separation of Alcian Blue 8GX. (e) Image of an SNF/HAP membrane after metal ions were adsorbed through flux-controllable filtration. (f) Time-dependent changes in the flux of water and dye solution within 24 hours of flow through the SNF/HAP filter. (Image copied from *Sci. Adv.* 2017, **3**, e1601939.)

Wang *et al.* designed a 3D mesoporous sulfhydryl-functionalized wood (SH-wood) membrane fabricated via embedding sulfhydryl groups on the cellulosic network of a natural wood, which can serve as a metal ion trapper and realized an efficient and scalable removal of heavy metal ions.[29] With the presence of hierarchically aligned micro and nanochannels and the strong interaction between sulfhydryl and metal ions, metal ions are adsorbed onto the sulfhydryl group while water molecules are allowing to pass through it with a high flux rate of 1.3×10^3

L m^{-2} h^{-1}. Furthermore, stacking several SH-wood membranes, a multilayers filter is designed for scalable and highly efficient removal of heavy metal ions from sewage for environmental remediation.

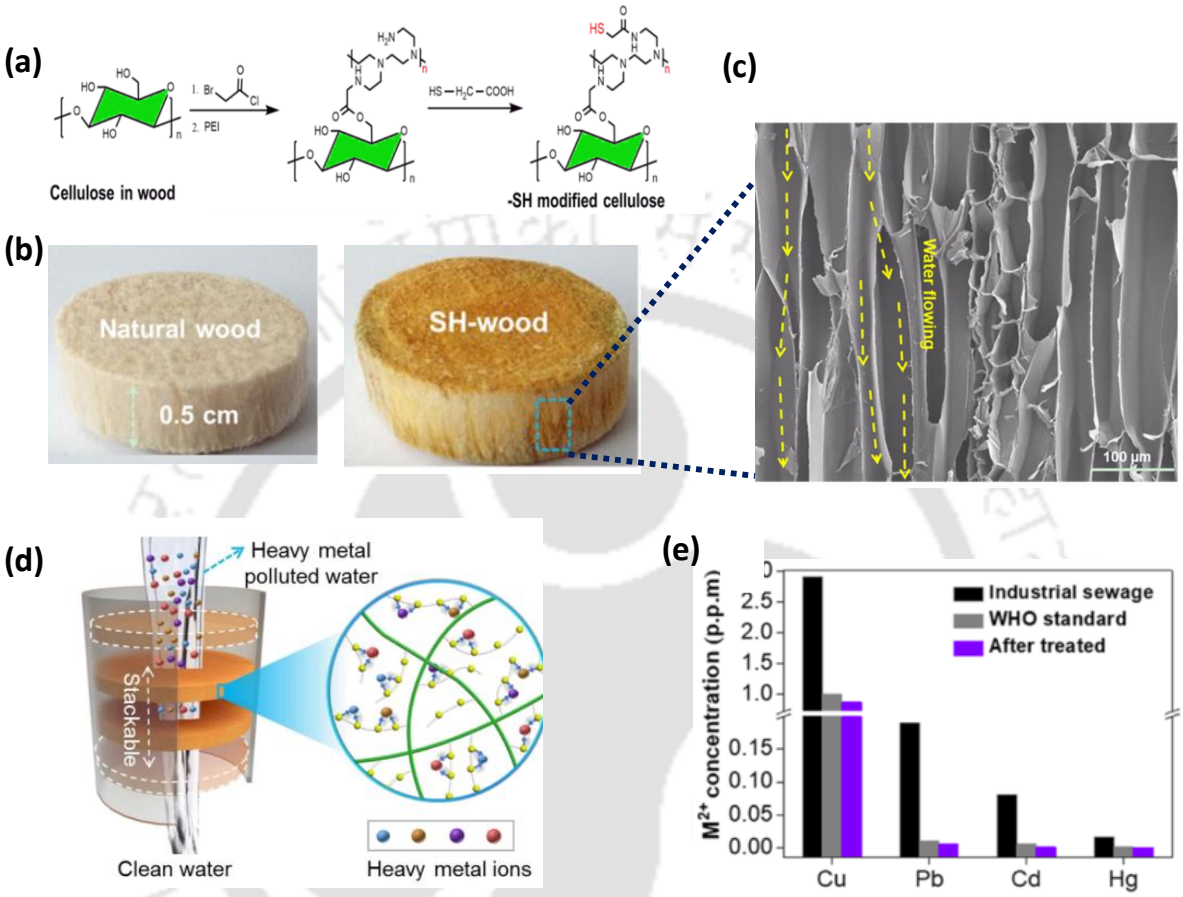

Fig. 4.12: Sulfhydryl-Functionalized Wood Membrane Stacks as a high-throughput metal trap: (a) Schematic showing the sulfhydryl-functionalization of native wood membrane. (b) Photos of the natural wood and SH-wood membrane. (c) SEM image of showing the water passage channels in SH-wood membrane. (d) The multilayer device of SH-wood utilized in large-scale separation of heavy-metal ion. The magnified schematic diagram shows the rejection mechanism of heavy metal, where the ions get adsorbed onto the -SH groups. (e) The concentrations of different metal ions in polluted water before and after treatment by the three-layer filter of SH-wood. (Image copied from *ACS Appl. Mater. Interfaces* 2020, **12**, 15002.)

Chen *et al.* demonstrate a Pd nanoparticle decorated 3D mesoporous wood-based membrane for highly efficient wastewater treatment.[30] The hierarchically arranged wood channels supported Pd NPs in its mesostructured organization, thereby increases the extent of interaction of the water pollutants with the NPs catalyst. To demonstrated the efficiency of the Wood-based device, methylene blue (MB) solution of 40 mg L^{-1} concentration was passed through

the filtration membrane, and degradation efficiency of 99.8% was achieved in the presence of $NaBH_4$, with an accompanying water flow rate up to 1 × 105 L m^{-2} h^{-1}. Moreover, a turnover frequency of 2.02 mol_{MB} mol_{Pd}^{-1} min^{-1} is achieved for the dye degradation process, which was much higher than the values reported in earlier literature.

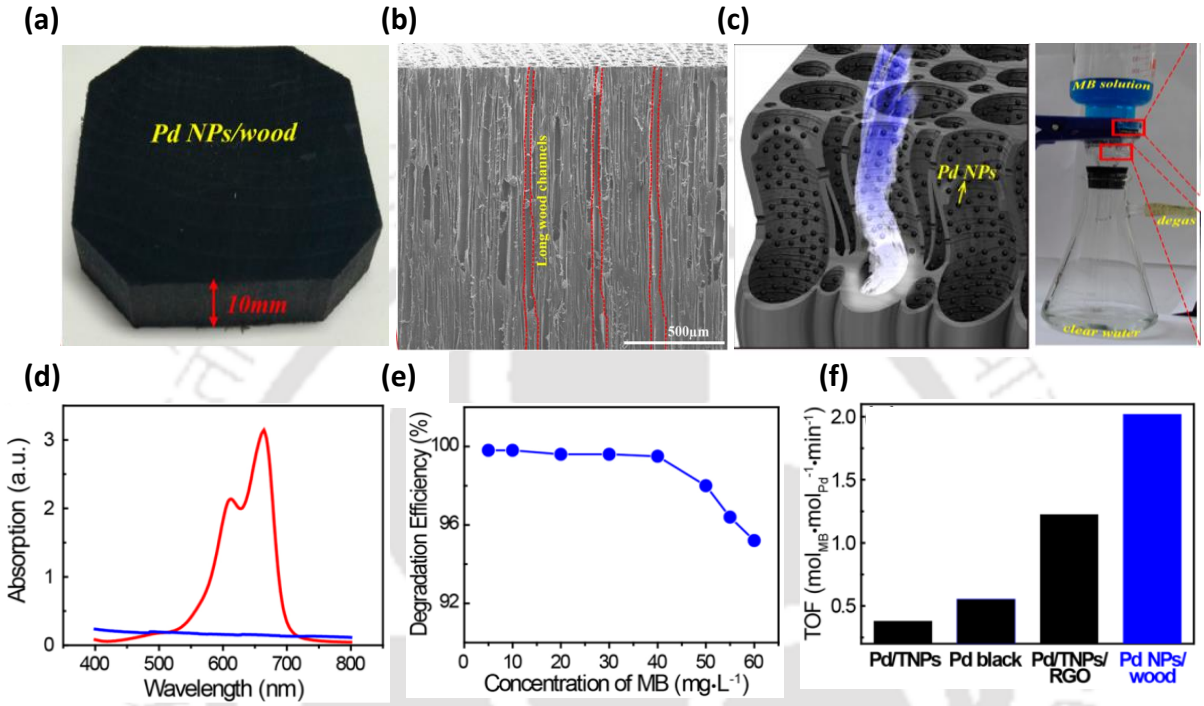

Fig. 4.13: Pd Nanoparticles Decorated Wood Membrane for Highly Efficient Water Treatment: (a) Digital image of a Pd NPs/wood membrane. (b) SEM image of a natural wood showing its hierarchical channels. (c) Schematic image showing the Pd NPs/wood mesoporous membrane, because of the reducing nature of the Pd NPs, the colour of the permeate solution changes (blue to colourless) as the MB solution flows through the membrane. (d) UV-vis spectra of the MB solution before (in red) and after (in blue) filtering through NPs/wood membrane. (e) The degradation efficiency at different concentrations of the MB solution. (f) Turnover frequency (TOF) of the Pd NPs/wood membrane. (Image copied from *ACS Nano* 2017, **11**, 4275.)

Jiao *et al.* reported a highly efficient water filtration membrane fabricated from natural wood via a facile carbonization and activation process.[31] The vertically aligned hydrophilic wood channels enable ultrafast permeation of water through the membrane, while negative surface charges present on the wall of the channel absorbed the water pollutants. As a result, the mesoporous wood-based activated filter demonstrates a higher removal efficiency of MB (50 mg L^{-1}) up to 99.95% for static adsorption process and 99.33% removal efficiency at a high

flow rate of 300 mL min^{-1} for dynamic adsorption process.

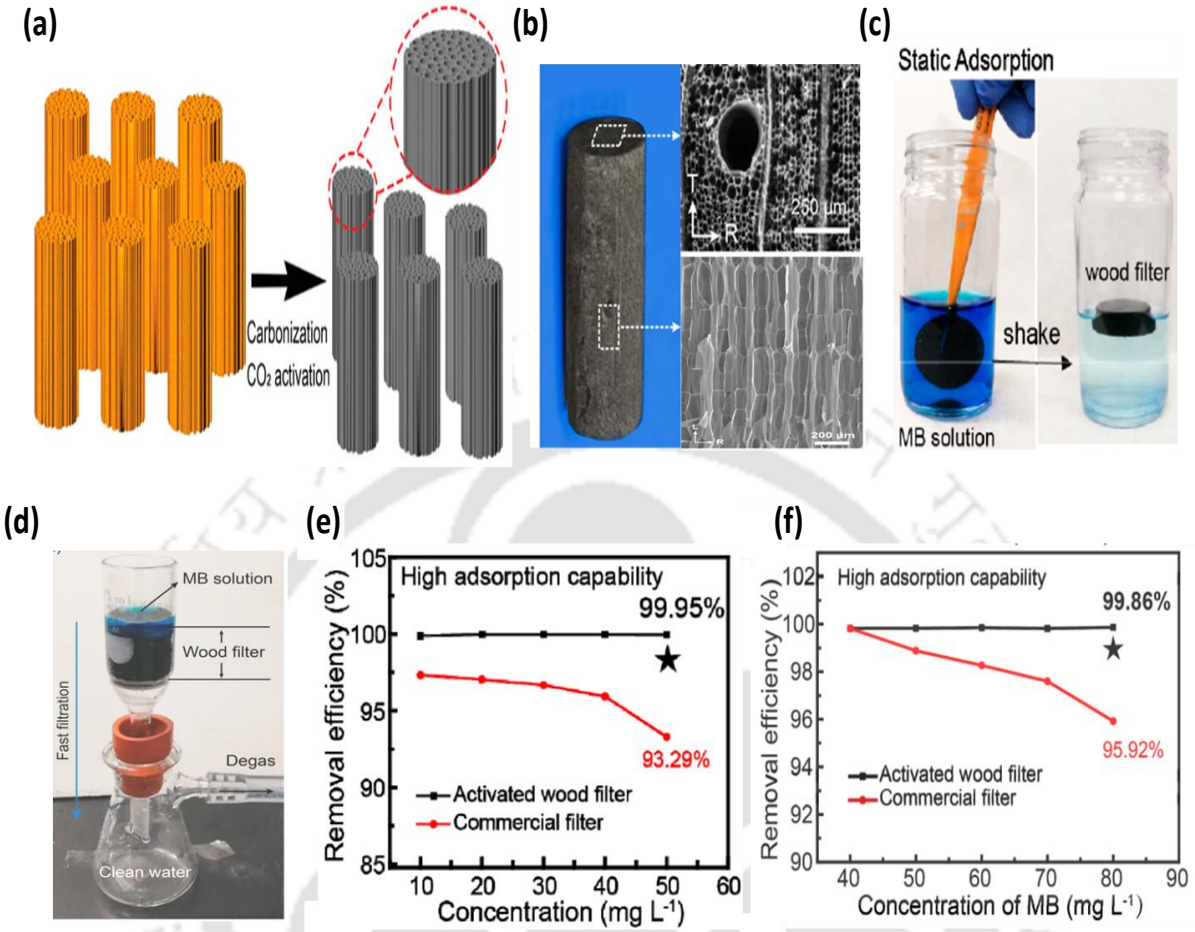

Fig. 4.14: Wood-based reusable filter for water treatment: (a) Schematic showing the fabrication of the 3D-activated wood filter from natural wood via carbonization. (b) Photograph of the novel 3D wood filter and corresponding SEM image showing its porosity. (c) static adsorption of MB onto the wood filter. (d) The dynamic adsorption setup for the wood-based filter. (e) The removal efficiency of the MB solution at various concentrations under static conditions. (f) The removal efficiency of the wood filter and commercial filter at different concentrations of the MB solution, under dynamic condition. (Image copied from *ACS Materials Lett.* 2020, **2**, 430.)

4.2.3.2: Solar steam generation:

The solar steam generation process, which is similar to the natural water cycle, is considered a promising approach to mitigating global water scarcity issues. In a typical solar steam generation process, saltwater is heated inside a desalination chamber by utilizing the sun's intensity, transferring the liquid water molecules into the vapour phase. As it is heated, the water vapour rises to the top of the chamber, gets condensed into its wall, and finally collected

as freshwater deprived of any salty impurities. In recent days, the use of new innovative materials such as graphene, plasmatic nanoparticles, and amorphous carbon has advanced solar-driven water desalination and help in achieving new milestones.[32-36] However, there are still some challenges such as complex device fabrications, high material cost, and short-time stability of the device that need to be addressed to fully functional the solar steam generation process. Therefore, research efforts have been carried out to incorporate inexpensive and naturally abundant materials that can flourish the economic viability of the overall solar steam generation process. In this context, bio-derived materials have the intrinsic ability to outperform conventional materials, abundant, environmentally friendly, and possess excellent mechanical robustness. More importantly, bio-derived materials contain numerous hydrophilic micro/nanochannels that felicitate ultra-fast transportation of water. They also benefit from the low thermal conductivity along the channel axis, which provides excellent thermal management in solar steam generation.[37,38]

Inspired by the tree function, Zhu *et al*. demonstrated a bilayer structure of natural basswood as a high-performance solar steam generator.[39] The tree-inspired design of bilayer wood is achieved via top surface carbonization of natural balsa wood, where the hierarchical mesostructure of wood is retained at the carbonized portions. Now the carbonized surface can act as a light absorption layer capable of harvesting 99% of the incident light due to 3D absorption effects. The wood matrix possesses numerous hydrophilic aligned mass transport conduits that can effectively pump water vertically in the tree growth direction. The bilayer wood-based evaporator enables fast water evaporation from different ground sources such as soil and sand, and as well as from sea surface. Extraction of groundwater from sand and soil occurs with an evaporation rate of 11 kg m^{-2} h^{-1} and in the extracted water ion concentration values meet the WHO and the US EPA standards.

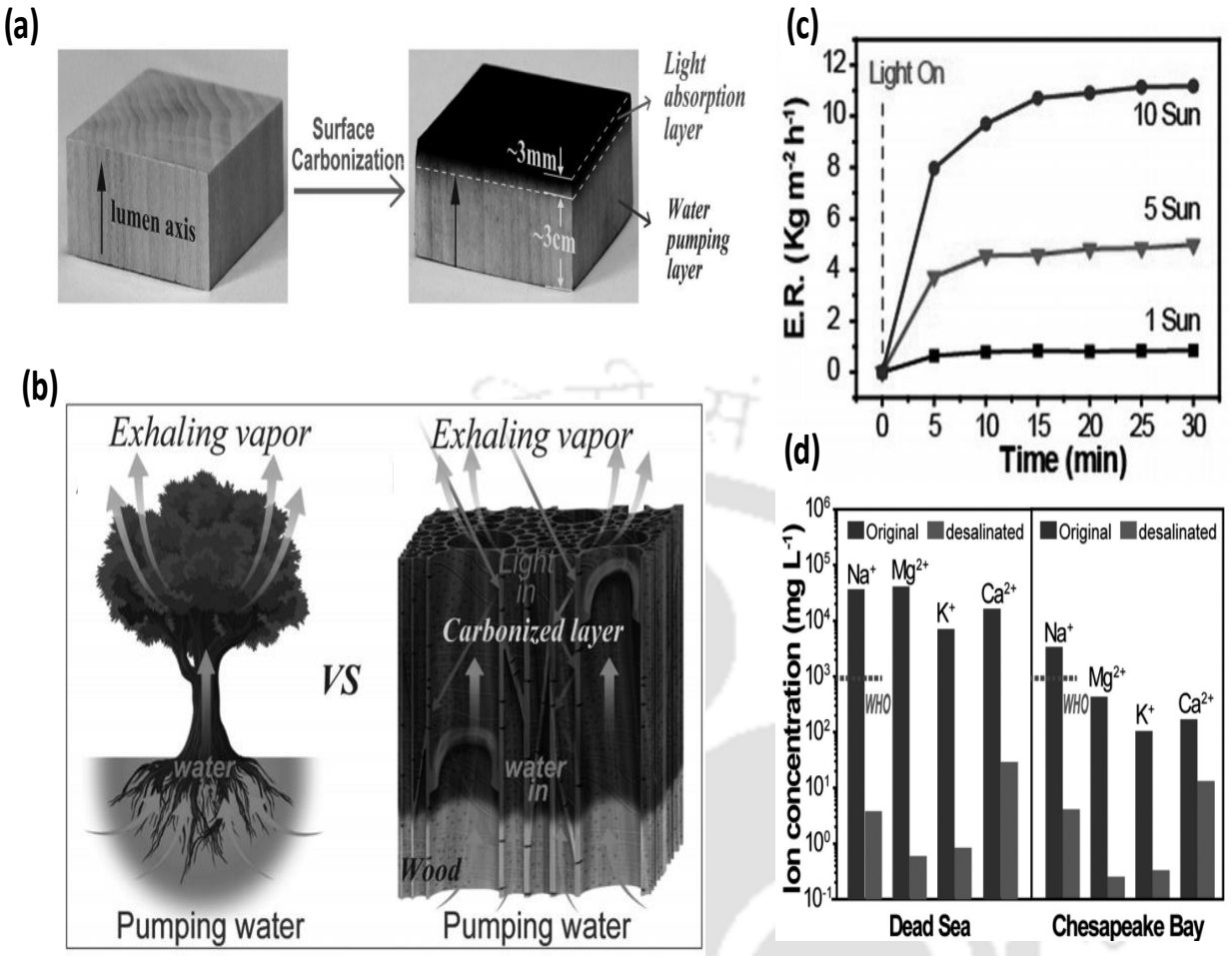

Fig. 4.15: Tree-inspired design for high-efficiency water extraction: (a) The fabrication process used to create bilayer wood via surface carbonization of natural balsa wood. (b) Illustration of the tree-inspired design using a bilayer wood structure. (c) Water evaporation rate through the bilayer wood shows a function of time at different light intensities. (d) Concentration of different ions present in the seawater sample before and after evaporating through the bilayer wood. (Image copied from *Adv. Mater*. 2017, **29**, 1704107.)

Xu *et al.* designed an efficient solar steam-generation device based on carbonized mushrooms.[40] The solar steam generation property of the carbonized mushroom can be relating to its unique structural properties that exhibit excellent light absorption, proper thermal management with heat loss minimization, efficient water supply to the evaporating surface, and high vapour escaping rate. Experiment with carbonized mushroom shows its true potential as a low-cost solar steam generator with a high water evaporation rate of 1.5 Kg m^{-2} and inspire the future development of excellent solar thermal conversion devices from bio-derived materials.

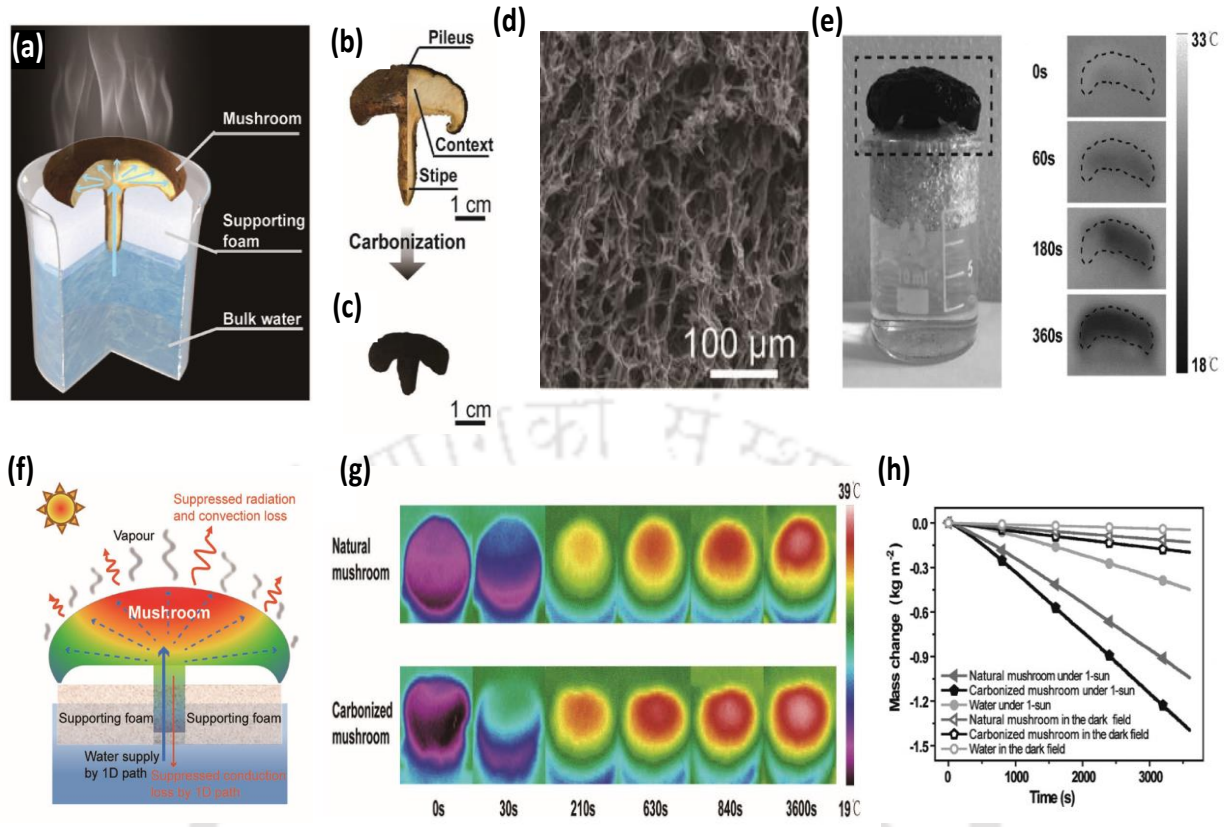

Fig. 4.16: Mushrooms as efficient solar steam generator: (a) Schematic of a mushroom based solar steam-generation device. Physical picture of a mushroom (b) before and (c) after carbonization. (d) SEM image of the pileus portion of carbonized mushroom. (e) Digital image of the mushroom based steam generator (left) and the corresponding infra-red images showing its hydrophilicity. (f) Schematic of the heat behaviour in a mushroom-based structure. (g) Infrared photos of the natural and carbonized mushroom surfaces on exposure to sunlight. (h) Mass change of water over time in the dark field and under 1 sun illumination. (Image copied from *Adv. Mater*., 2017, **29**, 1606762.)

Zhang *et al.* reported a highly efficient solar-steam generation device fabricated from reduced graphene oxide (rGO) and silk fabric.[41] The unique structure of the silk fabric and the broadband absorption capacity of rGO allowed the rGO-silk hybrid fabric to absorbed light in a broad range wavelength from 300 to 2500 nm. Again, benefitting from the capillary effect and excellent air permeability, the rGO-silk hybrid system shows excellent water evaporation efficiency, which approaches as high as 1.48 kg m^{-2} h^{-1} under one sun illumination. Moreover, the rGO-silk hybrid system displayed remarkable mechanical and aqueous stability, demonstrating its excellency as a low-cost, durable, and portable solar-steam generator.

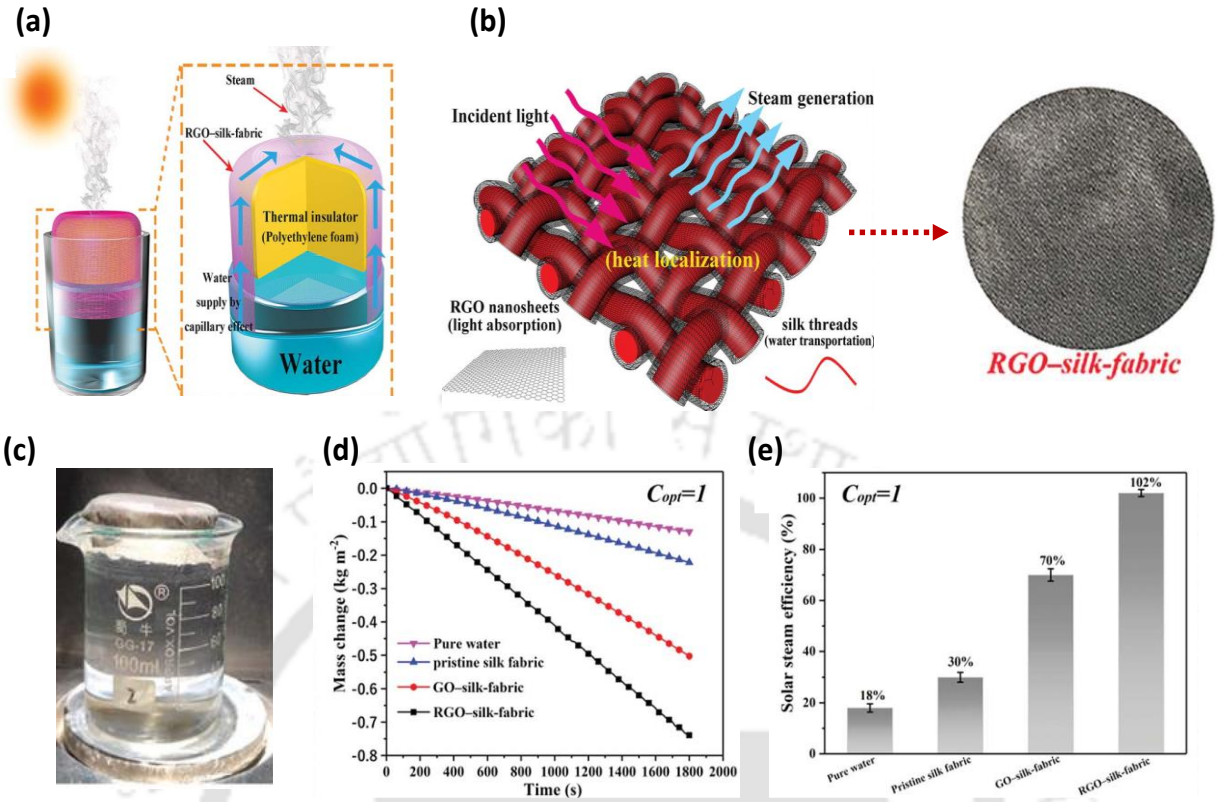

Fig.4.17: Silk-based solar steam generator: (a) schematic diagrams of the silk-based solar steam device. (b) Digital image of an rGO-silk-fabric and its steam generation mechanism. (c) steam generation under solar irradiation through rGO-silk-fabric. (d) Mass loss of pure water through different fabric composite under one sun illumination. (e) Comparison of average solar steam-generation efficiency. (Image copied from *J. Mater. Chem. A*, 2018, **6**, 17212.)

Liu *et al.* reported a scalable steam-generation device based on surface carbonized longitudinal wood integrated with a reverse-tree design.[42] The design is reversed to the natural tree because water transportation in this particular design occurred in the cross-plane direction opposite to what happens in a natural tree. The device was fabricated via cutting natural wood along the longitudinal direction, followed by subsequent surface carbonization. The hierarchical micro/nanochannels in the wood matrix enable fast water transpiration and provide adequate thermal management via minimizing heat loss. So a much lower thermal conductivity of 0.11 $Wm^{-1}K^{-1}$ was achieved with reverse tree design, which is 33% smaller than that of horizontally cut wood. Again, the carbonized surface of the wood can absorb incident light with near perfection and an appreciable water evaporation rate of 1.2 kg m^{-2} h^{-1} is achieved under one sun illumination.

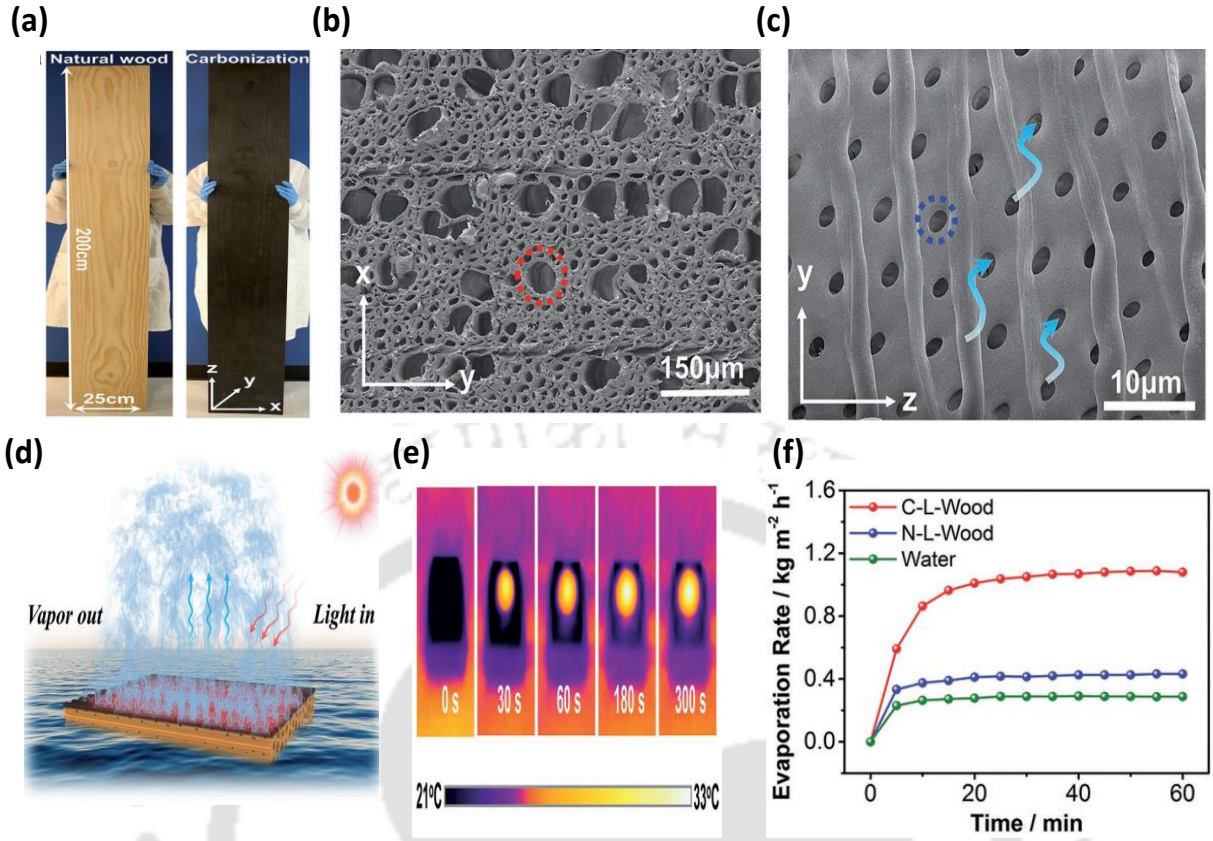

Fig. 4.18: Artificial tree with a reversed design for solar steam generation: (a) Digital image of natural wood (left) and carbonized wood (right). SEM images (b) showing the hierarchical channels in carbonized wood along the growth direction and (c) the nano-porous pits present in the cell wall. (d) Reverse-tree design of carbonized wood-based solar steam generator. (e) IR images of the carbonized wood showing the temperature rise under one sun illumination. (f) Water evaporation rate through different wood systems showing as a function of time. (Image copied from *Adv. Energy Mater*., 2018, **8**, 1701616.)

4.3: Conclusion

The ever increasing necessities of well-equipped smart electronic gadgets lead to the continuous up-gradation of the existing equipment and hence a rising environmental concern to be reckoned with a fresh mountain of outdated devices. In recent days, tremendous attention has been paid to the utilize biogenic materials in different branches of applied science and engineering including in the field of applied nanofluidics. Bio-derived materials are abundant, renewable, and environmentally friendly, which can mitigate the environmental challenges associated with the disposal of artificial machinery. Moreover, enriched with numerous charged nano capillaries, bio-derived materials show characteristics of nanofluidic phenomena

analogous to 2D nanomaterials, enabling them to utilize in the nanofluidic study as an alternative to artificial devices. However, there are certain hurdles such as relatively low output performance and the short time stability of bio-derived nanofluidic devices need to be overcome in this area. Hence, extensive research is obligatory towards an ecological approach to develop cost-effective and environmental friendly intelligent nanofluidic devices.

4.4: References:

1. P. Tseng, B. Napier, S. W. Zhao, A. N. Mitropoulos, M. B. Applegate, B. Marelli, D. L. Kaplan and F. G. Omenetto, *Nat. Nanotechnol*., 2017, **12**, 474.
2. J. Jin, P. Hassanzadeh, G. Perotto, W. Sun, M. A. Brenckle, D. Kaplan, F. G. Omenetto and M. Rolandi, *Adv. Mater.*, 2013, **25**, 4482.
3. S. Ling, D. L. Kaplan and M. J. Buehler, *Nat. Rev. Mater*., 2018, **3**, 18016.
4. P. Gatenholm and D. Klemm, *MRS Bull*., 2010, **35**, 208.
5. J. Moon, A. Martini, J. Nairn, J. Simonsen and J. Youngblood, *Chem. Soc. Rev*., 2011, **40**, 3941.
6. C. Wang, S. Wang, G. Chen, W. Kong, W. Ping, J. Dai, G. Pastel, H. Xie, S. He and S. Das, *Chem. Mater*., 2018, **30**, 7707.
7. G. Q. Xu, L. Gong, Z. Yang and X. Y. Liu, *Soft Matter*, 2014, **10**, 2116.
8. L. L. Lv, X. S. Han, L. Zong, M. J. Li, J. You, X. C. Wu and C. X. Li, *ACS Nano*, 2017, **11,** 8178.
9. W. Xin, H. Xiao, X. Kong, J. Chen, L. Yang, B. Niu, Y. Qian, Y. Teng, L. Jiang and L. Wen, *ACS Nano*, 2020, **14**, 9701.
10. R. Ajdary, B. L. Tardy, B. D. Mattos, L. Bai and O. J. Rojas, *Adv. Mater*., 2020, 2001085.
11. L. Chen, J. Zhu, C. Baez, P. Kitin and T. Elder, *Green Chem*., 2016, **18**, 3835.
12. H. Bian, L. Chen, R. Gleisner, H. Dai and J. Zhu, *Green Chem*., 2017, **19**, 3370.

13. I. A. Sacui, R. C. Nieuwendaal, D. J. Burnett, S. J. Stranick, M. Jorfi, C. Weder, E. J. Foster, R. T. Olsson andJ. W. Gilman, *ACS Appl. Mater. Interfaces*, 2014, **6**, 6127.

14. W. Kong, C. Wang, C. Jia, Y. Kuang, G. Pastel, C. Chen, G. Chen, S. He, H. Huang, J. Zhang, S. Wang and L. Hu, *Adv. Mater.*, 2018, **30**, 1801934.

15. T. Li, S. X. Li, W. Q. Kong, C. J. Chen, E. Hitz, C. Jia, J. Q. Dai, X. Zhang, R. Briber, Z. Siwy, M. Reed and L. B. Hu, *Sci. Adv.* 2019, **5**, No. eaau4238.

16. T. Li, X. Zhang, S. D. Lacey, R. Mi, X. Zhao, F. Jiang and Y. Yao, *Nat. Mater*., 2019, **6**, 608.

17. W. Kong, T. Li, C. Chen, G. Chen, A. H. Brozena, D. Liu, Y. Liu, C. Wang, W. Gan, S. Wang, S. He and L. Hu, *Chem. Mater*. 2019, **31**, 9288.

18. W. Yang, X. Li, X. Han, W. Zhang, Z. Wang, X. Ma, M. Li and C. Li, *Nano Energy*, 2020, **71**, 104610.

19. Q. Wu, C. Wang, R. Wang, C. Chen, J. Gao, J. Dai, D. Liu, Z. Lin and L. Hu, *Adv. Energy Mater.*, 2019, **10,** 1902590.

20. W. Xin, Z. Zhang, X. Huang, Y. Hu, T. Zhou, C. Zhu, X.-Y. Kong, L. Jiang and L. Wen, *Nat. Commun*., 2019, **10**, 3876.

21. Z. Wu, P. Ji, B. Wang, N. Sheng, M. Zhang, S. Chen and Wang, H. *Nano Energy* 2021, **80**, No. 105554.

22. S. H. Joo and B. Tansel, *J. Environ. Manage*., 2015, **150**, 322.

23. M. Ersahin, H. Ozgun, R. Dereli, I. Ozturk, K. Roest and J. van Lier, *Bioresour. Technol*., 2012, **122**, 196.

24. A. J. H. Pieterse and A. Cloot, *Water Sci. Technol*. 1997, **36**, 111.

25. M. M. Shirazi and A. Kargari, *J. Membr. Sci. Res.* 2015, **98**, 101.

26. Y. Lin, H. Xu, X. Shan, Y. Di, A. Zhao, Y. Hu and Z. Gan, *J. Mater. Chem. A*, 2019, **7**, 19203.

27. S. J. Ling, Z. Qin, W. W. Huang, S. F. Cao, D. L. Kaplan and M. J. Buehler, *Sci. Adv.*, 2017, **3**, e1601939.

28. 8 Z. Yang, H. Liu, J. Li, K. Yang, Z. Zhang, F. Chen and B. Wang, *ACS Appl. Mater. Interfaces*, 2020, 12, 15002.

29. F. Chen, A. S. Gong, M. Zhu, G. Chen, S. D. Lacey, F. Jiang, Y. Li, Y. Wang, J. Dai, Y. Yao, J. Song, B. Liu, K. Fu, S. Das and L. Hu, *ACS Nano*, 2017, **11**, 4275.

30. M. Jiao, Y. Yao, C. Chen, B. Jiang, G. Pastel, Z. Lin, Q. Wu, M. Cui, S. He and L. Hu, *ACS Mater. Lett.*, 2020, **2**, 430.

31. J. Zhou, Y. Gu, P. Liu, P. Wang, L. Miao, J. Liu, A. Wei, X. Mu, J. Li and J. Zhu, *Adv. Funct. Mater.*, 2019, **29**, 1903255.

32. Z. Deng, J. Zhou, L. Miao, C. Liu, Y. Peng, L. Sun and S. Tanemura, *J. Mater. Chem. A*, 2017, **5**, 7691.

33. V. D. Dao and H. S. Choi, *Global Chall.*, 2018, **2**, 1700094.

34. X. Wang, Y. He, X. Liu, L. Shi and J. Zhu, *Sol. Energy*, 2017, **157**, 35.

35. X. Hu, W. Xu, L. Zhou, Y. Tan, Y. Wang, S. Zhu and J. Zhu, *Adv. Mater.*, 2017, **29**, 1604031.

36. M. Zhu, Y. Li, F. Chen, X. Zhu, J. Dai, Y. Li, Z. Yang, X. Yan, J. Song, Y. Wang, E. Hitz, W. Luo, M. Lu, B. Yang and L. Hu, *Adv. Energy Mater.*, 2018, **8**, 1701028.

37. C. Jia, F. Jiang, P. Hu, Y. Kuang, S. He, T. Li, C. Chen, A. Murphy, C. Yang and Y. Yao, *ACS Appl. Mater. Interfaces*, 2018, **10**, 7362.

38. M. W. Zhu, Y. J. Li, G. Chen, F. Jiang, Z. Yang, X. G. Luo, Y. B. Wang, S. D. Lacey, J. Q. Dai, C. W. Wang, C. Jia, J. Y. Wan, Y. G. Yao, A. Gong, B. Yang, Z. F. Yu, S. Das and L. B. Hu, *Adv. Mater*., 2017, **29**, 1704107.

39. N. Xu, X. Hu, W. Xu, X. Li, L. Zhou, S. Zhu and J. Zhu, *Adv. Mater*., 2017, **29**, 1606762.

40. Q. Zhang, X. Xiao, G. Wang, X. Ming, X. Liu, H. Wang, H. Yang, W. Xu and X. Wang, *J. Mater. Chem. A*, 2018, **6**, 17212.

41. H. Liu, C. Chen, G. Chen, Y. Kuang, X. Zhao, J. Song, C. Jia, X. Xu, E. Hitz, H. Xie, S. Wang, F. Jiang, T. Li, Y. Li, A. Gong, R. Yang, S. Das and L. Hu, *Adv. Energy Mater*. 2018, **8**, 170161.

Chapter 5

Disposable Fluidic Devices of Bio-nanochannels for Enzymatic Energy Harvesting

Summary*

Nature produces a plethora of nanochannels to carry out highly complex biological tasks in a sophisticated manner. There have been several studies to understand the characteristics of these channels; however, efforts to apply them for technological advancements are still scarce. Here, we have demonstrated that the fluidic channels of biomaterials can be harvested as nanofluidic devices to produce energy from enzymatic chemical reactions. The bio-nanochannels-based nanofluidic devices exhibit various nanofluidic phenomena like surface-charged-governed ionic conductivity and thereby help in the development of transmembrane potential. The mobility of ions in the hydrated bio-nanochannels is found to be higher than that of bulk water. The cation-selective nature of bio-channels was also exploited to harvest a continuous supply of power up to 74 mWm^{-2} for 3 hours from the enzymatic decomposition of urea. The transmembrane potential across the bio-channels was also explored for level-free electrical monitoring of enzymatic reactions inside the biological medium. Electrical monitoring on the kinetics of urease at different reaction temperatures suggested that inside the biological medium, the reaction goes through a pathway of lower activation energy (31.1 KJ) than that in the bulk environment (34.1 KJ). Enzyme urease was found to be more sustainable in bio-nanochannels than that in the glass vials.

---

* Paper based on these studies has appeared in *ACS Appl. Bio Mater.* 2019, **2**, 2549.

5.1: Introduction

Solanum tuberosum or Potato is one of the most widely used staple foods globally. It exhibits exciting internal features in the micro and nanometer regime, just like any other biological system.[1,2] It also possesses a highly active fluidic network across the cell walls to facilitate communications and transport of materials between the plant cells. The transport pathways of plants are divided into two types, the "living symplastic pathway" and "dead apoplastic pathway" [3] In the symplastic pathway, movement of masses from one cell to another occurs through the plasmodesmata. These narrow channels act as an intercellular cytoplasmic gate between the cells. While in the active or regulated transport, plasmodesmata dilate to accommodate much larger macromolecules or viruses through a set of precise and complex molecular interactions, in the passive mode, it possesses a size exclusion limit of ~ one kDa (2 - 3 nm^2). In the apoplastic pathway, the mass is transported through narrow interfibrillar and intermicellar space of the cell walls and channels formed between the adjacent cell units[4-7]. Carpita *et al.* and Marchner *et al.* demonstrated that the nature of molecular/ionic transport through the narrow (3-5 nm) channels of cell wells are *not free* or *bulk-like*; it is strongly influenced by the interactions with the non-diffusible anions of the cell wall, like carboxyl groups of galacturonic acids of the pectins.[8,9] Motivated by the interesting nanofluidic properties of biological nanochannels, tremendous research efforts have been devoted to preparing artificial nanochannels involving various expensive and sophisticated instrumentation. However, the abundant nanofluidic channels ubiquitous in the biological systems around us have not been considered yet for technological applications. Here, as proof of the concept, the intracellular transport pathways of raw Potato are harvested as biodegradable nanofluidic devices to produce energy from enzyme-catalyzed chemical reactions. The Potato derived nanofluidic channels are also exploited to study the kinetics of

enzymatic reaction inside the biological medium.

5.2: Scope of the present investigation

While artificial devices and machinery provide countless conveniences to modern life, their disposals are creating major havoc in the environment.[10] Therefore, in recent years, numerous research efforts are being dedicated to replacing unsustainable materials and devices with environmentally benign alternatives of similar functionalities. For example, different kinds of electronic devices such as solar cells, diagnostic tools, sensors, electrochromic displays, artificial tissues, etc.[11-15] have been developed based on sustainable materials obtained from the environment. Similarly, the outstanding new properties of liquids confined inside nanometer-sized containers promise numerous technological breakthroughs in water treatment, energy harvesting, and molecular sieving.[16-19] Studies on confined liquid also open up an avenue to understand the activity of biological nanochannels creating a platform to exploit them for various biomedical and chemical applications.[20,21] However, little effort has been put forward to utilized these excellent properties of biological channels in nanofluidic applications. In the present chapter, we have extracted biological nanochannel from potato tuber, which is cost-effective, environmentally friendly, and possesses intracellular transport pathways with define surface charges. The presence of numerous nanofibrils in the bio-derived nanochannels avoids additional sophisticated nano fabrications techniques such as lithography, ion etching, nano-pattering, etc. This provides a much easier and cheaper platform to study nanofluidic phenomena equal footing to its artificial analogs. The dense surface charges on the biological nanochannel walls show excellent perm selective behaviour and provide a way to harvest electricity from salt concentration gradient and ionic gradient induced by enzymatic decomposition reaction of bio-waste. Moreover, the generated trans-membrane voltage in the enzymatic reaction also makes it possible to trace enzymatic reaction kinetics in a label-free

manner. Looking at the large variety of nanofluidic channels designed by nature to carry out highly complex biological tasks very sophisticatedly, it should be possible to create/develop different kinds of nanofluidic devices for future applications.

5.3: EXPERIMENTAL SECTION

Surface charge governed ionic transport:

Nanofluidic devices of potato bio-channels were fabricated by embedding strips of the freeze-dried potato tubers of known dimensions in PDMS elastomer. The ends of the strips were exposed to electrolyte solutions by carving out reservoirs on the PDMS stub at either end of the strip. Ag/AgCl electrodes connected to the terminals of a Keithley source meter (Model: 2450) were immersed in the reservoirs filled with electrolytes at both ends of the strip. Representative *I-V* curves for potato stripes were recorded at different electrolyte concentrations ranging from 10^{-6} M to 1 M by sweeping voltage from -0.5V to 0.5 across each strip. Conductivity calculations were done by using the following equation:

$$C = G \times \text{cell constant}$$

Where C is the conductivity, G is the conductance.

Enzyme sustainability measurement:

Multiple strips of freeze-dried potatoes of similar dimensions were soaked with identical amount of urease solutions (300 µL, 1 mg/ml) and stored in a hydrated environment. After every 24 hours, 1 ml urea was injected into one of the urease soaked potato strips. Enzymatic decomposition of urea release ammonium ions, which was sensed by introducing a dilute solution of Nessler reagent. The initially colourless solution of ammonium ion turns into light yellow upon addition of Nessler reagent. The concentration of ammonium ion produced during the enzymatic decomposition was quantified from the absorbance values of the Millon's base

$HgO.Hg(NH_2)I$ in UV-Vis spectroscopy. Simultaneously, several glass vials containing 300 µL of 1 mg/ml urease solutions were stored separately, and activity of the same was determined by the same method and compared with the samples stored in the biological channels.

Characterization:

The potato samples were lyophilized with the help of Labconco Freezone 4.5 liter-50C Benchtop freeze dryer. The morphology of the potato samples was characterized by field emission scanning electron microscope (FESEM) (Zeiss, Model: Sigma). All the electrochemical measurement was performed with the help of a source meter (Keithley 2450 model). The concentration of the coloured complex $HgO.(HgNH_2)I$ was determined by using a UV-Vis spectrophotometer (Systronics, UV-VIS Spectrophotometer 117).

5.4: Results and discussion

In order to harvest nanofluidic channels of the biological system, rectangular pieces of raw potato were first dipped into liquid nitrogen, which was followed by sublimation of the frozen solvents under ultrahigh vacuum in a lypholizer instrument. After 24 h of lypholization, potato pieces were examined under electron microscopes and preserved in a desiccator until further use. A field emission scanning electron microscopic (FESEM) image of the cross-section of freeze dried potato is shown in Fig. 5.1b. The three major components of potato tissues, viz., cortex, storage parenchyma, and pith, are composed of tightly packed isodiametric cells, and hence under electron microscope it appears as a network of tightly packed polygonal cells. The tiny oval shaped structures (~3-50 µm) seen in the parenchyma cellular compartments are the starch granules, the most important energy reservoir of the plants[22] (Fig. 5.1b). Nanofluidic devices of bio-channels were fabricated by immersing freeze dried pieces of potato (dimensions ~ $20 \times 4 \times 0.5$ mm^3) in a freshly prepared polydimethylsiloxane (PDMS) elastomer

solution. After curing the elastomer at 60 °C, two reservoirs of about 0.6 mL in volume were carved out to expose both the ends of the potato strips to electrolyte solutions (Fig.5.1c). The as-prepared nanofluidic devices were then soaked in deionized water for 1 day to ensure complete re-hydration of the bio-channels. After hydration, the reservoirs were filled with

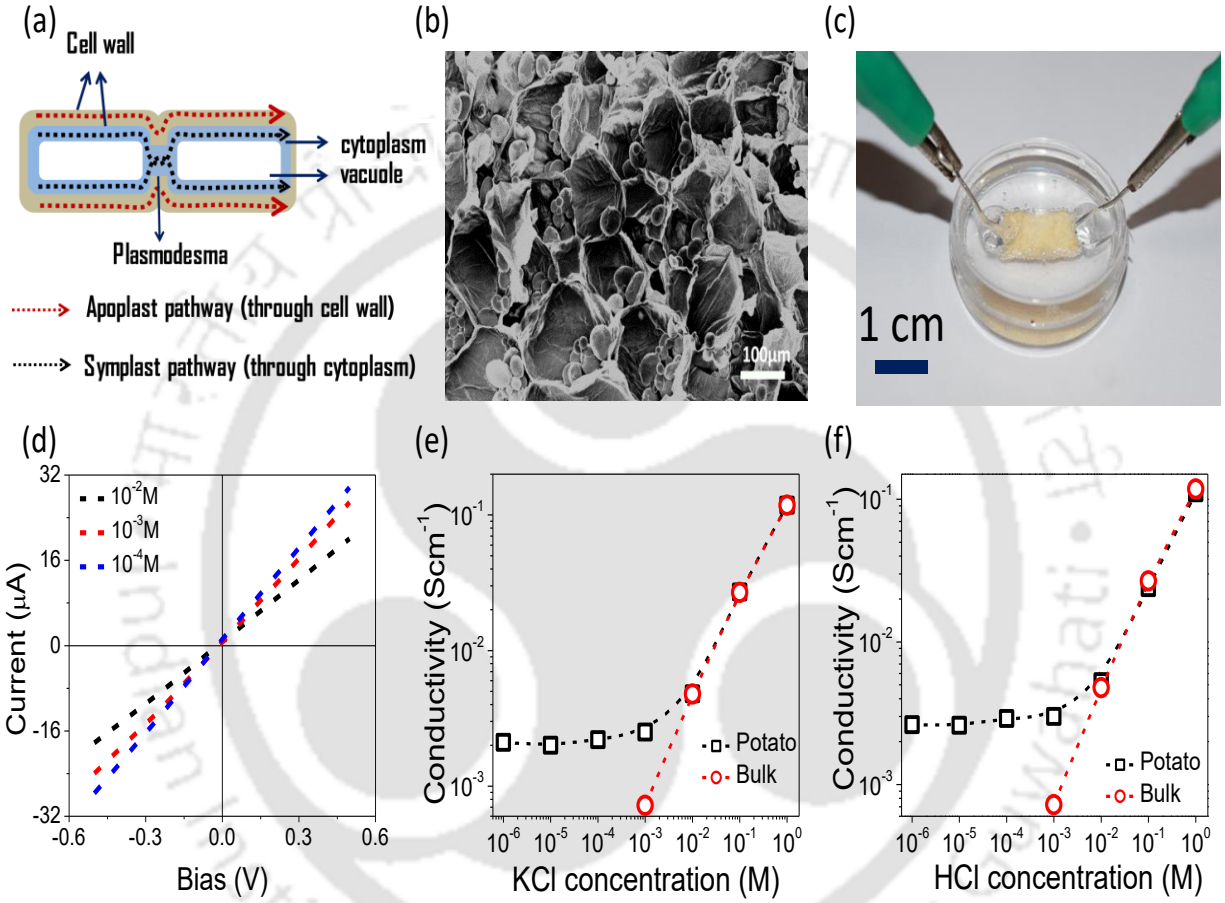

Fig. 5.1: Bio-derived nanofluidic system: (a) Schematic illustration of the ion transportation pathways in the plant cell. (b) FESEM image of the cross-section of freeze dried potato sample. (c) Digital image of the nanofluidic device, (d) *I-V* curves recorded through bio-nanochannels of Solanum tuberosum. The ionic conductivity of bio-nanofluidic device with different concentration of (e) KCl, and (f) HCl.

electrolyte solutions of known concentrations and allowed for 6 hours to reach the equilibrium. The ionic current through the bio-channels were measured through Ag/AgCl electrodes inserted into the reservoirs by employing a Keithley 2450 source meter instrument. Fig. 5.1d shows the *I-V* curves recorded through a potato device with different concentrations of KCl. The linearity in the *I-V* curve confirms the presence of continuous network of hydrated

channels throughout the potato tuber. The ionic conductivity of the nanofluidic device was calculated by normalizing the slope of the *I-V* curves with the overall dimensions of the potato strip, that is length (l), width (w), and thickness (t) of the rectangular pieces used for the device fabrication. In Fig. 5.1e, conductivity values calculated for potato strip are compared with that of bulk solutions as a function of KCl concentration. As typical artificial nanofluidic devices, bio-channels of potato strip also shows the characteristics of surface-charged-governed ionic conductivity. At the high concentration regime (10^{-2} M to 1 M), the conductivity values increase linearly with that of salt concentration, but at the low concentration regime (10^{-3} M to 10^{-6} M) it did not change even for orders of magnitude change in the salt concentration. On the contrary, in the bulk water conductivity decreases linearly with decreasing salt concentration. Such drastic different behaviour of water molecules inside the biological systems from that of bulk water was also predicted by Sahu *et al.* and Esch *et al.*[23, 24] The walls of plant cells are made up of various polymeric materials with negative surface charges such as cellulose, hemicelluloses, pectins and phenolics. These negative surface charges create an electrical double layer by attracting the co-ions and repelling the counter ions. When Debye lengths of the channel surfaces overlaps, the concentration of ions inside the channels is determined by the surface charge density of the surrounding walls, not by the concentration of the reservoirs, leading to the surface-charged-governed ionic conductivity.[25,26] The existence of surface-charged-governed ionic conductivity not only confirmed successful construction of the bio-channel based nanofluidic devices but also indicated absence of large interconnected macrospores inside the freeze-dried potato. In order to further confirm, the HCl conductivity of bio-channels was also measured as a function of time. As shown in Fig. 5.1f, for protons also bio-nanofluidic device displayed the characteristic surface-charged-governed conductivity.

The fluidic network of potato tuber contains a range of nanochannels of different sizes and shapes with specific functionalities, however, in the bio-derived nanofluidic devices it is important to know the combined effective dimension (h_{eff}) of the nanochannels. The h_{eff} of potato tuber was determined from the transition point (C_t) of conductivity vs concentration plot, the point at which the characteristics of ionic current changes from *bulk-like* regime to surface-charged-governed regime, shown in the Fig. 5.2 From the relationship between surface charge density (σ_s) and C_t of nanofluidic channels, shown in Eqn (1), the h_{eff} of potato nanochannels were calculated to be 6 nm.[27]

$$h = \frac{10^{-3}\sigma_s}{eN_A c_t} \text{ ---------- (1)}$$

Where, N_A, and e stands for Avogadro's number and elementary charge respectively. The σ_s value of cell wall (- 2.3 mCm^{-2}) was determined by Obi *et al.* by employing electrophoresis method based on Gouy-Champman-Stern model.[28]

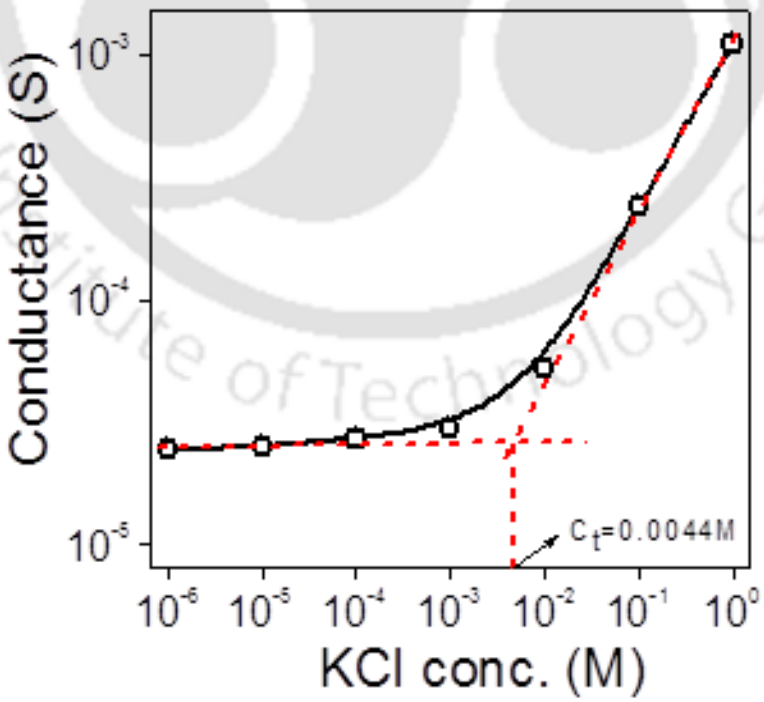

Fig. 5.2: Ionic conductance of potato nanofluidic device as a function of KCl concentration showing the transition point concentration (C_t).

The re-hydration characteristics of freeze-dried potato tuber was studied by monitoring emergence of ionic current in the otherwise insulating ion channels. As shown in the Fig. 5.3, liquid water was introduced to a rectangular strip of freeze dried potato embedded in PDMS from one side and allowed to diffuse towards the other end. Ionic current was measured at two different points (near and far end) of the potato strip to determine the rate of diffusion. At the

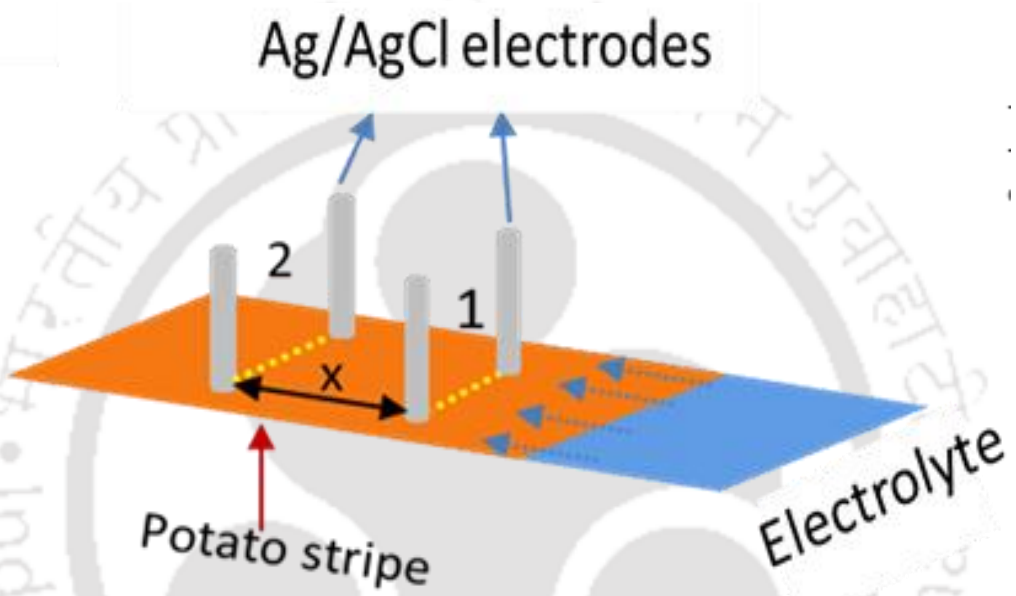

Fig. 5.3: In plane diffusivity: Schematic diagram of the experimental set-up used for the diffusivity measurement.

beginning no current was observed at either ends, however, as soon as the liquid water diffused through the strip, it hydrated the ion channels displaying a sharp rise in the current values. In Fig. 5.4, ionic current measured at the *near* and *far* end is plotted as a function of time, and the time difference between the saturation points at either ends of the potato strip is taken as the time required for water molecules to travel the distance. The diffusivity (D) of water through the freeze-dried strip were calculated to be 1.58×10^{-6} $cm^2\,s^{-1}$, from the time (t) taken by water molecules to travel the distance (x) between near and far end by using Einstein's approximation for the three dimensional diffusions, equation [29] (2).

$$x^2 = 6.D.t \text{ ---------- (2)}$$

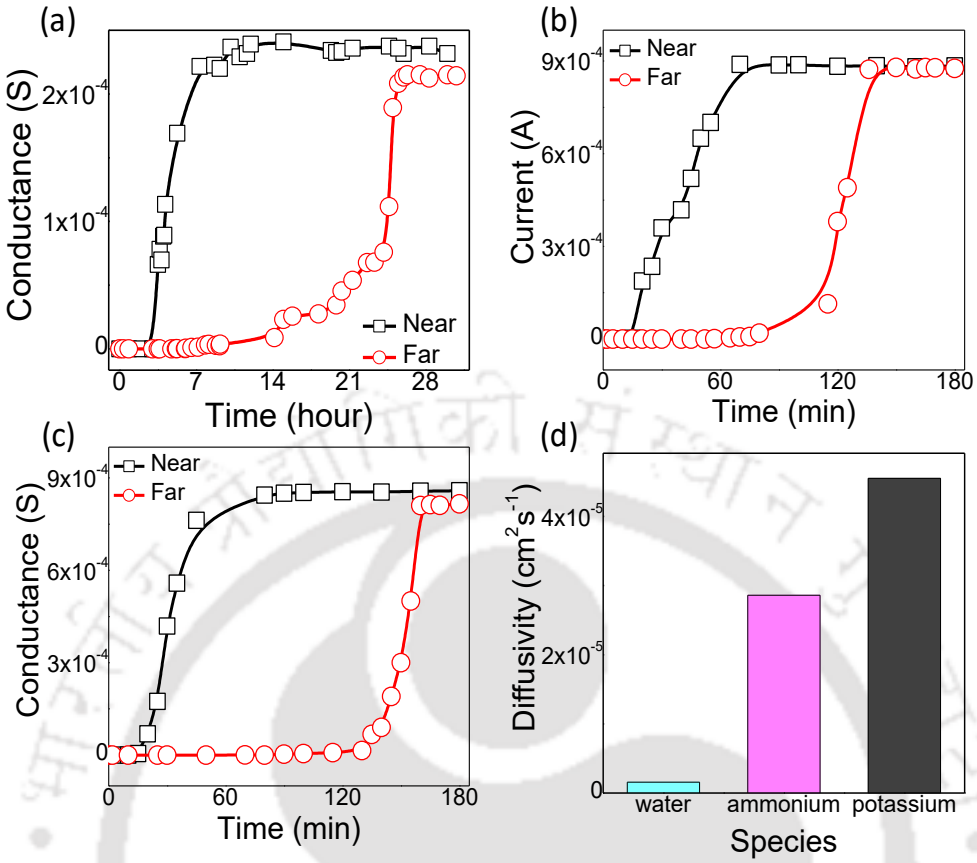

Fig. 5.4: Diffusivity of different ionic species: Development of ionic current as function of time at near and far ends of potato strip from the direction of (a) water, (b) potassium, and (c) ammonium ions reservoirs. (d) Comparison of diffusivity values for water and ions in bio-channels of potato.

The same method was also employed to determine mobility of K^+ and NH_4^+ ions by allowing 0.1 M aqueous solutions of KCl and NH_4Cl to diffuse from one end of the rehydrated potato tuber to the other end. The ionic current values recorded at the *near* and *far* ends for KCl and NH_4Cl solutions are shown in Fig. 5.4b and 5.4c, respectively. The diffusivity values of K^+ and NH_4^+ ions calculated as such was used for calculating the mobility of the ions through the potato nanochannels by employing Nernst-Einstein equation [30] (3) (Fig. 5.5a,).

$$\mu = \frac{eD}{kT} \text{ ---------- (3)}$$

Where, *k* is Boltzmann constant and T is the absolute temperature. Remarkably, the mobility of K^+ and NH_4^+ ions calculated as such are found to be higher than that in the bulk liquid.

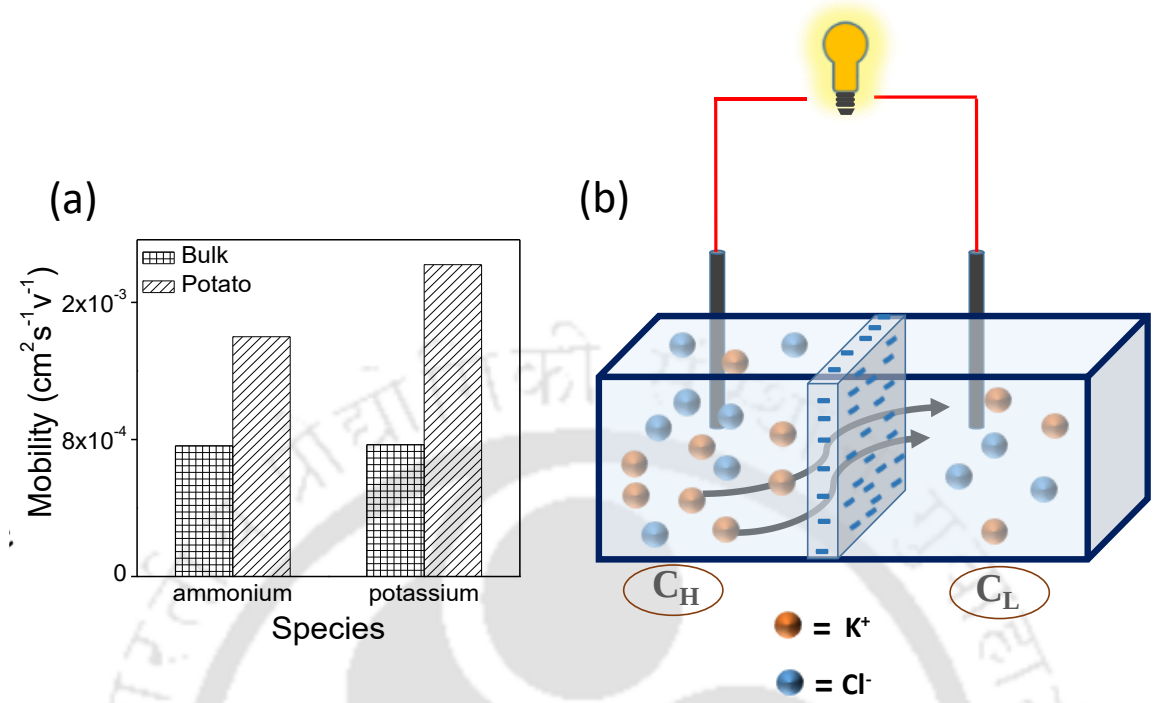

Fig. 5.5: (a) Mobility values of different ions inside bio-nanochannels are compared that with of bulk water (b) Schematic of the bio-channel based device utilized for harvesting osmotic energy.

The large number of ion selective channels readily available in freeze dried potato could have multiple applications. As a proof of concept, the same has been employed to harvest green energy from concentration difference. A device comprising of two compartments separated by a potato tuber membrane (dimension 12.5 mm^2 × 2 mm) was fabricated by using PDMS elastomer as shown in Fig. 5.5b. The high concentration compartments (C_H) were filled with KCl solutions of 1M concentration and the low concentration (C_L) chamber was filled with 10^{-3} M KCl solution. The trans-membrane potentials originating from the selective transport of the cations through the potato membranes were measured by inserting two Ag/AgCl electrodes into the reservoirs. The green curve in Fig. 5.6a shows the trans-membrane potential originating from three-fold concentration gradient across a potato membrane. The transmembrane potential developed as such declines quickly with increasing time, suggesting that the potato membrane could not hold the concentration gradient for long time. Therefore, the thickness of

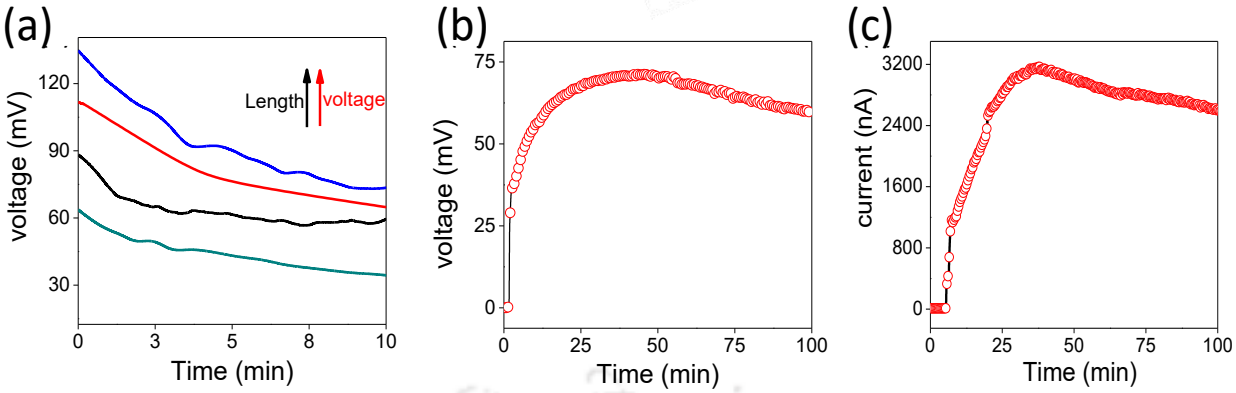

Fig. 5.6.: Energy from ionic gradient: (a) The transmembrane potential harvested from the concentration gradient across the potato membrane as a function of time. (b) The transmembrane potential, and (c) ionic current across the potato membrane developed by the enzymatic decomposition of urea by urease.

the membranes were successively increased from 2 mm to 15 mm, and a concomitant improvement in both the open circuit voltage and voltage stability were observed with the increasing membrane thickness. However, in order to get a constant voltage, supply for a longer duration it will be ideal to have a system that constantly produces ions in an environment friendly manner. For the proof of concept, a nickel-dependent metalloenzyme (urease), synthesized by plants, bacteria, and fungi is used for the constant supply of ions. When urease decomposes the substrate (urea), it produces ionic products like OH^-, HCO_3^-, and NH_4^+, which increases the conductivity of the reaction medium. It offers a convenient electrical monitoring of the enzymatic reaction. The inherent cation selectivity of potato membrane preferentially allows transport of the cations (NH_4^+) generated in the enzymatic reaction creating a potential gradient across the membrane.[18] In typical experiments, both the reservoirs were initially filled with a buffer solution (0.01 mM KCl, 1 mg/ml urease, pH 7) and waited 4 hours to ensure complete rehydration of the bio-channels. After attaining the equilibrium, 0.1 M urea was added to one of the reservoirs to carry out the enzymatic decomposition reaction. As the enzymatic reaction started producing the ions, both open circuit potential and current started rising and reached saturation after 50 minutes, see Fig. 5.6b and 5.6c. In contrast to KCl

electrolyte based concentration gradient, the open circuit potential in enzymatic reaction did not decline with time, and provided a stable power supply ~ 74 mWm^{-2}, up to the observation limit of the instrument (3 hours).

As the enzyme catalysed reactions are crucial for the functioning of numerous biological systems, several research efforts are being devoted to unveil its characteristics, both in the *in vitro* and *in vivo* conditions. While, *in vivo* studies are extremely challenging, *in vitro* studies offer the convenience of applying various analytical tools to obtain detail information about the samples. Unfortunately, the *in vitro* studies do not reflect the actual activities of enzymes inside the confinement of complex biological medium, which motivated the researchers to synthetically imitate the molecularly crowded environment inside the channels of nanofluidic devices.[31, 32] These artificial channels allow to study activities of enzymes under confinement, but it is still far from mimicking the actual conditions of biological environment. The nanofluidic devices of potato offers label-free electrical detection of enzymatic reactions under the confinement of biological nanochannels. The straightforward utilization of biological channels not only avoided the discrepancies frequently encountered in developing bio-mimicking artificial devices but also provided a physiological environment which is otherwise difficult to conserve in artificial units. Here, the transmembrane potential developed by the preferential migration of NH_4^+ ions was employed to monitor the characteristics of the enzymatic reactions inside biological medium. A potato strip embedded inside PDMS elastomer was soaked with 10^{-2} M aqueous solution of urea for 6 hours to make sure complete rehydration of the channels. After rehydration, 0.5 ml aqueous solution of urease at different concentrations (10 mM, 8 mM, 5 mM and 1mM) were injected into one end of the potato strip, as shown in the schematic Fig. 5.7a. Here, one side of the bio-nanofluidic system act as

enzymatic reaction chamber and the other part as the ion-selective membrane. The membrane potentials developed as such is shown as a function of time in Fig. 5.7b.

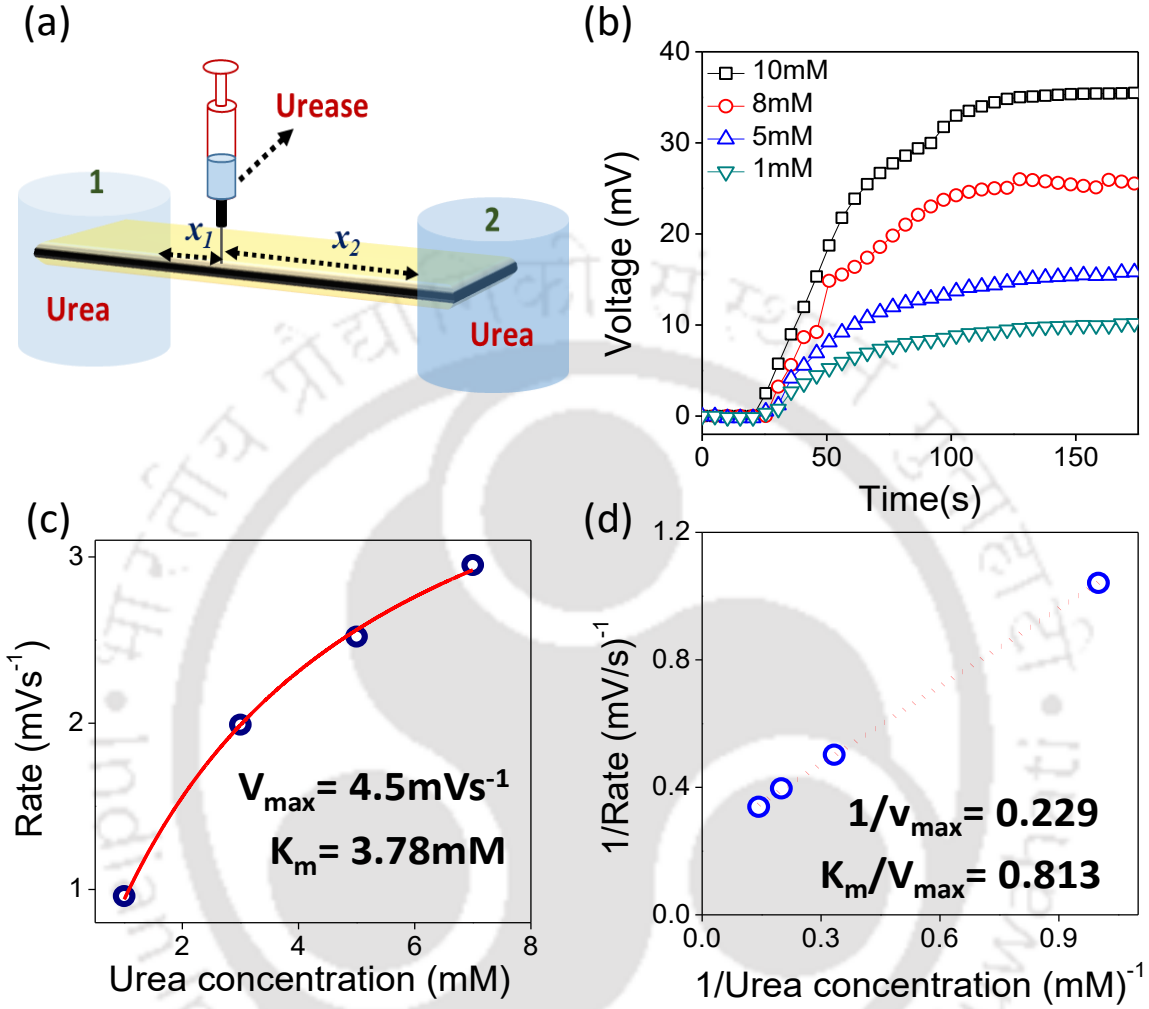

Fig. 5.7: Electrical monitoring of enzyme kinetics: (a) Schematic illustration of the bio-nanofluidic device utilized for the study of enzyme kinetics inside bio-nanochannels. (b) The open circuit voltage generated from the enzymatic reaction of urease starting with different substrate (urea) concentration. (c) Michaelis-Menten plot of initial reaction rate versus substrate concentration. (d) Lineweaver-burk double reciprocal plot of initial reaction rate vs substrate concentration. The linearization of the plot signifies the enzymatic reaction to be of first-order kinetics with respect to the substrate concentration.

Here, the rate of the potential development at different substrate (urea) concentrations can also be considered as the rate of ionic product formation. The initial reaction velocity (V_{int}) that is the mass of the product formed per unit time during the initial stage of the reaction was found to be proportional to the value of membrane potential. [33] The V_{int} values for urease catalyzed decomposition of urea for different starting concentration of substrate (urea) were obtained by

linear fit of the curves shown in Fig. 5.7c. The V_{int} values obtained as such are plotted as a function of urea concentration which follow the Michaelis–Menten equation (4).[34]

$$V = \frac{V_{max}[S]}{K_m + [S]} \quad \text{--------} \quad (4)$$

Where V_{max} represents the maximum velocity achieved by the system, [S] is the substrate concentration and K_m is the Michaelis constant. From the data shown in Fig. 5.7c the maximum reaction velocity (V_{max}) and Michaelis–Menten constant (K_m) were found to be 4.5 mVs^{-1} and 3.78 mM respectively. Similarly, a double reciprocal Lineweaver - Burk plot (Fig. 5.7d) of the initial enzymatic reaction rate vs concentration of urea was found to be linear, confirming the reaction to be of first order with respect to the substrate concentration. [33]

$$\frac{1}{V} = \frac{K_m}{V_{max}}\frac{1}{[S]} + \frac{1}{V_{max}} \quad \text{--------} \quad (5)$$

From linearization method V_{max} and K_m values were calculated to be 4.36 mVs^{-1} and 3.54 mM, respectively which are in agreement with the values obtained from Michaelis-Menten method.

The transmembrane potential was also exploited to study the effect of reaction temperature on the enzyme kinetics. Here, the trans-membrane potential developed by the preferential migration of NH_4^+ ions was employed to study enzyme kinetics at different temperature. For the temperature dependent studies, devices were prepared by encapsulating a thermometer along with potato strip into freshly prepared PDMS elastomer and cured at 60° C. The specific temperature of the reaction was maintained by placing the devices on a hot plate and the temperature was monitored by the thermometer inserted just next to the potato channels. After soaking these devices with 10^{-2} M urea solution, 0.5 ml of urease (1mg/ml) was injected to one end of the potato strip (schematic Fig. 5.8a1) and monitored the development of open circuit

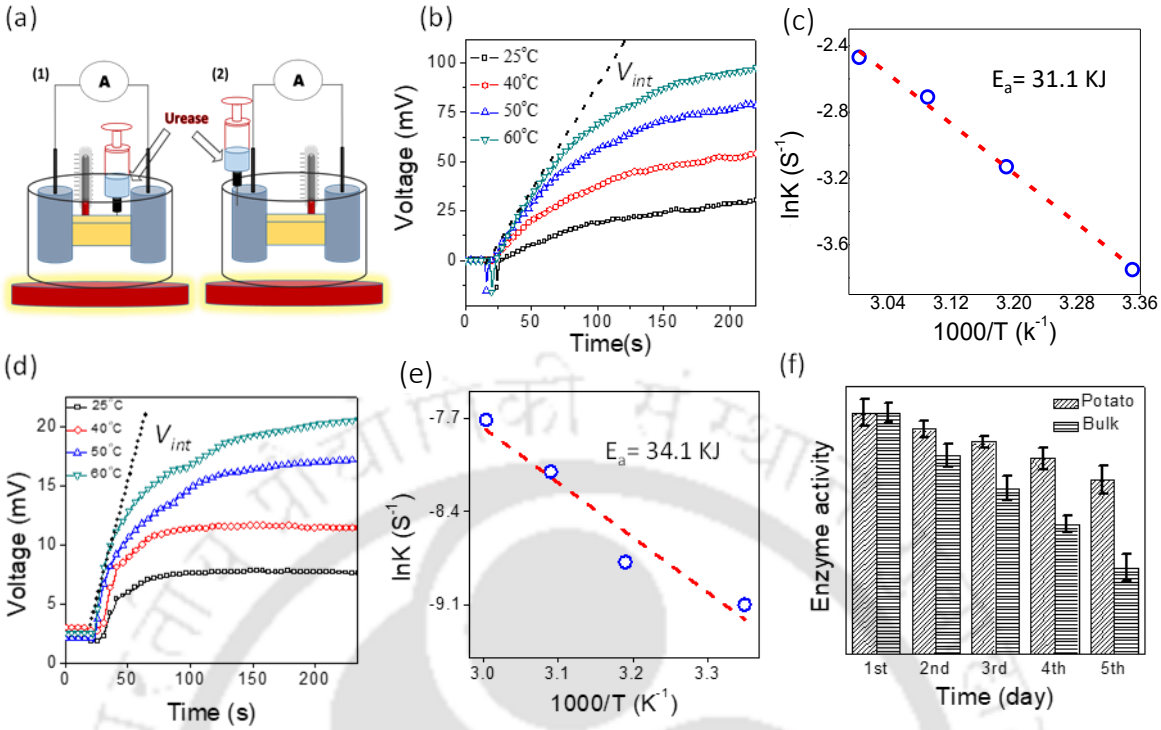

Fig. 5.8: (a) Schematic illustration of the experimental set-up used for the comparative study of enzyme kinetics. Open circuit membrane potentials developed as a function of time (b) inside versus (d) outside bio-channels at the different reaction temperature. Arrhenius plot of the rate constants for enzymatic reaction (c) inside, and (e) outside bio-channels, respectively. (f) Comparison of the activity of urease inside and outside the bio-channels as a function of time.

membrane potentials as a function of time with a source meter instrument. Fig. 5.8b shows the potential developed as a function of time at different reaction temperatures, and from the slope of the linear segments of the curves the initial rates of the urea-urease reaction was determined. As the enzymatic reaction follows 1st order kinetics with respect to the substrate (urea) concentration, the rate constant values (k_{30}, k_{40}, k_{50} and k_{60}) at different temperature were obtained by employing Eqn (6).

$$V = K[S] \text{---------- (6)}$$

From the Arrhenius plot of the rate constants as shown in Fig. 5.8c the activation energy of the reactions was found to be 31.1 KJ. For the comparison purpose, the activation energy of the enzymatic reaction was also evaluated in the bulk condition. Here, instead of injecting directly

into the potato strip, urease solutions were added to one of the reservoirs as shown in schematic of Fig. 5.8a2. The potentials developed under such condition are plotted as a function of time at different reaction temperature and shown in Fig. 5.8d. From the Arrhenius plot of the rate constants the activation energy of the reactions (Fig 5.8e) in the bulk condition was found to 34.1 KJ, which is in a good agreement with the values reported earlier in the literature.[35]

Similarly, the sustainability of urease inside the potato channels were compared with that of bulk environment. Multiple strips of freeze dried potatoes of similar dimensions (7 × 4 × 1 mm^3) were soaked with identical amount of urease solutions, (300 µL, 1 mg/ml) and stored in a hydrated environment. In order to monitor the activity of urease as a function of time, after every 24 hours 1 ml urea (.01M) was injected to one of the urease soaked potato strips, and the amount of NH_4^+ ions released from the reaction was determined by employing Nessler reagent. Simultaneously, several glass vials containing 300 µL of 1 mg/ml urease solutions were stored separately, and activity of the same were determined by the same method and compared with the samples stored in the biological channels. As shown in the bar diagrams of Figure 5.8f, the activity of urease was found to be declining in the glass vials at a much faster rate than that inside the bio-channels, suggesting the latter to be a better medium for the enzyme activity. Similar observations about superior activity and specificity of enzymes in the biological medium are already reported in the literature.[36-40]

Based on the existing knowledge, the enhancement of the activity of urease inside potato nanochannels is attributed to conducive biological environment, like compartmentalization of enzymes by the cells. Compartmentalization enhances the efficiency of enzymes metabolic pathways by not only maintaining a high local concentration but also providing favourable spatial and temporal organization of molecules within the cell. These complexes allow

optimized substrate channelling and thereby prevent loss of intermediates and improve control and efficiency of catalysis. [37,38]

5.5: Conclusions

In conclusion, we have demonstrated the possibilities of employing large number of bio-channels readily available in our surroundings for the technological advancements in multiple directions. The nanofluidic channels harvested from potato tuber exhibit surface-charge-govern ionic transport and cross membrane potentials just like artificially fabricated nanofluidic membranes. As expected, inside bio-nanofluidic channels cations such as K^+, and NH_4^+ exhibits mobility values higher than that of bulk water. The ion-selective nature of bio-channels was also exploited for energy harvesting from concentration difference and enzymatic chemical reaction. It also provided a platform for convenient electrical monitoring of enzyme kinetics inside biological systems. The studies on the kinetics of enzymatic decomposition of urea by urease at different reaction temperature revealed that inside biological medium the reaction goes through a pathway of lower activation energy than that in the bulk environment. Similarly, inside bio-channels, the activity of urease was found to be active for a longer duration of time than that in the glass vials.

5.6: References:

1. T. Vaananen, T. Ikonen, V.-M. Rokka, P. Kuronen, R. Sermiaa and V. Ollilainen, *J. Agric. Food Chem.,* 2005**, 53**, 5313.
2. K. Konstankiewicz, H. Czachor, M. Gancarz, A. Król, K. Pawlak and A. Zdunek *Int. Agrophysics.,* 2002, **16**, 119.
3. B. Sattelmacher, *New Phytologist*., 2001, **149**, 167.
4. J.-Y. Lee and H, Lu, *Trends Plant Sci*., 2011, **16**, 201.
5. J. P. Gogarten, Planta., 1988, **174**, 333.
6. A. Chesson, P. T. Gardner and T. J. Wood, *J Sci Food Agric*., 1997, **75**, 289.
7. R. J. Moon, A. Martini, J. Nairn, J. Simonsen and J. Youngblood, *Chem. Soc. Rev.*, 2011, **40**, 3941.
8. N. Carpita, D. Sabularse, D. Monotezinos and D. Delmer, *Science*, 1979, **205**, 1147.
9. Marschner, H. *Mineral nutrition of higher plants*. *San Diego, CA, USA: Academic Press*, 1995.
10. M. Irimia-Vladu, *Chem. Soc. Rev*., 2014, **43**, 588.
11. Q. Cheng, D. Ye, W. Yang, S. Zhang, H. Chen, C. Chang and L. Zhang, *ACS Sustainable Chem. Eng.*, 2018, **6**, 8040.
12. Y. J. Kim, W. Wu, S.-E. Chun, J. F. Whitacre and C. J. Bettinger, *Proc. Natl. Acad. Sci. U. S. A.*, 2013, **110**, 20912.

13. L. Yin, H. Y. Cheng, S. M. Mao, R. Haasch, Y. H. Liu, X. Xie, S. W. Hwang, H. Jain, S. K. Kang, Y. W. Su, R. Li, Y. G. Huang and J. A. Rogers, *Adv. Funct. Mater*., 2014, **24**, 645.

14. C. Rullyani, C.-F. Sung, H.-C. Lin and C.-W. Chu, *Sci. Rep.*, 2018, **8**, 8146.

15. M. Song, M. Cheng, M. Xiao, L. Zhang, G. Ju and F. Shi, *Adv. Mater*., 2017, **29**, 1603312.

16. W. Li, W. Wu and Z. Li, *ACS Nano*, 2018, **12**, 9309.

17. J. Ji, Q. Kang, Y. Zhou, Y. Feng, X. Chen, J. Yuan, W. Guo, Y. Wei and j. Li, *Adv. Funct. Mater*., 2017, **27**, 1603623.

18. L. Lin, L. Zhang, L. Wang and J. Li, *Chem. Sci*., 2016, **7**, 3645.

19. H. Li, Z. Song, X. Zhang, Y. Huang, S. Li, Y. Mao, H. J. Ploehn, Y. Bao and M. Yu, *Science*, 2013, **32**, 95.

20. A. D. L. Escosura-Muniz and A. Merkoci, *ACS. Nano*, 2012, **6**, 7556.

21. R. Li, X. Fan, Z. Liu and J. Zhai, *Adv. Mater*., 2017, **29**, 1702983.

22. A. M. Smith, *Biomacromolecules*, 2001, **2**, 335-341.

23. K. Sahu, S. K. Mondal, S. Ghosh and K. Bhattacharyya, *Bull. Chem. Soc. Jpn.*, 2007, **80**, 1033.

24. M. Esch, V.L. Sukhorukov, M. Kurschner and U. Zimmermann, *Biopolymers*, 1999, **50**, 227.

25. C. Wang, S. Wang, G. Chen, W. Kong, W. Ping, J. Dai, G. Pastel, H. Xie, S. He, S. Das and L Hu, *Chem. Mater*., 2018, **30**, 7707.

26. K. Raidongia and J. Huang, *J.Am.Chem.Soc*., 2012, **134**, *16528*.

27. R. B. Schoch and P. Renaud, *Appl. Phys. Lett*., 2005, **86**, 253111.

28. I. Obi, T. Kakutani, N. Imaizumi, Y. Ichikawa and M. Senda, *Plant Cell Physiol.*, 1990, **31**, 1031.

29. A. Einstein, *Ann. Phys. (Leipzig)*, 1905**, 17**, 549.

30. R. A. Marsh, S. G. Waight and H. Wycombe, *Starch.*, 1982, **34**, 149.

31. A. Küchler, M. Yoshimoto, S. Luginbühl, F. Mavelli and P. Walde, *Nat. Nanotech.*, 2016, **11**, 409.

32. N. F. Y. Durand and P. Renaud, *Lab Chip*., 2009, **9**, 319.

33. M. M. Orosco, C. Pacholski and M. J. Sailo, *Nat. Nanotech*., 2009, **4**, 255.

34. L. Casali, L. Mazzei, O. Shemchuk, K. Honer, F. Grepioni, S. Ciurli and D. Bragaa, J. Baltrusaitis, *Chem. Commun.*, 2018, **54**, 7637.

35. M. Fidaleo and R. Lavecchia, *Chem. Biochem. Eng*., 2003, **17**, 311.

36. H. Wang, Z. Zhao, Y. Liu, C. Shao, F. Bian and Y. Zhao, *Sci. Adv*., 2018, **4**, eaat2816.

37. R. J. Conrado, J. D. Varner and M. P. DeLisa, *Curr. Opin. Biotechnol*., 2008, **19**, 492.

38. Z. Zhao, J. Fu, S. Dhakal, A. Buck, M. Liu, T. Zhang, N. Woodbury, Y. Liu, N. Walter and H. Yan, *Nat. Commun*., 2016, **7**, 10619.

39. J. Ge, J. Lei and R. N. Zare, *Nat. Nanotechnol*., 2012, **7**, 428.

40. Y. Ming, J. Ge, Z. Liu and P. Ouyang, *J. Am. Chem. Soc*. 2006, **128**, 11008.

Chapter 6

Remarkable Rate of Water Evaporation through Naked Veins of Natural Tree-leaf

Summary*

In the present work we have demonstrated vein network of the natural leaf as low-energy steam-generator and utilized its steam generation property to harvest electricity from streaming potential. The network of hierarchical channels, precisely designed by nature for efficient transportation of liquids were extracted from matured and fallen leaf samples via microbial delignification. The naked leaf veins exhibit remarkable flux (evaporation rate 1.5 kg m^{-2} h^{-1}) of capillary evaporation under ambient condition (25 °C and 30 % RH), close to the photothermal material-based evaporators reported in the recent literature. The mechanistic studies performed with variable atmospheric conditions (temperature, humidity, wind-speed) suggest the evaporation process through the naked veins to be a kinetic-limited process. Naked veins with remarkable evaporation efficiency are found to be suitable for applications like water desalination and streaming potential harvesting. Experiments with the naked veins also unveiled that the biofluidic channels in leaf not only exhibit the characteristics of surface-charge-governed ionic transport but also support an exceptional water transport velocity of 1444 µm.s^{-1}.

* An article based on these studies has been just accepted for publication in *ACS omega*.

6.1: Introduction

In the last few decades, numerous unforeseen properties and phenomena specific to nanometer size regime systems have been uncovered, and many of them were also exploited for technological applications.[1] One of the recently discovered astonishing nanoscale phenomena is the enormous rate of evaporation from capillary nanochannels.[2-6] Despite being a ubiquitous natural phenomenon, evaporation through nanoscale capillary channels still lacks thorough understanding and undisputed mechanism.[2] Remarkable evaporation efficiency demonstrated by different nano-capillary systems has been attributed to diverse mechanisms. For example, evaporation fluxes of ultrathin graphene capillaries were observed to be up to two orders of magnitude higher than the one predicted by the classical Hertz-Knudsen (H-K) equation attributed to an extension of the actual evaporation areas.[3] Similarly, in precisely controlled experiments with hybrid two-dimensional nanochannels, Li *et al.* observed that the velocities of water vapour leaving the interface can be larger than the root mean square (RMS) velocities of the same vapour temperature.[2] This extraordinary observation with individual nanochannels was credited to decreasing thermal resistance between the solid substrate and the liquid/vapor interface, along with an efficient heat and mass transfer process. Similarly, in clear contrast to the typical evaporation behaviour, Gimenez *et al.* observed that sessile droplets placed on nonporous surfaces evaporate more rapidly when salt concentration increases and temperature decreases. This unexpected evaporation behaviour was related to the generation of a steady-state wetted annulus in the droplet periphery.[4] In spite of being a poorly understood phenomenon, evaporation from nano capillaries significantly impacts our ecological systems. For example, the remarkable capillary evaporation through natural tree leaves is the root of the environmental water cycle.[7] Natural plant leaf transpires massive amounts of water from the soil. Above 95 % of the water absorbed by the roots is lost through stomata openings via transpiration.[8,9] The rapid evaporation of water through plant leaves is supported by the highly

specialized network of xylem.[10-12] The hierarchical and porous veins provide the leaf with physical and chemical robustness and an ideal platform for the rapid evaporation of water molecules.[13] In this article, we have studied evaporation behaviour through the hierarchical structure of the vein network extracted from the fallen leaves and exploited the same for seawater desalinations. We observed that even in the absence of photoactive materials, the naked vein network exhibited an evaporation rate at par with the man-made systems with highly efficient photothermal materials. A remarkable kinetically controlled evaporation process powered by extended evaporation area, decreasing thermal resistance between the solid substrate and the liquid/vapor interface, and efficient exchange of heat and mass between water molecules confined inside porous biological channels and atmosphere is accounted for the remarkable performance of the leaf vein based natural evaporator.

6.2: Scope of the present investigation

In this chapter, we have studied evaporation behaviour through the hierarchical structure of the vein network extracted from the fallen leaves. The extraordinary ability of naked leaf veins extracted from fallen tree leaves to evaporate water at an expedited rate under ambient conditions could find multiple technological applications in areas like water desalination, harvesting of exquisite salts or molecules, humidification, and energy conversion. Steam generation through naked leaf veins could have several advantages over the solar stream generator. For example, in solar steam generation, photo-thermal materials are employed to convert sunlight into heat, which induces rapid evaporation of the surrounding water molecules.[14,15] While solar steam generation is one of the most promising methods of treating water in an environment-friendly manner, the involvement of photo-thermal materials complicates the process. The complication with photoactive material-based devices arises from requirements such as homogeneous exposure of light throughout the photoactive material,

thermal insulation between the active material and bulk liquid, and periodic removal of the deposited salts to avoid blocking the capillary pores.[16,17] No such complication would occur in the case of non-solar steam generation through naked leaf veins. So leaf vein network felicitates an efficient way to generate water steam in a cost effective manner.

The excellent steam generation characteristics of the leaf vein system paved a way to harvest electricity via applying the principle of streaming potential. The elementary micro/nano fibrils present in the leaf vein possess negative surface charges and can break the electrical neutrality of electrolytes when flowing through it.[18-20] So when electrolyte flows through the charged veins it creates potential gradient typically known as the streaming potential. By interposing suitable series connections of several leaf based device, electrical energy can be harvested which is sufficient enough to power small electronic device such as LED. With such superiority, our leaf vein-based evaporator has the potential to perform multiple valuable works such as water desalination, humidification, and electricity generation in a single operation.

6.3: Experimental section

Extraction of vein network from natural leaf:

A collection of aged and fallen leaves (typically 60 numbers) of Peepal tree (*Ficus religiosa*) was immersed into a tape water-filled closed container (25 litters) for about 25 days. After 25 days, the upper epidermis and mesophyll layers of the leaf blade turned into a soft, smelly and brownish coloured loosely bound material. The network of naked leaf veins was obtained after gently removing those loosely bound material by using a soft nylon brush. The as-obtained vein network was dried by using a heat gun (approximate temperature ~ 50 °C).

Evaporation of water through leaf veins:

For the evaporation experiment, glass ampoules containing 15 mL of deionized water were

first sealed with a parafilm cover. The parafilm sealing was pierced with the help of a needle to immerse the isolated midrib part of the naked leaf vein systems. Glass ampoules containing the naked vein network was kept in a controlled environment (30 %, RH, 25 °C, 50 lux and 0.54 km h^{-1}) for a recorded amount of time. The evaporated amount of water through the midrib vein was gravimetrically estimated by measuring the weight change of the ampoule at consistent intervals of time. In order to study the effect of temperature on evaporation rates, naked veins immersed in glass ampoules were kept at a fixed distance from the heater under a controlled environment with RH, and airflow rate measured to be 30 %, and 0.54 km h^{-1}, respectively. Thermometer, Digital Lux Meter, Thermo-Hygrometer, and Thermal anemometer instruments were installed at the same levels of the vein network in order to record the respective parameters in real-time. Similarly, for the measurements of evaporation rate under varying humidity conditions, the humidity level of the chamber was varied by using a combination of the required amounts of desiccants (calcium chloride) inside the chamber and warm N_2 flow. Dependence of the evaporation rate on the airflow velocity was studied by using a domestic table fan. LED light with different luminous flux was employed to study the evaporation rate under varying light intensity.

Water diffusivity experiment:

An ampoule containing 15 ml of DI water was sealed with parafilm, and a small hole was pierced through the parafilm to insert the midrib part of an isolated vein network. Two Ag/AgCl electrodes (7 mm apart) were installed to the midrib of the naked vein network (area 13 cm^2) by applying the conductive silver paste. The electrodes were attached to a source meter instrument (Keithley 2450) and recorded the development of current values as a function of time (time interval of 1.33 seconds).

Surface Charge Governed Ionic Transport:

The nanofluidic device was prepared by embedding an isolated midrib (dimension = 20 mm × 1 mm × 0. 3 mm) into a blend of polydimethylsiloxane (PDMS) prepolymer and curing agent. Once the PDMS stub was fully cured, two reservoirs of volume 0.4 ml were carved out at both ends of the midrib to expose the same into electrolyte. Electrical measurements were done with a source meter instrument connected with Ag/AgCl electrodes, which were immersed into the reservoirs filled with electrolyte of different concentrations (from 10^{-6} M to 1 M). Conductance values (G) at different electrolyte concentrations were calculated from the slope of the *I-V* curves recorded by sweeping the voltage from -1 V to 1 V. The following equation was used for the calculations of conductivity values (C): C = G × cell constant.

Characterisations:

The microstructure of leaf vein was characterised by optical (Olympus BX51) and Field Emission Scanning Electron Microscope (FESEM) (Zeiss, Model: Sigma). Spectroscopic techniques such as UV-Vis spectrometer (PerkinElmer, Model: Lambda 750) and Fourier transform Infrared Spectroscopy (Perkin Elmer IR spectrometer) was used for functional group identification. The light intensity was measured using a Digital Lux Meter (Model: LX1330B). The relative humidity, temperature and the wind speed of the surrounding environment was measured using Thermo-Hygrometer (testo 605i), thermometer and Thermal anemometer (testo 405i) instruments. Electrochemical measurements were done with the help of a sourcemeter instrument (Keithley 2450 model). Dye separation experiments were studied by using a UV-Vis Spectrophotometer (Systronics, Model: 117).

6.4: Results and discussions

The network of hierarchical channels, precisely designed by nature for efficient transportation

of liquids were extracted from matured and fallen leaf samples collected directly from nature. To begin with, the leaves of *Ficus religiosa* (Peepal tree) were soaked in tape water for around 25 days. During the prolonged soaking period, most of the soft cells of the leaf blade (cuticle, epidermis, the mesophyll) were digested by the microbes releasing a funky smell. Remarkably, the vein structure of leaf epipodium was not affected by the digestion process. The hierarchical structure of natural leaf is primarily comprised of high-crystalline cellulose, hemicellulose, and lignin. While lignin possesses an extremely complex structure and dark colour, cellulose and

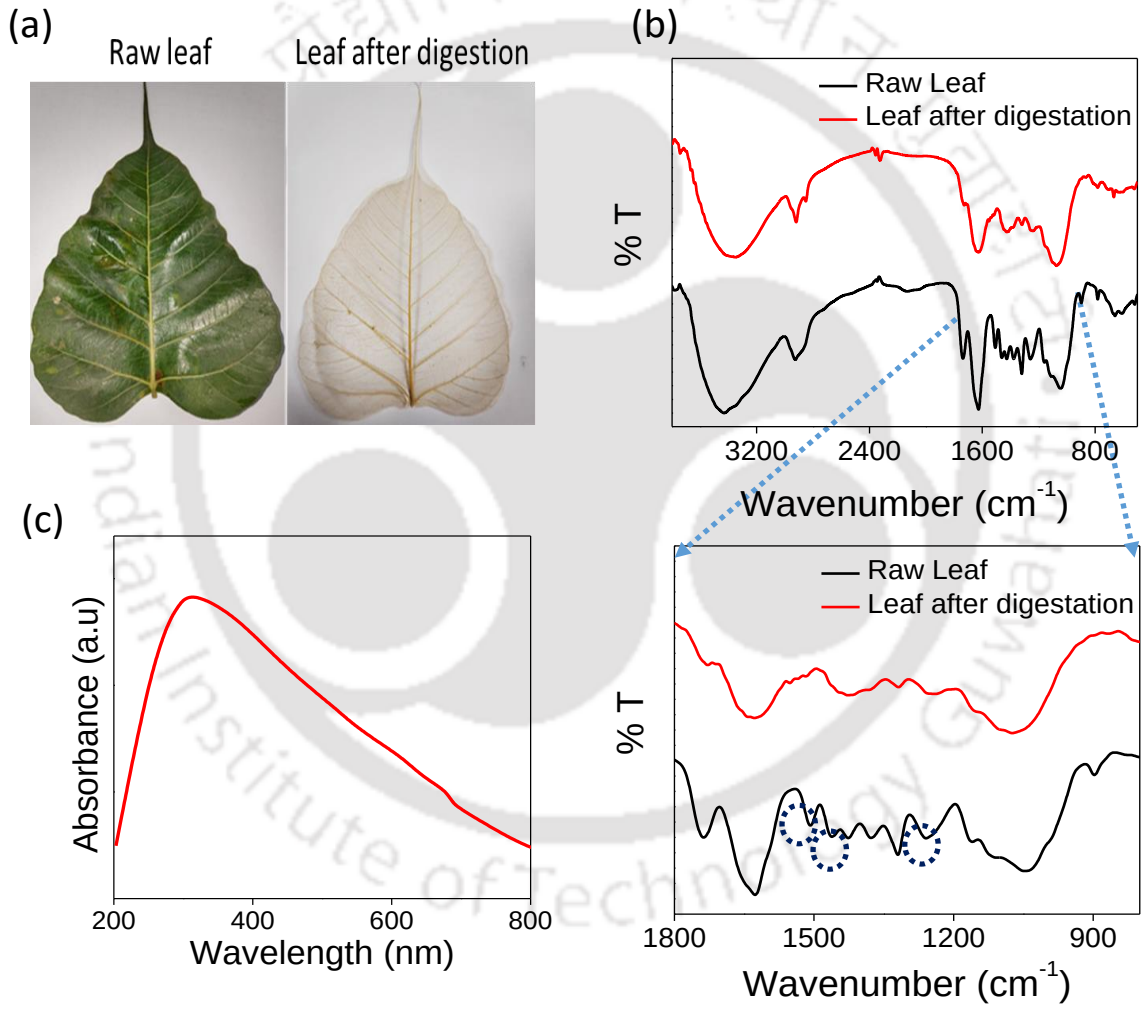

Fig. 6.1: Characterization of leaf vein network: (a) Digital images of raw leaf and digested leaf, showing the decolourisation after lignin removal (b) IR spectra of the isolated vein network of natural raw leaf compared to the leaf after digestion process. (c) DRS spectra of leaf vein after digestion process.

hemicellulose are colourless.[21] The digestive process removed most of the soft cells of the leaf blade along with the lignin portion producing a light-coloured system as compared to its natural

analogue, shown in Fig. 6.1a. The FT-IR spectra of raw leaf vein (Fig. 6.1b) exhibit intense bands in the regions of 3430 cm^{-1} (O-H stretching vibration), 2900 cm^{-1} (C-H stretching vibration), 1734 cm^{-1} (C=O stretching vibration), 1506 and 1460 cm^{-1} (aromatic C=C stretching vibration), and 1260 cm^{-1} (C-O-C stretching vibration). These bands are related to the hydroxyl groups in celluloses, carbonyl group of acetyl ester in hemicelluloses and carbonyl aldehyde, aromatic skeleton in lignin and guaiacyl ring breathing with C-O stretching, respectively.[21-24] After the digestive process, the intensity of aromatic skeletal bands at 1506 cm^{-1} and 1460 cm^{-1} along with the guaiacyl ring breathing with C-O stretching has been significantly reduced confirming partial removal of the lignin.[24] However, the lignin removal did not seem to perturb the inherent cellulosic skeleton as most of the cellulosic hydroxyl groups are retained.

Moreover, the digestive process did not seem to alter the dimension of the leaf veins, suggesting that the original hierarchical alignment of microchannel are well-preserved. Instead the lignin removal creates additional micro capillary which can be viewed from the optical microscopic images (Fig. 6.2).

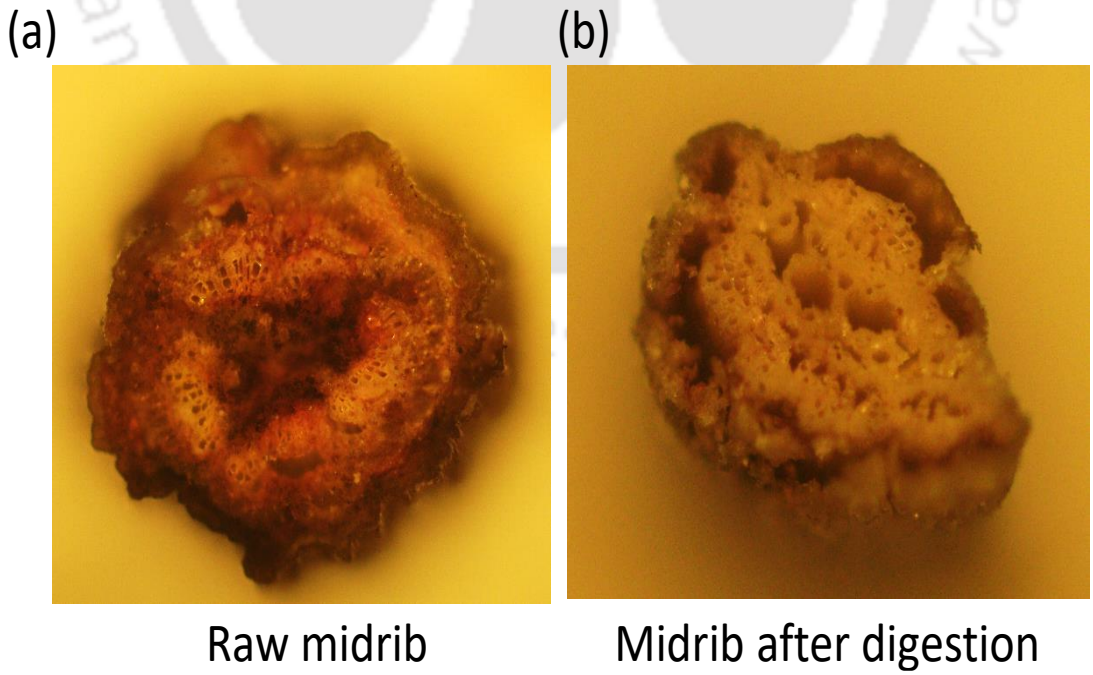

Fig. 6.2: Optical microscopic images of leaf midrib vein: Cross sectional microscopic images of (a) Raw midrib vein and (b) Midrib vein after digestion process.

The digested soft cells were gently removed with a soft brush in order to isolate the naked vein structure. The veins of Peepal leaf was chosen due to its mechanical robustness, a typical midrib of Peepal leaf weighing 50 mg can hold around 400 mg of weight as shown in Fig. 6.3a. The tensile stress vs strain curve for de-lignified midrib vein is shown in Fig. 6.3b and comared the same with that of green midrib vein. It indicates that the lignification process made the leaf vein more ductile. Young's modules of the pristine and de-lignified midrib veins were calculated to be 30 MPa and 12 MPa respectively.

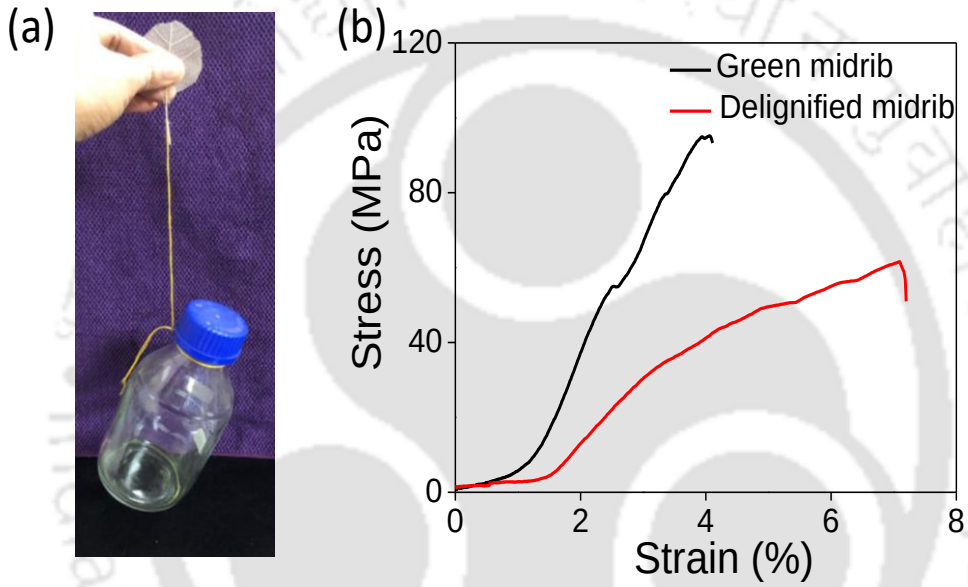

Fig. 6.3: Mechanical property of leaf vein: Mechanical robustness of the veins of Peepal leaf (a) Image showing mechanical strength of the veins that can hold a weight 8 times higher than its inherent weight (b) Tensile strain vs stress curve for delifnified midrib and green midrib vein.

A digital photo of the extracted vein network is shown in Fig. 6.4a. Thorough examination on multiple optical and electron microscopic images of the vein network (Fig. 6.4b) with the help of image processing software (Image J) revealed that about 70 % area of the naked vein network is empty or bereft of any channels. The density of the midrib vein was evaluated with the help of BJH analysis to be 1.75 gcm^{-3}. Moreover, the leaf vein density which is defined as the total length of veins per unit area was evaluated with the help of image processing software image J and was found to be 2.5 cm^{-1}. The optical microscopic image of the cross-section of an

isolated midrib vein, shown in the inset of Fig. 6.4b, reveals the presence of large empty channels with diameters extending up to hundreds of microns. The optical microscopic investigation also revealed that the typically isolated midrib veins exhibit an oval-like shape. The hierarchical nature of the naked veins can be visualized from field emission scanning electron microscopic (FESEM) image in Fig. 6.4c. Primarily, natural leaf veins are made of three kinds of cells, fiber tracheids, vessels, and parenchyma cells as shown in Fig. 6.4c and Fig.6.4f. Owing to their large lumen diameter and open-ended wall structure, vessels are the primary conduits for mass transport, whereas the thinner fiber tracheids with closed tapered ends are attributed for the mechanical support.[25,26] Moreover, small pits with an average diameter of ~1 μm are visible on the internal surface of the microchannels, Fig. 6.4e.

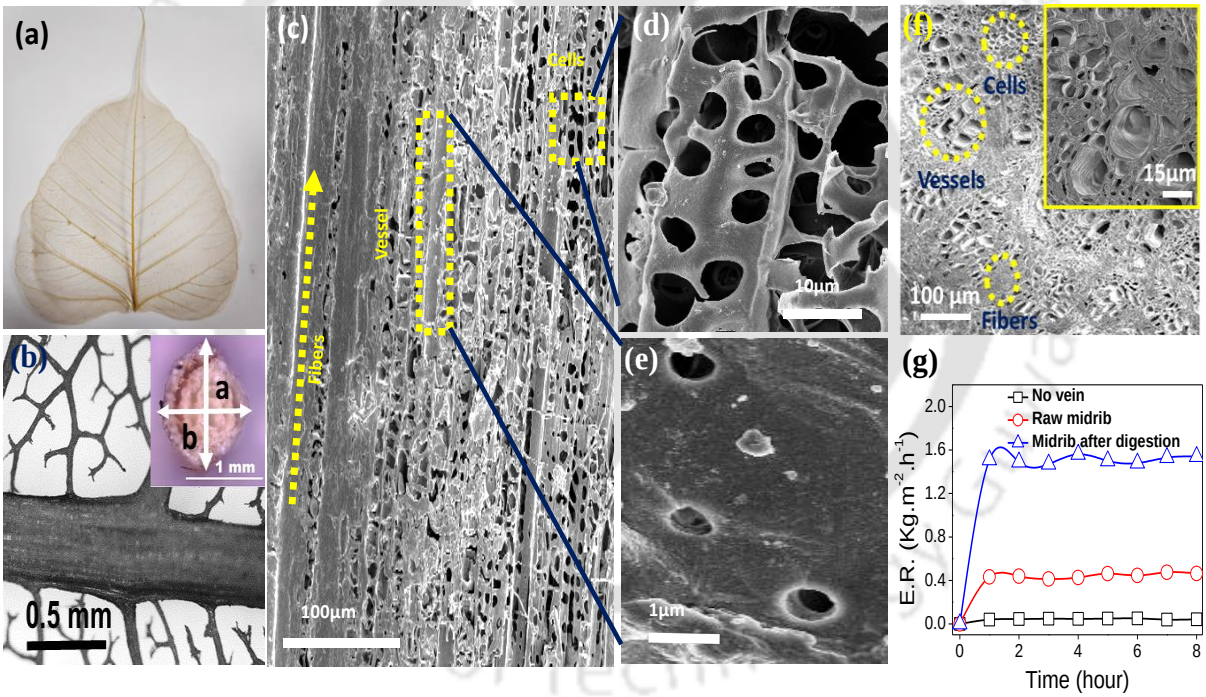

Fig. 6.4: Naked veins of a tree leaf: (a) Digital photo, and (b) optical microscopic image of a vein network extracted by removing the digested soft cells of a fallen leaf of *Ficus religiosa (*peepal tree). Inset showing optical microscopic image of the cross-section of an isolated midrib vein (c) FESEM image of the outer surface of an isolated midrib vein along the growth direction showing the different water transportation pathway *Viz.* vessels, parenchyma cells and fibre tracheids. FESEM images showing zoom-in view of (d) parenchyma cells and (e) inter-vessel pits (f) Cross-sectional FESEM image of leaf midrib vein (inset shows higher magnification view) (g) Evaporation rate ($E.R._{vein}$) of DI water through a raw midrib vein and isolated midrib vein extracted via digestion process is compared with that of a similar ample without the vein.

In order to study the evaporation behaviour through naked leaf veins, a portion of the midrib (length = 4.7 cm) was isolated from the network by cutting away the secondary veins. The bottom part of the isolated midrib (3.12 cm) was soaked into a glass ampoule containing 15 ml of deionized (DI) water. Parafilm covers were applied all around the vein to restrict evaporation of water molecules through secondary pathways, directly from the container. The evaporation behaviour was monitored by measuring the weight change of the ampoule at a consistent interval of time. The experiment was performed in a controlled environment (inside a stainless steel chamber (diameter 27 cm, height 30 cm) with controlled RH, temperature, light intensity and wind velocity. In Fig. 6.4g, the water evaporation rate through the raw leaf vein and extracted leaf vein via digestion process is compared with that of a similar ampoule minus the vein structure. Remarkably, even under dark condition, inside a stainless steel chamber (30 % RH and 25 °C) the $E.R._{vein}$ value was found to be 1.5 $kg.m^{-2}.h^{-1}$, which is nearly 50 times higher than a similar ampule covered with a parafilm having a hole similar to the diameter of the vein structure. Evaporation rates ($E.R._{vein}$) through the midrib vein under different conditions were calculated by employing Eqn (1).

$$E.R._{vein} = \frac{Change\ in\ weight\ (kg)}{Evaporating\ area\ (m^2) \times Time\ (h)} \text{ – – – – – – – –} (1)$$

Where, the circumference (A) of the isolated midrib vein exposed to the atmosphere was considered as the evaporating area. It was determined by assuming the vein to be an oval shaped cylinder, in the inset of Figure 1b. The diameter was measured along two perpendicular lines, or axes at two positions, at the tip of the exposed midrib vein and at the bottom just above the parafilm cover. L is the length of the vein above the parafilm cover. The details of the calculation of evaporating area is discussed in the Fig. 6.5.

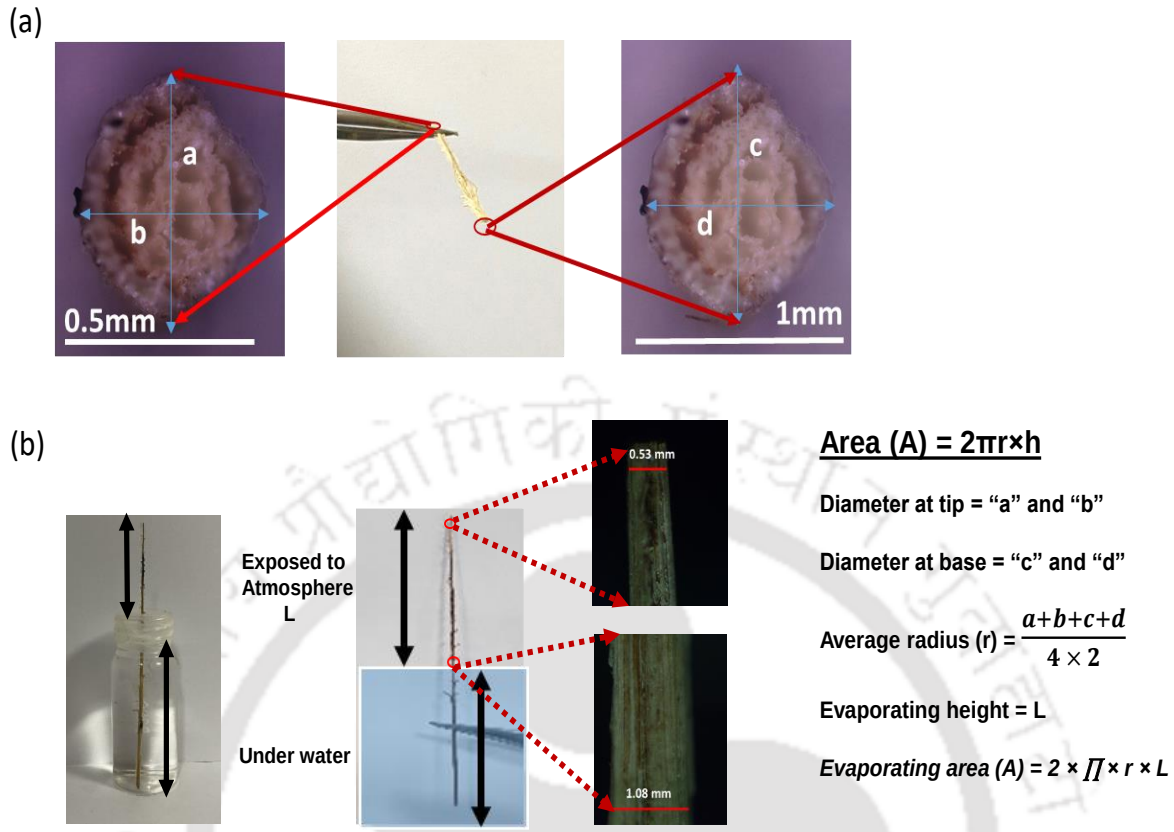

Fig. 6.5: Calculation of evaporating area: (a) Optical microscopic image of the cross-section of an isolated midrib vein measured along the vertical growth direction at two different positions. It revealed that vein is an oval shaped cylinder and the diameter of the circular base is different at different vertical growth direction. (b) The evaporating area of the vein was considered to be the circumference (A) of the isolated midrib vein exposed to the atmosphere. It was determined by assuming the vein to be an oval shaped cylinder. The diameter was measured along two perpendicular lines, or axes at two positions, at the tip of the exposed midrib vein and at the bottom just above the parafilm cover. L is the length of the vein above the parafilm cover.

The incredible evaporation process through the vein of naked leaf can be subdivided into two steps. The first step involves transportation of water molecules from the container to the evaporating surface through hierarchal capillaries of natural leaf vein. In the second step, the transported water molecules diffuse and/or evaporate of into surrounding atmosphere. With a view to find out the rate determining step, evaporation rate through leaf vein was studied by varying the parameters of surrounding atmosphere (like relative humidity (RH), temperature, and wind velocity). As shown in Fig. 6.6a, the rate of evaporation through the naked leaf vein was found to be dependent on the atmospheric humidity levels, which was varied by employing

a combination of calcium chloride desiccant inside a closed chamber and control flow of warm N_2 gas. With the decreasing humidity level, the $E.R._{vein}$ value was found to be increased from 0.77 kg m^{-2} h^{-1} at 50 % RH to 1.76 kg m^{-2} h^{-1} at 25 % RH, see Fig. 6.6a. The enhancement in

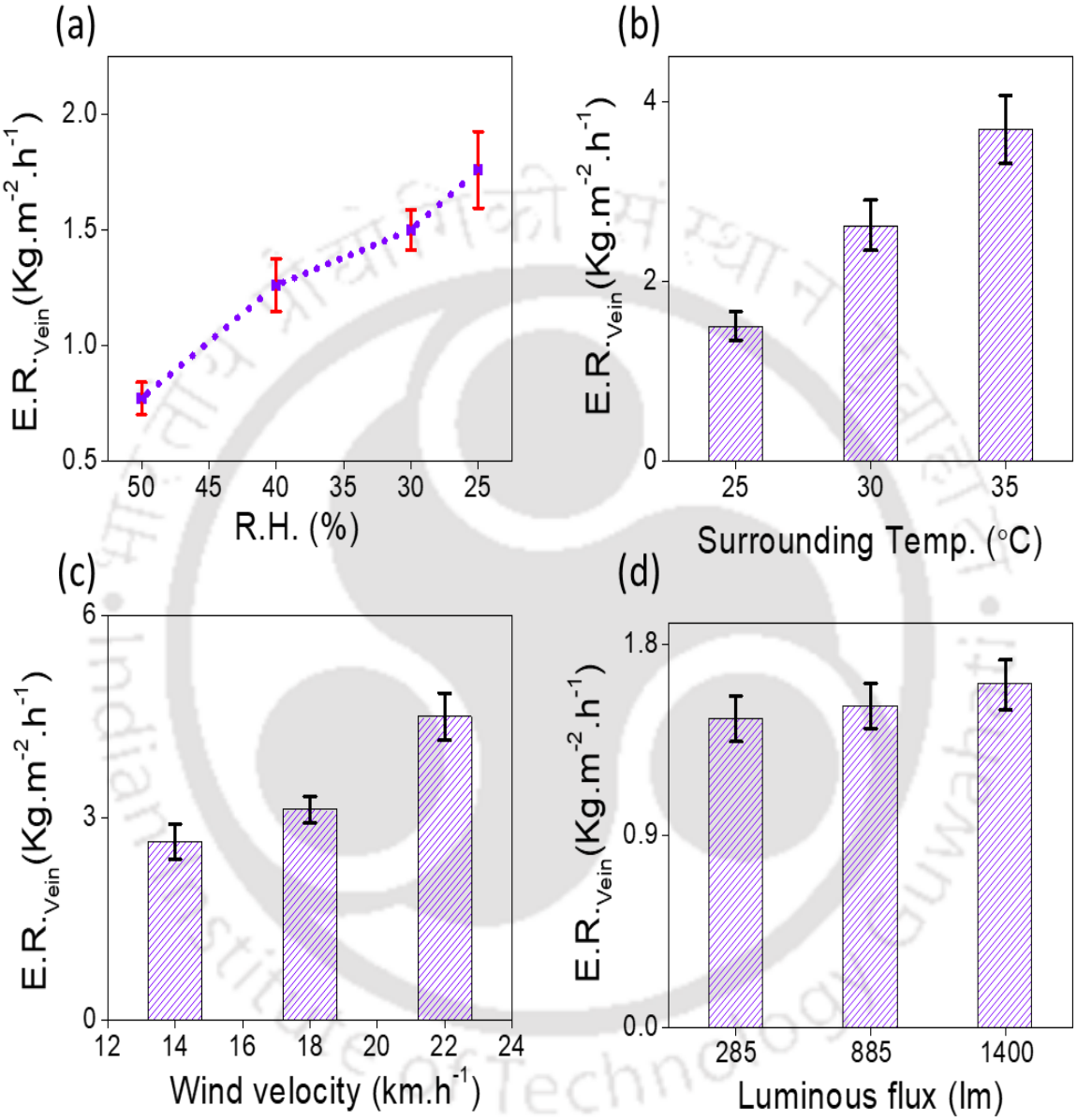

Fig. 6.6: Evaporation through isolated leaf veins: $E.R._{vein}$ of DI water through isolated midrib vein with varying (a) relative humidity levels, (b) atmospheric temperature, (c) wind velocity, and (d) light intensity under controlled environmental conditions. In order to study the dependence of $E.R._{vein}$ on a particular parameter the remaining parameters were fixed at 30 % RH, 25 °C, 50 lux, and 0.54 km hr^{-1}.

the evaporation rate with the decreasing humidity level suggests that the rate determining step involves diffusion and evaporation of the transported water molecules from the capillary mouth

into air atmosphere, which is also called as kinetic-limited evaporation process. The dependence of humidity in kinetic-limited evaporation process is attributed to the increasing difference between the partial pressure and vapour pressure of the water molecules. The occurrence of kinetic-limited evaporation process was also supported by a drastic improvement in the $E.R._{vein}$ values with increasing atmospheric temperature (the bar diagram in Fig. 6.6b). In the kinetic-limited evaporation process, the elevated atmospheric temperature aids the evaporation process by increasing both kinetic energy of the molecules as well as the saturation vapor density of the atmosphere. A similar escalation in the evaporation rates through the naked leaf vein was also observed with increasing air velocity of the surrounding environment. Fig. 6.6c shows the bar diagram of $E.R._{vein}$ values calculated for the leaf vein at different air velocity created by a domestic table fan under dark conditions. The decreasing boundary layer at the evaporating surface with increasing air velocity creates a conducive environment for the mass transfer, which in turn leads to the remarkable enhancement in the evaporation rate.

One of the pre-requisite of kinetic-limited evaporation process is the seamless supply of water molecules from the reservoirs to the evaporating surface, which require a tremendous flow rate of water through the capillary channels of naked leaf veins. In natural leaf veins, the fiber tracheids and vessels, collectively called microchannels, are the major conduits for water transportation. The digestive process consumes the lignin embeds in the cellulose and hemicellulose matrix of leaf vein and generate numerous hydrophilic nanochannels among the microfibers tracheids.[27] These newly generated hydrophilic nanochannels, previously occupied by hydrophobic lignin provides an additional means for fluid transport, through increasing the hydrophilicity and available surface area. The occurrence of numerous nanopores in the dignified leaf can be verified from BET surface area and BJH pore distribution analysis, where the leaf vein possesses a high surface area of approximately 240 $m^2 g^{-1}$.

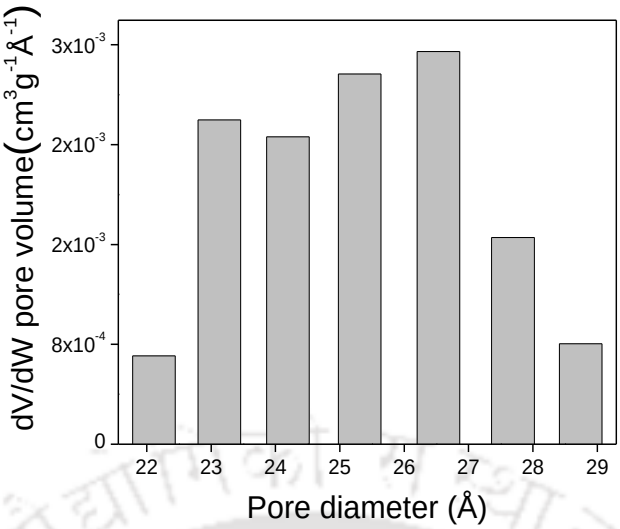

Fig. 6.7: Nanopores in leaf midrib vein: BJH pore size distribution in leaf midrib vein.

The observed smaller pore distribution shown in Fig. 6.7 can be attributed to the presence of nanopores.[28] These inherent microchannels of low-tortuosity and open-structures are oriented along the growth direction, resulting in efficient mass transport in the upward direction as shown in the schematic diagram of Fig. 6.8a. Moreover, some small pits with an average diameter of ~1 μm are present on the internal surface of the microchannels, which enable a transverse mass transport between the adjacent vessels.[29,30] The porous leaf vein with numerous aligned hydrophilic micro and nanochannels can effectively transport water molecules from the bottom to the evaporating surface, maintaining a continuous network of water channel throughout the vein structure. As water molecules evaporate from the upper surface, it is simultaneously compensated by capillary induced pumping from the bottom through the vessels and other interconnected-channels in the leaf vein, ensuring an uninterrupted supply of water molecules for the evaporation process. The negative pressure at the top of the open veins originated from water evaporation, induces large capillary force inside the micron- and nano-sized channels of the leaf vein.[29-31] Water molecules can also flow in the transverse direction in between the adjacent vessels channels via the interconnected pits (Fig. 6.8a). But this transvers flow occurs via slow diffusion form one vessel to another instead of free liquid advection and hence the pits have little impact on water transport along the vessels in the

vertical direction, but it contributes towards over-all evaporation process from the outer surface.[29, 32] The upward water transportation along the growth direction can be visualized from optical microscopic investigation shown in Fig.6.8b and Fig. 6.8c. In order to study the water transport velocity from the reservoirs to the evaporating surface through capillary channels of

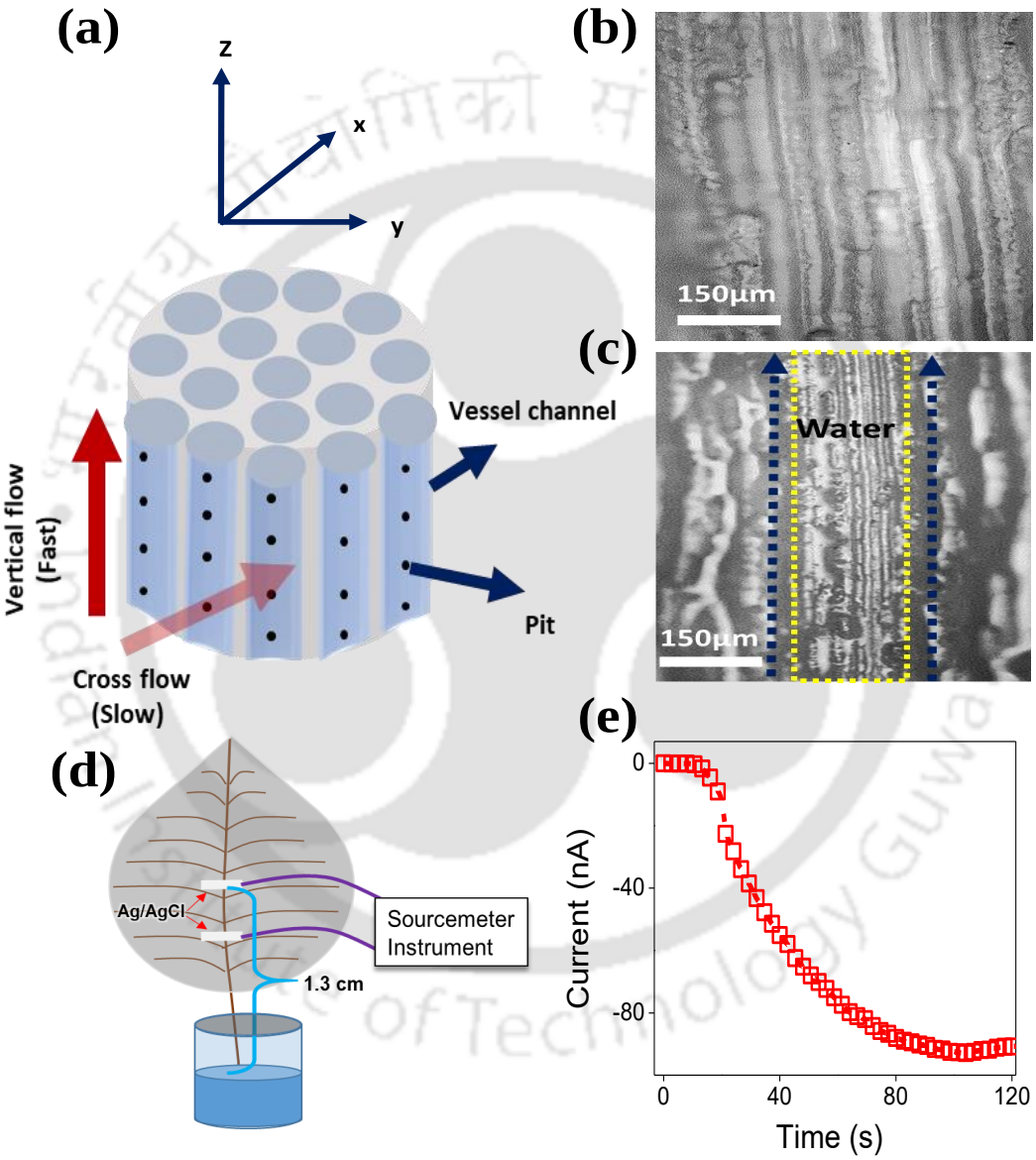

Fig.6.8: Mechanism of water transportation: (a) Schematic diagram showing anisotropic water transportation through the vessel channels and the interconnected pits in leaf midrib vein. Optical microscopic images of leaf midrib vein (b) before and (c) after water transportation, showing upward flow of water along the growth direction. (d) Schematic illustration of the experimental set-up used for the measurement of water transport velocity through naked leaf veins. (e) Development of ionic current as a function of time between the Ag/AgCl electrodes installed at the midrib vein after dipping the base into liquid DI water.

naked leaf veins, two Ag/AgCl electrodes were mounted on the midrib vein of a naked vein network at a distance of 7 mm apart, see the schematic of Fig. 6.8d. In order to detect the development of ionic current, both these electrodes were connected to a sourcemeter instrument. As the cellulose-based leaf veins are electrically insulating, under dry conditions no detectable current was observed. Once the base of the midrib vein touched the water surface, the water molecules started moving towards the vein network through the midrib vein. As soon as the vein between the electrodes got wetted a sudden increase in the current value was detected. The ionic current thus recorded by the sourcemeter instrument is plotted as a function of time (Fig. 6.8e). The time lag between the midrib vein touching the water surface and appearance of ionic current at the sourcemeter instrument was taken as the time (t = 9 s) required by the water molecules to travel the distance (x = 1.3 cm). Accordingly, the water transport velocity was calculated to be 1444 µm s^{-1}. Just for the comparison, the spider silk and cactus spine exhibit water transport velocity of ~30 and ~12 µm s^{-1}, respectively.[33,34] Radha *et al*. measured the flow velocity of water in ultra-thin graphene nanocapillaries to be ~1,00,000 µm.s^{-1}.[2] Similarly, the velocity of water on the Sarracenia trichome is reported to be ~11,738 µm.s^{-1}.[27] The diffusivity of water (D) through the midrib vein was calculated to be $D = 3.1 \times 10^6$ µm^2 s^{-1} by using Einstein's approximation for three-dimensional diffusions (Eqn 2).[35]

$$x^2 = 6Dt \ldots\ldots\ldots\ldots\ldots\ldots (2)$$

Typically, the theoretical limit of the kinetic-limited evaporation flux (m_k'') is predicted by the classical H-K Eqn (3).

$$m_k'' = \left(\frac{M}{2\pi R}\right)^{\frac{1}{2}} \left(\sigma_e \frac{P_{v,eq}}{\sqrt{T_i}} - \sigma_c \frac{P_v}{\sqrt{T_v}}\right) \ldots\ldots\ldots (3)$$

Where, M is the Molar mass of water, R is the Universal Gas Constant. σ_e is the evaporation coefficient, the fraction of molecules that strike the interface and change phase from the liquid

to vapour state (typical values varies between 1 and 0.001).[5] σ_c is the Condensation coefficient the fraction of molecules that strike the interface and change phase from the vapor to liquid state (typically varies between 1 and 0.001).[5] $P_{v,eq}$ is the Equilibrium vapor pressure of the liquid at the interface, P_v is the Partial pressure of the vapour in the gas phase calculated from relative humidity of the experimental condition (RH = $P_v/P_{v,eq}$). T_i is the temperature of the liquid (the temperature of the evaporating area of the vein measured by a non-contact IR camera) and T_v is the vapor temperature (measured by thermometer at a distance of 10 mm from the vein). The kinetic-limited evaporation flux calculated by the H-K equation considering the current experimental conditions was found to be 2.5 kg m^{-2} h^{-1} (considering both σ_e and σ_c to be 0.001),[5] which is in same order of magnitude with the experimental results. The experimental evaporation rate at 25 °C corresponds to a heat flux of 0.08 Wcm^{-2}, which is easily achievable under the current experimental conditions. Similarly, the velocities of water vapour leaving the interface from the volumetric flux was calculated to be 20 mm s^{-1}, which is several times smaller than that of the RMS velocities of vapour at the same temperature.

To the best of our knowledge, the $E.R._{vein}$ value recorded with the midrib vein inside an indoor environment with a RH (30 %), and temperature (25 °C) is at par with the recently published evaporation rates for the solar steam generators under intense simulated sun light (1 sun or higher. Moreover, the naked leaf veins are deprived of any photo-thermal materials. The evaporation rate through the leaf vein was also studied at different light intensity by employing LED lights of different luminous flux. As can be seen from the bar diagram in Fig. 6.6d, the $E.R._{vein}$ value does not alter significantly with increasing luminous flux of the employed LEDs, the slight variation in $E.R._{vein}$ can be attributed to the little rise in temperature of the surrounding atmosphere. So it can be argued that in a direct contrast to the solar steam generators, the naked leaf vein exhibits remarkable evaporation rates even in the absence of light.

The amount of water evaporating through the midrib vein can be further improved by keeping a definite portion of the vein network at their natural position. A photo of the same is shown in of Fig. 6.9a. When the mass lost from the glass bottle was normalized by the circumference of the midrib vein it yielded remarkable values of $E.R._{vein}$. For example, with a vein network of area 6 cm^2 the $E.R._{vein}$ was calculated to be 8.34 kg m^{-2} h^{-1} (30 % RH and 25°C). However, when evaporation rate was normalized by the total area covered by the vein network ($E.R._{network}$) it yielded humble values of evaporation rate (~ 0.25 kg m^{-2} h^{-1}). Large void spaces in the vein network area and the small cross-section of the midribs that connects the vein network with the water reservoirs is believed to be the reason behind the humble $E.R._{network}$ values. However, it is worth noting that even though, in the presence of extended network area, the value of evaporation rate is lower but the actual mass of water evaporating through the network will be more beneficial for the practical applications. The extraordinary ability of naked leaf veins extracted from fallen tree leaves to evaporate water at an expedited rate under ambient conditions could find multiple technological applications in areas like water desalination, harvesting of exquisite salts or molecules, humidification, and energy conversion. As a proof of concept, here we have studied the evaporation of water molecules from saltwater by employing midrib veins with an extended vein network (area 6 cm^2). Fig. 6.9b shows the $E.R._{network}$ values as a function of NaCl concentration at an elevated room temperature of 35 °C and 30 % RH. The decreasing evaporation rate with increasing salt concentration is attributed to the increase in the osmotic pressure that needs to be overcome by the evaporating water molecules. Such evaporation of water molecule from the salt solutions would be suitable for applications like water desalination or wastewater treatment. As a proof of concept, an experimental set-up was designed to collect the water molecules evaporating from the wastewater samples, a schematic illustration of the same is shown in Fig. 6.9c. A midrib of a naked vein network (area 13 cm^2) was immersed into a solution of simulated seawater (0.6 M

NaCl) inside a glass chamber, where except the collection chamber (at the bottom), the entire set-up was exposed to direct sun light on a bright sunny day (temperature and light intensity were recorded to be 30 °C and ~77×10^3 Lux respectively). Parafilm covers were applied in the

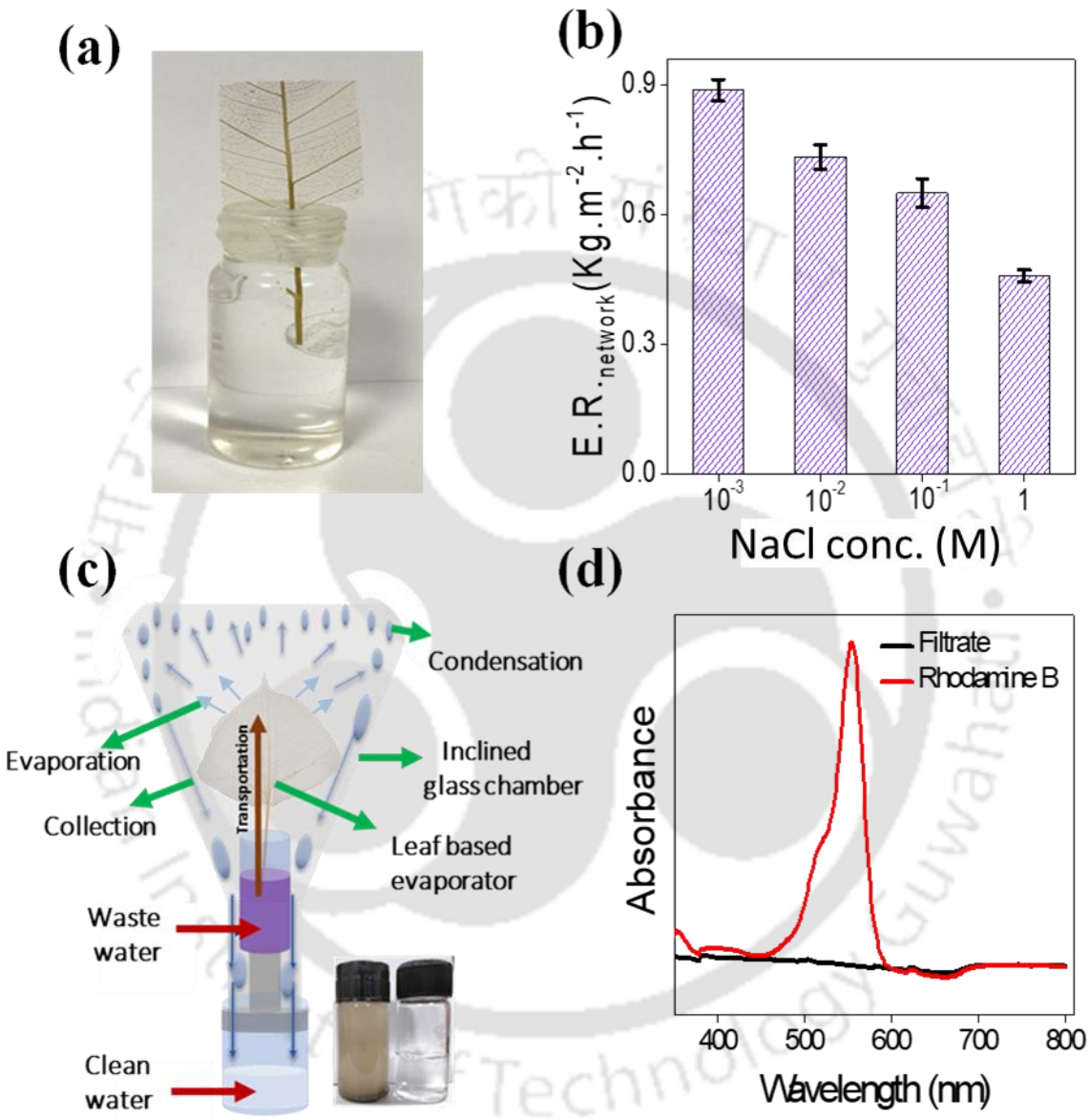

Fig. 6.9: Application of isolated leaf veins: (a) Digital photo of the E.R.$_{network}$ based Evaporating system, where midrib veins are extended with definite portion (6 cm^2) of venation network. (b) E.R.$_{network}$ values through naked vein network with varying salt concentrations under 35 °C atmospheric temperature and 30 % RH (c) Schematic illustration of the experimental set up used for condensing the molecules evaporating from waste water (mud water, sea water, and dye solution) through naked vein network. Inset shows photo of the mud water before and after evaporation. (d) UV-vis spectra and digital photos of Rhodamine B (0.01 M) solution before and after evaporation through the vein network.

vials all around the vein structures to limit the evaporation of water molecules through secondary pathways. Remarkably, within 5 hours of the experiment, ~ 5 ml of clean water was collected at the water collection chamber. The experiment was also repeated for muddy water and 0.01 M rhodamine B dye. The water samples collected from concentrated salt and dye solutions did not show any salt or dye ions in the detectable range. UV-Vis spectra and digital photos of the dye solutions before and after evaporation through the vein network is shown in Fig. 6.9d. However, after 48 hours of operation time salts molecules tends to deposit on the surface of the leaf evaporator as shown in Fig. 6.10, resulting in the reduction of the E.R. value. But the accumulated salts can be removed via simple physical shaking or by washing with water and removal of salts via washing process did not seem to have significant impact in the evaporation efficiency of the leaf based evaporator.

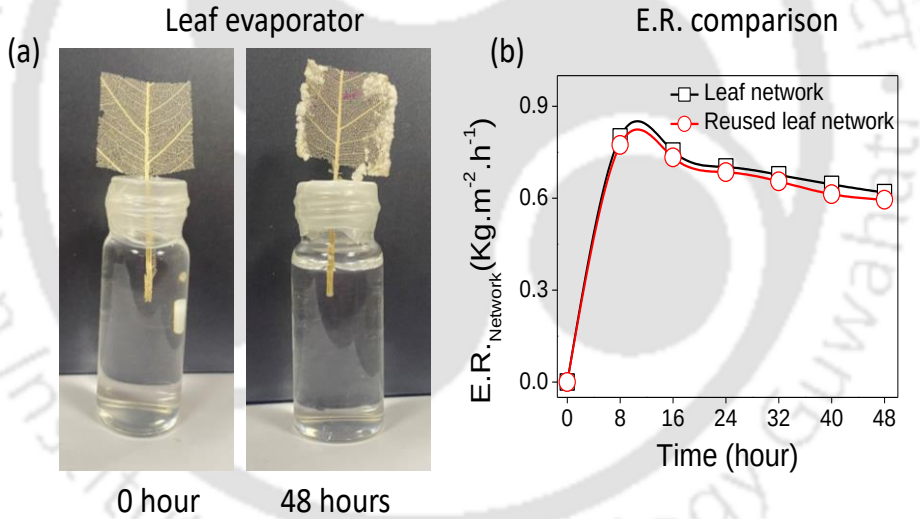

Fig. 6.10: Stability of the leaf vein based evaporator: (a) Digital images of the leaf based evaporator showing the accumulation of salt over its surfaces after 48 hours of operation. (b) E. R. comparison of the reused leaf after removing the accumulated salt via normal washing process.

Leaf based Steam generators possesses some decisive advantages over conventional solar stream generator. In solar steam generator devices photo-active materials are employed to convert sunlight into heat, which in turn induces rapid evaporation of the surrounding water molecules. However, utilization of photo-active materials complicated the overall process by invoking some exclusive requirement such homogeneous exposure of light throughout the

photoactive material, thermal insulation between the active material and bulk liquid, and periodic removal of the deposited salts in order to avoid blocking of light and capillary pores.[16,17] Being non-dependent on the light irradiation process, leaf based steam generator excluded such requirement and make the steam generation process facile and cost effective.

Leaf veins are made of dense micro and nanofibrils bearing negative surface charges, and such charges on the walls of tiny channels possess the ability to break electrical neutrality of electrolytes flowing through it.[36,37] This property of the minuscule biochannels is exploited here to harvest electrical energy through electrokinetic streaming potential. As a proof of the concept, two Ag/AgCl electrodes were installed in the midrib vein of a vein network (area 13 cm^2) at a distance of 7 mm apart. As soon as the base of the midrib vein was immersed into liquid water, a constant flow of water molecules occurs through the channels of midrib vein. The rapid evaporation in the vein network is the driving force behind this uphill flow of the liquid water. The flow of DI water generated an open-circuit potential of 120 mV between the two Ag/AgCl electrodes installed along the midrib vein (Fig. 6.11 a). Further, the potential generated by water transportation can be easily controlled by tuning the evaporation rate. For example, exposure of halogen light (at 30 °C) drastically improved the evaporation rate from 0.133 to 2.1 kg m^{-2} h^{-1}, and concomitant with this enhanced evaporation rate the open-circuit potential was also improved from 120 mV to 280 mV, shown in Fig. 6.11a. As soon as the light was put off, the voltage went down to original values and these cycles of controlling the output voltage by applying light/heat energy can be repeated multiple times, see Fig. 6.11b. The experiment of streaming potential generation was also repeated with salt solutions of different concentrations (10^{-6} to 1 M). As shown in Figure 6.11c, the plot of salt-concentrations vs open-circuit voltage shows two distinct characteristic regimes. In the low concentration regime (10^{-6} to 10^{-2} M), the voltage increases with increasing salt concentration, but in the high concentration regime (10^{-2} to 1 M), it decreases with increasing salt concentration. In order to

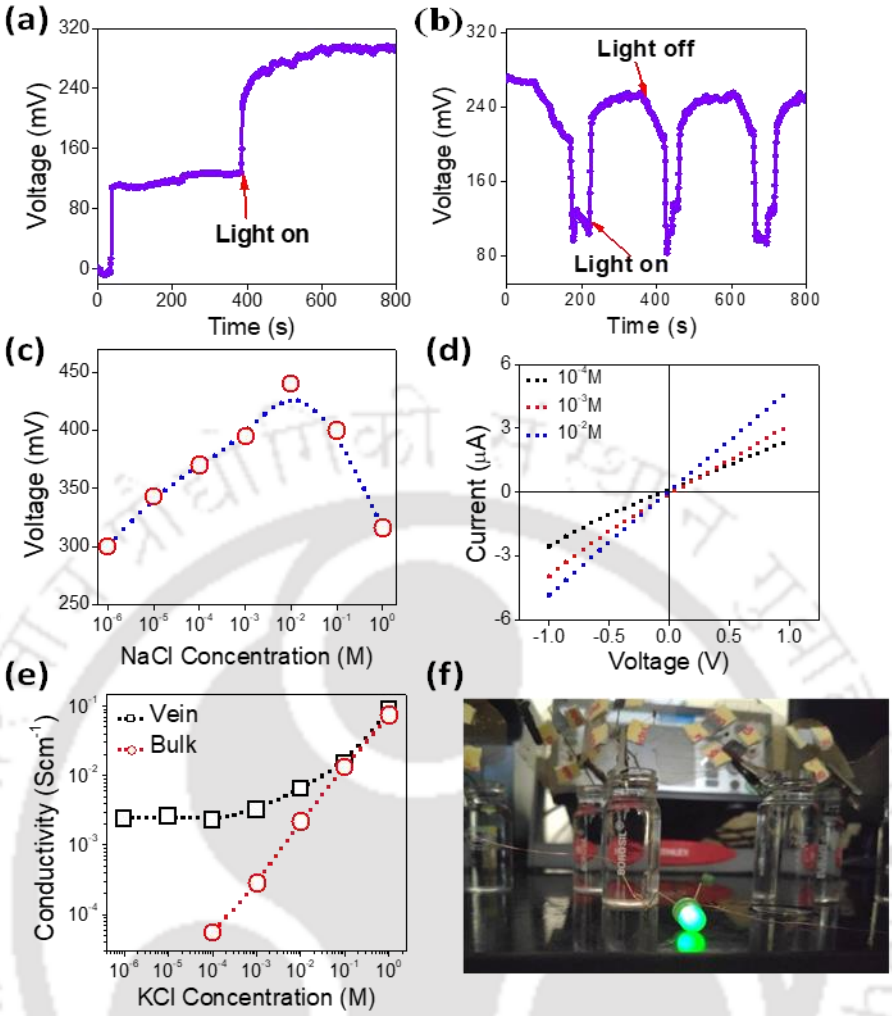

Fig. 6.11: Streaming potential through naked leaf veins: (a) Plot of open circuit potential generated by the water molecules streaming through the leaf veins as a function of time. Exposure of a halogen light (intensity 10^4 lux, at 30 °C) drastically improves the evaporation rate (from 0.133 to 2.5 kg/m2h), a concomitant enhancement is also reflected in the values of open circuit potential (b) Tuning of open circuit voltage of leaf vein by the exposure of halogen light (intensity 10^4 lux, at 30 °C) in repetitive cycles. (c) Open circuit voltage of leaf veins as a function of the NaCl concentration in the water reservoir. (d) Current-voltage (*I-V*) curves, and (e) Ionic conductivity as a function of KCl concentration through the nanofluidic device of isolated midrib vein. Vein-based nanofluidic device shows the typical characteristics of surface-charge-governed ionic conductivity. (f) Application of streaming potential generated in the leaf vein to power an LED (3V).

understand this behaviour, a nanofluidic device of isolated midrib vein was constructed and *I-V* curves were measured through the leaf vein-based nanofluidic device. As shown in Fig. 6.11e, the biochannels of leaf vein exhibit the characteristic surface-charge-governed ionic

conductivity of nanofluidic channels. Comparison of the curves in Fig. 6.11c and Fig. 6.11e suggests that in the low concentration regime (10^{-6} to 10^{-2} M), where transport of the ions is controlled by the surface charges of the biochannels, the open-circuit voltage increases with increasing concentration of the ionic species. On the other hand, at the high concentration regime (10^{-2} to 1 M), the increasing salt concentrations increase the shielding of negative surface charges. As a result, the effectiveness of the surface charges in breaking the charge neutrality decreases, and concomitantly the magnitude of open circuit potential decreases [38-40]. The voltage generated from the solutions streaming through the leaf veins can also be used to carry out useful works such as lighting of LED. Fig. 6.11f shows lighting of a 3V LED by connecting ten number of leaf vein network based devices in series.

5.5: Conclusion

In conclusion, we have demonstrated that the veins of natural leaf exhibit remarkable evaporation efficiency under ambient conditions. The evaporation rates can be further improved by tuning the environmental conditions like temperature, humidity, and wind speed. Even in the dark conditions, with the help of air flow, naked leaf veins exhibit an evaporation rate at par with the best photo-thermal material-based solar steam generators under intense light (one sun). Materials with such a high evaporation rate could find multiple applications in areas like water desalination, harvesting of streaming potential, harnessing of exquisite salts and molecules, and humidification. The isolated leaf veins can be an ideal host for photo-thermal materials like plasmonic nanoparticles or carbon-based nanomaterials in order to develop solar vein-based evaporator for futuristic water treatment and energy harvesting.

6.6: References:

1. X. Zhang, H. Liu and L. Jiang, *Adv. Mater*., 2019, **31**, 1804508
2. Y. Li, M. A. Alibakhshi, Y. Zhao and C. Duan, *Nano Lett*., 2017, **17**, 4813.
3. B. Radha, A. Esfandiar, F. C. Wang, A. P. Rooney, K. Gopinadhan, A. Keerthi, A. Mishchenko, A. Janardanan, P. Blake, L. Fumagalli, M. Lozada-Hidalgo, S. Garaj, S. J. Haigh, I. V. Grigorieva, H. A. Wu and A. K. Geim, *Nature*, 2016, **538**, 222.
4. R. Gimenez, G.J. Soler-Illia, C.L.A. Berli and M.G. Bellino, ACS nano, 2020, 14, 2702-2708.
5. A.H. Persad and C.A. Ward, *Chem. Rev.*, 2016, **116**, 7727.
6. S. Narayanan, A.G. Fedorov and Y.K. Joshi, *Langmuir*, 2011, **27**, 10666.
7. X. Wu, G.Y. Chen, W. Zhang, X. Liu and H. A. Xu, *Adv. Sustainable Syst*., 2017, **1**, 1700046.
8. E. Steudle, *J. Exp. Bot.*, 2000**, 51**, 1531.
9. P. S. Nobel, Physicochemical and Environmental Plant Physiology. pp. 635 (Academic Press, Inc., San Diego, CA. 1991).
10. H. Zhou, X. Li, T. Fan, F. E. Osterloh, J. Ding, E. M. Sabio, D. Zhang and Q. Guo, *Adv. Mater*., 2010, **22**, 951.
11. G.G. Coté and M. Gibernau, *Am. J. Bot.*, 2012, **99**, 1231.
12. B. Han, Y. Huang, R. Li, Q. Peng, J. Luo, K. Pei, A. Herczynski, K. Kempa, Z. Ren and J. Gao, *Nat. Commun*., 2014, **5**, 1.
13. H.K. Kim, J. Park and I. Hwang, *J. Exp. Bot*., 2014, **65**, 1895-1904.
14. F. Jiang, H. Liu, Y. Li, Y. Kuang, X. Xu, C. Chen, H. Huang, C. Jia, X. Zhao, E. Hitz and Y. Zhou, *ACS Appl. Mater. Interfaces*, 2018, **10**, 1104.
15. Y. Lin, H. Xu, X. Shan, Y. Di, A. Zhao, Y. Hu and Z. Gan, *J. Mater. Chem. A*, 2019**, 7**, 19203.

16. S. He, C. Chen, Y. Kuang, R. Mi, Y. Liu, Y. Pei, W. Kong, W. Gan, H. Xie, E. Hitz, C. Jia, X. Chen, A. Gong, J. Liao, J. Li, Z. J. Ren, B. Yang, S. Das and L. Hu, *Energy Environ. Sci*., 2019, **12**, 1558.

17. G. Ni, S. H. Zandavi, S. M. Javid, S. V. Boriskina, T. A. Cooper and G. Chen, *Energy Environ. Sci.*, 2018, **11**, 1510.

18. T. Li, S.X. Li, W. Kong, C. Chen, E. Hitz, C. Jia, J. Dai, X. Zhang, R. Briber, Z. Siwy, M. Reed and l. Hu, *Sci. Adv.*, 2019**, 5**, eaau4238.

19. T. Li, X. Zhang, S. D. Lacey, R. Mi, X. Zhao, F. Jiang, J. Song, Z. Liu, G. Chen, J. Dai, Y. Yao, S. Das, R. Yang, R. M. Briber and L. Hu, *Nat. Mater*., 2019, **18**, 608.

20. S. S. Das, V. M. Pedireddi, A. Bandopadhyay, P. Saha and S. Chakraborty, *Nano Lett*., 2019, **19**, 7191.

21. M.-B. Wu, Y.-M. Hong, C. Liu, J. Yang, X.-P. Wang, S. Agarwal, A. Greiner and Z.-K. Xu, *J. Mater. Chem. A*, 2019, **7**, 16735.

22. T. Yang, J. Cao and E. Ma, *Ind. Crops Prod*. 2019, **135**, 91.

23. J. Wu, Y. Wu, F. Yang, C. Tang, Q. Huang and J. Zhang, *Composites, Part A*, 2019, **117**, 324.

24. A. Khakalo, A. Tanaka, A. Korpela and H. Orelma, *ACS Appl. Mater. Interfaces*, 2020, **12**, 23532.

25. Z. Li, C. Chen, R. Mi, W. Gan, J. Dai, M. Jiao, H. Xie, Y. Yao, S. Xiao and L. Hu, *Adv. Mater.*, 2020, **32**, 1906308.

26. D. Hou, T. Li, X. Chen, S. He, J. Dai, S. A. Mo□d, D. Hou, A. Iddya, D. Jassby, R. Yang, L. Hu and Z. J. Ren, *Sci. Adv*., 2019, **5**, eaaw3203.

27. X. Chen, X. Zhu, S. He, L. Hu and Z. J. Ren, *Adv. Mater.*, 2020, 2001240.

28. Y. Wu, J. Zhou, Q. Huang, F. Yang, Y. Wang and J. Wang, *Polymers*, 2020, **123**, 661.

29. C. Jia, F. Jiang, P. Hu, Y. Kuang, S. He, T. Li, C. Chen, A. Murphy, C. Yang and Y. Yao, *ACS Appl. Mater. Interfaces*, 2018, **10,** 7362.

30. C. Jia, Y. Li, Z. Yang, G. Chen, Y. Yao, F. Jiang, Y. Kuang, G. Pastel, H. Xie, B. Yang, S. Das and L. Hu, *Joule*, 2017, **1**, 588.

31. M. Zhu, Y. Li, G. Chen, F. Jiang, Z. Yang, X. Luo, Y. Wang, S. D. Lacey, J. Dai, C. Wang, C. Jia, J. Wan, Y. Yao, A. Gong, B. Yang, Z. Yu, S. Das and L. Hu, *Adv. Mater*., 2017, **29**, 1704107.

32. F. Chen, A. S. Gong, M. Zhu, G. Chen, S. D. Lacey, F. Jiang, Y. Li, Y. Wang, J. Dai, Y. Yao, J. Song, B. Liu, K. Fu, S. Das and L. Hu, *ACS Nano*, 2017, **11**, 4275.

33. Y. Zheng, H. Bai, Z. Huang, X. Tian, F.-Q. Nie, Y. Zhao, J. Zhai and L. Jiang, *Nature*, 2010, **463**, 640.

34. J. Ju, H. Bai, Y. Zheng, T. Zhao, R. Fang and L. Jiang, *Nat. Commun*., 2012, **3**, 1247.

35. A. Einstein, *Ann. Phys. (Berlin, Ger.)* 1905, **322**, 549.

36. J. Yin, X. Li, J. Yu, Z. Zhang, J. Zhou, W. Guo, *Nat. Nanotechnol*. 2014, **9**, 378.

37. G. Xue, Y. Xu, T. Ding, J. Li, J. Yin, W. Fei, Y. Cao, J. Yu, L. Yuan, L. Gong, J. Chen, S. Deng, J. Zhou and W. Guo, *Nat. Nanotechnol*., 2017, **12**, 317.

38. F. H. van der Heyden, D. Stein and C. Dekker, *Phys. Rev. Lett*., 2005, **95**, 116104.

39. P. Yang, K. Liu, Q. Chen, J. Li, J. Duan, G. Xue, Z. Xu, W. Xie and J. Zhou, *Energy Environ. Sci.*, 2017, **10**, 1923.

40. H. Ren, M. Tang, B. Guan, K. Wang, J. Yang, F. Wang, M. Wang, J. Shan, Z. Chen, D. Wei, H. Peng and Z. Liu, *Adv. Mater*., 2017, **29**, 1702590.

Thesis overview and future outlook:

One major challenge faced by the researchers in the field of nanofluidic study is extrapolating the property and phenomena observed in the individual nanochannels into a macroscopic platform toward practical applications/demonstrations. So the aim of this research work is to explore the properties of biomimetic and bio-derived nanofluidic systems and is to demonstrate their potential in different real time applications. To accomplish the research aim, research methodology was designed and implemented and the major achievement of the thesis work is listed below in chapter-wise manner:

Summary of Chapter 2:

Chapter 2 demonstrated a biomimetic approach of fabrication of hybrid nanofluidic system via self-assembling colloidal dispersions of graphene oxide (GO) and humic acid (HA). Here, we have explored the possibility of tuning the transport characteristics of GO nanofluidic membranes without sacrificing their lamellar structure or altering the channel's heights. Humic acid, a naturally occurring organic material, is applied here as a synergistic spacer to tune the network of GO nanochannels. With a structure chemically and physically similar to that of GO, humic acid caused an all-around improvement of the GO lamellar membrane. With such improvement, the hybrid GO-HA lamellar membranes were found to be ideal for applications like water desalination and renewable energy harvesting from reverse electrodialysis.

Summary of Chapter 3:

Chapter 3 demonstrated another biomimetic approach of fabrication of nanofluidic system via self-assembling exfoliated colloidal dispersion of positively charged CoAl layered double hydroxide (CoAl LDH). Unlike the conventional 2D materials, LDH panoply remarkable anion selectivity and the inherent anion selectivity of CoAl layered double hydroxide is exploited in this work to achieved multidirectional application. Due to the perm-selective nature of

positively charged layered double hydroxide membrane (P-LDHM), it panoply remarkable anion conductivity in the surface charge governed region and this ion selective features of P-LDHM is also utilized to harvest electricity from salt concentration gradient via applying the principle of RED. Moreover, the p-LDHM based device shows shape dependence ionic transport behaviour, while a rectangularly cut p-LDHM device shows linear *I-V* curve, the triangularly cut p-LDHM shows non-linear *I-V* curves similar to a diode. The ionic current rectifying behaviour of triangular p-LDHM can also be utilized to achieve anion pumping under the presence of a fluctuating electrical potential with a mean value of zero.

Summary of chapter 5:

In chapter 5, we have demonstrated the utilization of biological nanochannels extracted from potato tuber for nanofluidic study. The biological nanochannels possess various elementary nanofibrils with permanent negative charges and hence panoply several nanofluidic phenomena analogous to its artificial nanofluidic devices. The bio-nanochannels-based nanofluidic devices exhibit various nanofluidic phenomena like surface-charged-governed ionic conductivity and thereby help in the development of transmembrane potential. The mobility of ions in the hydrated bio-nanochannels is found to be higher than that of bulk water. The cation-selective nature of bio-channels was also exploited to harvest a continuous supply of power up to 74 mWm^{-2} for 3 hours from the enzymatic decomposition of urea. The transmembrane potential generated across the bio-channels was also explored for level-free electrical monitoring of enzymatic reactions inside the biological medium.

Summary of Chapter 6:

In chapter 6, we have utilized another bio-derived material in the form of leaf vein network extracted from peepal tree via microbial delignification process. The naked leaf veins exhibit remarkable flux (evaporation rate 1.5 kg m^{-2} h^{-1}) of capillary evaporation under ambient

condition (25 °C and 30 % RH), close to the photothermal material-based evaporators reported in the recent literature. The evaporation rates can be further improved by tuning the environmental conditions like temperature, humidity, and wind speed. Even in the dark conditions, with the help of air flow, naked leaf veins exhibit an evaporation rate at par with the best photo-thermal material-based solar steam generators under intense light (one sun). Leaf veins are made of dense micro and nanofibrils bearing negative surface charges, and such charges on the walls of tiny channels possess the ability to break electrical neutrality of electrolytes flowing through it. This property of the minuscule biochannels is exploited here to harvest electrical energy through electrokinetic streaming potential. With such superiority, our leaf vein-based evaporator has the potential to perform multiple valuable works such as water desalination, humidification, and electricity generation in a single operation.

Future outlook:

We have noticed several significant outcomes of the as conducted research work related to facile fabrication and applications of biomimetic and bio-derived nanofluidic systems. The current thesis work has explored the properties of biomimetic and bio-derived nanochannels and of utilized the same to fabricate nanofluidic conduits for multiple application purposes, notably for manipulating molecular/ionic transportation, concentration gradient based energy harvesting, uphill ion pumping, level free monitoring of enzymatic reactions and water steam generation. Indeed, there are so many possibilities that can be explored in future to extend the presented work which been proposed below.

- A major problem faced by the traditional proton exchanged membranes like nafion in direct methanol fuel cell (DMFC) applications is the high methanol permeability, which leads to a crossover effect. As we have already highlighted in chapter 2, incorporation of humic acid as a synergistic spacer in GO laminates not only improves the proton

conductivity of pristine GO membrane but also reduce the methanol permeability through it. With such improvement GO-HA membranes may be a preferred candidate of choice over GO membranes for DMFC applications.

- Utilization of both the cation and anion-selective membrane is desired to enhance the operational performance of several futuristic applications such as osmotic power generation, seawater desalination, and regulated ionic/molecular transportations. Utilization of cation selective 2D membrane is well documented in literature and hence we put emphasis on the development of anion selective 2D membrane. However as compared to the cation selective 2D membranes like GO, Clay, MXene etc., LDH is comparatively less stable and hence future research can be conducted to provided rigidity to LDH based system to make it more appealing from industrial point of view.
- Nature produces a plethora of nanochannels to carry out highly complex biological tasks in a sophisticated manner. There have been several studies to understand the characteristics of these channels; however, efforts to apply them for technological advancements are still scarce. Here, we have demonstrated that the fluidic channels of biomaterials can be harvested as nanofluidic devices to produce energy from enzymatic chemical reactions. Looking at the large variety of natural nanofluidic channels, it should be possible to create/develop different kinds of nanofluidic devices for future applications.
- Electricity is produced in leaf vein base system, when the charge nano- capillaries break the electrical neutrality of electrolytes flowing through it. The magnitude of electricity generation is dependent on two parameter *viz* surface charged density on the walls of vein nano- capillaries and electrolyte flow rate through it. So we could have possibly enhanced the magnitude of streaming potential generation by either incorporating a charge polymer/nanoparticles that might increases the overall surface charge density or

via incorporating plasmonic nanomaterials that will possibly increase the mass of flow due to its localised heating effect.

List of works performed during Ph.D. tenure

Included in thesis:

1. Nanofluidic Transport through Humic Acid Modified Graphene Oxide Nanochannels.

   T. J. Konch, R. K. Gogoi, A. Gogoi, K. Saha, J. Deka, K. Anki Reddy and K. Raidongia, *Mater. Chem. Front*., 2018, 2, 1647.

2. Uphill Anion-Pumping through Triangular Nanofluidic Device of Reconstructed Layered Double Hydroxide.

   T. J. Konch, T. Dutta, R. Gogoi, A. B. Neog and K. Raidongia, (Just accepted in *J. Phys. Chem. C.*)

3. Disposable Fluidic Devices of Bionanochannels for Enzymatic Monitoring and Energy Harvesting.

   T. J. Konch, A. P. Bora and K. Raidongia, *ACS Appl. Bio Mater.,* 2019, **2**, 2549.

4. Remarkable Rate of Water Evaporation through Naked Veins of Natural Tree-leaf.

   T. J. Konch, T. Dutta, and K. Raidongia, (Just accepted in *ACS omega*)

Excluded from thesis:

5. Water and Salt Dynamics in Multilayer Graphene Oxide (GO) Membrane: Role of Lateral Sheet Dimensions.

   A. Gogoi, **T. J. Konch**, K. Raidongia and K. Anki Reddy, *J. Membr. Sci.,* 2018, **563** 785.

6. A two-Dimensional Ion-Pump of a Vanadium Pentoxide Nanofluidic Membrane.

   R. K. Gogoi, A. B. Neog, **T. J. Konch**, N. Sarmah and K. Raidongia, *J. Mater. Chem. A,* 2019, **7**, 10552.

7. Reconstruction of Soil Components into Multifunctional Freestanding Membranes. J. Deka, K. Saha, **T. J. Konch**, R. K. Gogoi, S. Saikia, P. P. Saikia, G. K. Dutta and K. Raidongia, *ACS Omega,* 2019, **4**, 1292.
8. The range of antiferromagnetic coupling governs the conductivity: semiconducting behavior and ammonia gas sensing property of diamagnetic hexaradical-containing tetranuclear Co^{III}_4 cluster and its nonradical congener.

   P. Sarkar, **T. J. Konch**, T. Kamilya, K. Raidongia, S. Acharya and C. Mukherjee, *Chem. Commun.,* 2020, **56**, 15220.

List of Conferences/Seminars attended during the Ph.D. tenure

1. Presented poster entitled "**Nanofluidic Transport through Humic Acid Modified Graphene Oxide Nanochannels**" in Chemconvene-2017, organized by department of chemistry IIT Guwahati, Assam.
2. Presented poster entitled "**Disposable Fluidic Devices of Bionanochannels for Enzymatic Monitoring and Energy Harvesting**" in National conference on Recent Advances in Chemistry (RAC) - 2019, organised by NIT Megalaya.
3. Presented poster entitled "**Disposable Fluidic Devices of Bionanochannels for Enzymatic Monitoring and Energy Harvesting**" in Chemistry and Physics of Materials (ChemPhysMat) - 2019, organised by JNCASR, Bengaluru.
4. Presented poster entitled "**Uphill Anion-Pumping through Triangular Nanofluidic Device of Reconstructed Layered Double Hydroxide**" in Engineering Sciences and Technologies for Environmental Care (ESTEC) - 2020, organised by CSIR NEIST, Jorhat, Assam.

Awards achieved during the Ph. D. tenure

1. Best poster award entitled "**Nanofluidic Transport through Humic Acid Modified Graphene Oxide Nanochannels**" in Chemconvene-2017, organized by department of chemistry IIT Guwahati, Assam.
2. Best poster award entitled "**Uphill Anion-Pumping through Triangular Nanofluidic Device of Reconstructed Layered Double Hydroxide**" in Engineering Sciences and Technologies for Environmental Care (ESTEC)-2020 organised by CSIR NEIST, Jorhat, Assam.